# Table of contents

# List of figures

# List of Tables

# Chapter 1: Introduction to aluminium reduction cell structure and properties

## 1.1. Introduction to aluminium reduction cell structure and operations

### 1.1.1. Aluminium reduction cell structure

The commercial aluminium production process invented by Hall and Héroult in 1886 has not changed fundamentally for the last 120 years. It involves the dissolution of aluminium oxide (alumina) in an electrolyte bath consisting mostly of cryolite ($Na_3AlF_6$), with other fluoride additives such as $AlF_3$, $CaF_2$ and $NaF$, at a temperature of around 960° C. The dissolved alumina is reduced electrochemically to produce aluminium metal, according to Equation 1-1:

*Equation 1-1    $2Al_2O_3\,(soln) + 3C\,(s) = 4Al\,(l) + 3CO_2\,(g)$*
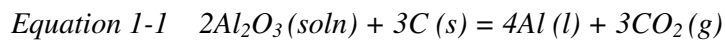
Since the reaction does not occur spontaneously, energy in the form of electrical current at a total cell voltage of around 4-4.5 V is supplied.  The current is passed through carbon electrodes arranged in a horizontal configuration. The carbon electrodes, the lining surrounding them, and the alumina feeder make up the electrolysis cell (Figure 1-1).
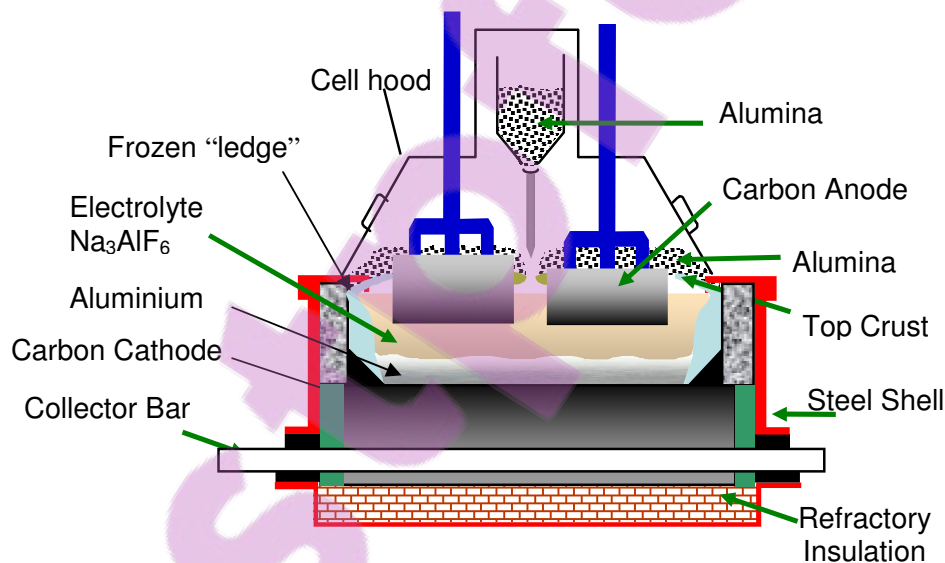


*Figure 1-1: Aluminium reduction cell structure (prebaked anode configuration).*

The individual reduction cell operates at a high electrical current (modern smelters operate above 300,000 A) with voltage in the range of 4 to 4.3V and a typical energy requirement of around 13 kW/kg Al. There are two major types of reduction cells which are distinguished by their anode configuration: the Söderberg cell, which is increasingly rare in modern smelters and found in

around 30% of the world smelters (only 10% of the metal is now produced by this technology), and the modern, and more common, prebaked anode cell.

The Söderberg cell (Figure 1-2) consists of a self-baking anode where carbon paste briquettes are added at the top of the anode. While the anode paste moves slowly downward through the rectangular steel casing, it is softened and gradually baked into a solid composite by pyrolysis of the pitch from the heat coming from the electrolyte bath. Iron studs are immersed into the anode body, either in a vertical or horizontal configuration, and these carry the current. The studs are routinely changed to maintain even current distribution and to avoid severe stud corrosion.
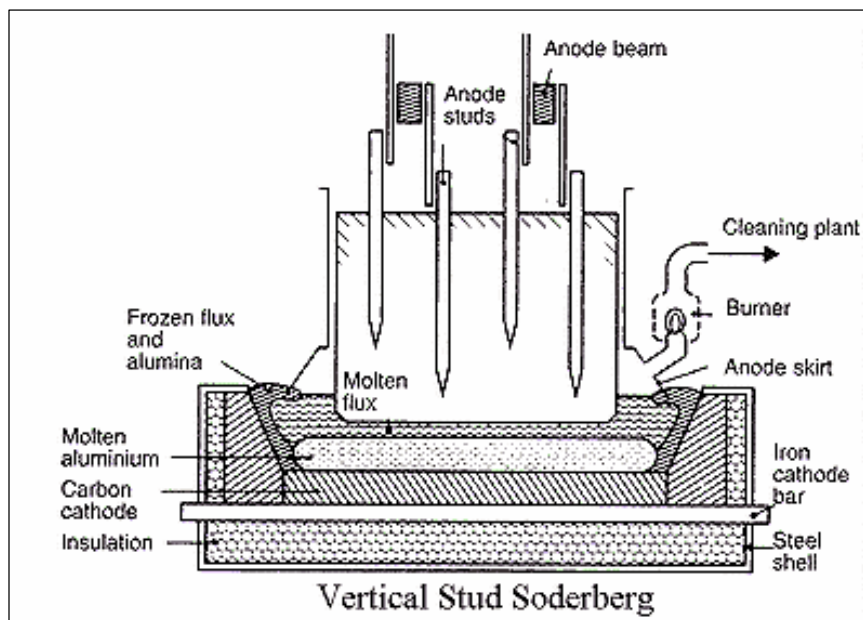


*Figure 1-2: Söderberg cell with vertical studs' configuration [IPAI, 1996].*

In a prebaked anode cell (Figures 1-1 and 1-3) the anodes are made of petroleum coke and cold pitch tar (acting as a binder) and are baked in a separate anode plant. Every cell has between 20 to 40 anodes suspended in the electrolyte by a rod clamped onto a beam supported by the cell superstructure. The beam moves downwards as the anodes are consumed. Used anodes (known as "anode butts") are replaced after a period of 22 -30 days or when ~80% of the carbon is consumed.
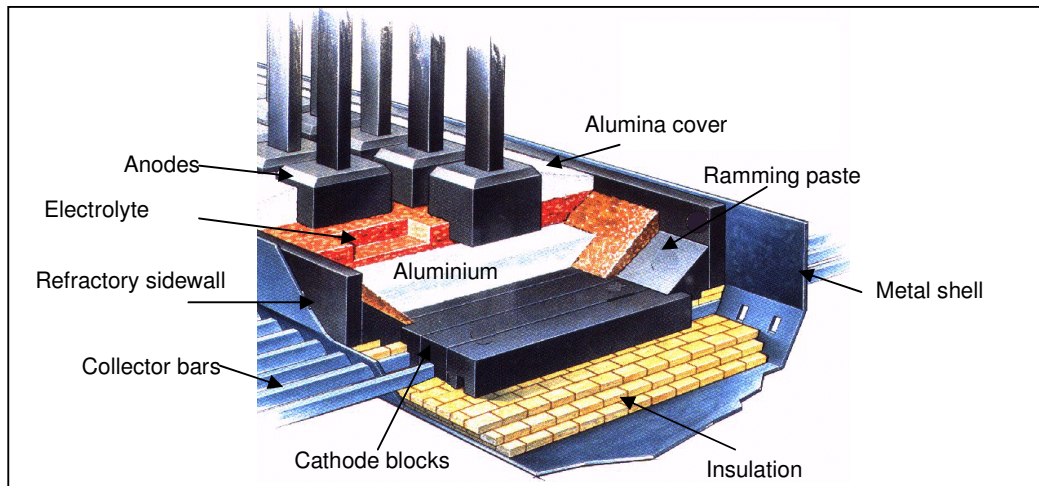
*Figure 1-3: Prebaked cell [1].*

The molten aluminium formed during the reduction process accumulates on the carbon cathode surface and due to its high electrical conductivity acts as the effective cathode. The distance between the anode surface and the aluminium pad, called anode cathode distance (ACD), and it is used to control the cell voltage (to a certain degree). Although the acting cathode in aluminium reduction cell is the molten metal surface, it is common in the industry to use the term cathode to describe the carbon block, as well as the collector bars that carry the current to it. Except for the different anode configuration, the structure of the cell in the prebaked anode cell or Söderberg cell is similar. The reduction cell is encapsulated in a metal shell lined with refractory materials on the sidewalls and a carbon cathode block with insulation at the bottom. The molten metal and electrolyte are contained between the cathode surface and the sidewalls.

The cathodes are made of anthracitic aggregates and synthetic graphite as filler material, with a coal-tar pitch as binder. These are made into prebaked cathode blocks, and when joined together they form the cathode surface. In modern smelters the cathode block design can appear in two different configurations:

- Prebaked cathode blocks, with carbon paste rammed between the joints and seams that surround them, are the most common configuration. The rammed joints are, however, perceived as a weak link that can lead to metal or bath leak.
- Advanced technology consisting of prebaked cathode blocks precisely machined with glued joints which aim to overcome the leak problem of standard rammed joints.

Monolithic cathodes, where the entire carbonaceous body of the lining is made of rammed paste, were historically in common use, but they are rarely used these days.

The non-carbon lining layers below the cathode can be classified into three functional types:

- Bedding materials, acting as a soft and level support for the cathode blocks.
- Dense refractory materials, acting as a diffusion and penetration barrier inhibiting the penetration of corrosive bath constituents and molten metal.
- Insulating low thermal conductivity materials, aiming to reduce the heat loss from the cell.

The ultimate role of lining materials placed below the cathode carbon blocks is to maintain the thermal balance. This balance is important in order to avoid cathode sludge freezing (cold cathode) that will insulate the cathode, or minimize deterioration of under cathode refractory insulation by penetration of liquid (bath or metal) through the cathode (hot cathode). One of the techniques to stop the percolation of molten bath from the cathode is to use a layer of semi insulating materials between the refractory material and the insulation layer. This stabilises the insulation and brings the temperature on the hot side of the highly insulating layer to below the liquidus temperature of the penetrating bath. However, the most popular lining design includes dense refractories at the top, with a soft insulating layer at the bottom (Figure 1-4).
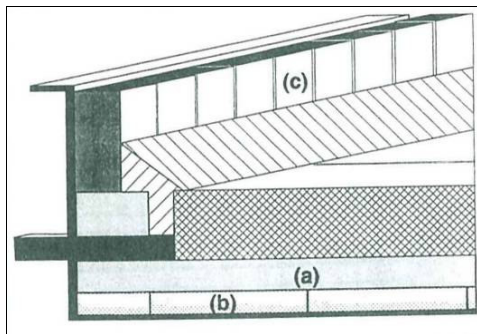


*Figure 1-4: Location of lining in reduction cell, a) high temperature refractory, b) lightweight insulation, c) SiC bricks [2].*

Although both the refractory and the insulation materials are made of inorganic oxides, they present different characteristics. The high density refractory materials (bulk density above 1000 kg/m$^3$) provide resistance to liquid bath and molten aluminium but results in poorer insulating properties, while the low density materials provide good insulation with very poor chemical and physical resistance. Typical compositions of refractory and insulation materials are shown in Table 1-1.

*Table 1-1: Typical composition and approximate densities of refractory and insulating materials used in aluminium reduction cell [3].*

|  | Insulation materials | | Refractory materials | |
|---|---|---|---|---|
| Material | Diatomite | Vermiculite | Chamotte | High alumina |
| $SiO_2$ (%) | 75 | 51 | 56 | 26 |
| $Al_2O_3$ (%) | 12 | 10 | 36 | 71 |
| $Fe_2O_3$ (%) | 6 | 5 | 1.9 | 0.6 |
| CaO (%) | 1 | 1 | | |
| MgO (%) | 2 | 19 | | |
| $K_2O$ (%) | 0.6 | 11 | | |
| $Na_2O$ (%) | | 1 | | |
| $TiO_2$ (%) | | 1 | 1.7 | 1.3 |
| Density (kg/m$^3$) | 750 | 350 | 2100 | 2700 |

The refractory materials protecting the insulation layer form a barrier to prevent bath or liquid metal percolation. This barrier can be a **physical barrier** made of impenetrable or less penetrable materials that slow the bath penetration, or a **chemical barrier** made of materials that are not impenetrable to bath but which can react with the percolating bath components to form an in-situ barrier. These chemical barrier materials consist of calcium silicate or calcium aluminium silicate and can react with sodium fluoride at temperatures of 900°C to form solid compounds resulting in a "freezing" of the molten phase.

The insulation materials can come in the form of molar bricks made of microscopic fossil diatomic skeletons of silica and clay. These bricks provide excellent thermal insulation due to their high porosity (in the range of 65-85%). However, due to their low resistivity toward molten bath, the insulation bricks should be kept below the freezing isotherms of bath components in order to be protected.

The cathode blocks are placed around 15 to 25 cm from the sidewall and the industry terminology of the gap is the "Big joint". On the bottom half of the cathode block the gap is filled with a "compressible" material to accommodate the expansion of the cathode during the heating stage prior to the introduction of molten bath (the bake out stage of cell start-up). Above the compressible material, the gap between the upper half of the cathode block and the refractory material can be filled with carbon paste or precast block. The carbon paste is rammed above the cathode surface to form a slope. The precast block can be made of either anthracite or silicon carbide (especially when the refractory sidewalls are made of silicon carbide). Figures 1-5 and 1-6 depict the different components of the cathode linings.
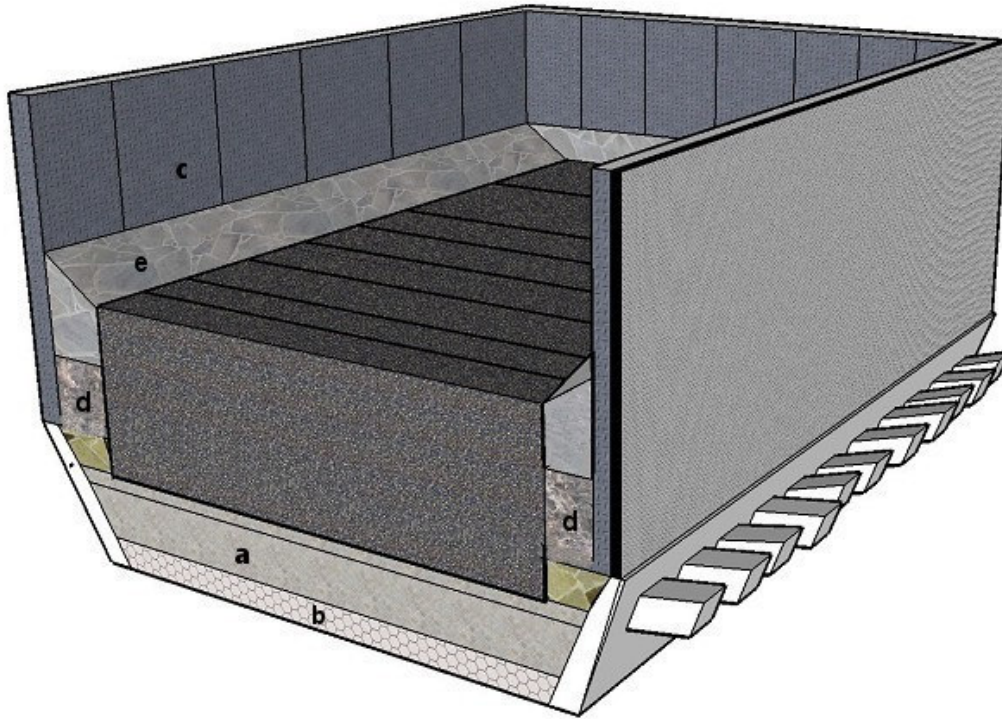
*Figure 1-5: Cross section of aluminium reduction cell (without anodes) a- refractory barrier material, b- insulation material, c- SNBSC sidewall bricks, d-"compressible" material, e-precast block.*



*Figure 1-6: Picture taken from reduction cell, the sidewall with SNBSC bricks at the top and ramming paste slope at the bottom above the cathode surface.*

The sidewall lining is made of insulation material up to half of the cathode block level to ensure minimum heat loss from the cathode block. Heat loss in this area can lead to accumulation of the undissolved alumina (sludge) that will insulate the cathode surface. The area above the insulating material in the sidewall (see Figure 1-6) is lined with refractory material resistant to attack by electrolyte, molten aluminium and air oxidation. Anthracite carbon was used as the traditional

sidewall material and is still in use in some smelters. However in the last two decades, silicon nitride bonded silicon carbide (SNBSC) has become the state of art material for sidewall lining, replacing the carbon materials, and is used in most modern smelters.

After the cell lining installation is completed, the cell is heated up to above 900°C prior to the introduction of molten bath and metal (baked out period) to allow expansion of the cathode blocks and baking of the rammed paste that fills the gaps and seams in order to seal the cell cavity. The molten bath is introduced into the cell only after the lining materials in contact with it have reached the desired temperature (above 900°C).

The life of the reduction cell is critically dependent on the performance of these cell lining materials. The early failure of aluminium reduction cell sidewalls equipped with the state of the art silicon nitride bonded silicon carbide refractories is the reason for conducting this study.

The central aim of this research work is to understand the degradation mechanism of silicon nitride bonded silicon carbide refractories degrade in the industrial reduction cell environment and to explore options for improved materials. In this thesis, the properties and performance of SNBSC sidewall refractory materials used in aluminium smelters are examined, in particular their resistance to degradation in the reduction cell environment. The thesis experimentally tests the corrosion resistance and examines the degradation mechanism for these SNBSC sidewall materials.

**1.1.2. Cell heat balance**

The molten electrolyte in the reduction cell provides resistance to the passage of current. Therefore the heat-generating parameters in the cell are the current density and the anode cathode distance (ACD). For an operating cell where parameters like cell design, anode size, amperage, and thermal insulation are predetermined, the heat loss is controlled only by managing the cell voltage which is governed by ACD. It is difficult to reduce the ACD below around 4 cm in order to avoid short circuits, or extensive back reaction between the aluminium and carbon dioxide which would lead to reduction of the current efficiency. The cell design should optimize the cell performance, allow for the extraction of enough heat to maintain a protective frozen ledge on the sidewall, while maintaining bath temperature above the bath freezing point and allowing sufficient superheat to ensure rapid dissolution of alumina.

In a cell requiring 14 kWh to produce 1 kg of metal, approximately half the energy is lost as heat. Therefore in a 150 kA cell the heat loss rate is in the order of 380kWh. The heat losses from a cell can be subdivided into three zones:

- The top
- The ends and sidewalls
- The bottom of the cell (including collector bars)

The heat loss from the top of the cell can be as high as 40 to 60% of the overall heat loss; this includes heat loss from the anode body, the stubs and the solid alumina/crashed bath crust that covers the anode top as well as the gap between the anode blocks and the sidewalls. Control of the heat losses from the top of the cell can be achieved by adjusting the thickness and composition of the anode cover.

The heat loss from the bottom of the cell is dominated by thermal conduction and is therefore related to the thermal conductivity of the insulating materials. Penetration of molten bath into the cathode block and to the lining beneath it will damage it and will change the thermal conductivity of both the cathode and the lining materials under it. In order to minimize the damage of the percolating bath, the thermal isotherms should be located in a way that the eutectic freeze of the bath will be in the refractory layer above the insulation layer. Figure 1-7 depicts the heat losses of various parts of the reduction cell expressed as a percentage of the total heat losses.
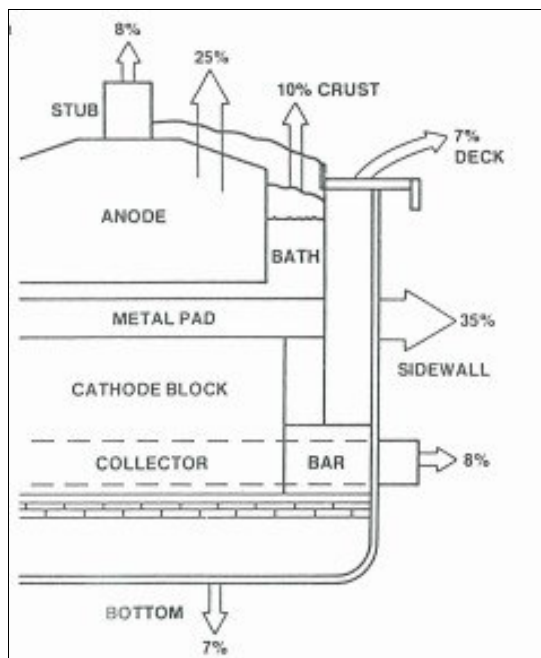


*Figure 1-7: Typical heat losses distribution in a prebaked anode cell [4].*

It is evident from figure 1-7 that the thermal conductivity of the sidewall materials is of great importance in cell design and maintenance of the thermal balance. A sidewall with high thermal resistivity (due to the thermal properties of refractory brick or thick insulation layer) will not maintain a protective frozen ledge, and will be exposed to chemical attack from the liquid bath and the corrosive vapors. Such attack will erode or disintegrate the sidewall material until the thermal resistivity is reduced sufficiently to form a frozen ledge. Alternatively, if the heat conductivity of the sidewall materials is too high, a thick frozen ledge will be formed, increasing the sidewall thermal resistivity. It seems that, to a certain degree, the cell can self-compensate for design errors, however, in extreme cases, high thermal resistivity of the sidewall can lead to refractory failure and tap-out from the metallic shell. On the other hand, high thermal conductivity of the sidewall could form a thick ledge layer that would entrap the anodes and insulate the cathode.

The heat losses from the sidewalls, in a typical 150 kA cell with carbon sidewalls, are in range of 90-130 kWh, depending on the insulation. The conductive heat transport through the sidewall is influenced by the sum of the thermal resistance of the frozen ledge, the sidewall refractory blocks, the insulation layer and the steel shell (as shown in Figure 1-8).
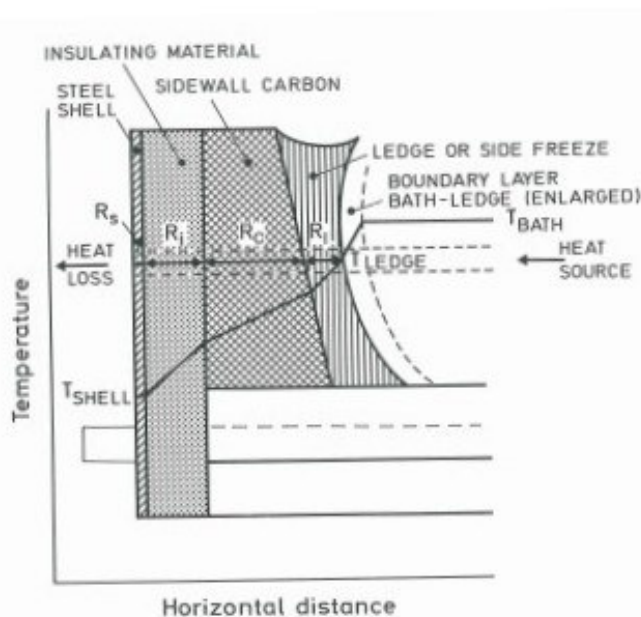


*Figure 1-8: Steady state one-dimensional heat transfer through the sidewall section [5].*

In a steady state condition, the heat dissipation through the sidewall is given by Equation 1-2:

*Equation 1-2*  $(T_B\text{-}T_L) = \dfrac{(T_L - T_S)}{h_B(R_S + R_l + R_c + R_i + \dfrac{t_L}{K_L})}$

Where $T_B$ is the bath temperature and $T_L$ is the bath liquidus temperature. The left side of Equation 2 represents the superheat - the degrees centigrade above the minimum operating temperature for the electrolyte composition. $h_B$ on the right side of the equation represents the boundary layer bath-ledge heat transfer coefficient, $T_S$ is the outer steel shell temperature. $R_S$, $R_W$, $R_i$ are the thermal resistances of steel, the sidewall refractory and the insulation layer. $t_L$ is the thickness of the ledge, with $K_L$ its thermal conductivity.

A change in the superheat introduces a transient state by ledge melting. The frozen ledge tends to act as a thermal buffer by the self-control of thermal resistance. The melting or formation of the ledge is dependent on the amount of heat dissipated.

There are other potential sources of thermal disruption. In the case of anode effect, where a voltage excursion arises due to the depletion of dissolved alumina, the cell voltage will increase to above 25 volts within seconds and will steadily rise to around 40 volts or beyond within two minutes, and the ledge will melt at a rate of 10 mm of the side freeze within one minute [5].

### 1.1.3. The reduction cell sidewalls

It can be seen from the discussion above that the aluminium reduction cell sidewalls are subjected to an unusual combination of conditions, varying from extremely reducing to mildly oxidizing. The sidewalls are potentially in contact with different chemical environments:

- Metallic liquid aluminium that also contains some sodium
- Cryolite based electrolyte, containing corrosive fluoride compounds, and having zones saturated with dissolved metal, mainly sodium.
- A gas phase zone higher up the sidewall, saturated with oxidizing species such as $CO_2/CO$, and corrosive gases such as HF and $NaAlF_4$ that can attack the sidewall materials.

This combination of environments means that the sidewall materials should be selected carefully. Any metal or alloy material found in the sidewall will dissolve in the cryolite based electrolyte as cryolite is a universal high temperature solvent and dissolves almost all oxides and most

inorganic salts. Many of the dissolved contaminant metals will eventually end up in the metal pad as contaminants after being reduced at the cathode.

It must be remembered that so far no sidewall material has been developed that is totally corrosion resistant. Thus, in addition to corrosion resistance to the harsh environment of the reduction cell, the sidewall materials should have high thermal conductivity to allow enough heat to dissipate through the walls and form a frozen layer of bath (frozen ledge) that will act as a protective layer against the corrosive electrolyte and gases.

The importance of maintaining frozen ledge to protect the sidewall from corrosion can be seen in trends of bath temperature and presence of silicon contamination in the metal pad. Silicon spikes were associated with high superheat (bath temperature above the melting point of the bath) due to melting of the frozen ledge, high temperature on the sidewall face leading to corrosion of the sidewall (Figure 1-9).
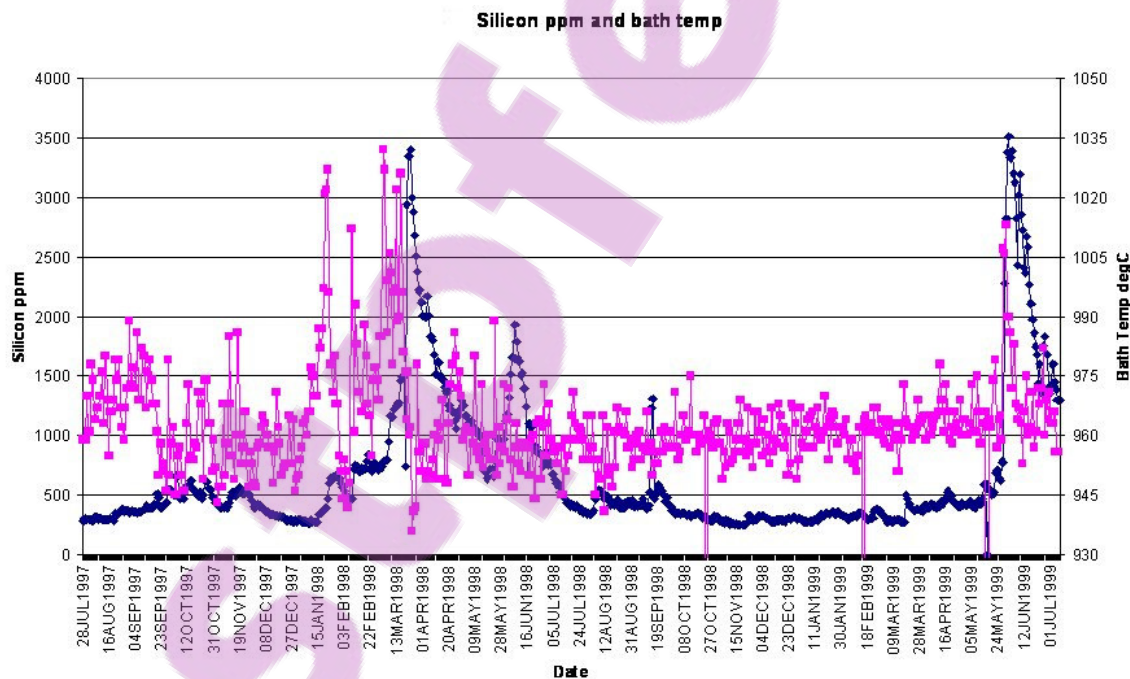


*Figure 1-9: Trends of Si in the metal and bath temperature taken from an operating aluminium reduction cell. High concentrations of silicon in the metal pad (dark blue) are associated with periods of high bath temperature (pink trend). [Courtesy of Rio Tinto]*

Electrical conduction by the sidewall materials, which have a cathodic potential, will alter the current distribution in the cell, thereby causing magneto-hydrodynamic imbalances that will affect the metal pad flow. In the case of carbon based sidewall materials, the current conductivity

11

will create a problem of high corrosion associated with cathodic carbon dissolution. This is one of a number of factors that have led to the adoption of SNBSC materials as the sidewall of choice in modern reduction cells, however as will be detailed, these materials also provide imperfect resistance to the cell environment.

### 1.1.4. Summary

Heat balance is of great importance for the successful operation of the aluminum reduction cell. The cell design should optimize the cell performance: allow for extracting enough heat to maintain a protective frozen ledge on the sidewall, while maintaining bath temperature above the bath freezing point and allowing sufficient superheat to ensure rapid dissolution of alumina.
The use of lining materials should be governed according to the desired functionality of the different components of the reduction cell; sufficient insulation of the cathode to avoid insulation by sludge of the cathode surface and a corrosion resistant material with high thermal conductivity for the sidewalls to allow formation of protective layer.

The sidewall materials should be selected carefully, it should not contain any metal, alloy material, or oxide that could dissolve in the cryolite based electrolyte and end up in the metal pad as contaminants, after being reduced at the cathode. Material with good corrosion resistance is needed to withstand contact with the molten bath in cases of thermal disruption events such as anode effects that could melt the protective frozen ledge.

## 1.2. Review of sidewall refractory materials for aluminium smelting.

### 1.2.1. Carbon based sidewall materials

1.2.1.1. Types and properties

In aluminium smelting cells, the traditional sidewall technology involved prebaked carbon blocks, ramming paste and a combination of both. In some smelters this technology is still in use. The prebaked sidewall blocks are usually manufactured from similar materials as the bottom cathode blocks or even cut from scrap or rejected materials from the cathode production process. Therefore these sidewall materials have similar properties to the cathode materials although the desired sidewall properties should be different from the cathode blocks, especially in their electrical conductivity. The main reasons for using carbon, as a sidelining material, are it is cryolite resistance and low cost (compared to other materials). The lining can be designed and shaped to ensure protection by frozen bath, and its corrosion products: aluminium carbide and sodium saturated carbon particulates, do not introduce contaminants into the metal.

The carbon lining (cathodes and sidewalls) may be divided into three main groups:

1. **Graphitized carbon**- The whole block (aggregate and binder) consists of graphitizable materials that have been heat treated, usually to 3000°C, producing graphitic materials.
2. **Semi-graphitic-** The aggregate is graphitized, but the binder has only been heat treated to normal baking temperatures of ≈1200°C
3. **Amorphous carbon**- None or only part of the filler material is graphitized. The block is baked to 1200°C.

The typical properties of the different carbon lining materials can bee seen in Table 1-2:

*Table 1-2: Carbon lining materials for aluminium electrolysis pots [3].*

| Properties | Amorphous | Semi graphitic | Graphitized |
|---|---|---|---|
| Apparent density ($g/cm^3$) | 1.54 | 1.70 | 1.62 |
| Real density ($g/cm^3$) | 1.90 | 1.92 | 1.95 |
| Total open porosity (%) | 16 | 15 | 21 |
| Specific electrical resistivity ($\Omega/\mu m$) | 40 | 15 | 12 |
| Heat conductivity ( W/mK) | 8 | 45 | 116 |
| Alkaline resistance (ASTM C 454) | 2 | 1 | 1 |
| Oxidation resistance (burn-off test) | 0-1 | 1-2 | 3-4 |

Amorphous carbon linings were typically used for side fed Söderberg cells, whereas graphitic linings are used in modern point fed prebaked cells. Proper sealing between the blocks, and good connection between the carbon side wall and the steel shell are necessary to prevent bath penetration into voids and to ensure overall good stable heat conductivity of the sidewall. Carbon (in various structural forms) has been the dominant material used to contain both the electrolyte and the molten metal. However, it suffers from wear causing degradation of the sidewall that affect the thermal balance of the pot, as well as influencing its stability.

1.2.1.2. Wear mechanisms of carbon sidewall

When exposed to cryolite, the reactive carbon sidewall melt and cathodic potential wear occurs through the following four mechanisms [1]:

- Swelling of the carbon due to sodium intercalation.
- Particle detachment through preferential erosion and swelling.
- Formation of aluminium carbide, especially at the metal-bath interface, which dissolves in a more acidic electrolyte.
- Oxidation caused by air leaks between the metal shell and the lining.
- Cathodic dissolution of sidewall carbon into the melt.

**Swelling due to sodium intercalation-** Neither aluminium, nor the cryolite melt, wet carbon, but the carbon sidewall blocks (and the carbon cathode blocks) are impregnated with sodium by a diffusion mechanism. The interaction between Na and C are enhanced by bond formation through intercalation forming compounds such as $C_{64}Na$ or $C_{12}Na$. [6, 7] The intercalation

compounds are usually accompanied by a molar expansion, which cause mechanical failure due to differential swelling (Figure1-10). This effect will be more substantial in amorphous carbons with poorly developed crystalinity, as the sodium uptake will be higher than for graphitized carbon blocks.
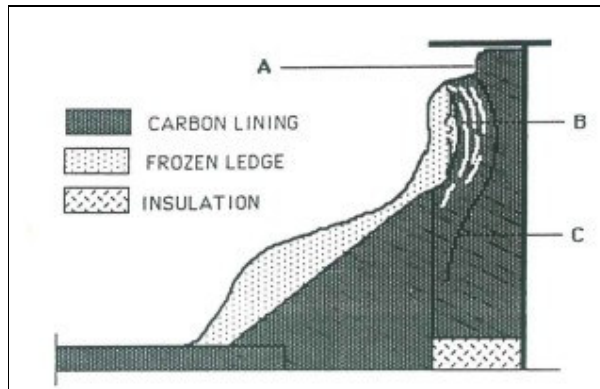


*Figure 1-10: Spalling caused by sodium swelling. This mechanism is combined with air oxidation. A: air oxidation, B: sodium exfoliation cracks, C: isotherm profile [8].*

**Oxidation of the carbon sideline**

Oxidation of the carbon occurs in air at high temperature according to:

*Equation 1-3*          $C_{(s)} + O_2 = CO_{2\,(g)}$

Air-oxidation is enhanced by the presence of impurities, largely metal ions derived from salts. V, Na, Pb, and Cu and catalyse this reaction in high porosity materials in the pore size range of 0.15-15 µm while halogens (F, Cl, Br, and I), boron and phosphorus are inhibitors. High temperature is also a major contributor to air oxidation making thermal conductivity and insulation design an important parameter.

The sidelining could be oxidized from either the bath side, or the top and the back sides. The liquid aluminium pool usually protects the bottom part of the sidelining from oxidation. Oxidation that occurs on the backside could have a cumulative effect since the oxidation will create a gap between the carbon blocks and the steel shell and this air gap will reduce the thermal conductivity of the sidewall leading to melt of the protective frozen ledge, thereby exposing the carbon blocks to chemical attack from the bath (Figure 1-11).
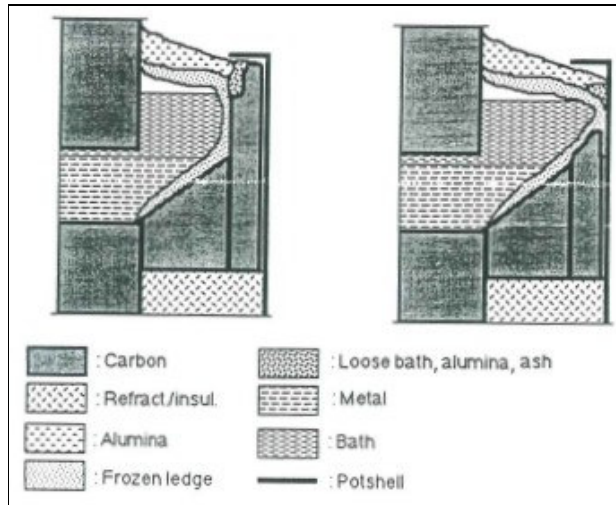
*Figure 1-11: Progressive deterioration of the carbon sidewall due to air oxidation [8].*

A stable protective cover, both as frozen ledge and top cover (anode cover made of a crushed bath-alumina mix), should be maintained to minimize the air oxidation and high temperatures on the exposed surfaces, and should be avoided.

**Formation of aluminium carbide**: The proposed chemical reaction between the molten aluminum and carbon sidewall is:

*Equation 1-4*         $4Al_{(l)} + 3C_{(s)} = Al_4C_{3(s)}$         $\Delta G°_{(970°C)} = -147\ kJ$
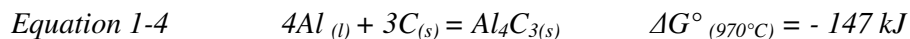
The reaction is thermodynamically favored at all reduction cell operating temperatures. At temperatures below 1000°C, the contact between liquid aluminium and carbon does cause the reaction to form an appreciable concentration of aluminium carbide. The reaction is enhanced by cryolite or cryolitic-containing melt which serves as a wetting agent. The aluminium carbide formation reaction proceeds until saturation of the melt, or until a certain layer thickness has formed on the carbon surface serving as a diffusion barrier. The solubility of $Al_4C_3$ in the bath depends on the electrolyte composition and temperature according to [9] Equation 1-5:

*Equation 1-5   Log $(C_{Al_4C_3})$ = -0.4149 – 0.3960CR + 1.894\*10³/T- 0.3112[$C_{Al2O3}$/$C_{Al_2O_3\ (sat)}$] - 2.49\*10⁻²[$C_{CaF_2}$]*

Where $C_{Al_4C_3}$ is mass % $Al_4C_3$, Equation 1-5 shows that the dissolution in constant temperature is increased with increasing cryolite ratio (CR – molar ratio of NaF/AlF$_3$, in pure cryolite CR is 3) reaching a maximum of 2.15 mass % at CR =1.8.

16

**Abrasion and erosion-** The sidewall is exposed to erosion especially at the metal-bath interface. In the absence of a protecting frozen ledge, the abrasion and erosion probably occurs as a result of electromagnetically caused metal and bath movement. In the presence of undissolved hard alumina (sludge) the erosion could damage the soft carbon wall. Thus the combined effect of $Al_4C_3$ formation and abrasion by alumina could increase the destruction of the carbon sidewall.

**Cathodic dissolution of the carbon sidewall**: One liability of a conductive sidewall is that current can flow via this pathway. According to Gudbrandsen et al [10] the carbon loss from cathode blocks and the carbon sidewall is mainly due to a cathodic carbon dissolution process. The cathodic dissolution of carbon into the melt takes place according to:

*Equation 1-6*   $C_{(s)} + 3AlF_{3\,(l)} + 4Na^+ + 4e = Na_3Al_3CF_{8\,(l)} + NaF$
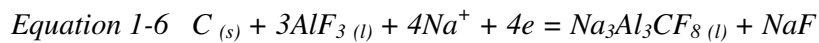
Therefore it can be expected that the cathodically polarized sidewall will corrode in the bath phase zone and the carbon will be deposited on the anode. In the absence of a frozen ledge, the unprotected carbon sidewall will be polarized to cathodic current density probably higher than the limiting current for carbon dissolution.

 Laboratory scale experiments [10], show that a steady state loss was reached at a cathodic current density of $0.1A/cm^2$  (Figure 1-12).
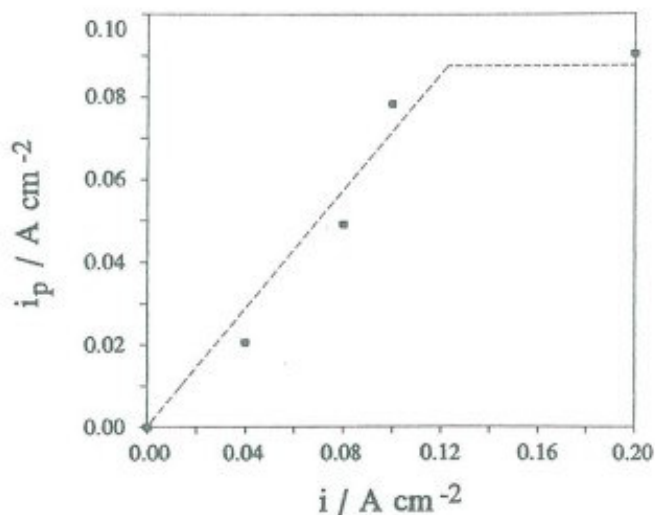


*Figure 1-12: Partial current density ($i_p$) for dissolution of carbon as a function of total current density.  [10].*

The dissolution rate that was calculated, based on the laboratory scale experiment, was 1.2 cm/week and is in good agreement with the commercial corrosion rate measured by Taylor et al [11] of 1.3mm/day for the non protected sidewall.

The extensive wear of the carbon sidewall was part of the driving force to change to ceramic based materials. However there are other major driving forces for changing sidewall technology [1]:

- **High heat loss** - from cells with carbon sidewalls results in high electrical energy consumption. Maintaining heat balance was less of a concern in the older inefficient reduction cells, however; modern technology limits the amount of voltage that can be reduced.
- **High capital cost** -expensive automation and large low-productivity cells result in high capital cost per unit.
- **High maintenance cost**- due to expensive feeding mechanism and degradation of cell materials the reconstruction and repair cost are substantial. The cell life becomes a limiting cost factor.
- **Carbon dioxide emissions** must be reduced to conform to increasingly tight regulations of green house emissions.

These problems compound as productivity per cell has increased to reduce the capital cost. The increased productivity is largely achieved by increasing the line current which increases the heat generation because of the ohmic resistance of cell components. The heat dissipation becomes a problem in the high current cells and increases the wear rate of cell materials. Furthermore the increased wear rate gave a major impetus to development of new and better materials in the sidewall.

### 1.2.2. Alternative materials for sidewall

The alternative materials for sidewall construction have to solve some of the problems that the carbon based materials faced. Researchers have listed a selection criteria for alternative sidewall materials for aluminium electrolysis cell [12-14]:

- High electrical resistivity
- High thermal conductivity to maintain a stable frozen ledge.

- Good resistance to cryolite bath attack when the frozen ledge melts due to cell excursions such as anode effects.
- Unreactive with aluminium and sodium.
- Insoluble in cryolite or aluminium.
- Impervious/ low porosity/ high bulk density.
- Not wetted by bath or metal.
- High resistance to oxidation by air, as the top and the back areas of the sidewall will be exposed to hot air with temperatures between 500-600°C for several years.
- Ease of fabrication.
- Ease of joining.
- Resistant to $CO_2/CO$ and HF vapors.
- Have high strength.
- Superior abrasion resistance for resistance to sludge in the cell.

With these criteria in mind, SiC based refractories have particular advantages as materials for sidewall refractories [15, 16] and began to replace the traditional carbon based sidewall materials. They are used as sidewall lining primarily for the following reasons:

- Improved resistance to air burn and hence increased service life.
- Increased cavity volume: carbon blocks have a thickness of 150-200 mm whereas SNBSC materials are manufactured as blocks 50-100 mm in thickness (75 mm is a very common brick thickness). Reduced sidewall thickness and increased cavity permit the use of larger anodes, resulting in increased productivity from the same metal shell configuration.
- Thermal conductivity is 2.5 times that of rammed sidewall lining. This allows the formation of a stable layer of frozen protective bath ("frozen ledge") on the hot face of the brick, when the cell is operated in a normal bath temperature.
- Low electrical conductivity.
- High thermal shock resistance to resist thermal variations.
- Does not react with molten metal.
- Good mechanical properties.

These materials are most often used as prefabricated blocks and bricks but could also be partially achieved by using a SiC-containing ramming paste.

1.2.2.1. Types and properties of SiC based materials:

Silicon carbide itself does not show the usual sinterability as other ceramic raw materials do and hence different binder materials were required. Although the use of pitch-bonded SiC sidewall materials in aluminium reduction cells has been utilized, ceramic bonded material are needed to achieve good corrosion resistance. Bonding systems based on $Si_2ON_2$, $Si_3N_4$, $\beta$-SiC, recrystalized $\alpha$-SiC, and possibly SiAlON, were recognized as good candidates for production of SiC based refractories with a good cryolite bath, aluminium corrosion and abrasion resistance, high thermal conductivity as well as resistance towards air oxidation. A qualitative property comparison between silicon carbide and carbonaceous sidewall materials can be seen in Table 1-3.

*Table 1-3: A qualitative comparison of sidewall materials [17].*

| Property | Material | | |
| --- | --- | --- | --- |
| | Prebaked carbon | Silicon carbide | Graphite |
| Apparent porosity | Fair | Low | Fair |
| Oxidation resistance | Reasonable | Very good | Poor |
| Electrical resistivity | Low | High | Very low |
| Thermal conductivity | Good | High | Very high |
| Corrosion/erosion resistance | Reasonable | Very good | Poor |
| Strength | Reasonable | Very high | Low |

It is clear that the bonding phase is a major determinant of the chemical and physical properties of the composite material. The bonding phases can be separated into two categories:

- **Oxide bonded SiC**: Clay, mullite alumina or silica.
- **Non oxide bonded SiC**: $Si_2N_2O$, $Si_3N_4$, SiAlON, and $\alpha$-SiC.

Typical properties of SiC based material can be seen in Tables 1-4 and 1-5.

*Table 1-4: Silicon carbide refractories, typical properties by bonding phase [17].*

| Property | Bond Phase | | |
|---|---|---|---|
| | Direct | $Si_3N_4$ | SiAlON |
| Bulk density ($g/cm^3$) | 2.65 | 2.62 | 2.65 |
| Apparent porosity (%) | 15.0 | 14.5 | 15.0 |
| Modulus of rupture<br>- at $20°$ C ($N/M^2$)<br>- at $1350°$ C ($N/M^2$) | 42<br>41 | 41.8<br>41.1 | 32<br>35 |
| Morgan Marshall Abrasion index | 20 | 20 | 20 |
| Thermal conductivity<br>- at $400°$ C (W/mK)<br>- at $600°$ C (W/mK)<br>- at $1000°$ C (W/mK) | 34.5<br>30.7<br>23.3 | 24.5<br>21.5<br>19.2 | 27.9<br>24.7<br>19.9 |

*Table 1-5: Properties and composition of different bonding phase SiC bricks [2].*

| Property | Bond Material | | | |
|---|---|---|---|---|
| | Nitride $Si_3N_4$ | SiAlON ( Si, Al, O, N) | Oxynitride ($Si_2ON_2$) | Oxide ($Al_2O_3$) |
| Max hot face temperature (°C) | 1600-1700 | 1650 | 1500 | - |
| Thermal conductivity (W/mK) | 16-17 | 15 | 15 | - |
| HMOR ($N/mm^2$ ) | 44-31 | 52 | 44 | 17 |
| Porosity (%) | 15 | 14-16 | 16 | 18 |
| Erosion/corrosion resistance | Excellent | Good | Fair | Poor |
| Chemical composition (wt. %)<br>SiC<br>$Si_3N_4$<br>SiAlON<br>$Si_2ON_2$<br>$Al_2O_3$ | <br>75-78<br>20-25<br>-<br>-<br>- | <br>73-76<br>-<br>19-20<br>-<br>- | <br>78<br>-<br>-<br>20<br>- | <br>48<br>-<br>-<br>-<br>50 |

A Scanning Electron Microscopy (SEM) study of the different materials sheds some light on the different bonding phase structures and adherence of the bonding matrix to the SiC grains. [18, 19]. The **oxide bonded SiC** shown in Figure 1-13 indicates that the $SiO_2$ bonding phase completely covers the SiC grains but a large number of cracks in the bonding phase open the way for oxygen diffusion into the SiC grains.
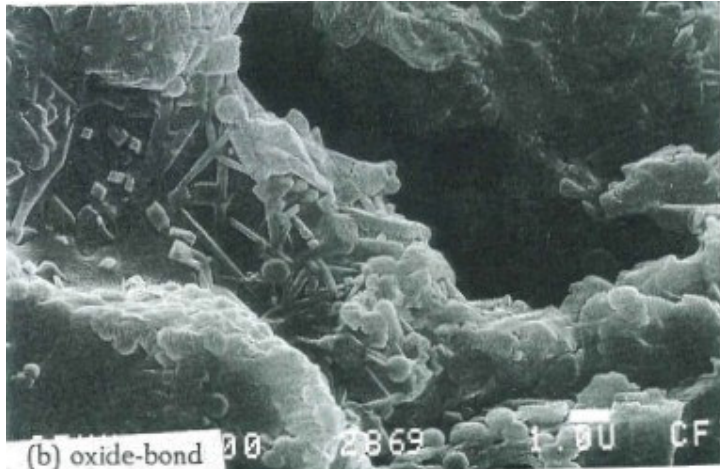
*Figure 1-13: SEM image of oxide bonded SiC material [19].*

**Silicon oxynitride** ($Si_2ON_2$) as a binding phase is produced by reaction firing of SiC grains with Si metal particles in a $N_2$-$O_2$ atmosphere. It could also form during oxidation of $Si_3N_4$ bonded SiC as an intermediate material before complete oxidation to $SiO_2$. The good adherence of the bonding phase to the SiC grains can be seen in the SEM image (Figure 1-14). The superior adherence of the oxynitride phase to SiC compared to $Si_3N_4$ bonding can give it improved thermal shock resistance [20].
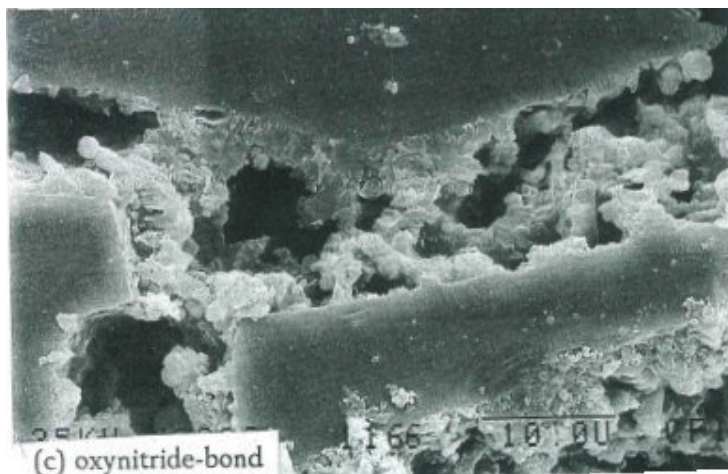


*Figure 1-14: SEM micrograph showing bonding phase of oxynitride bonded silicon carbide [19].*

**SiAlON** (silicon aluminium oxynitride) takes the general formula $Si_{6-z}Al_zO_zN_{8-z}$ where Z varies from 0-4.2. When Z= 0, the equation is $Si_3N_4$. It could also be seen as solid solution of $Si_3N_4$ and alumina. The dense SiAlON bond phase with the compact crystals, (Figure 1-15) indicates that the material possesses high strength.
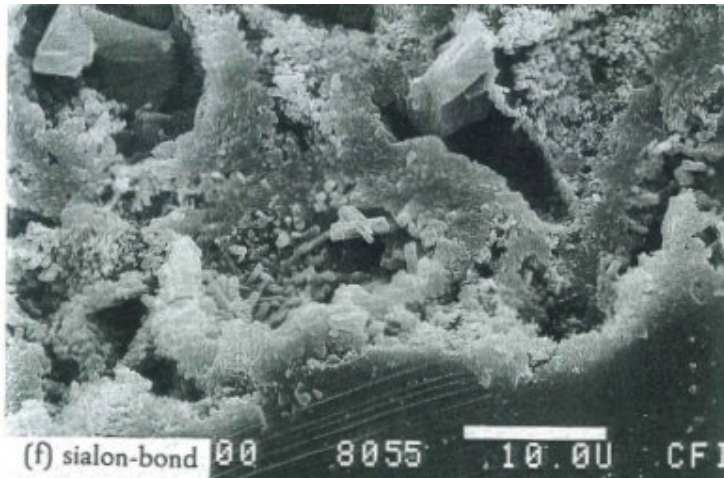
*Figure 1-15: SEM micrograph of bonding phase of SiAlON bonded silicon carbide [19].*

Production of a **β silicon nitride** bonding phase is achieved by firing a mixture of SiC grains and Si metal powder in nitrogen atmosphere at temperatures of 1400 - 1600°C. The micrograph in Figure 1-16, shows dense, needle-like crystals of the bonding phase that fill the gap between the SiC grains, and lead to a compact bond with high strength.
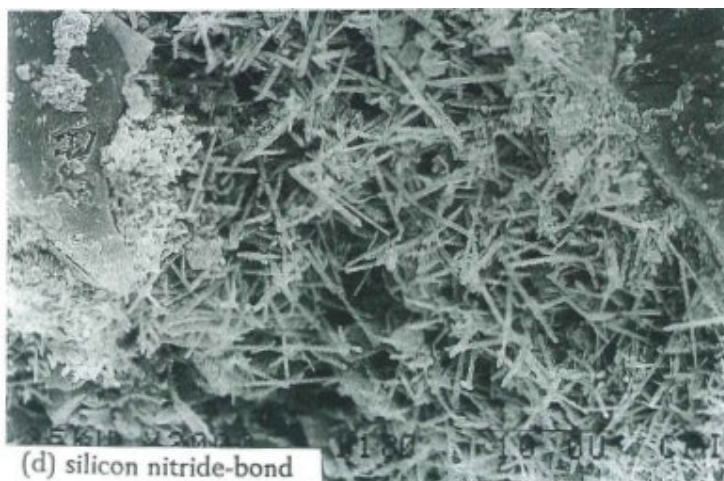


*Figure 1-16: SEM micrograph of the bonding phase of silicon nitride bonded silicon carbide [19].*

The method to produce **self bonded SiC** is adding silicon metal in a stoichiometric ratio to the SiC grains with a carbon binder, and firing the mixture in oxygen free environment at 1400°C. The resulting **β-SiC bonded SiC** phase appears as illustrated in Figure 1-17, and provides solidification of the brick.
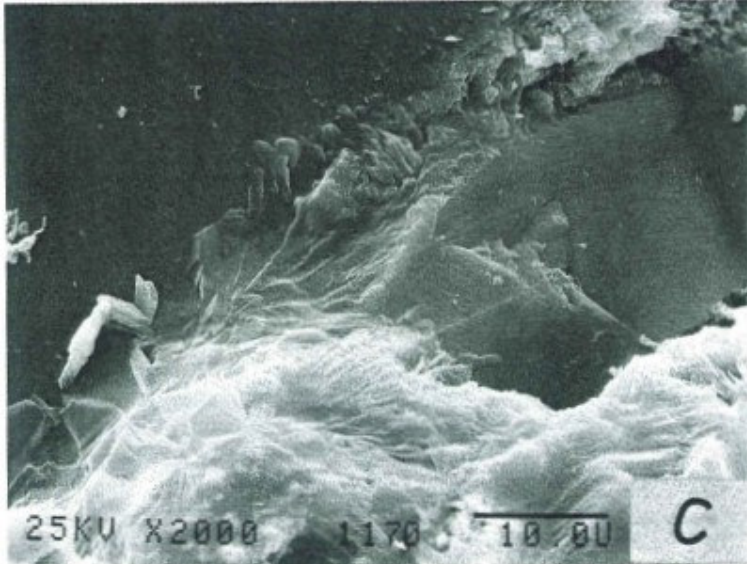
*Figure 1-17: Self bonded SiC, β-SiC bonding phase [18].*

In **α-SiC bonded SiC** (Figure 1-18) a strong bond is formed due to the direct connection of the hexagonal α- SiC grains. This bonding phase is created by re-crystallizing very fine-grained SiC mixtures at a temperature in excess of 2400°C [18] which produces >99% SiC containing material. The absence of a sensitive inter-granular bond phase renders a strong and chemical inert material. This material has a high corrosion resistance, regardless of the big pores in the bonding phase.
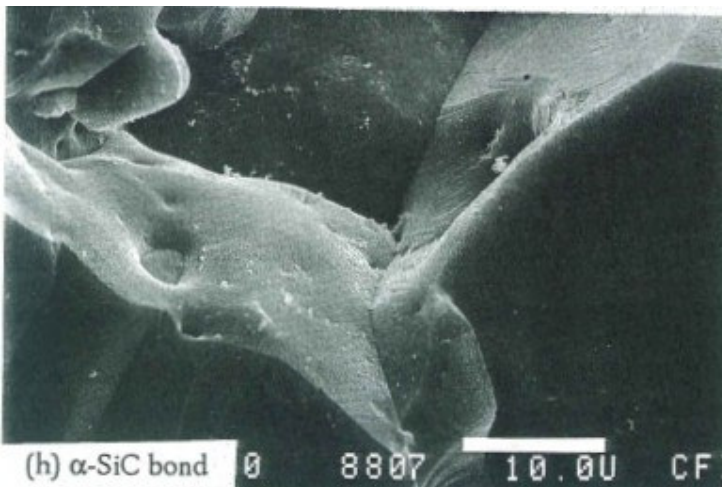


*Figure 1-18: SEM micrograph of the bonding phase of α-SiC bonded silicon carbide [19].*

1.2.2.2 Wear mechanism of SiC-based refractories.

**Oxidation resistance**

The oxidation products of SiC based materials are quite different from carbon based materials: while the oxidation of carbon materials produces a volatile gaseous product such as $CO/CO_2$, the

SiC based materials produce a solid product such as $SiO_2$ from the SiC and $Si_2ON_2$ or mullite in a partly oxidized $Si_3N_4$ and SiAlON. The solid oxide products are much more sensitive toward corrosive attack by cryolite or alkaline vapours, than the un-oxidized starting materials.

A comparison test for oxidation resistance in air for both carbon based materials and SiC based materials was conducted at temperatures of 550°C and 960°C. [8]  The carbon based materials were semi-graphitic, produced at 1200°C, and graphitized materials produced at >2600°C. The SiC based materials were nitride bonded, SiAlON bonded, and α-SiC bonded silicon carbide. These materials were tested in shaped and unshaped configurations. The unshaped carbon- based materials, showed noticeable attack at 550°C, and were heavily attacked at higher temperatures, while the shaped graphitic material showed medium resistance to oxidation. The SiC based materials proved their excellent resistance both at 550 and at 960°C as can be seen in Table 1-6.

*Table 1-6: Mass change during oxidation test, test condition: heating rate 120°K/hour, air flow rate: 4m³/hour at 30Pa, sample size 8-15kg [8].*

| Temperature / Material | RT- 550°C 4,4 hours | 550°C 3 hours | 550 °C - 960°C 3,4 hours | 960 °C 24 hours | Total change % |
|---|---|---|---|---|---|
| **Unshaped refractories** | | | | | |
| Cold tamping anthracite | -7.6 | -5.7 | -7.7 | -43.0 | -71.3 |
| Cold tamping paste | -7.4 | -8.1 | -9.6 | -48.2 | -80.1 |
| SiC-mortar phosphate bonding | -2.0 | +0.1 | +0.3 | +1.2 | -0.6 |
| SiC mortar silicate bonding | -6.4 | -0.1 | +0.2 | +0.4 | -6.2 |
| SiC- ramming hydraulic bonding | -3.0 | -0.1 | 0 | +2.0 | -1.3 |
| **Shaped refractories** | | | | | |
| Graphitized carbon (at 2600°C) | 0 | - 0.9 | - 4.8 | - 27.3 | -33.0 |
| Semi graphitic carbon (at 1200°C) | - 0.3 | - 3.8 | - 6.7 | - 33.8 | -48.1 |
| $Si_3N_4$ bonded SiC | - 0.1 | - 0.1 | - 0.1 | + 0.7 | +0.19 |
| SiAlON bonded SiC | - 0.1 | 0 | 0 | + 0.5 | +0.38 |
| α-SiC bonded SiC | - 0.2 | 0 | 0 | + 0.1 | -0.08 |

The oxidation resistance of nitride bonded SiC, recrystalized α-SiC, bonded SiC, and pore free dense SiC was measured in thermo balance of 1250°C and 1400°C by Tabereaux and Fickel [19].  The recrystalized α-SiC which had the same porosity level as the nitride bonded, but much

coarser individual pores and a lower specific surface area, showed a lower degree of oxidation when compared to the nitride bonded material, as can be seen in Figure 1-19.
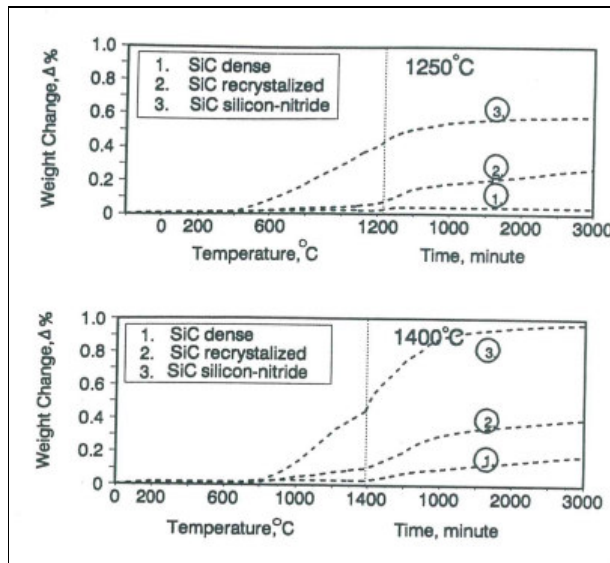


*Figure 1-19: Oxidation of $Si_3N_4$ bonded SiC and α-SiC bonded SiC refractories at 1250°C and 1400°C [19].*

Observation of the oxidized materials show that the nitride bonded surface was completely covered by a layer of $SiO_2$ and a "warty" cristobalite layer appeared on the SiC grains. A long term oxidation layer of cristobalite crystals was observed in the α-bonded SiC.

The oxidation resistance characteristics of nitride bonded SiC are due to the formation of a protective oxidation film rather than to the inherent oxidation resistance of the underlying materials. This "self sealing effect" occurs due to formation of a nitrogen-containing duplex film consisting of an outer layer of $SiO_2$ and an interfacial layer of amorphous $Si_2N_2O$ which merges seamlessly with the $Si_3N_4$ and $SiO_2$ surfaces (Figure 1-20) [21]. Oxygen permeation through this sub-oxide layer is the oxygen-rate-limiting factor which inhibits further oxidation of the nitride phase.
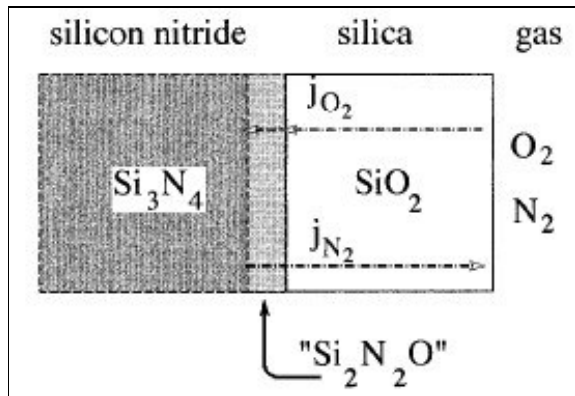
*Figure 1-20: Schematic view of the oxide layer structure on oxidized $Si_3N_4$ surface [21].*

**Corrosion resistance**

The oxide bonded phases, which employ a phase such as clay, $SiO_2$, mullite or alumina, were found to be unsuitable as sidewall materials in the corrosive environment of the aluminium reduction cells. In this environment unprotected silicon carbide materials oxidize rapidly in the temperature range of 800-1150°C [22]. Corrosion experiment in a 1:1 mixture of cryolite and alumina (at 1030°C for 24 hours) showed that all the oxide and silicate bonded SiC materials tested were completely infiltrated with the cryolite melt. The crystalline bond phase was completely dissolved and a large glass phase area was observed between the SiC grains [15].

Zhao et al [23] compared the corrosion resistance of $Si_3N_4$, $Si_2ON_2$ and SiAlON bonded SiC, by adding oxides to the fabrication mixture of SiC grain and Si particles prior to firing. Silica was added to form a $Si_2ON_2$ bonding phase, and alumina was added to form SiAlON. The bonding phase changed to $Si_2ON_2$ at addition of 3% $SiO_2$ to the mixture, and than converted to $SiO_2$ at ~7% $SiO_2$ addition. $Si_2ON_2$ showed less resistance to cryolite than $Si_3N_4$ bonded SiC in the corrosion test. The corrosion index of samples, exposed to a cryolite melt at 975°C for 16 hours, increased sharply after the addition of $SiO_2$ exceeded 3% (Figure 1-21).
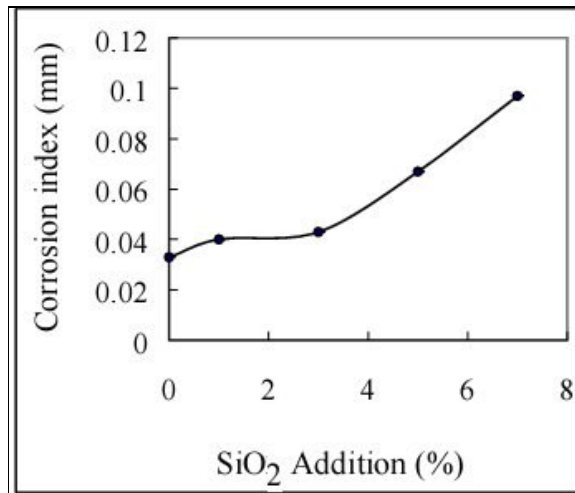
*Figure 1-21: Influence of added amount of SiO$_2$ on corrosion index [23].*

The same trend was observed when alumina was added to the reaction mixture and the bonding phase changed from Si$_3$N$_4$ (at Z=0) to SiAlON (at Z>1). Adding additional alumina changes the bonding phase to a mixture of SiAlON and Al$_2$O$_3$. Figure 1-22 shows that the cryolite resistance of Si$_3$N$_4$ bonded SiC was higher than SiAlON and Al$_2$O$_3$ as a bonding phase.
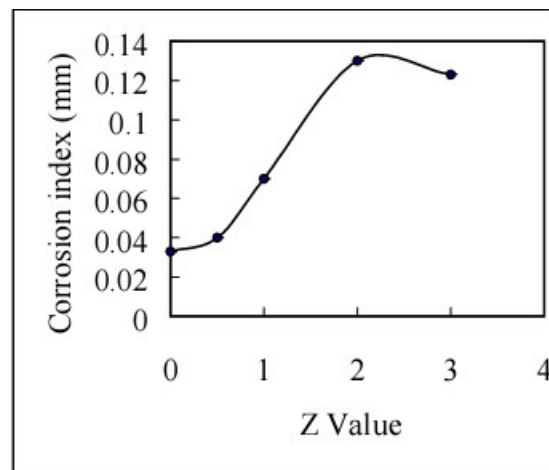


*Figure 1-22: Influence of Z value of SiAlON on the corrosion index [23].*

SiC bonded SiC showed superior chemical resistance compared to Si$_3$N$_4$ bonded SiC materials in a polarized corrosion test simulating the reduction cell environment, which included exposure to molten bath and gaseous CO$_2$ at 955°C for 50 hours, with an electrical current of 2A [24].

Additional comparative information about the strength of the different refractory materials can be obtained by a High temperature Modulus of Rapture (HMOR) measurement. This measurement is important since the sidewall materials must have sufficient strength and

mechanical stability at high temperature to support the cathode assembly during cell operation. HMOR of various SiC based bricks was measured on both fresh and corroded samples [19]. The results shown in Table 1-7 indicate that the HMOR of the corroded samples decreased by around half.

*Table 1-7: Comparison HMOR of cryolite corroded SiC materials and unreacted SiC materials [19].*

| HMOR at 1000 °C MPa | | | |
|---|---|---|---|
| Material | Original | Corroded | Change |
| Graphite | 14 | 15 | 0 |
| SiC oxide bond | 32 | Destroyed | Destroyed |
| SiC SiAlON bond | 60 | 25 | 35 |
| SiC $Si_3N_4$ bond | 44 | 20 | 24 |
| SiC α- bond | 75 | 44 | 31 |

The α-bond SiC results show the best strength. The nitride bonded and the SiAlON bonded show good quality, however, the oxide bonded material was completely destroyed during the corrosion test, and had a lower hot strength.

## 1.3 Summary and conclusions

Carbon-based sidewall materials have been used for many years as sidewall materials due to their low cost of production, the chemical inertness to aluminium metal and the corrosion products that have no effect on the metal purity. However these materials showed poor performance as sidewalls material in terms of corrosion and oxidation resistance, and undesired electrical conductivity. The transition to higher current cells created the need for material with better corrosion resistance, good thermal conductivity and reduced dimensions in order to increase the cell cavity to accommodate bigger anodes. The studies above have demonstrated that SiC-based materials are well suited to duty as sidewall refractories. They can be made with various types of bonding phases; although only nitride bonded and silicon carbide bonded materials have demonstrated superior performance due to the combination of thermal conductivity, electrical insulation, oxidation resistance and mechanical strength which make them the favoured material for sidewalls. Thus nitride bonded SiC materials provide the current benchmark in large reduction cell application, although cost and ease of fabrication favour the carbon-based materials.

# Chapter 2: Review of production of silicon nitride bonded silicon carbide (SNBSC) by reaction bonding.

Silicon nitride bonded silicon carbide (SNBSC) refractory bricks are produced commercially by a reaction bonding technique with silicon nitride (RBSN) as the binder phase. Unlike pure silicon nitride products, silicon carbide grains and an organic binder are added to silicon powder to form a compact. The mixture is shaped into a "green" brick by vibration and pressing (Figure 2-1).



*Figure 2-1: "Green" brick during pressing in the mold box (Courtesy LIRR).*

After shaping, the green bricks are stacked onto trolleys, inserted into a controlled atmosphere furnace (Figure 2-2) and heated. Initially the bricks are heated under normal atmospheric conditions with temperature up to 400°C, in order to burn out the binder. Then the temperature is raised to 1100-1450°C and the materials are held at this temperature in a nitrogen atmosphere while an exothermic nitridation reaction -bonding occurs (Equation 2-1)[25].

*Equation 2-1*   $3Si_{(s)} + 2N_{2\,(g)} = Si_3N_{4\,(s)}$        $\Delta H_{(1100°C)} = -723.3\ kJ/Mole$
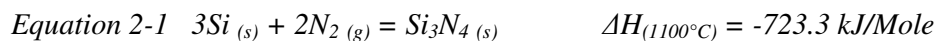
The heat generated due to the exothermic nature of the nitridation reaction should be considered when calculating the total heat balance of the nitridation process. Failing to include this additional heat in the overall heat balance, could lead to increased temperature above the melting temperature of silicon (1410°C) in the "green" bricks. This will cause premature local melting of the silicon powder, reduction of the surface area exposed to nitrogen, and complete nitridation

will be impossible, leaving unreacted silicon in the final product. Temperatures above the 1500°C, and the presence of molten liquid silicon, will make the conversion from α to β $Si_3N_4$ feasible resulting in β $Si_3N_4$ rich bonding phase.



*Figure 2-2: SNBSC bricks are stacked onto trolleys before nitridation (Courtesy LIRR).*

SNBSC refractories are usually fabricated from "commercial grade" silicon powder with a typical mean particle size varying between 10-25 µm and a green bulk density of 1500-1600 kg/ $m^3$ [25]. An unusual and beneficial feature of the RBSN fabrication route is the fact that the overall dimensions of the "green" compact do not change during "firing", despite a 22% increase in volume on conversion of Si to $Si_3N_4$. A close tolerance (approximately 0.1%) on the dimensions of a finished component can readily be maintained, thereby avoiding expensive machining after firing. The reason for this phenomenon lies in the fact that the only reduction in void space in the compacted powder is the consequence of the molar volume expansion on conversion of silicon to silicon nitride. There is no sintering in the normal sense and the volume expansion is accommodated entirely within the pore structure of the nitriding powder. The density of Si and $Si_3N_4$ are 2.32 and 3.19 mg/m$^3$ respectively and their molar volumes are 0.363 cm$^3$/mol for the Si and 0.440 cm$^3$/mol for the $Si_3N_4$ [21].

The nitridation of a compact involves the following two steps:

1. Movement of nitrogen into the continuously changing pore system of the compact.
2. Chemical reaction between silicon and nitrogen.

The nitridation process can proceed via two different mechanisms which will then determine the type of product produced[21, 25]:

31

- The dominant process is a vapour phase reaction which involves vaporization of silicon and a vapour phase reaction with nitrogen. The vapour pressure of Si at 1350°C is $10^{-7}$ atmospheres and it implies a silicon evaporation rate of $10^{-6} kg/m^2 sec^1$ [25]. The supply of silicon vapours and reaction with nitrogen according to Equation 2-2 is in accordance with the observed reaction rates.

*Equation 2-2*        $3Si\ (l) + 2N_2\ (g) = Si_3N_4\ (s)$

This process is a typical chemical vapour deposit (CVD) reaction, which lead to formation of α $Si_3N_4$. The reason α $Si_3N_4$ phase dominates in products from the vapour phase reaction could be related to the lack of freedom of the species to order themselves into the energetically favoured β $Si_3N_4$ structure at the growth site. The independent mobility of the reactants in this process is restricted when precipitation occurs in a host solid.

- A vapour liquid solid (VLS) reaction process which involves solution of nitrogen in liquid silicon alloys that are formed in the presence of contaminations such as Al, or Fe (commercial silicon powders can contain 0.9wt% Fe). The impurities will reduce the formation temperatures of liquid phase to below 1207°C creating the condition to formation of β $Si_3N_4.$

- A minor process, occurring in a presence of high-purity silicon, is the adsorption/reaction, in which nucleation of silicon nitride on a solid silicon surface leads to formation of a coherent layer of silicon nitride (mostly β $Si_3N_4$). The formation of this layer is rapid when $P_{N2} = 1$ atmosphere. This nitridation process follows several stages which control the kinetics of the reaction:

  1. The first stage involves the formation of $Si_3N_4$ nuclei on the Si surface, followed by growth of these nuclei. This is thought to be initiated by the reaction between chemisorbed nitrogen and silicon, the latter arriving at the reaction site by a combination of surface diffusion and an evaporation/condensation process (in this stage, formation of $Si_3N_4$ could also proceed according to the CVD process mentioned above) (Figure 2-3). During this stage the kinetics are linear with time.
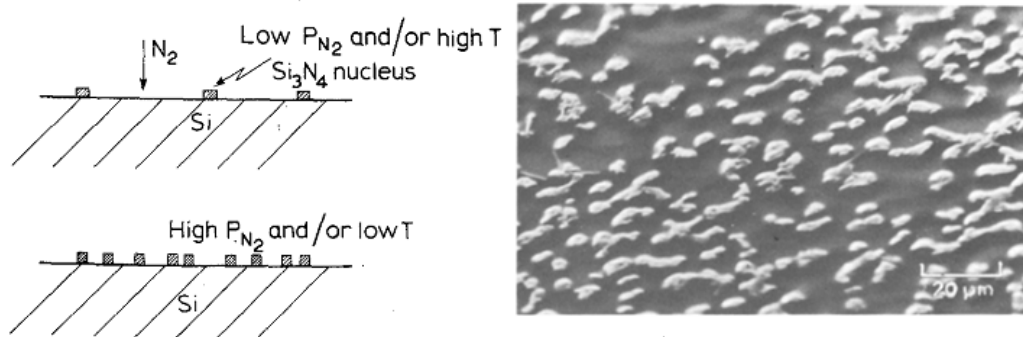
*Figure 2-3: Formation of $Si_3N_4$ nuclei on Si surface real density of nuclei is increase as $P_{N2}$ increase and temperature decrease [25].*

2.  As the nitrided layer extends over the surface, supply of Si to reaction sites decreases (Figure 2-4) and, as a consequence, the kinetics slow.
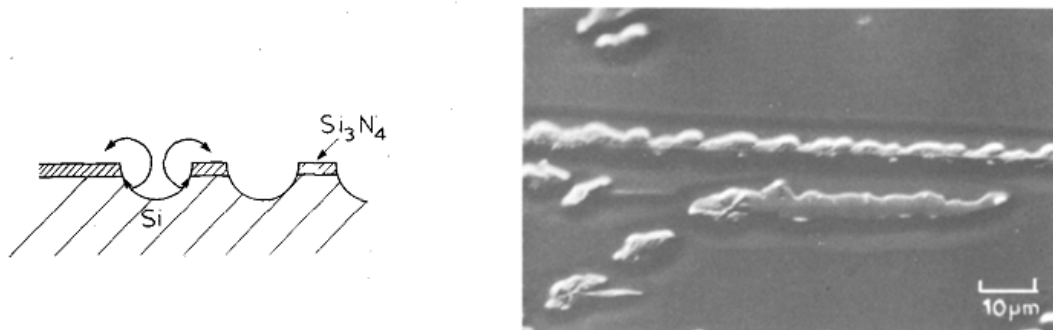


*Figure 2-4: Nuclei grow laterally and vertically: Si supplied to growth sites by combination of surface diffusion and evaporation [25].*

3.  Finally, as the film effectively separates the reactants (Figure 2-5), the rate falls to nearly zero.
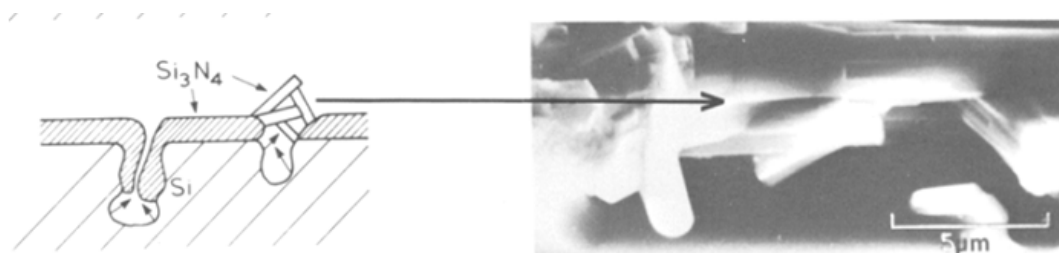


*Figure 2-5: As free Si surface area decreases, surface diffusion distances increase and so direct nitridation slows [25].*

This model qualitatively explains the need to use a finely ground Si powder in the reaction mixture, and the dependence of the kinetics on changes in temperature and nitrogen pressure.

A few parameters influence the nitridation process:

1. Silicon nitridation is a temperature sensitive and strongly exothermic reaction (Equation 2-1). Thus overheating could lead to premature melting of the silicon and reduction of its surface area. In contrast, if the temperature is kept below 1400°C, the nitridation reaction of conventional silicon powder become very slowly and ultimately effectively stops; completion of the nitridation thus becomes very difficult.

2. Nitrogen and silicon diffusion in the $Si_3N_4$ crystal lattice is too slow to give significant rates of nitride formation.

3. The nitridation reaction bonding process is extremely sensitive to impurities in the silicon powder and/or in the furnace environment. Reproducibility of product quality is hard to ensure.

During the nitridation process the temperature in the core of the brick can easily rise above the melting point of Si due to the heat generated from the exothermic reaction (Equation 2-1) and the lack of heat dissipation from the brick core to the exterior surface. This can happen even at heating temperatures of 1100°C and it will determine the properties of the finished refractory. Thus in this work, a computer model that estimates the temperature profile in the brick cross section during the nitridation reaction has been developed using the following assumptions:

- Ambient (furnace) temperature: 1100°C,
- Thermal conductivity at 1100°C= 20 W/(m*K),
- Si conversion rate: 4%/hour [25],
- Nitrogen velocity at the brick surface 2m/sec.

As seen in Figures 2-6 and 2-7, the temperature on the outer surface of the brick could reach 1442 ºC and 1452 ºC in the core due to the heat generated by the exothermic reaction and the poor heat dissipation from the core of the brick to its exterior surface. Temperature overshoot is generally controlled in practice by controlling the rate of nitrogen supply [25]. However, it is expected that during the nitridation process the heat dissipation from bricks which are surrounded in the furnace by other bricks may give rise to highly inhomogeneous surface cooling. Hence the temperatures in the core of the brick could get significantly higher than predicted by the model.
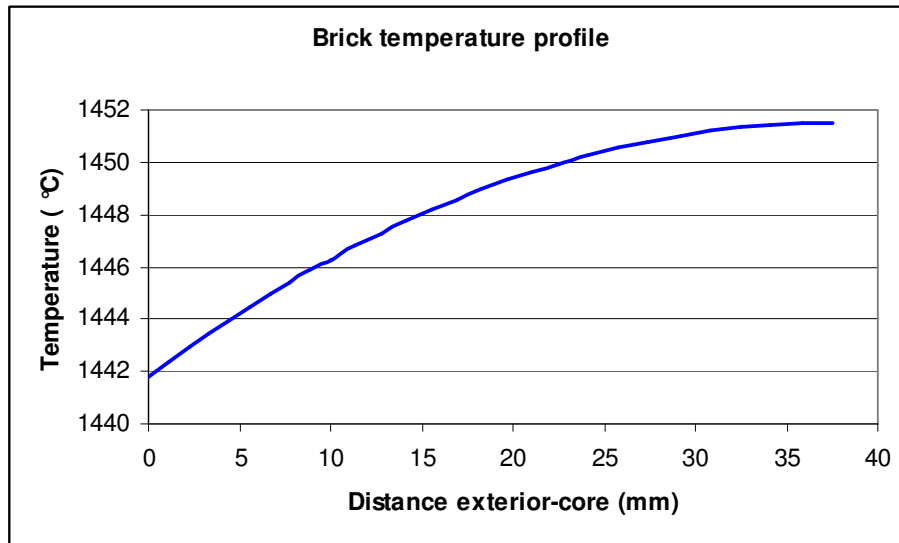
*Figure 2-6: Temperature profile of SNBSC brick cross section represents the distance from outer surface inward.*
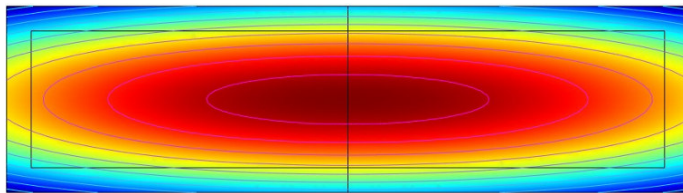


*Figure 2-7: Temperature profile of cross section of a SNBSC brick.*

Temperatures above the silicon melting point (1410°C) would lead to premature local melting of the silicon powder, particularly in a poorly mixed green block, and will form of an amorphous glassy phase thus reduce the surface area exposed to nitrogen. Excessive heat also influences α to β $Si_3N_4$ conversion, that could occur in temperatures as low as 1450°C [26] and will result in formation of β $Si_3N_4$ especially in the hotter parts of the brick.

To overcome the overheating problem, the nitrogen supply can be constrained to allow initial nitridation to build up an adequate restraining, skeletal microstructure of bridging $Si_3N_4$ [21], which will then limits coalescence of the molten silicon particles. Only then is the temperature increased in order to accelerate and complete the nitridation reaction. This is usually achieved using multi step time-temperature furnace control, with a program which consists of a slow ramp to 1300°C followed by a holding time until the reaction rate has virtually ceased and than followed by a final period at 1450°C to complete the conversion of the silicon to nitride. The reason for the step increase in the nitridation rate with increasing temperature has not been satisfactory explained [21].

In laboratory trials using microprocessor control, the heating rate could be linked to the nitrogen uptake to achieve a linear reaction rate over the entire nitridation process, although total reaction time remained very long (12-36 hours) [27].

## 2.1. Nitrogen and silicon diffusion in the $Si_3N_4$ crystal lattice

In a gas/solid reaction yielding a solid reaction product, solid-state diffusion within the product may be the rate-determining step. Measurement of nitrogen and silicon tracer diffusion coefficients in $Si_3N_4$ is not easy because of two major problems:

- The lack of large, high-purity, single crystals of $\alpha$ and $\beta$ phase material.
- The lack of suitable sources of silicon and nitrogen isotopes to use labelled reactions to eliminate the uncertainties of gas-phase/ solid-phase boundary reactions.

Values for ^{15}N self diffusion between 1200°C and 1400°C were measured [28] in polycrystalline $\alpha$ and $\beta$ $Si_3N_4$ RBSN materials and found to be:

$(D_N)_\alpha = 3.7 *10^{-8} \exp (-233 \text{ kJ*mol}^{-1}/RT) \text{ m}^2\text{s}^{-1}$.

$(D_N)_\beta = 6.8 *10^{10} \exp (-777 \text{ kJ*mol}^{-1}/RT) \text{ m}^2\text{s}^{-1}$.

The difference between the activation energies was viewed as surprisingly large and the activation energy of $\alpha$ $Si_3N_4$ surprisingly low, suggesting that maybe not all appropriate corrections were made. The diffusion coefficient of [29]Si was measured [29] in high purity, chemical vapour deposited $\alpha$ $Si_3N_4$ over a temperature range of 1400-1600°C. $D_{Si\alpha}$ value was between $0.45*10^{-19}$ and $2*10^{-19}$ $m^2$/s, with activation energy of 97 kJ/mol. This data emphasises the lack of mobility of silicon and nitrogen in the $Si_3N_4$ lattice and suggests that nitrogen diffusion might be the rate controlling step in the nitridation process.

## 2.2. The effects of contamination in the nitridation system

The nitridation reaction is sensitive to contaminants which may arise from several sources:

- Contaminations of the gaseous atmosphere, e.g. water, oxygen and addition of hydrogen have a significant effect on nitridation rate, $\alpha/\beta$ $Si_3N_4$ ratio, and on the overall microstructure. These contaminants can be released from the hot furnace refractories.
- Contamination introduced through the silicon powder e.g. the native $SiO_2$ film on the silicon particles or iron that originates from earlier stage processing during milling of the fabricated silicon powder.

In the presence of excess oxygen, nitridation rates are slowed and $Si_2N_2O$ becomes a significant product. On the other hand, an accelerated rate of nitridation was observed in the presence of fluorides [30]. The addition of Fe has the following significant effects on the nitridation process [31]:

1. It catalyzes the removal of the native oxide film covering the silicon particle as $SiO_2$. The iron contamination devitrifies the surface of the silica and reduces its adhesion to the underlying silicon, leading to the formation of $SiO(g)$ at the $Si/SiO_2$ interface (according to the equation: $Si(s) + SiO_2(s) \leftrightarrow 2SiO(g)$ ) which escapes through fissures in the disrupted silica film. This reaction will continue until the silica film is removed completely.

2. It promotes the silicon nitridation in general and $\beta$ $Si_3N_4$ formation in particular. Small additions of Fe (55 ppm) showed a three-fold increase in the extent of the reaction compared to that observed for the pure powder compacts. At levels higher than 1000 ppm, the formation rate of $\alpha$ $Si_3N_4$ declined while the formation of the $\beta$ phase remained linear with Fe addition (Figure 2-8).
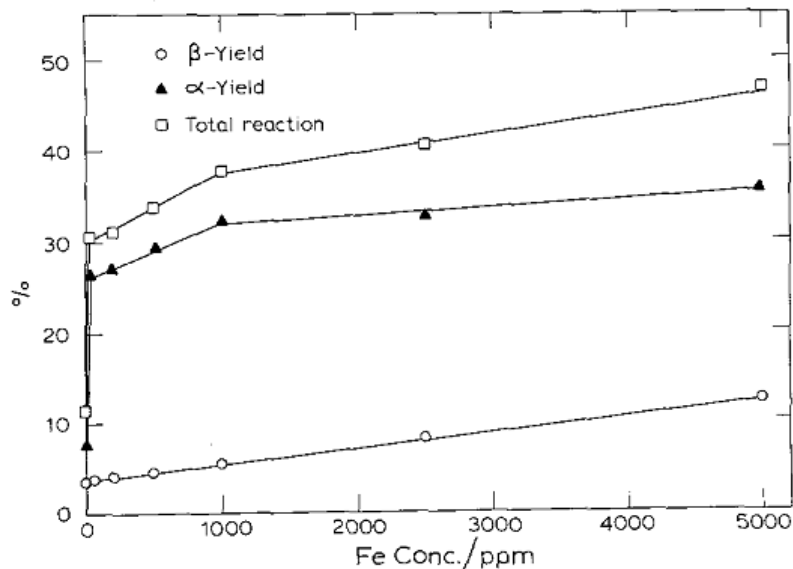


*Figure 2-8: The dependence of reaction extent and phase composition on Fe concentration after 10hr nitridation at 1350°C. • β-yield; ▲ α-yield; X % reaction [31].*

The reason for this behaviour lies in the formation mechanism for each phase. The $\alpha$ $Si_3N_4$ which is formed in the vapour phase above the iron-silicon liquid, by the vaporization of silicon, is dependent on the presence of an iron-silicon liquid to allow an effective route via which silicon could move from the solid to the vapour phase. In the absence of this liquid, the formation of a silicon nitride layer seals the surface of the solid silicon. The iron –silicon liquid, which wets the

37

silicon nitride, prevents the inhibition of silicon vaporization, hence allowing vaporization to continue and α $Si_3N_4$ to be formed.

The amount of silicon vapour generated is proportional to the surface area of the iron-silicon liquid. At low contamination levels, the rate of α-formation would be proportional to the Fe concentration, but when the Fe concentration reaches the point where further iron will produce a deeper liquid pool and the surface area of the iron-silicon will be constant the formation of α $Si_3N_4$ will stay constant as well. In contrast, β- growth is expected to be linear with $FeSi_2$ liquid concentration (which could accommodate its growth) as seen in Figure 2-9.
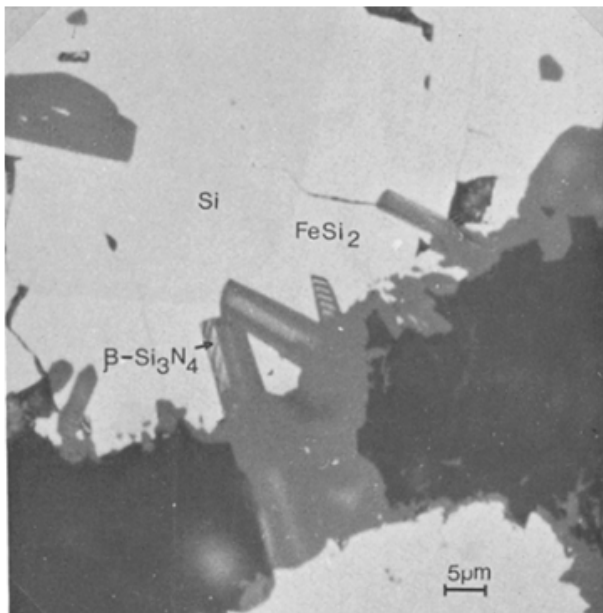


*Figure 2-9: Optical micrograph showing β $Si_3N_4$ growth into $FeSi_2$ phase, molten at reaction temperatures [31].*

3. The formation of a metallic alloy between the iron and silicon could also lead to creation of voids and microstructural defects. The Fe particles can promote local melting by reacting with silicon to form a liquid, and when the liquid migrates into the microstructure a pore is left at the site of each Fe particle. As nitridation proceeds, the areas contaminated with iron will develop voids (usually ~20 μm in diameter) surrounded by a dense region of β $Si_3N_4$. With the increased nitriding temperature the Fe/Si melt will move out further into the surrounding microstructure leaving a larger area of voids which will reduce the materials compact strength. Therefore to successfully reduce Fe contamination, the silicon powder milling stage must be near perfect to ensure maximum strength and consistency.

## 2.3. α/β Si$_3$N$_4$ ratio and conversion of α to β Si$_3$N$_4$

From the discussion above, the main parameters that control the production of α or β Si$_3$N$_4$ are:

1. The two different mechanisms of nitridation lead to different Si$_3$N$_4$ phases. While the formation of α-Si$_3$N$_4$ is occurring via a process of volatilization of silicon and a chemical vapour –phase deposition (CVD) with N$_2$, the β-phase formation occurs in a solution of nitrogen and liquid silicon alloys and is essentially a vapour liquid solid (VLS) process. An additional minor process which leads to the formation of β Si$_3$N$_4$ involves nucleation of Si$_3$N$_4$ on solid silicon and subsequent growth, following surface diffusion of silicon to reaction sites.

2. The presence of Fe contamination in the silicon promotes the growth of β Si$_3$N$_4$ by formation of silicon-iron liquid, at temperatures lower than the melting point of silicon. The correlation between the formation of β Si$_3$N$_4$ and the amount of Fe added is consistent with the typical α/β ratios found in commercial RBSN.

3. The α/β Si$_3$N$_4$ ratio depends markedly on the particular nitridation temperature schedule. High nitriding temperatures favour the growth of β Si$_3$N$_4$ as it is the presence of liquid at the reaction temperature, rather than the presence of Fe that leads to formation of high β Si$_3$N$_4$. The presence of liquid favours growth of β Si$_3$N$_4$, and promotes conversion of α to β Si$_3$N$_4$ due to the relatively small difference between the Gibbs free energy of β and α Si$_3$N$_4$ (30kJ/mol at 25°C [21]) and the high activation energy, hence the process can proceed readily only in the presence of liquids (silicon, silicides, or silicates), which lowers the activation energy for this transformation.

The proportion of β Si$_3$N$_4$ will, therefore, be largely determined by the liquid present and the relative rates of the vapour- and liquid-phase reactions. Below the melting point of Si, the amount of β-Si$_3$N$_4$ grown correlates well with the Fe content of the powder, and the proportion of β-Si$_3$N$_4$ commonly found in commercial RBSN is consistent with this indicating reasonable temperature control.

The phase composition of α and β Si$_3$N$_4$ in the bond phase as nitridation proceeds indicates that under low nitrogen pressures, the supply of nitrogen to the reaction sites is rate-determining up to approximately 70 percent conversion, and the α and β Si$_3$N$_4$ forming reactions are, therefore, competing for nitrogen as indicated in Figure 2-10 [32]. It is apparent from the curves in Figure 2-10 that the nitridation on the silicon surface leads to the formation of β Si$_3$N$_4$, while the

vapour-phase reaction leads to formation of $\alpha$ Si$_3$N$_4$. As the $\beta$-forming reaction slows, because surface diffusion distances for Si increase, the $\alpha$-forming vapour-phase reaction continues.
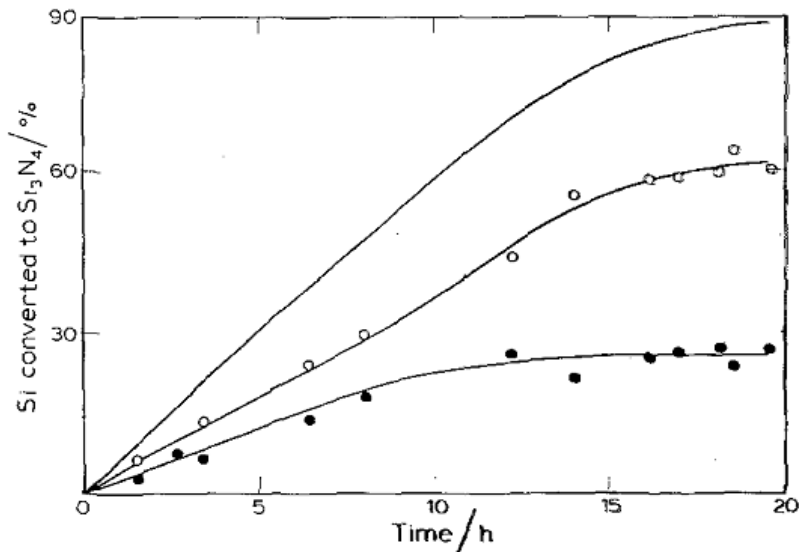


*Figure 2-10: Growth kinetics of $\alpha$ Si$_3$N$_4$ and $\beta$ Si$_3$N$_4$ (99.999% Si, <45$\mu$m; 1370°C and 50TorrN$_2$): --total; $^o$ $\alpha$-Si$_3$N$_4$; • $\beta$-Si$_3$N$_4$ [32].*

## 2.4. Summary

SNBSC refractories are formed by encapsulation of SiC particles in a silicon nitride matrix. The formation of the silicon nitride matrix occur via nitridation of silicon (at temperatures around 1100-1450°C) under nitrogen at atmospheric pressure. The nitridation reaction can proceed through two main mechanisms producing different Si$_3$N$_4$ phases. The dominant process is a typical chemical vapour deposition (CVD) reaction, which leads to the formation of $\alpha$ Si$_3$N$_4$ while the other process is a vapour liquid solid (VLS) reaction that promotes the formation of $\beta$ Si$_3$N$_4$. Another process that occurs to a minor extent involves the nucleation of silicon nitride on a solid silicon surface which leads to formation of a coherent layer of $\beta$ Si$_3$N$_4$.

The nitridation reaction is an exothermic reaction and is sensitive both to temperature and the presence of contaminants. Uncontrolled temperature rise during reaction can occur as a result of excessive heat generation due to the exothermic reaction, relative to the rate of heat dissipation through the bulk of the compact to the walls. Overheating can lead to melting of Si and the formation of a glassy phase that reduces the Si reactivity due to reduction in surface area. The formation of $\beta$ Si$_3$N$_4$ will be enhanced due to the presence of the liquid phase, known to promote its growth. The presence of impurities, both in the furnace atmosphere (oxygen, water vapour,

fluorides) and in the silicon (due to its fabrication process) will influence the nitridation process and the particular nitride phase formed.

The presence of iron has a significant impact on the nitridation process; it can catalyze the removal of the native oxide film covering the silicon particle, promoting silicon nitridation in general and $\beta$ $Si_3N_4$ formation in particular. The formation of a silicon-iron liquid occurs at temperatures lower than the melting point of silicon and as low as 1150°C. The direct consequence of this melting is the creation of voids and microstructural inhomogeneities which occur locally throughout the ceramic. During nitridation, growth of $\beta$ $Si_3N_4$ crystals will occur in the impurity-contaminated zones. The $\beta$ $Si_3N_4$ content of a completely nitrided compact is related to the amount of impurity through its control of the amount of liquid formed during nitridation. This liquid is needed to accommodate the growth of $\beta$ $Si_3N_4$ crystals and to reduce the activation energy needed for $\alpha$ to $\beta$ $Si_3N_4$ conversion.

From the discussion above, it is clear that good quality SNBSC refractory material can only be obtained by using good quality starting materials, and a carefully controlled RBSN process. Care is needed particularly in limiting the concentration of contaminants such as Fe in the silicon, usually introduced during the milling process. Controlling the nitridation reaction can be achieved by taking into account the heat generated in the exothermic reaction, especially in the initial stages when reaction rate is linear with time. The heating process thus should be controlled using a multi step time-temperature strategy in furnace control. Ideally this is linked to monitoring nitrogen uptake to achieve linear reaction rate over the entire extent of the process. The downside for commercial production is the excessively long reaction times which this feedback control requires to achieve complete nitridation.

## Chapter 3: Previous studies of the oxidation and corrosion resistance of $Si_3N_4$ bonded SiC

### 3.1. Introduction

$Si_3N_4$ bonded SiC materials, when compared with most other binders for SiC refractories, show superior performance as sidewalls for aluminium reduction cells due to higher corrosion resistance. The high electrical resistivity limits the role of electrochemically driven processes in its degradation. Hence, SNBSC is the material of choice as the state-of-the-art of sidelining material for modern, high-amperage cells. SNBSC materials are, however, still prone to oxidation and corrosion in the very aggressive corrosive atmosphere of the aluminium reduction cell.

The SNBSC sidewall is subjected to several distinct environments in the cell and these can be divided by location:

1. In the gas phase above the liquid electrolyte (bath) level.
2. In the bath and at the bath/air interface.
3. At the level of the molten metal.

The sidewall temperature varies in the different locations, with the highest temperature being on the metal/bath interface (Figure 3-1).
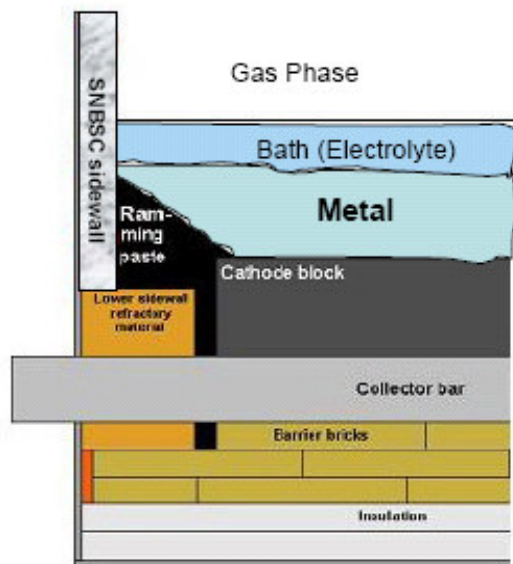


*Figure 3-1: Cross section of aluminium reduction cell [33] .*

Sidewall materials in these different locations are subjected to different pathways of chemical attack, and thus different corrosion rates.

Observations and autopsies of failed industrial cells provide some insight into the mechanism and key contributors to the corrosion of the sidewalls. In most cases, strong oxidation and degradation has been observed above the bath level in the gas phase zone (Figure 3-2) [34]. Below the gas phase zone, the blocks are typically penetrated by sodium salts, and the formation of sodium silicates is observed [33].



*Figure 3-2: Degradation of SNBSC at the upper level of the sidelining [35].*

Analysis of sidewall materials taken from different locations of cells after cut-out shows different characteristics [33]: Material taken from the zone subjected to **gas phase** attack was very porous, with a grey colour, and disintegrates upon touching. XRD analysis of powdered samples did not reveal any oxidation products in the bulk of the sample and a soapy fluid was observed containing mostly sodium carbonate hydrate, sodium silicate and sodium bicarbonate.

Samples taken from the **bath level locations** were porous, partly reacted and were severely contaminated with cryolite. SEM analysis showed rimmed remnants of SiC grains in a sodium silicate matrix with some $Si_3N_4$ (Figure 3-3).
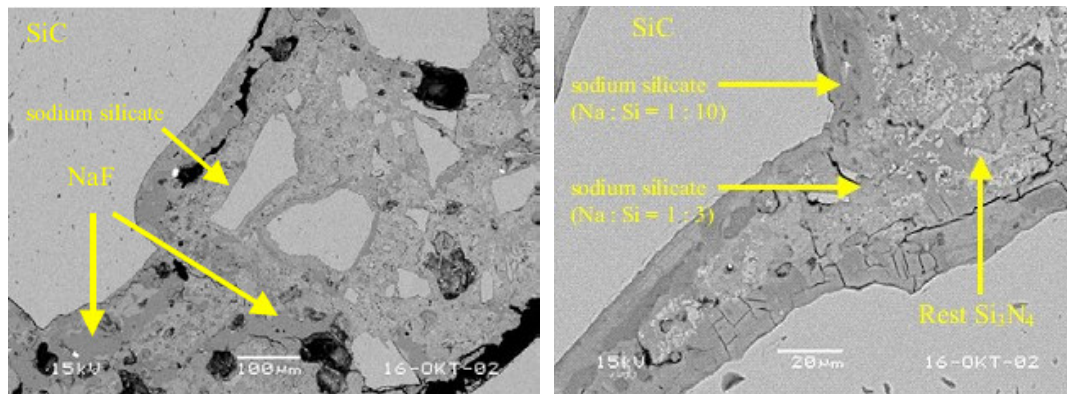
*Figure 3-3: SEM micrograph showing sodium silicate rimmed SiC grains in matrix of sodium silicate with sporadic NaF (left figure). The right figure shows increasing sodium contents (weight ratio) into the matrix of sodium silicates from rimmed SiC grain and remainder of the initial $Si_3N_4$ binder [33].*

NaF and $SiO_2$ were mainly observed in the reaction zone around the SiC grains rather than in the matrix; $CaF_2$ and NaF were the only fluoride phases that were observed.

In the molten **metal zone** sample, (taken from the sidewall behind the ramming paste that seals the big join) the refractory looks visually undamaged. However in the SEM analysis of samples taken from this location, the SiC grains seemed damaged, with irregular shapes in a highly hygroscopic matrix. Sodium and oxygen were found in the matrix as replacement for $Si_3N_4$ (Figure 3-4), while no fluorides or Al-containing phases were observed.
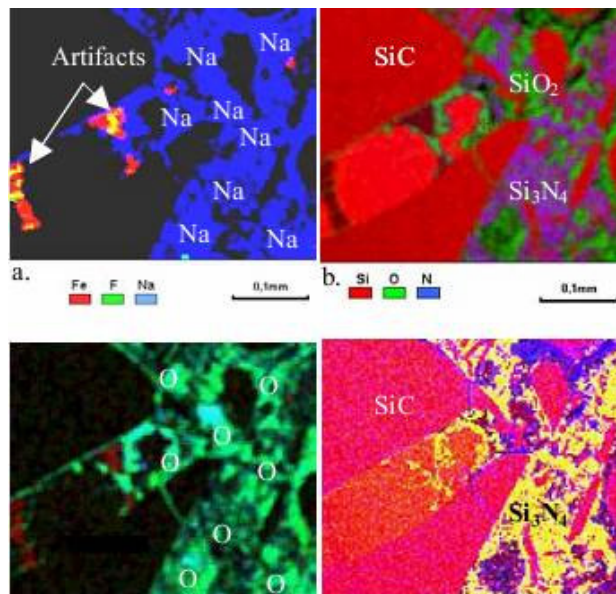


*Figure 3-4: Element distribution from sample taken from sidewall behind the ramming paste [33].*

44

## 3.2. Laboratory scale corrosion test methods

Developing a laboratory method that will closely simulate the chemical and physical conditions that exist in the industrial reduction cell is challenging. Unlike an industrial reduction cell, where the sidewalls may be exposed to the corrosive atmosphere for up to ten years, the laboratory test needs to have a shorter test period. The tests need to provide realistic data within a limited time-frame and with controlled parameters which simulate the conditions of an industrial cell.

SNBSC materials have been tested by various researchers [19, 35-37] on a laboratory scale, for oxidation resistance in various environments: air oxidation, oxygen attack, $CO/CO_2$ attack and water vapour saturated air. More realistic tests methods that simulate the conditions of the reduction cell included exposure of the materials to molten electrolyte and molten metal, or polarized test where electrolysis took place and exposure of the SNBSC materials to the corrosive vapours from the operating laboratory cell.

### 3.2.1. Oxidation tests in air and $CO_2/O_2$ atmospheres

Oxidation tests for SNBSC materials have been carried out by various researchers [19, 35-37] in $CO_2$ /oxygen/air and humid air atmospheres. Typically the weight gain of the sample is measured in order to evaluate its oxidation rate. The transformation of $Si_3N_4$ or SiC to $SiO_2$ and $Si_2N_2O$ is accompanied by a weight gain of the material due to the higher molecular weight of the oxide phases.

Tabereaux and Fickel carried out oxidation trials of SNBSC and α SiC bonded SiC refractories in humid air for 100 hours at 1000°C and 1300°C [19]. The oxidation of SNBSC was initially higher than α SiC bonded SiC, but then decreases significantly due to formation of a protective oxynitride layer, while the oxidation of the porous α SiC continued owing to a larger pore diameter.

An oxidation study using thermogravimetry analysis (TGA) was conducted on SNBSC material in air and $CO_2$ atmospheres[36]. The experiment was carried out over a temperature range of 800°C to 1300°C. It was shown that the extent of oxidation in air goes through a maximum of around 1050°C, while the oxidation in $CO_2$ produces more extensive reaction at temperatures above 1050°C (Figure 3-5). This effect could be explained by the inhibition of formation of a protective glaze on the material in a $CO_2$ atmosphere.
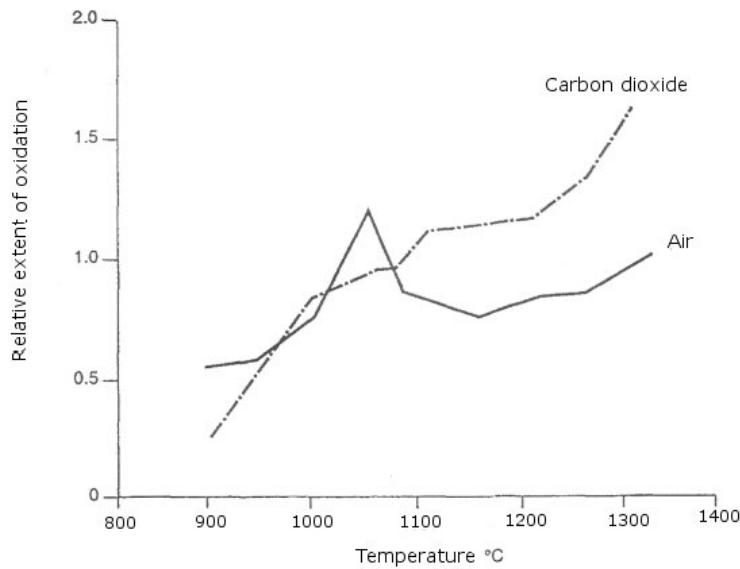
*Figure 3-5: Comparison of oxidation of SNBSC ceramic in air and CO₂ atmospheres [36].*

Oxidation tests in both **air, CO, and steam** were conducted by Zhao [37]. The condition and results shown in Table 3-1 indicate higher oxidation in CO atmosphere compared to air, and highest oxidation in steam.

*Table 3-1: Results of oxidation test of SNBSC materials in different oxidation environments [37].*

| Test condition | | Weight gain ($mg/cm^2$) | MOR change (%) |
|---|---|---|---|
| Oxidation | Temperature, Time | | |
| Air | $1100°C \times 20h$ | 8.4 | $+1.0$ |
| CO (30 L/h) | $500°C \times 200h$ | 34.5 | $-1.7$ |
| Water steam | 350ml/h | $1150°C \times 100h$ | 0 | $+5.5$ |
| | $32kg/m^3 \cdot h$ | $1000°C \times 500h$ | 63.6 | |

The oxidation resistance to **O₂ compared with CO₂ atmosphere** was conducted in a laboratory scale electrolytic cell by replacing the graphite anode with a Pt anode [35]. Two materials from similar SNBSC block half immersed in the bath were tested and the degree of corrosion was measured by volume loss. Figure 3-6 shows clearly a significantly higher degree of corrosion in the $O_2$ atmosphere compared to the $CO_2$ atmosphere.
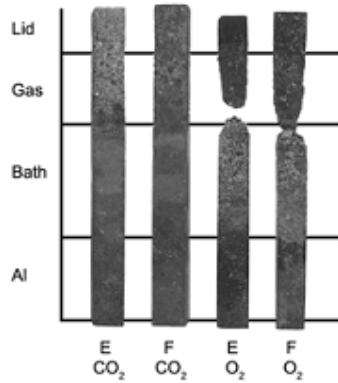
*Figure 3-6: Test samples E and F taken from similar commercial material after exposure to $CO_2$ and $O_2$ atmospheres [35].*

These results are expected because the Gibbs energy of reaction is higher in the case of exposure to $O_2$ due to its higher oxidation potential, as can be seen from Equations 3-1 to 3-3:

*Equation 3-1*       $Si_3N_4 + 6CO = 3SiO_2 + 2N_2 + 6C$       *$\Delta G = -69\ kJ$*

*Equation 3-2*       $Si_3N_4 + 3CO_2 = 3SiO_2 + 2N_2 + 6C$       *$\Delta G = -182\ kJ$*

*Equation 3-3*       $Si_3N_4 + 3O_2 = 3SiO_2 + 2N_2$       *$\Delta G = -576\ kJ$*
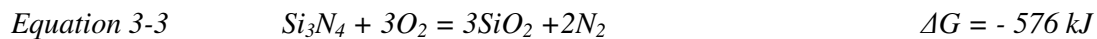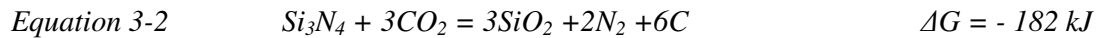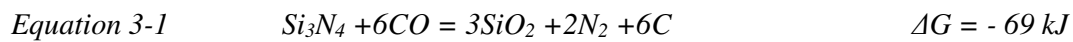
The higher oxidation rate in the oxygen atmosphere could be a concern in the future if and when inert anodes, instead of the conventional carbon based anodes, are used in reduction cells.

**Corrosion test methods in cryolite bath**

Several bath resistance tests have been developed to evaluate SNBSC materials for the aluminium reduction cell. SNBSC refractories were exposed to the cryolitic bath by filling a hole in the refractory with cryolite, heating it to 1050°C for 26 hours and then studying the microstructure of the treated brick [38].

A similar cup test method was used by Tabereaux and Fickel [19]. Range of SiC based refractories test samples were heated in a furnace at 950°C for 144 hours after a high cryolite ratio bath was placed in holes drilled in them. The samples were cut in half, after cooling, to reveal the cryolite-brick reaction zone. The overall volume loss and the percent of volume change were calculated by measuring the cryolite-bath reacted zone using a digital Vernier calliper. These researchers also studied the wetting of SiC-based refractories by cryolite using a high temperature microscope. Pressed cryolite pellets were placed on top of cylindrical samples,

and heated in a high temperature microscope to 960°C. The degree of wetting was measured from shadow photographs (Figure 3-7).
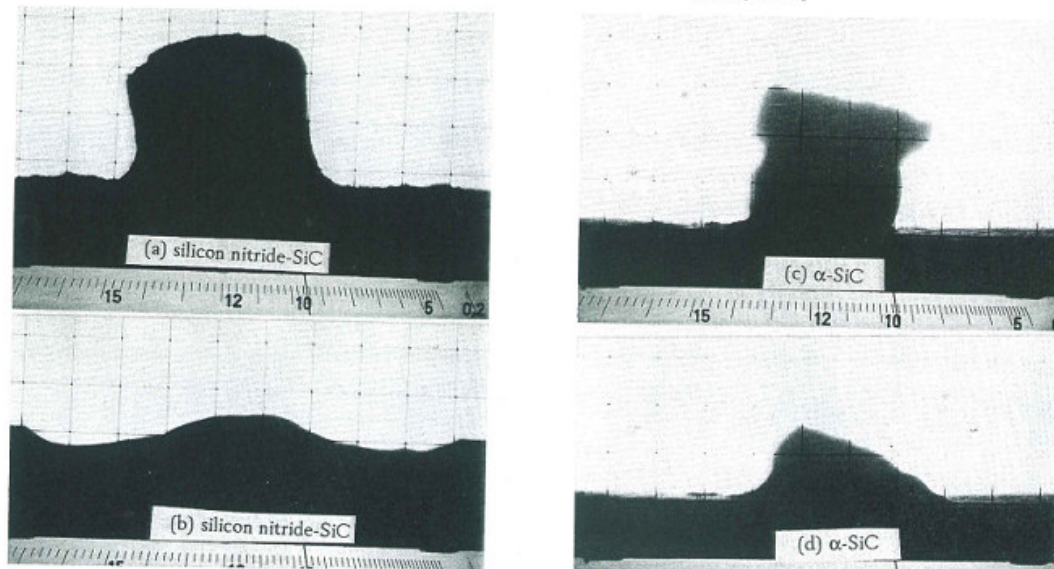


*Figure 3-7: Optical micrographs showing the wetting of SiC refractories by cryolite [19].*

Various SiC based materials with different bonding phases were tested at a temperature of 1030°C for 24 hours by immersion of samples in a mixture of 1:1 cryolite and alumina. The lower part of the samples was in direct contact with the molten bath, while the upper part was exposed to the gaseous attack above the molten bath (Figure 3-8) [15]. The samples were later examined by a light microscope to study the degree and mechanism of corrosion. All the oxide or silicate bonded SiC materials tested showed complete cryolite melt infiltration with dissolution of the crystalline bond phase and formation of large glass phase areas between the SiC grains The dissolution of the crystalline bond phase means that oxide bonded SiC should be regarded as inappropriate for use as a refractory material for aluminium cells [15].

: Steel-box with refractory lining.
: Cryolite-alumina-mixture.
: Alkaline gasphase.
: SiC test samples 50 x 20 x 20 mm.
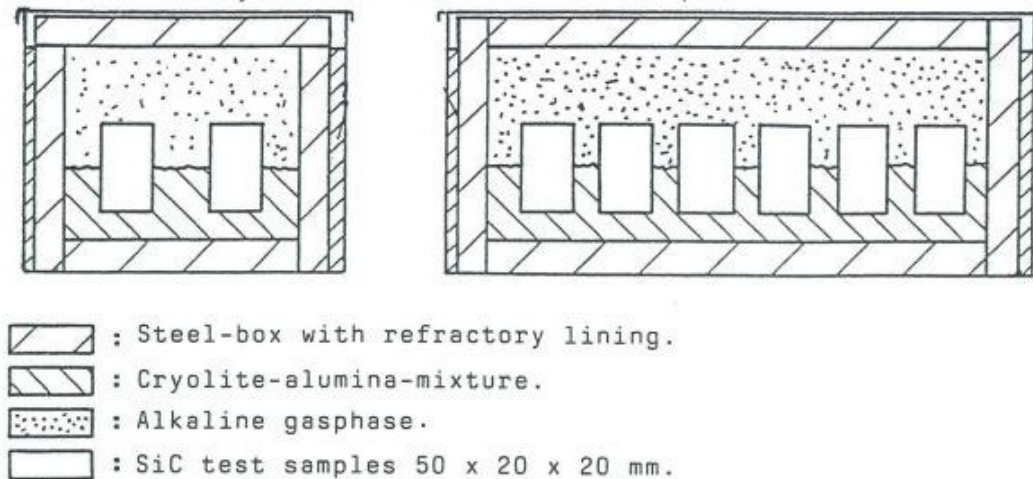
*Figure 3-8: Schematic drawing of cryolite corrosion test set up [15].*

Jorge et al [39] observed the reduction of thermal conductivity of the sidewalls due to oxidation of the sidewalls and tried to integrate this oxidation phenomenon into a laboratory scale test. The SNBSC test samples were pre oxidized by steam for 100 hours at 900°C prior to corrosion testing, where the pre-oxidized samples and untreated samples were half immersed in the cryolite bath, and the top part exposed to an air flow of 1 litre/minute. The degree of corrosion and the bath infiltration of the pre-oxidized samples were compared to the non treated samples. The pre-oxidized materials showed deeper infiltration of bath and the reaction zone shows increased wear.

In order to investigate oxidation in a cryolite environment, a $CO_2$-cryolite ($CO_2$-cry) test was developed by Hagen [40]. In this test SNBSC samples were partly immersed in a bath (with similar composition to that of industrial cells) and $CO_2$ gas was bubbled into the bath at a flow of 60ml/min. The crucible containing the bath was heated in a vertical tube furnace to 980 °C for 2 hours as illustrated in Figure 3-9.
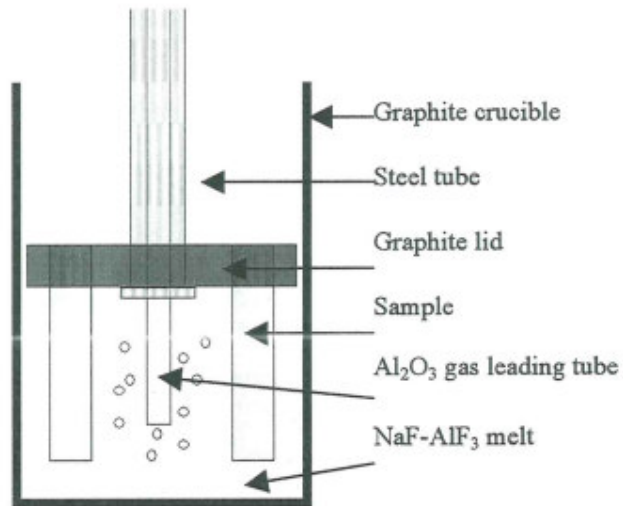
*Figure 3-9: Schematic drawing of $CO_2$ and Cryolite test [40].*

Skybakmoen and the SINTEF Research Centre team [24] have developed a standardized test procedure in order to evaluate and rank the quality of SNBSC refractory bricks for the aluminium industry. The test method involves exposure to all the environments existing in industrial cells: liquid aluminium, cryolite melt and its vapour (HF and $NaAlF_4$) as well as $CO/CO_2$ gas from the anode.

In this electrolysis test, four samples were placed in a laboratory scale reduction cell made of a graphite crucible which sits in a high temperature furnace. The crucible, which also served as the cathode, was lined with alumina walls to prevent current flow from the crucible side. $TiB_2$ disc was placed on the bottom to allow better wettability of aluminium. A 10mm in diameter graphite cylinder served as anode and a constant current of 2A was passed through the electrolyte, which simulate the composition of typical industrial reduction cell. The temperature of the cell was kept at 955 °C during the 50 hours of the experiment. Figure 3-10 depicts the configuration of the standard test cell.
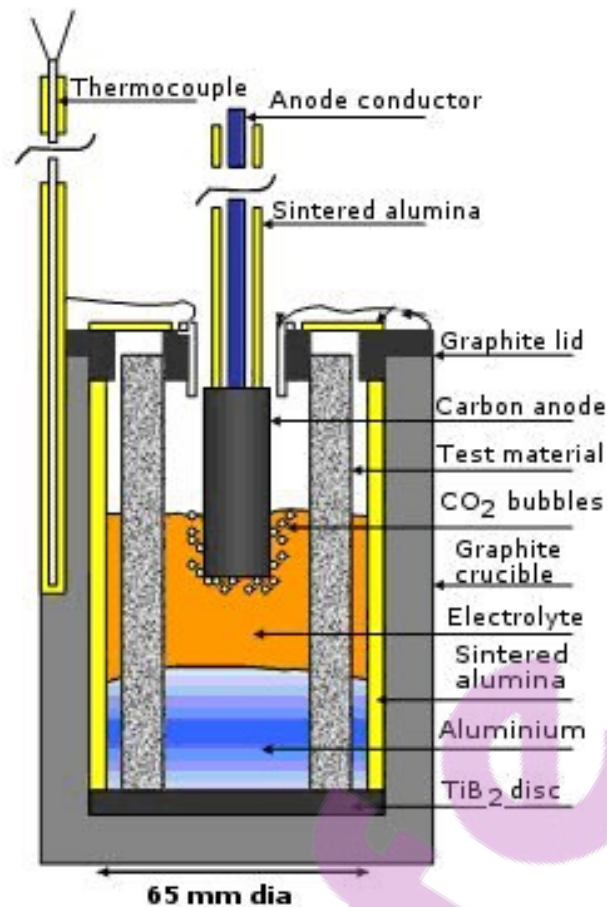
*Figure 3-10: Standard lab scale cell set up for testing SiC based sidelining refractories [35].*

The degree of corrosion was calculated by measuring the volume loss of the sample before and after the corrosion test using the ISO 5017 standard method (sees Chapter 5.1).

The materials tested in this test procedure normally undergo corrosion preferentially in the gas phase zone (zone above the bath) similar to observations from industrial cells. Strongly corroded samples even showed visible corrosion in the upper bath level zone. In some cases the test samples were completely corroded in the gas phase zone as it can be seen in Figure 3-11, where samples from material D showed higher corrosion resistance from sample from material C.
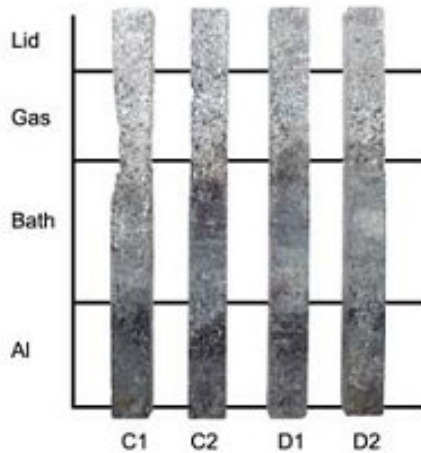
*Figure 3-11: SNBSC samples after corrosion polarized test, samples C1 and C2 showed less corrosion resistance comparing to samples D1 and D2 [35].*

## 3.3. Corrosion mechanisms

The different zones the sidewall material is exposed to, have different species that attack the sidewall; hence, the attack mechanism in each zone will be different. Figure 3-12 shows the different chemical environment surrounding the sidelining in different zones (with an absence of frozen ledge).
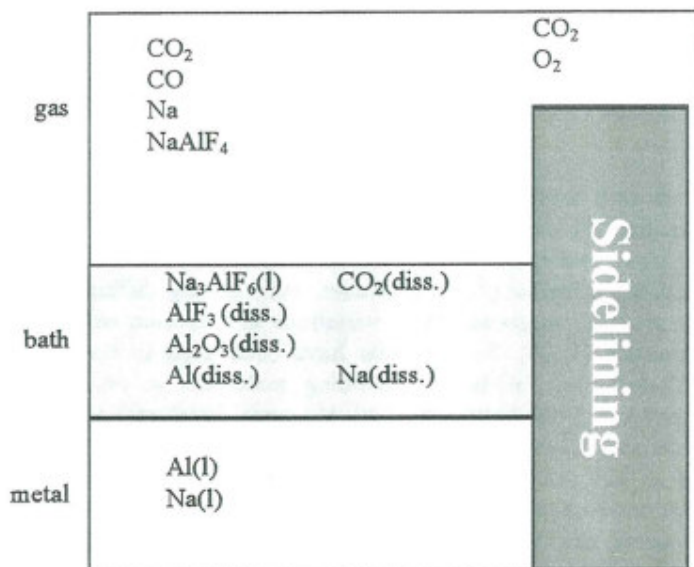


*Figure 3-12: The different chemical environment surrounding the sidelining in a reduction cell [40].*

There is general agreement that the $Si_3N_4$ binder phase is the first phase to be attacked both by cryolite in the bath zone and by the corrosive gases in the gas phase [24, 33, 36, 38].

Thermodynamically the $Si_3N_4$ phase is less stable compared to SiC grains both for oxidation in the gas phase by $CO/CO_2/O_2/ H_2O$ or in the bath by cryolite (Chapter 7.1).

**In the metal zone** Al can react with $Si_3N_4$ to form AlN, and SiC that will dissolve in the metal can react to form $Al_4C_3$ and Si. A protective oxide layer is partially active in the Aluminium zone [41].

**In the bath zone** the silicon nitride bonding phase is first to be attacked by the cryolite and the subsequent attack is on the carbide particles which appears to be by oxidation with the formation of silica, probably tridymite [38]. The cryolite infiltration in SNBSC proceeds by dissolution of the nitride bonding phase prior to attack on the silicon carbide grains [42]. The dominant oxidation mechanism is believed to be penetration and reaction of sodium from the bath with the binder around the SiC grain to form sodium silicates [13, 33, 41]. Any protective layer of $SiO_2$ that forms will dissolve into the bath providing little protection [24, 41].

According to Kvam and Oye [41], the reaction of the binder with sodium will form $Na_2O \cdot SiO_2$ or $Na_2O \cdot 2SiO_2$ around the SiC grains. This may cause stress and strain on the SiC grain, which would result in spalling off of the SiC grain into the electrolyte. Alternatively, the binder, locally around the SiC grain will react completely with the bath leading to wash out of the grain into the bath. Other possible reactions that may take place in the bath zone are listed in Table 3-2.

*Table 3-2: Possible reactions in the bath zone $\Delta G_{1200k}$ in kJ [41].*

| Reaction | $\Delta G$ |
|---|---|
| $2Si_3N_4 + 3Na_3AlF_6 + 6CO_2 = 6NaF_{(l)} + 3SiF_4 + 3NaAlSiO_4 + 4N_2 + 6C$ | -892 |
| $Si_3N_4(s) + 4AlF_3(l) = 3SiF_4(g) + 4AlN(s)$ | 58 |
| $5SiO_2(s) + 4NaF(l) = 2(Na_2O \cdot 2SiO_2)(s) + SiF_4(g)$ | 63 |
| $SiO_2(s) + Na_2O(s) = Na_2SO_3(s)$, possible rapid corrosion to:$Na_2O$ or $Na_2CO_3$ (or $NaNO_3$) | -228 |
| $2Si_3N_4(s) + 3Na_3AlF_6(l) + 12CO(g) = 6NaF(l) + 3SiF_4(g) + 3NaAlSO_4 + 4N_2 + 12C$ | 657 |
| $Na_2SiF_6(l) = 2NaF(l) + SiF_4(g)$ | -43 |
| $2Na_3AlF_6(l) + 3Al_2O_3(diss) + 9SiO_2(s) = 6NaAlSiO_4(s) + 3SiF_4(g)$ | |

Andersen et al [33] claimed that penetration of the bath into the sidewall will lead to oxidation of the binder phase to sodium silicate, while the outer surface of the silicon carbide grains is

oxidized to $SiO_2$ (Figure 3-13). The presence of sodium hydroxide found in the autopsies of cut-out cells lead them to the assumption that sodium metal or sodium oxide combined with moisture, is the cause of the chemical attack in the bath zone.
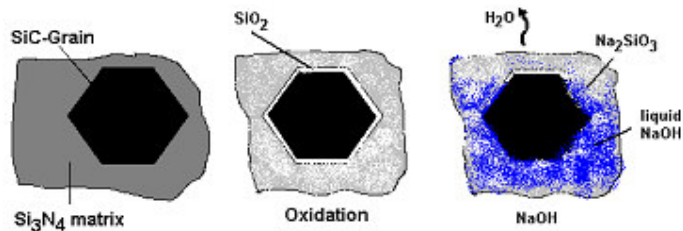


*Figure 3-13: Oxidation of SiC grain and $Si_3N_4$ matrix followed by secondary hydration [33].*

Jorge et al [39] distinguished different mechanisms where the first step involves oxidation without penetration of the bath, which is indicated by the fast drop of thermal conductivity of the sidewall material. This increases the sidewall hot face temperature and reduces the stability of the frozen ledge, causing more frequent exposures of the sidewall to the molten bath and gaseous components. The formation of the oxide layer increases the wettability of the sidelining, leading to infiltration of the molten bath or the gaseous component. In extreme cases the penetrated molten bath can attack the steel shell. Metal exfoliation from the shell provides extra insulation that increases temperature and could dramatically increase the risk of tap-out where molten electrolyte breaches the shell.

Electrolyte acidity also influences the corrosion rate; the rate increasing with increasing Cryolite Ratio (CR= mol ratio $NaF/AlF_3$) [35] as seen in Figure 3-14.
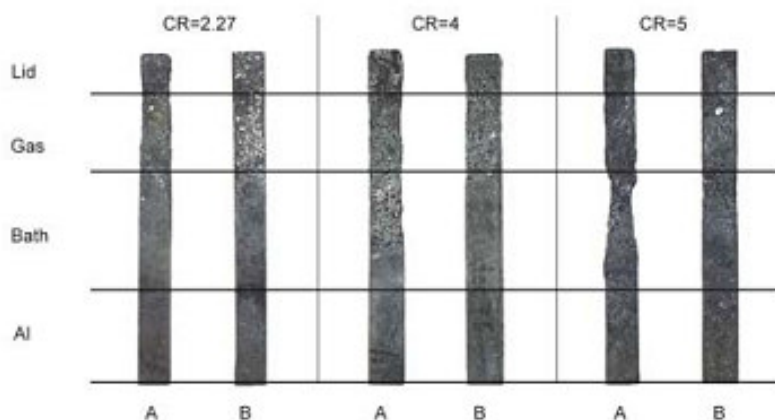


*Figure 3-14: SNBSC samples after lab scale polarized test with different CR [35].*

The increasing corrosion with activity of NaF leads to the proposed mechanism:

- Penetration of Na followed by

- Oxidation to $Na_2O$ and formation of $Na_2O \cdot SiO_2$

- Descaling /swelling and dissolution of the reaction products, opening the way to a new reaction cycle [2].

**In the gas zone** the sidewall is exposed to a variety of gaseous species: vapour from the bath such as $NaAlF_4$, and HF that originate from moisture in alumina and/or hydrogen from the anode [43], $CO/CO_2$ that is forming on the anode surface, and oxygen that may penetrate from the big joint through the collector bar in between the shell and the refractory bricks.(See Figure 1-4 and 1-5 the gap between the cathode block and the sidewall).

Earlier work by Skybakmoen [24] emphasises the importance of $NaAlF_4$, as the main agent in the corrosion mechanism in the gas phase. $NaAlF_4$ can attack the protective oxidized layer according to Equation 3-4:

*Equation 3-4   $2SiO_2(s) + NaAlF_4(g) = SiF_4(g) + NaAlSO_4(s)$   $\Delta G_{1200K}$ = -21.64 kJ*

Exposed $Si_3N_4$ and SiC are both unstable in the presence of $NaAlF_4$ and $CO_2$.  Of the two, the binder phase is more prone to attack and will react according to Equation 3-5:

*Equation 3-5   $2Si_3N_4 + 3NaAlF_{4\ (g)} + 6CO_{2\ (g)} = 3SiF_{4\ (g)} + 3NaAlSO_{4\ (s)} + 6C + 4N_2$   $\Delta G_{1200K}$ = -1166.82 kJ,*
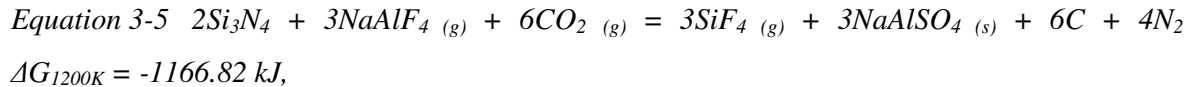
The SiC grain can react as follows:

*Equation 3-6   $2SiC + NaAlF_{4\ (g)} + 2CO_{2\ (g)} = SiF_{4\ (g)} + NaAlSiO_{4\ (s)} + 4C$   $\Delta G_{1200K}$ = -491.66kJ*

This author later tested the reactivity of $Si_3N_4$ on exposure to $CO_2$ versus $O_2$, and suggested that, in the first step, oxidation of the binder phase by $CO_2$, and to a higher degree by oxygen, will result in the formation of $SiO_2$, followed by exposure to the condensed fumes from the electrolyte and dissolution of the oxide product [35].

Others [41] added more possible reaction routes, which include passive oxidation of both the binder phase and SiC to form $SiO_2$ or active oxidation in the presence of CO to form SiO(g).

Andersen et al [33], in their analysis of samples taken above the bath line, observed the absence of aluminium containing phases. This led them to assume that HF might play a significant role in the chemical attack. The presence of sodium hydroxide can indicate that sodium metal and sodium oxide penetration, combined with the presence of moisture, are responsible for this chemical attack. Figure 3-15 shows the role of critical agents such as oxygen, water, sodium metal, and hydrogen fluoride in the corrosion mechanism.
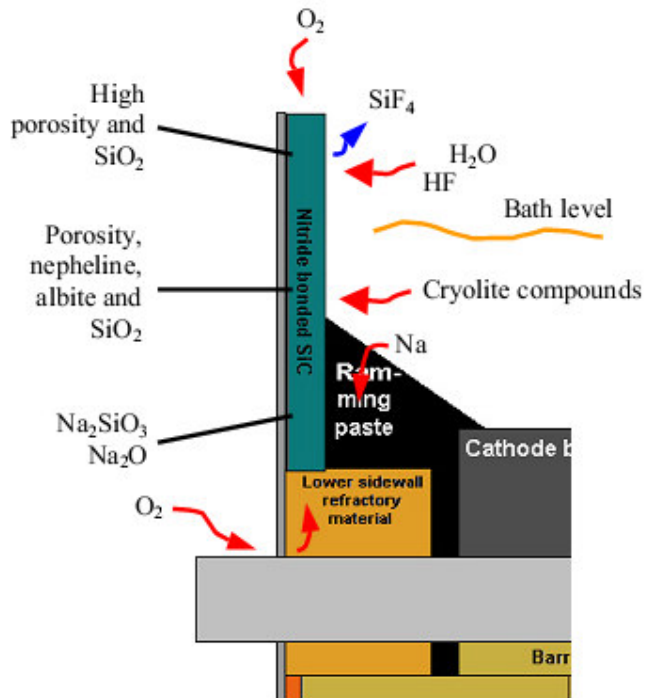


*Figure 3-15: Corrosion mechanism of SNBSC in aluminium reduction cell according to Andersen et al [33].*

## 3.4. The contribution of different parameters on the corrosion rate

Various parameters in the material properties have been proposed to contribute to the enhanced corrosion rate. The fact that these parameters are inter-linked makes it is extremely difficult to tested each independently. However, some of them can be singled out as theoretically having potential as the major contributors to the corrosion mechanism.

**Open porosity**: High open porosity means the bath or gaseous species can penetrate into the material more easily and have better contact with the matrix. The typical porosity of the industrial materials is in the range of 13-18% and the apparent density 2.6 to 2.7 $g/cm^3$. When exposed to the bath, the porosity decreases to 4-6% and the density increases to between 2.9 and

2.95 $g/cm^3$ due to the bath infiltration. These materials usually show high porosity in the internal part of the brick compared to the exterior [33, 35], as seen in Figure 3-16.



a) 75 mm thick blocks.

b) 100 mm thick blocks.
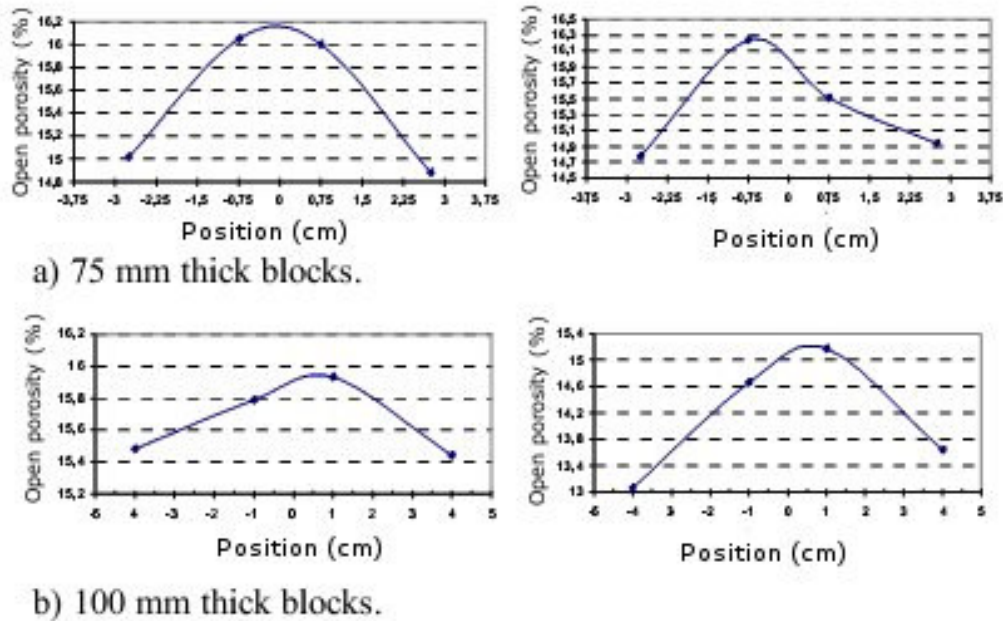
*Figure 3-16: Open porosity measurement show variations across four blocks within the block thickness. 0 is the centre of the block [35].*

Skybakmoen, who tested oxidation in air and corrosion in laboratory scale configuration, did not find correlation when plotting the degree of corrosion against open porosity (Figure 3-17) [35].
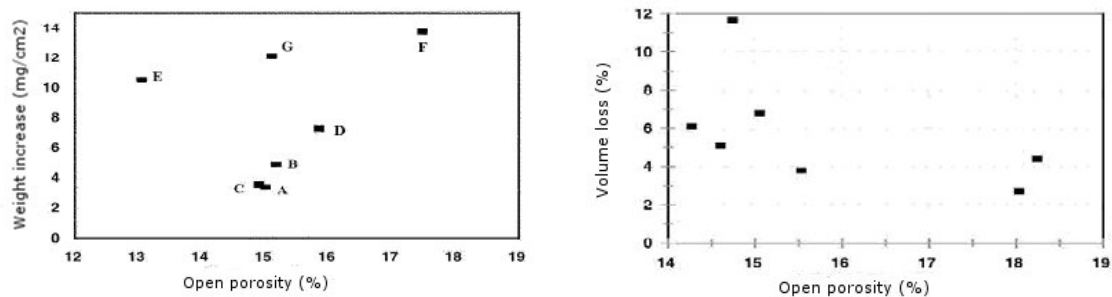


*Figure 3-17: Weight increase, due to oxidation in air at 950°C for 100 hours, of different types of SNBSC material as function of porosity (left). Volume loss as function of porosity in different SNBSC materials in polarized electrolysis test (right) [35].*

**Amount of binder**: Thermodynamically, $Si_3N_4$ is less stable than SiC for oxidation and reaction with corrosive gases such as HF and $NaAlF_4$, as previously mentioned. Hence, the $Si_3N_4$ binder is more prone to react than SiC in the reduction cell environment. Oxidation studies using TG/MS/EGA analysis confirm that $Si_3N_4$ oxidizes first rather than the SiC [36]. Observation of

corroded material which was exposed to reduction cell environment shows that the surface of the materials became porous and SiC grains seemed to be detached or sticking up out of the matrix (Figure 3-18).



*Figure 3-18: SNBSC sample taken out of industrial scale cell after 30 hours of immersion half dipped in the bath [This work].*

There is some motivation to increase the binder phase content in order to increase the cold crush strength, but higher levels of the $Si_3N_4$ bonding phase might lead to higher corrosion. This is indicated by the higher corrosion resistance of self-bonded SiC (α-SiC as a binder) compared to SNBSC materials. Figure 3-19 indicates that 23% $Si_3N_4$ was the optimum level amongst the samples tested in one study [16]. A balance should be maintained in the binder content because low content of the binder will reduce the penetration of bath and corrosion of the materials, but will compromise the strength of the material. Increasing the binder content will provide stronger material but will expose the material to a higher degree of corrosion.
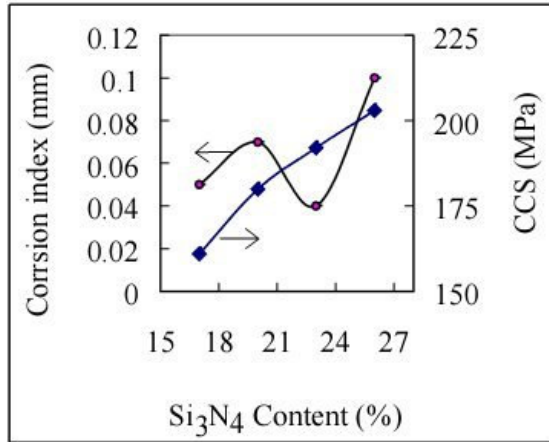
*Figure 3-19: Corrosion and cold crush strength as function of $Si_3N_4$ content in immersion test at 975°C for 16 hours [23].*

Electrolysis corrosion experiments with an SNBSC sample with 26.6% $Si_3N_4$ content showed more corrosion compared to samples with 22.5% $Si_3N_4$ binder phase[35]. Although this parameter seems to be of high importance for the corrosion mechanism it has never been systematically tested in a controlled experiment.

**Amount of oxides**: Oxides such as alumina and silica are usually added as a sintering aid to produce harder materials [44, 45]. However, adding silica or alumina has a negative effect on the resistance toward penetration of cryolite into the materials and resistance to corrosion [23] as shown in Figure 3-20.
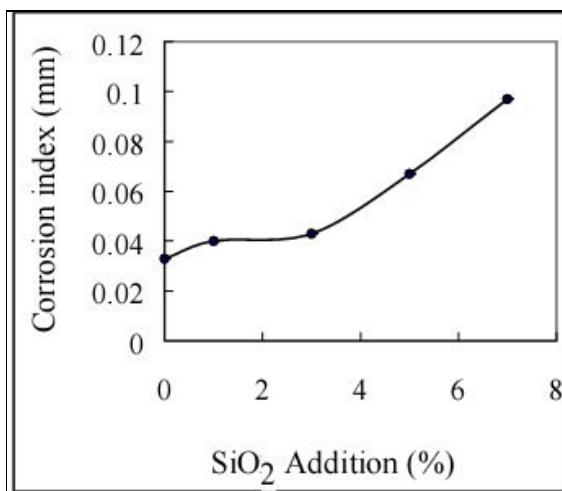


*Figure 3-20: Influence of added amount of silica on the corrosion index [23].*

Oxide bonded refractories based on $SiO_2$, Mullite, Clay and alumina, which employ a low melting point phase have been found to be unsuitable to the corrosive environment in the

aluminium cell [22]. Materials based on the oxide phase as a binder phase such as $SiO_2$ and alumina show lower resistance to cryolite compared to SiAlON and SNBSC. In an exposure of 10 hours to cryolite at 960°C, the oxide bonded SiC materials were completely destroyed, while the SiAlON materials show some penetration of bath, and the SNBSC appeared less infiltrated and reacted than the SiAlON [19].

**Amount of $Si_2N_2O$**- this phase can be formed due to oxide additives. These additives are used in order to promote liquid phase sintering and will enable the transformation of α $Si_3N_4$ to β $Si_3N_4$. The latter has high aspect-ratio grains that significantly improve the fracture toughness [46]. $Si_2N_2O$ can also be present due to poor control during the reaction bonding process as an oxidation product of silicon nitride. In industrial materials produced for the aluminium industry, the $Si_2N_2O$ content is usually low (<2%) [35] and seems to have no effect on the corrosion resistance. However no systematic study has been done to check this assumption.

**Amount of α $Si_3N_4$ and β $Si_3N_4$**: normally SNBSC materials contain both phases in a certain ratio which varies from different manufacturers or within the block itself. In general, a higher content of β $Si_3N_4$ was found in the central parts of the block while in the peripheral area high α $Si_3N_4$ was observed [35]. The presence of the high temperature β $Si_3N_4$ phase indicates that the conditions during manufacturing were favourable to the transformation of α $Si_3N_4$ to β $Si_3N_4$. This could be due to the presence of low melting temperature oxides that would form a liquid phase, or a presence of metallic contaminations that could form a liquid glass alloy (such as FeSi) that promote the growth of β $Si_3N_4$.

Lab test corrosion results [35] often show higher corrosion ratio for samples from the peripheral part of the block leading to a conclusion that α $Si_3N_4$ phase is more reactive than the high temperature β $Si_3N_4$ phase. However the influence of α $Si_3N_4$ / β $Si_3N_4$ ratio on chemical resistance has not yet been systematically studied.

## 3.5. Conclusions

SNBSC, although considered the state of the art refractory materials for aluminium reduction cells it is still subjected to oxidation and corrosion. Exposure to oxygen induced the most severe oxidation, in particular in the binding phase, when compared with other oxidants such as $CO_2$ and air, a problem that could impose challenges in the future in the use of inert anodes.

Many test methods have been used by various researchers to study the corrosion rate of SNBSC materials.    However the most realistic test method should simulate the conditions of an industrial reduction cell and involve exposure to all the environments existing in industrial cells: liquid aluminium, cryolite melt and its vapour (HF and $NaAlF_4$) as well as $CO/CO_2$ gas from the anode.

The SNBSC sidewall is exposed to different environments at different heights, hence different corrosion mechanisms are suggested for each zone. Exposure to the bath zone will lead to bath penetration and oxidation by sodium of the $Si_3N_4$ binding phase to form sodium silicates ($Na_2O{\cdot}SiO_2$ species), and formation of $SiO_2$ layer on the SiC grains.  In the gas zone the material is exposed to oxidation by $CO_2/CO$ to form $SiO_2$ or attack by corrosive gasses such as HF and $NaAlF_4$ to produce volatile products.

Although several parameters such as porosity levels, amount of binder, amount of $\alpha$ $Si_3N_4$ and $\beta$ $Si_3N_4$, and amount of oxides could contribute to the corrosion of SNBSC materials, the fact that they are inter-linked makes it extremely difficult to test each independently. Although these parameters seem to be of high importance for the corrosion mechanism they had never been systematically tested in controlled experiments.

## Chapter 4: Microstructural analysis

### 4.1. Crystal structures of α and β $Si_3N_4$

Silicon nitride is a highly covalent compound (70% covalence) with a density of 3.19 $g/cm^3$ and occurs in two different crystal structures, identified as α and β modifications. The basic building units of α and β $Si_3N_4$ crystal structures are the silicon-nitrogen tetrahedron $SiN_4$ ($sp^3$ hybridization of Si) and the planar $NSi_3$ ($sp^2$ hybridization of N). In the $SiN_4$ tetrahedron, the silicon atom lies at the centre of a tetrahedron, with nitrogen atoms at each corner (Figure 4-1).
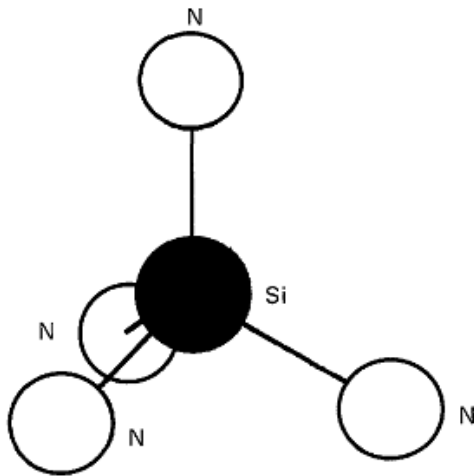


*Figure 4-1: The tetrahedral unit in silicon nitride [47].*

The $SiN_4$ tetrahedra are joined by sharing nitrogen corners so that each nitrogen atom is common to three such tetrahedra: thus each silicon atom has four nitrogen atoms as nearest neighbours, and each nitrogen atom has three silicon atoms as nearest neighbours (Figure 4-2).
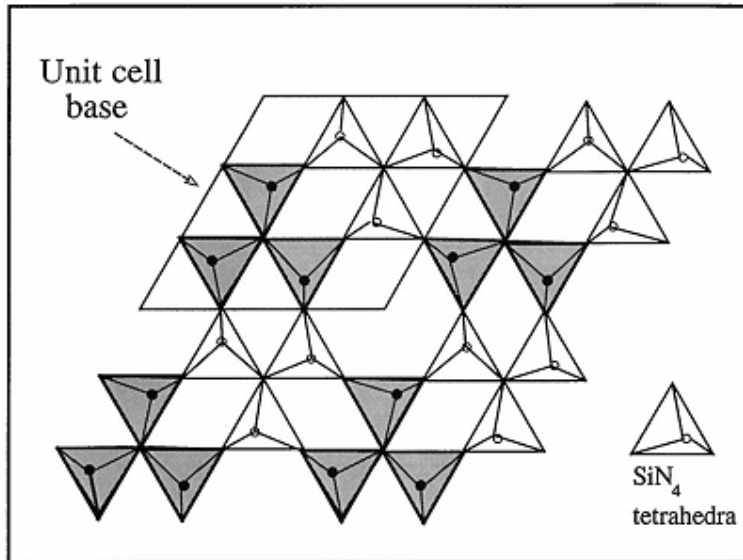
*Figure 4-2: Outline of Si₃N₄ crystal structure [21].*

The idealized $\alpha$ Si$_3$N$_4$ structure has a trigonal symmetry of space group P31c, each unit cell containing four Si$_3$N$_4$ units with c/a = 2/3. However, $\alpha$ Si$_3$N$_4$ can not be built with rigid, regular tetrahedra and different levels of distortion are introduced into the SiN$_4$ tetrahedra, resulting in the conversion of the planar Si$_3$N units into a slightly pyramidal shape. The c/a ratio measured for $\alpha$ Si$_3$N$_4$ with a stoichiometric composition of Si$_{12}$N$_{16}$, was 0.715 (the unit cell is shown in Figure 4-3).
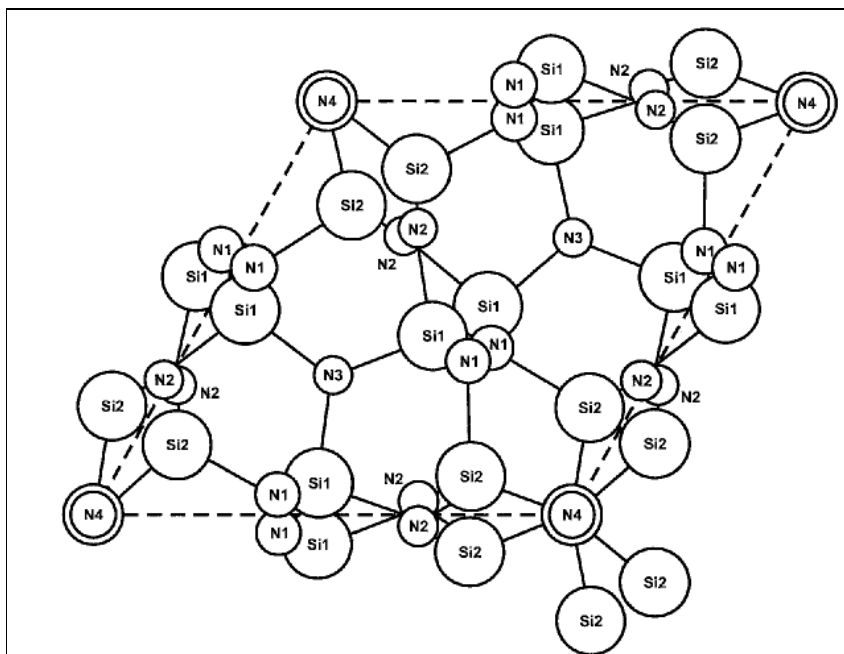


*Figure 4-3: α- Si₃N₄ unit cell [48].*

The idealised $\beta$ $Si_3N_4$ structure has hexagonal symmetry with space group $P6_3/m$ and each unit cell contains two $Si_3N_4$ units with $c/a=1/3$. Very little distortion of the tetrahedra or the $Si_3N$ groups occurs in the $\beta$ $Si_3N_4$ structure, however some distortion is introduced by forcing the Si-Si and N-N distances to be equal in the c direction. This results in $c/a = 0.385$ compared to $c/a = 0.333$ for the ideal structure with a stoichiometric composition of $Si_6N_8$ (Figure 4-4). Although there is debate concerning the real $\beta$ $Si_3N_4$ space group [49-51], the general view that $P6_3$ is the correct structure.
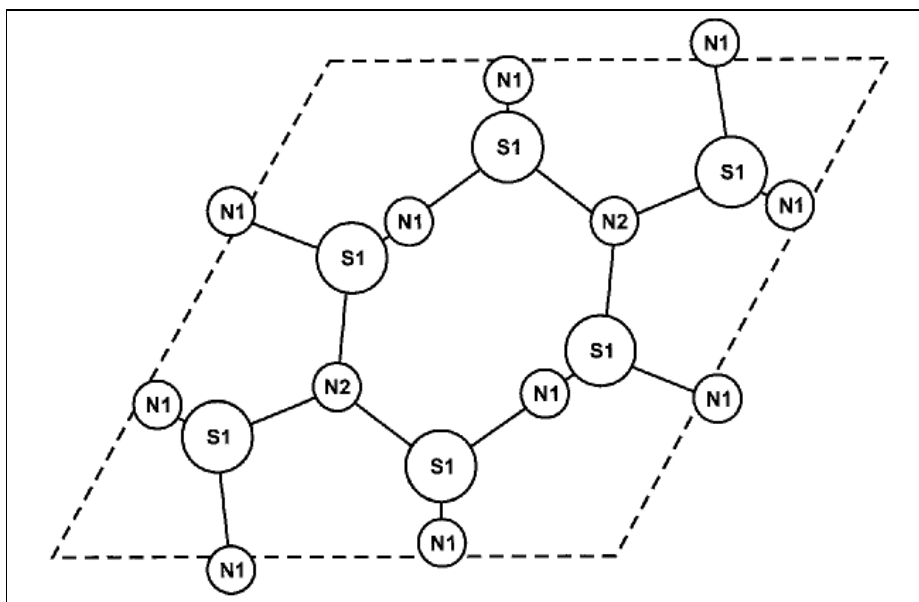


*Figure 4-4: $\beta$ $Si_3N_4$ unit cell [48].*

The $\beta$ $Si_3N_4$ structure is composed of superimposed layers of linked puckered rings, formed by joining six $SiN_4$ tetrahedra with little strain in bonds and bond angles. The alternating Si and N atoms, have a stacking sequence of ABAB, and form channels (diameter of 0.15nm) along the c direction. The $\alpha$ phase modification consists of alternate layers of similar AB layer and an additional mirror image CD, which is similar to AB but rotated by 180º on the c axis [52]. The edges of the double layer of the tetrahedra in the $\alpha$ $Si_3N_4$ are not exactly parallel to the c axis (as in the $\beta$ $Si_3N_4$ structure) but deviate to cause distortion allowing the individual tetrahedra to become more regular (Figure 4-10 Chapter 4.3). The c dimension of $\alpha$ $Si_3N_4$ (c = 0.5617nm) is approximately twice that of $\beta$ $Si_3N_4$ (c = 0.29107nm). The lattice parameters in **a** direction are similar: **a** ($\alpha$ $Si_3N_4$) = 0.7818nm, **a** ($\beta$ $Si_3N_4$) = 0.7595nm.

**The relationship between α and β Si₃N₄ structures**

The measured unit cell dimensions of α and β silicon nitride have the geometrical relationship of $a_\alpha > a_\beta$, $c_\alpha < 2c_\beta$ with c/a = 0.715 for α and c/a = 0.3826 for β Si₃N₄.

The following opinions, regarding α and β silicon nitride phase relationship, are documented in the literature:

- The α phase is in fact an oxynitride, while the β phase is pure silicon nitride [53] [54, 55].
- α and β phases are the low and high temperature modifications, respectively [45, 56]. This view is mostly based on the observations that during the nitridation of silicon the proportion of α phase increases with decreasing temperature, and that above 1400°C the α phase transforms to the β phase. However the reverse transformation from β Si₃N₄ to α Si₃N₄ at temperature below 1400°C has never been observed experimentally.
- The β phase is the thermodynamically more stable phase at all temperatures, and the development of the two modifications is controlled by the formation mechanism, rather than by thermodynamic considerations [51, 57].

The experimental evidence indicates that the formation of the two forms is mainly determined by kinetic factors, rather than by thermodynamic ones. Formation of α silicon nitride may by kinetically favoured by the vapour phase reaction in the presence of oxygen and other gaseous species such as silicon vapour and SiO. Formation of the β phase is mostly favoured through involvement of a liquid reactant phase.

Observations are indicating that with the same supply of nitrogen, solid silicon reacts to yield α phase with incorporation of oxygen into the lattice, while liquid silicon reacts to yield the β phase. Calculations show that the α Si₃N₄ phase is 30 kJ/mol (at 25°C) higher in free energy than the β phase and the driving force for the transformation from α to β Si₃N₄ lies in the higher thermodynamic stability of the β phase [21, 45]. The activation energy for this transformation is high hence the reconstructive transformation can proceed only via a liquid phase (metal silicon or metal silicides) which lowers the activation energy for transformation. A typical value for the activation energy in the presence of liquid is 405kJ/mol, which is close to the Si-N bond energy (435kJ/mol).

**Silicon carbide structure**

The industrial production of silicon carbide (α SiC polytype) is carried out by the carbothermic reduction of $SiO_2$ in the Acheson process. In this process a mixture of quartz sand or crushed quartzite (58-65%), graphite, petroleum coke or ash-free anthracite (35-42%) sodium chloride (1-2%) and wood chips (0.5-1%) are fused at temperatures between 2200°C and 2400°C using a graphite electrode, surrounded with a SiC rim for good electrical coupling. The reaction results in coarse grained α SiC according to Equation 4-1.

*Equation 4-1*    $SiO_2 + 3C \rightarrow SiC + 2CO$                  *ΔG = - 528 kJ/mol*
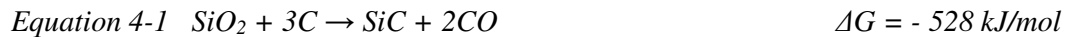
The produced α SiC has to be milled and leached in order to remove the metallic residue. The excess carbon is oxidized at 400°C and the resulting oxide layer is removed by hydrofluoric acid. The production of β SiC is conducted by the modified Acheson process, in a temperature range between 1500°C to 1800°C, where fine grained β SiC is formed via a solid-phase reaction. Ultra-fine pure β SiC is produced by gas phase reaction of $SiH_4$ or $SiCl_4$ with hydrocarbons such as $CH_4$ [58].

In addition to the synthetic production of SiC by the carbothermic reduction reaction, some natural deposits of α SiC known as Moissanite are found in Canyon Diablo meteorite association with diamond and iron. Natural occurrences are located in Bohemian volcanic breccias and Siberian Kimberlitic rocks [59]. The natural cubic β SiC polymorph has been found in the Green-River district in the USA [60].

The fundamental structural units of the various SiC polytypes are covalently (88% covalence) bonded $SiC_4$ ($sp^3$ hybridization of Si) and $CSi_4$ ($sp^3$ hybridization of C) tetrahedra that are arranged in planes, having common edges and one apex in the next plane of tetrahedra connecting the stacks. An ABC stacking sequence of the tetrahedra results in a cubic, zinc blend structure, designated as β-SiC, (Figure 4-5) whilst the ABAB sequence results in the hexagonal Wurtzite structure, denoted as α-SiC [60](Figure 4-6).
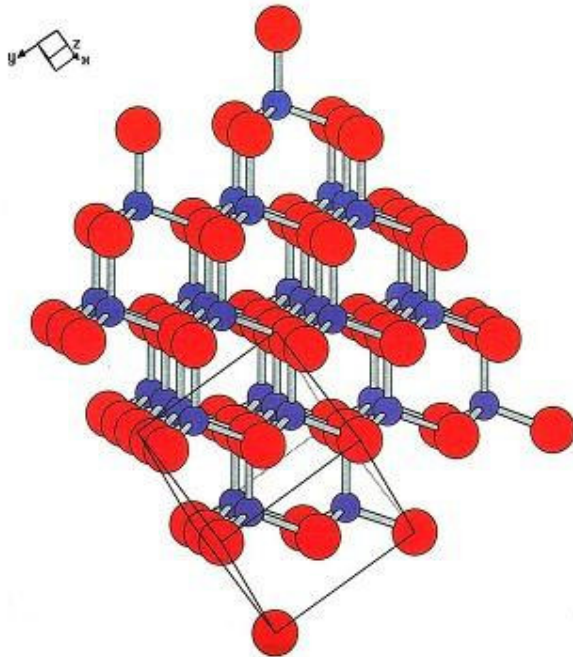
*Figure 4-5: Crystal structure of cubic β SiC polytype 6H 3C, Silicon atoms in red and carbon atoms in blue[60] .*
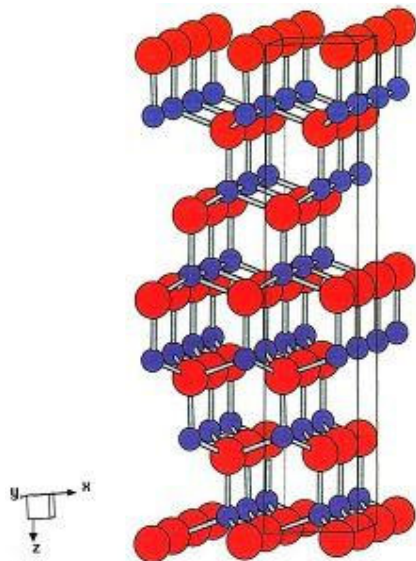


*Figure 4-6: Crystal structure of hexagonal α SiC polytype 6H (P63 mc)[60] .  Silicon atoms in red,  and carbon atoms in blue.*

The hexagonal or rhombohedral α-SiC exists in many polytypes (most frequently polymorphs: 2H, 4H, 6H and 15R) with 6H as the most common hexagonal α-SiC polytype. The various α-SiC structures are composed of intermixed more complex arrangements of the tetrahedral planes resulting in large stacking periods. Despite this structural difference, the density of all the SiC polymorphs is close to 3.17 g/cm$^3$.

## 4.2. Quantitative analysis of α and β $Si_3N_4$ using X-ray diffraction

Quantitative phase analysis of polycrystalline materials are often difficult due to the many variables that are involve in determining the relative amount of each phase. Among the important variables are: absorption coefficient, structure factor, particle size and identification and resolution of diffraction peaks.

In this study, powder X-ray diffraction patterns were acquired using a Bruker D8 Avance diffractometer operated at 40 kV and 40 mA, using CuKα radiation and a KF crystal monochromator. Diffraction patterns were recorded over a range of 10 to 70 degrees 2 theta, with step size 0.01 degree and counting time 1 sec per point. In the phase analysis of SNBSC materials, the phases of interest are SiC, α $Si_3N_4$, β $Si_3N_4$ unreacted metallic Si, $Si_2N_2O$, and $SiO_2$. The difficulties encountered when quantifying the different phases in these multi phase composites are:

1. Calculating the amount of SiC in the mixture. SiC shows strong preferred orientation effects due in part to its large particle size in comparison to other phases.
2. Calculation of the relative amounts of the $Si_3N_4$ phases is difficult due to:
    a. Extensive preferred orientation, particularly for α $Si_3N_4$ phase.
    b. The effect of overlap of the characteristic X-ray peaks means it can be difficult to separate these components.

To overcome the preferred orientation of the SiC phase, the samples were pulverized to a fine powder using a tungsten carbide crucible in a ROCKLABS shaker apparatus. The fine SNBSC powder samples showed reduced preferred orientation and higher homogeneity in comparison with the solid samples. In addition, the samples were rotated at rate of 60 rotations /minute during the analysis, in order to further reduce the preferred orientation effects.

A quantitative analysis method developed by Gazzara and Messier [61] was applied to overcome the preferred orientation effect of α $Si_3N_4$, and to reduce the quantification problem of the overlapping X-ray peaks of the two silicon nitride phases. Gazzara and Messier method is based on averaging the heights of several peaks of each phase, instead of integrated intensities; therefore reducing the error caused by preferred orientation effects. The criteria for peak selection included:

- Collection with sufficient pattern resolution.

- Freedom from diffraction peak overlap.
- Sufficient intensity to ensure statistical precision.

The peaks for both α and β $Si_3N_4$ phases including their 2 theta locations are listed in Table 4-1.

*Table 4-1: Main peaks with their 2 theta location, (CuKα X-rays) used in the calculation of phase quantity by Gazzara & Messier method*

| Peak(hkl) | 101 | 110 | 200 | 201 | 102 | 210 | 301 | 120 |
|---|---|---|---|---|---|---|---|---|
| 2theta α-$Si_3N_4$ | 20.594 | 22.925 | 26.532 | 31.006 | 34.577 | 35.343 | 43.492 | |
| 2 theta β-$Si_3N_4$ | 33.669 | 23.382 | 27.063 | | | | | 36.062 |

Once the peaks were determined, the following manipulations were carried out:

1. The intensity (peak height) of each peak was normalized by dividing the peak height with the appropriate value of L (L = $[(1/\upsilon^2 m \left| F \right|^2 (LP)])$. Values of L for each peak are listed in Table 4-2.

*Table 4-2: Values of L (hkl) for peaks of α and β $Si_3N_4$*

| Phase | Peak | 2θ (°) CuKα | L (hkl) |
|---|---|---|---|
| α $Si_3N_4$ | 101 | 20.594 | 7.50 |
| | 110 | 22.925 | 3.58 |
| | 200 | 26.532 | 2.44 |
| | 201 | 31.006 | 7.44 |
| | 102 | 34.577 | 6.66 |
| | 210 | 35.343 | 6.79 |
| | 301 | 43.492 | 3.13 |
| β $Si_3N_4$ | 110 | 23.382 | 4.21 |
| | 200 | 27.063 | 10.53 |
| | 101 | 33.669 | 10.90 |
| | 120 | 36.062 | 11.21 |

2. The values of the normalized peak heights (Yj) were averaged to give a "best value" $Y_{avg}$ for each phase.

3. The averaged normalized peak heights value $Y_{avg}$ was used to calculate the corrected intensity of each peak ($I_c$) for preferred orientation by multiplying it with the corresponding L e.g. $I_{\alpha (210)} = 6.79 \ Y_{\alpha \ avg}$

4. The weight fraction of each phase is determined by the sum of corrected intensities of the peaks of each phase according to the following equations:

   a. Weight % β $Si_3N_4$ = SUM $Ic_\beta$/( SUM $Ic_\alpha$+ SUM $Ic_\beta$)*100

   b. Weight % α $Si_3N_4$ = SUM $Ic_\alpha$/( SUM $Ic_\alpha$+ SUM $Ic_\beta$)*100

The weight percent of α and β Si$_3$N$_4$ for each sample were calculated using a spreadsheet which contains the calculation shown above. An example of such a spreadsheet is shown in Figure 4-7. This calculation method is used to produce quantitative analyses in the absence of standards of pure α and β Si$_3$N$_4$ single phase powders.

| **Sample name and identification** | | | | | C-3 | | |
|---|---|---|---|---|---|---|---|
| | Alpha | Beta | | | | | |
| **PDF card** | 76-1407 | 82-0698 | | | | | |
| **Analysis date** | 30/06/06 | | | | | | |
| **Exp date** | 13-16/6/06 | | | | | | |
| | **Peak** | **L(hkl)** | **2θ (°)** | **Intensity I(hkl)** | **I(hkl)/L(hkl)** | | **avg [I(hkl)/ L(hkl)]\* L (hkl)** |
| **α Si$_3$N$_4$** | 101 | 7.50 | 20.594 | 14 | 2 | | 23 |
| | 110 | 3.58 | 22.925 | 15 | 4 | | 11 |
| | 200 | 2.44 | 26.532 | 7 | 3 | | 8 |
| | 201 | 7.44 | 31.006 | 20 | 3 | | 23 |
| | 102 | 6.66 | 34.577 | 23 | 3 | | 21 |
| | 210 | 6.79 | 35.343 | 37 | 5 | | 21 |
| | 301 | 3.13 | 43.492 | 4 | 1 | | 10 |
| | | | | Average | 3 | Sum | 117 |
| **β Si$_3$N$_4$** | 110 | 4.2 | 23.382 | 16 | 4 | | 20 |
| | 200 | 10.5 | 27.063 | 35 | 3 | | 50 |
| | 101 | 10.9 | 33.669 | 56 | 5 | | 52 |
| | 120 | 11.2 | 36.062 | 75 | 7 | | 53 |
| | | | | Average | 5 | Sum | 175 |
| | **% α Si$_3$N$_4$** | **% β Si$_3$N$_4$** | **error** | | | | |
| | 40.1 | 59.9 | 1.4 | | | | |

*Figure 4-7: Example of spreadsheet using the Gazzara & Messier parameters to calculate the weight percent of α vs. β Si$_3$N$_4$.*

The silicon carbide to silicon nitride ratio was calculated by semi-quantitative analysis using the standard Eva XRD software package. The diffraction peaks were matched with standards from the software phase library. The software calculates the percentage of phases in the sample using the reference intensity ratio (I/Ic) specified for each phase. The standard diffraction files that were used for identification and quantification of the silicon nitride, silicon carbide, silicon oxide, silicon, and silicon oxynitride are listed in Table 4-3.

*Table 4-3: Diffraction files used for the silicon nitride /silicon carbide ratio, and silicon and silicon oxynitride quantification.*

| Phase | Lattice and Space group | Diffraction card | I/Ic |
|---|---|---|---|
| SiC | Hexagonal, P6$_3$mc | 72-0018 | 1.4 |
| SiC | Rhombohedral, R3m | 49-1429 | 0.9 (assumed) |
| Moissanite-4H, syn (SiC) | Hexagonal, P6$_3$mc | 29-1127 | 1.4 (assumed) |
| α Si$_3$N$_4$ | Hexagonal P31c | 76-1407 | 0.9 |
| β Si$_3$N$_4$ | Hexagonal, P6$_3$ | 82-0698 | 1.2 |
| Si$_2$N$_2$O | Orthorhombic Cmc21 | 79-1539 | 1.5 |
| Si | Hexagonal P6$_3$mc | 80-0005 | 2.0 |

In most of the samples analysed, the hexagonal P6$_3$mc phase was the main SiC phase observed (matched with card 72-0018). In some cases additional minor SiC phases were observed. The hexagonal Moissanite -4H and rhombohedral phases were observed in minor quantity and were matched with diffraction cards 29-1127 and 49-1429 respectively. For these minor SiC phases without reference intensity ratios, the I/Ic ratio was assumed based on SiC phases with similar unit cell parameters.

**Analysis of SNBSC samples**

Eight SNBSC bricks from seven different manufacturers have been analysed using XRD analysis to quantify the α and β Si$_3$N$_4$ content of the binder phase, using the Gazzara & Messier method [61] outlined above. A cross sectional slice was cut from each brick and samples were taken both from the exterior and interior parts of the brick. The analysis results (Table 4-4), showed an uneven distribution of α and β Si$_3$N$_4$ along the brick cross section. Higher β Si$_3$N$_4$ content was usually observed in the interior area of the brick, with considerable difference.

*Table 4-4: α and β $Si_3N_4$ content in samples from exterior and interior part of SNBSC brick cross sections.*

| Brick | Exterior | | Interior | |
|---|---|---|---|---|
| | % α $Si_3N_4$ | % β $Si_3N_4$ | % α $Si_3N_4$ | % β $Si_3N_4$ |
| A | 87.3 ± 1.4 | 12.7 ± 1.4 | 88.2 ± 1.4 | 11.8 ± 1.4 |
| B | 72.1± 1.4 | 27.9 ± 1.4 | 35.1 ± 1.4 | 64.9 ± 1.4 |
| C | 74.7 ± 1.4 | 25.3 ± 1.4 | 60.2 ± 1.4 | 39.8 ± 1.4 |
| D | 89.5 ± 1.4 | 10.4 ± 1.4 | 92.4 ± 1.4 | 7.5 ± 1.4 |
| E | 91.7 ± 1.4 | 8.3 ± 1.4 | 90.3 ± 1.4 | 9.7 ± 1.4 |
| F | 80.0 ± 1.4 | 20.0 ± 1.4 | 75.7 ± 1.4 | 24.3 ± 1.4 |
| G | 85.7 ± 1.4 | 14.3 ± 1.4 | 86.4 ± 1.4 | 13.6 ± 1.4 |
| H | 48.5 ± 1.4 | 51.5 ± 1.4 | 24.6 ± 1.4 | 75.4 ± 1.4 |

Higher concentration of $Si_2N_2O$ (up to 5%) and metallic Si (< 7%) were observed in samples taken from interior area of SNBSC bricks.

Analysis of samples taken from the exterior, interior and core part of the brick cross sections from the two bricks, showing the largest variation in α/β $Si_3N_4$, showed consistent decline in this ratio from core to exterior (Figure 4-8).
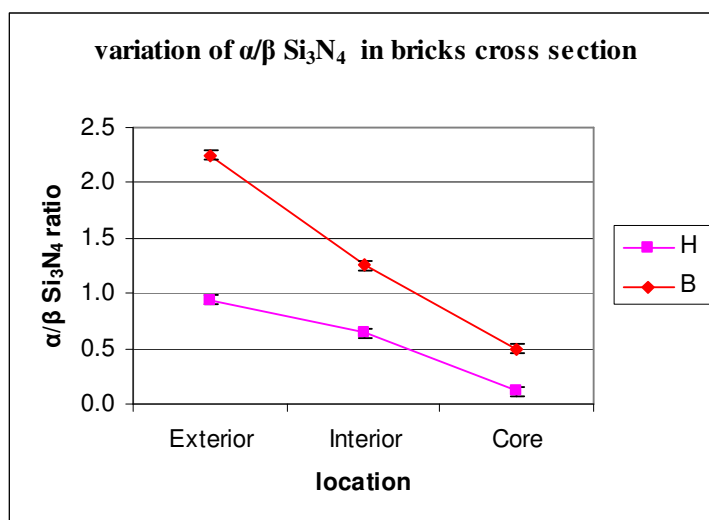


*Figure 4-8: α/β $Si_3N_4$ ratios detected in samples taken from two of the more differentiated SNBSC brick cross sections.*

The high $\beta$ $Si_3N_4$ content in the internal part of some bricks could be attributed to high temperatures during the nitridation stage of the fabrication process. Modelling suggests temperatures above 1500°C are reached due to the exothermic nitridation reaction and the difficulty in heat dissipation from the core of the brick, resulting in transformation of the $\alpha$ $Si_3N_4$ to the $\beta$ phase (see Chapter 2).

## 4.3. Solid state NMR analysis

### 4.3.1. Introduction

Solid State ^{29}Si MAS NMR analysis provides an ideal tool for the in-situ analysis of the chemical environment of Si in solids materials. It was used to get additional information about the microstructure of the SNBSC refractories, and in particular to determine both the presence and quantity of free Silicon and the relative ratio SiC to $Si_3N_4$. This data is sometimes complicated to gather using XRD, due to the fact that there is significant overlap in the powder diffraction patterns. An amorphous species could only be identified and quantified by the use of XRD standard samples. In the case of SNBSC, free silicon could be found as an amorphous phase if it arises from melting of the reactants and fusion into a glass phase. This phase will be difficult to identify using XRD as it largely contributes to the diffraction background signal. Preferential orientation of SiC in X-ray diffraction also leads to difficulties in quantifying its relative content. Reitvald analysis could be a solution to overcome the preferred orientation of SiC.

In ^{29}Si MAS NMR- Silicon, silicon oxynitride, and silicates, as well as $Si_3N_4$ and SiC are distinguished by their unique chemical shifts [62]. Because of its sensitivity to local chemical environment, NMR can quantify these species in both crystalline and amorphous phases. An experimentally well-established rule of thumb for the interpretation of solid-state NMR spectra is that broader line widths are associated with samples of lower crystalline order; hence an amorphous phase can be generally identified. In this case, the line shape does not correspond to either a Gaussian or Lorentzian line shape, and is characterized by a broad resonance with FWHH of $\approx 27$ ppm [62]. The greater linewidth is related to heterogeneity in the local silicon environment, with diverse but similar sites characteristic of an amorphous phase. An amorphous silicon nitride phase will show a broad peak centred at -46.4 ppm [63]. The presence of $SiO_2$ should give rise to a resonance at $\approx$ -110 ppm and the Si peak should be observed around -81 ppm [63].

The major drawback of ^{29}Si NMR spectroscopy is the long period of time required for the acquisition of spectra with a sufficient signal to noise ratio. In the quantitative analysis of α-$Si_3N_4$ and β-$Si_3N_4$ a long relaxation time between pulses is needed [62]. Also, the relatively low content of $Si_3N_4$ (compared to SiC in SNBSC samples) makes it difficult to distinguish between the two different phases of silicon nitride.

### 4.3.2. Experimental method

All solid-state NMR experiments were carried out on powder samples using a Bruker AVANCE 300 spectrometer operating at 300.13 MHz proton frequency, i.e. at 59.63 MHz silicon frequency. The basic spectra were obtained using "standard" one-pulse-and-collect experiments. The experiments were carried out using a 7mm Bruker spinning probe with zirconia rotors. The parameters used in the experiment are listed in Table 4-5:

*Table 4-5: Parameters used in the $^{29}$Si NMR experiments for various pure compounds.*

| Material | Pulse angle (°) | Pulse duration (µs) | Recycle delay (seconds) | Number of scans | Sweep width (Hz) |
|---|---|---|---|---|---|
| Pure α-Si$_3$N$_4$ | 37 | 1.69 | 3,600 | 22 | 19,960 |
| Pure β-Si$_3$N$_4$ | 68.4 | 3.1 | 2,400 | 22 | 19,960 |
| Pure α-SiC | 68.4 | 3.1 | 2,400 | 22 | 19,960 |
| Deconvolution | 37 | 1.69 | 3,600 | 44 | 19,960 |

The strategy was to apply the worst case scenario i.e. the repetition times based on the pure substances, although, for the commercial SNBSC samples, relaxation could be shorter. This phenomenon is due to contaminants which act as paramagnetic centres, and structural defects. Thus it could be deduced that the system is fully relaxed after 1 hour with a 37$^o$ pulse. This strategy was then applied to the rest of the samples.

All spectra were obtained at ambient temperature using samples enclosed in the rotors. The $^{29}$Si chemical shift scale is referenced to tetramethylsilane (TMS). The samples were rotated at 7000 ± 1 Hz, and the magic angle was adjusted by maximizing the sidebands of the $^{79}$Br signal of a KBr sample.

In the Si$_3$N$_4$ crystal structure each silicon atom is connected to four nitrogen atoms in a tetrahedral arrangement. The SiN$_4$ tetrahedrons are joined by sharing nitrogen corners so each nitrogen atom is linked to three silicon atoms in planar arrays which are stacked parallel to the basal (0 0 1) plane of a hexagonal-symmetry unit cell. The α-Si$_3$N$_4$ phase has a stacking sequence of ABCD and β-Si$_3$N$_4$ has an ABAB sequence and consequent halving of the hexagonal c lattice parameter. Both structures consist of interleaved sheets of 8 and 12 membered rings of silicon and nitrogen (Figure 4-9).
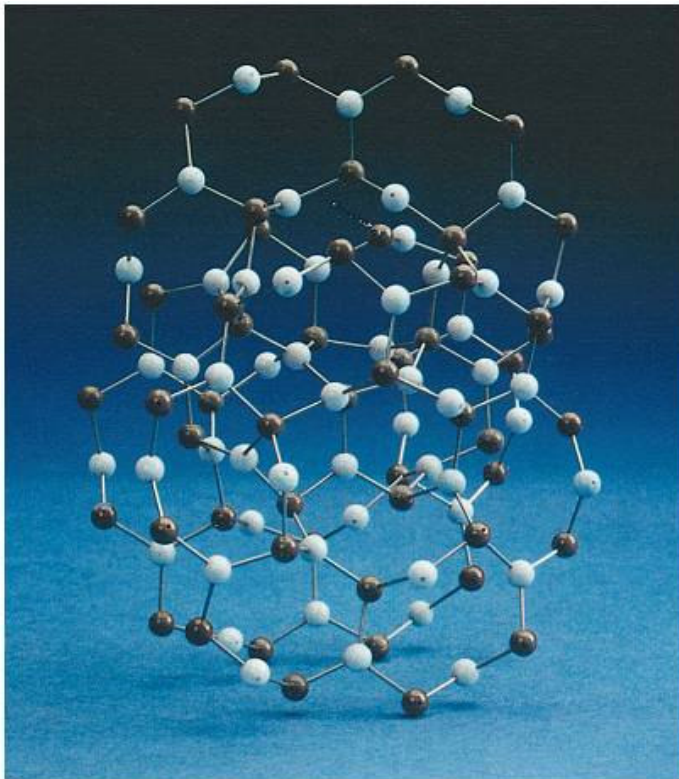
*Figure 4-9: Ball and stick model of α-Si₃N₄ showing 8-and12-membered rings and structural layers - nitrogen (brown) and silicon (blue) [21].*

In the α-form, each alternate sheet is inverted and offset slightly with respect to the underlying sheet, creating two unique silicon sites in the structure Si (1) and Si (2) which have small differences in tetrahedral bond-length and symmetry. These two different Si symmetries can be seen in a projection of the α-structure onto the basal (0 0 1) plane (Figure 4-10).
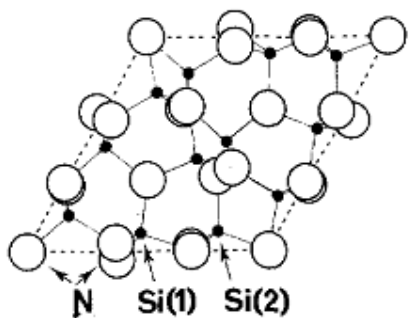


*Figure 4-10: Projection of the α-Si₃N₄ structure on to (0 0 1) plain  showing two different silicon site symmetries S1 and S2 [64].*

Standard samples of α-Si$_3$N$_4$, β-Si$_3$N$_4$ and α-SiC were analyzed in order to get accurate NMR information. Parameters such as chemical shifts, full width at half height (FWHH) and peak areas obtained from the standards samples were then employed in the analysis of the main components of Si$_3$N$_4$ bonded SiC refractories samples.

The difference in the two silicon symmetries in the $\alpha$-$Si_3N_4$ phase results in a spectrum which consists of two narrow peaks (FWHH of 80-85 Hz) centred at -46.7 and -48.8 ppm (Figure 4-11A). However, in the $\beta$ form the interleaved sheets of Si and N are stacked in a regular manner and all tetrahedra have the same dimensions, producing a single unique Si site.  Hence the ^{29}Si NMR spectrum of $\beta$-$Si_3N_4$ consists of a single sharp peak with a chemical shift of -48.6 ppm and FWHH of 120 Hz (Figure 4-11B).  The other small peak at -61.2 ppm in Figure 4-11B is due to impurities which can be assigned to silicon oxynitride [63].
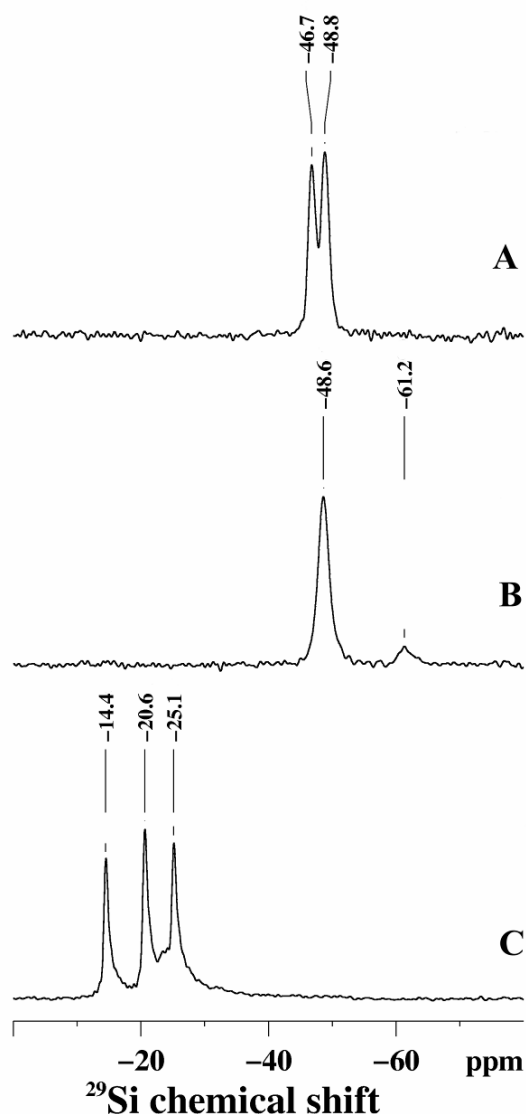


*Figure 4-11 [29]Si MAS spectra of α- Si₃N₄ (A), β-Si₃N₄ (B), and α-SiC (C)*

The [29]Si spectrum of $\alpha$-SiC is shown in Figure 4-11C. The NMR spectrum consists of three narrow lines (FWHH of $\approx$ 50 Hz), reflecting subtle differences in the nuclear environment. The

6H polytype of α-SiC reveals three types of silicon in a 1:1:1 ratio [65-67]. The peak positions for 6H are -14.4, -20.6 and -25.1 ppm [68].

**Comparison between exterior and interior zones of SNBSC bricks**

The [29]Si spectra of a sample from the interior part of brick A is shown in Figure 4-12. There are two regions identified in the [29]Si spectra. The first region consists of three narrow high intensity peaks at -14.3, -20.4, and -25.0 ppm, assigned to α-SiC according to their chemical shifts. The second part, with peaks at -47.2 ppm and -48.6 ppm, can be assigned to the minor $Si_3N_4$ phase.
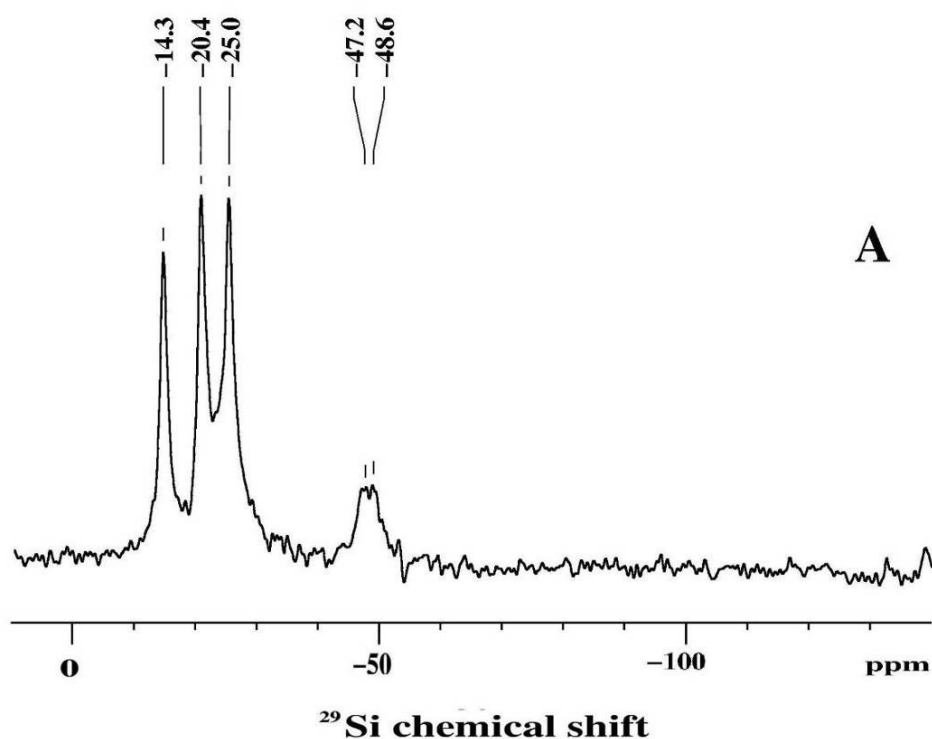


*Figure 4-12: [29]Si MAS spectra of interior part of sample A.*

In the samples analysed, neither the oxygen rich silicon compounds ($SiO_2$ and $Si_2N_2O$) nor the elemental silicon, which are included as an amorphous phase, were identified at significant levels. This observation is confirmed by the XRD results (Figure 4-13). The absence of amorphous phases indicates a highly crystalline structure in the sample.
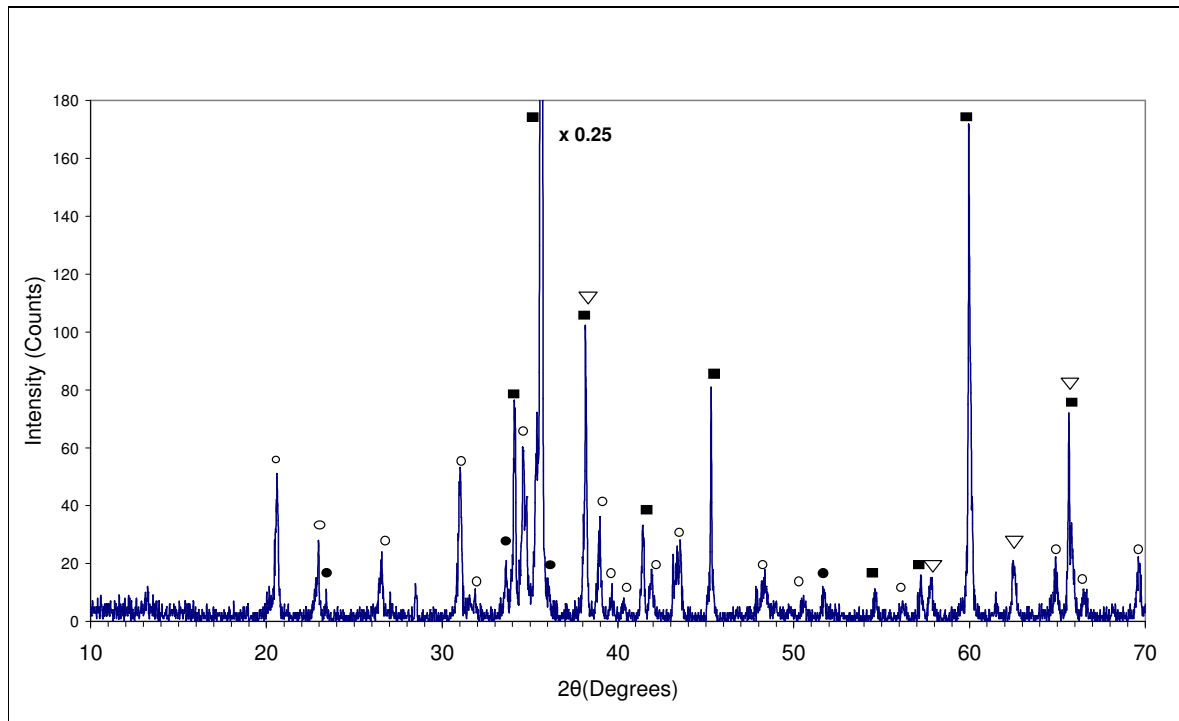
*Figure 4-13: X-ray diffraction pattern of a sample from the internal part of brick A. (○) α Si₃N₄ (● ) β Si₃N₄, ( ■) SiC, ( ▽) Moissanite.*

The spectra from the peripheral and inner core of brick H are shown in Figure 4-14.  In the sample from the interior part of the brick (Figure 4-14A), β-$Si_3N_4$ is the main phase detected in the $Si_3N_4$ chemical shift region. The sample from the external part (Figure 4-14B) shows also the presence of α-$Si_3N_4$ in the corresponding region.
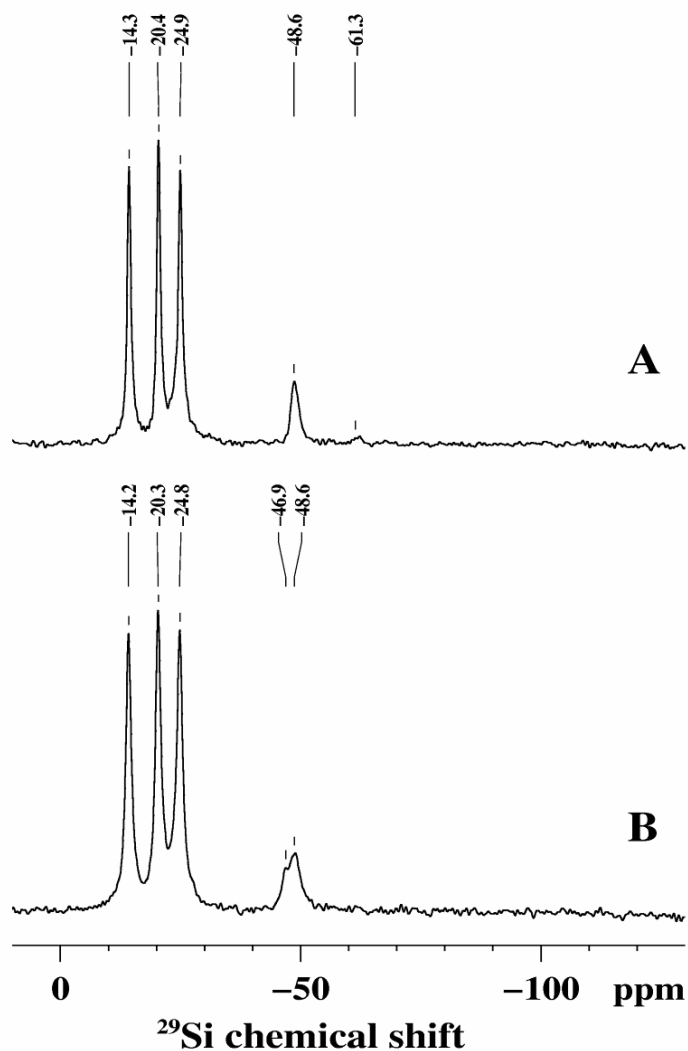
*Figure 4-14: [29]NMR spectra of sample H: A) Sample from interior part of brick, B) sample from exterior part of the brick.*

The line width in the spectra varies between 1.8 ppm for each $\alpha$-$Si_3N_4$ peak (Figure 4-14B) and 2.5 ppm for $\beta$-phase (Figure 4-14A). A small amount of $Si_2N_2O$ was detected at -61.3 ppm (Figure 4-14A) [69], but no amorphous phase such as free silicon was detected.

A peak fitting technique was applied to get a better understanding of the structure. The example deconvolution shown in Figure 4-15 was taken from the peripheral part of sample H (also shown in Figure 4-14B). The $\alpha/\beta$ silicon nitride ratio obtained by peak fitting using deconvolution is 0.5 and is in good agreement with XRD results (48.5 $\pm$1.4 % $\alpha$ vs. 51.5 $\pm$ 1.4 % $\beta$ $Si_3N_4$). The deconvolution technique was performed using the constraints of the known chemical shift positions and the linewidths and Lorentzian /Gaussian ratios obtained from standard samples of $\alpha$-$Si_3N_4$, $\beta$-$Si_3N_4$ and $\alpha$-SiC (see Figure 4-11). The calculated SiC/ $Si_3N_4$ ratio is around 9:1.

Table 4-6 summarizes the results obtained by deconvolution of spectra of samples taken from the interior and exterior part of brick H, whose spectra are shown in Figures 4-14.
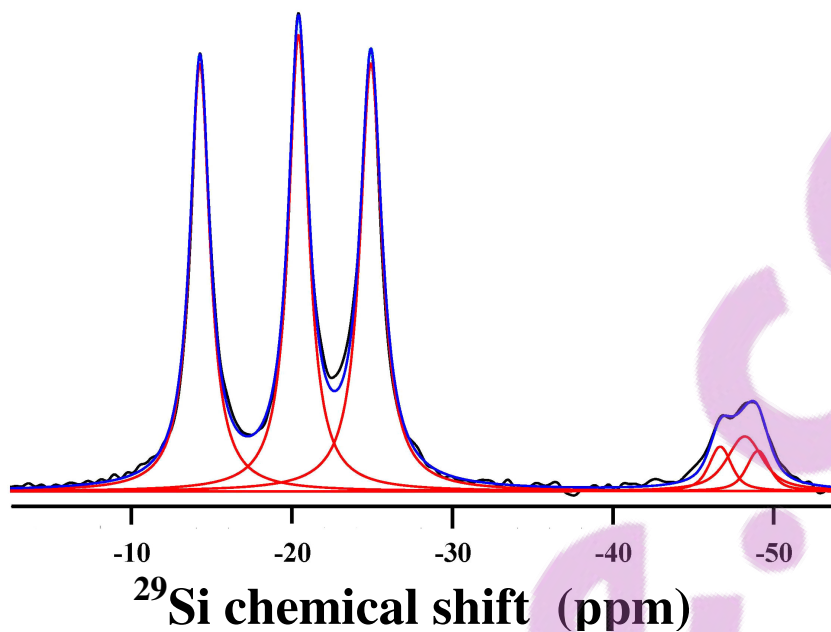


*Figure 4-15: $^{29}$Si MAS spectrum of the the exterior part of the sample H.*

*Table 4-6: Data obtained from deconvolution: (A)-interior part of the sample H, (B )-exterior parts of the sample H,*

| # | Phase | Chemical shift (±0.2 ppm) | FWHH (± 15 Hz) | | Peak area (± 1 %) | |
|---|---|---|---|---|---|---|
| | | | A | B | A | B |
| 1 | SiC | -14.2 | 75 | 90 | 27 | 28 |
| 2 | SiC | -20.4 | 80 | 85 | 31 | 30 |
| 3 | SiC | -24.9 | 85 | 90 | 31 | 30 |
| 4 | α $Si_3N_4$ | -46.7 | | 100 | | 3 |
| 5 | β $Si_3N_4$ | -48.3 | 127 | 155 | 11 | 6 |
| 6 | α $Si_3N_4$ | -49.0 | | 105 | | 3 |

## 4.4. Raman spectroscopy

A Renishaw 1000 Raman Imaging Microscope was used to identify the different phases in the SNBSC sample. The Raman imaging microscope consists of a single grating spectrograph, a Leitz microscope and an air-cooled CCD array detector. The laser used was a Renishaw solid-state diode laser emitting a line in the near-infrared region at ~785 nm at 26 mW with a grating of 1200 lines/mm. A 20x objective was used which focused the beam to a size of ~ 5 µm at the sample surface. The entrance slit width was 100 µm and the detector resolution was 4cm$^{-1}$. Each spectrum was recorded with 10 accumulations at an Integration time of 2 seconds.

Pure Si, SiC, α Si$_3$N$_4$ and β Si$_3$N$_4$ powders were analysed separately in order to obtain the characteristic spectra of each phase. The spectra of the different pure compound showed different Raman shifts for each phase with good separation between the shifts (Figure 4-16).
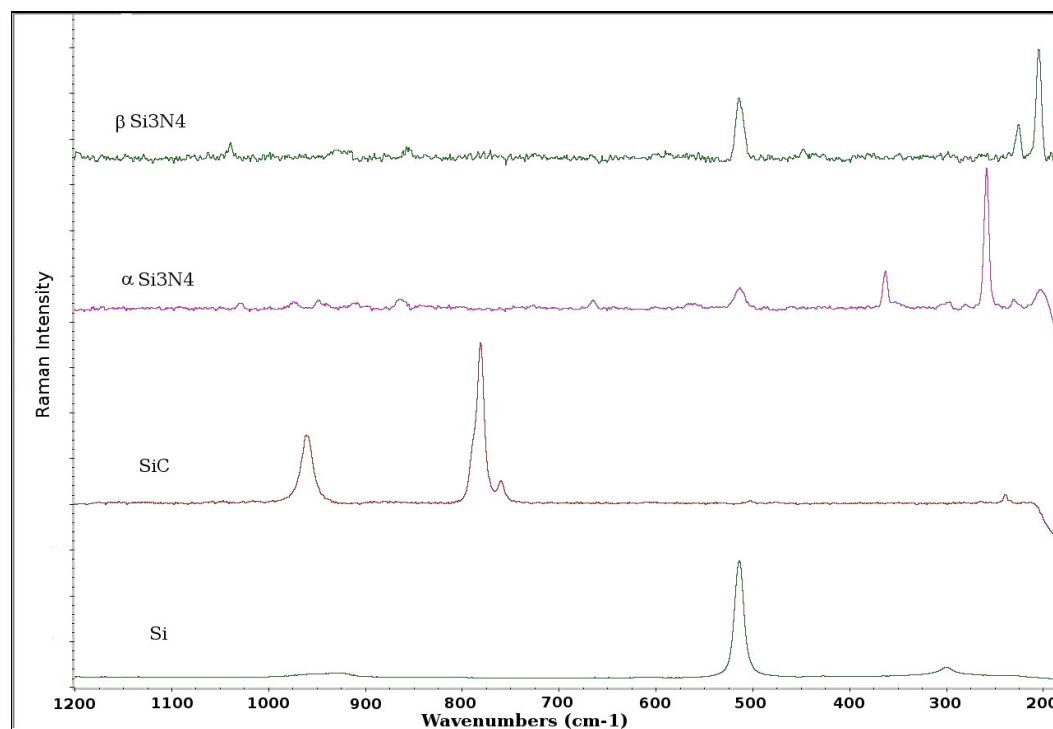


*Figure 4-16: Raman spectra of Si, SiC, α Si$_3$N$_4$, and β Si$_3$N$_4$.*

The characteristic Raman shifts that were observed for the different peaks of the standard pure materials are listed in Table 4-7.

*Table 4-7: Raman shifts of different pure phases.*

| Phase | Raman shifts |
|-------|--------------|
| Si | 502 |
| SiC | 789, 797 |
| α $Si_3N_4$ | 258, 365 |
| β $Si_3N_4$ | 204, 225 |

The bonding phase of SNBSC samples from the exterior and the interior parts of brick H were analysed and the spectra was compared to the spectra of the pure α and β $Si_3N_4$ (Figure 4-17).
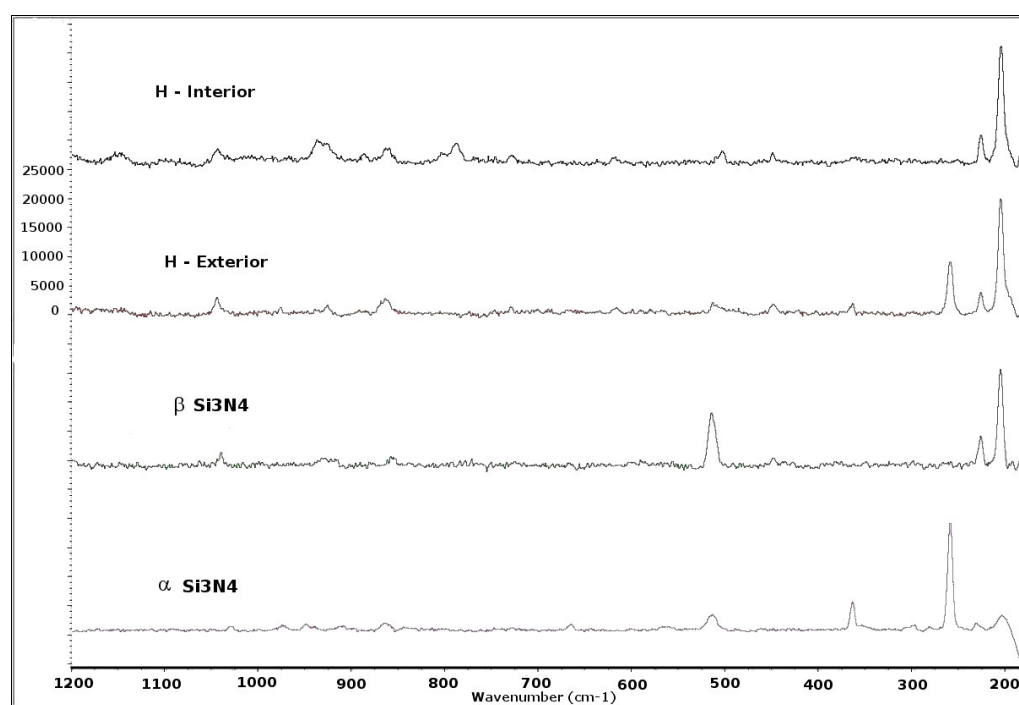


*Figure 4-17: Raman spectra of bonding phase of samples taken from the exterior and interior of brick H compared with spectra of pure α and β $Si_3N_4$.*

The spectra of the bonding phase of the sample from the exterior part of brick H reveal that the bonding phase of the sample consist of a mixture of both α and β $Si_3N_4$ while the bonding phase of the sample from the interior zone consist solely of β $Si_3N_4$.

In order to quantify the different $Si_3N_4$ phases in SNBSC samples, a mixtures of pure powders of α $Si_3N_4$ and β $Si_3N_4$ were made in the following ratios: 20α -80β, 40α -60β, 50α -50β, 60α -40β, 70α -30β, 80α -20β. The mixtures were analysed and the area under peak at 258 cm$^{-1}$ (characteristic peak for α $Si_3N_4$) and 204cm$^{-1}$ (the main peak for β $Si_3N_4$) was calculated. The

ratio of the 258/204 peak area was calculated and plotted as function of $\alpha$ /$\beta$ $Si_3N_4$ powder mix ratio (Figure 4-18),

Although a linear correlation can be seen in the high $\alpha$ /$\beta$ $Si_3N_4$ mix ratio, this correlation does not apply to all the mixture ratios, as seen in Figure 4-18, meaning an accurate quantification of different silicon nitride phases is not viable.
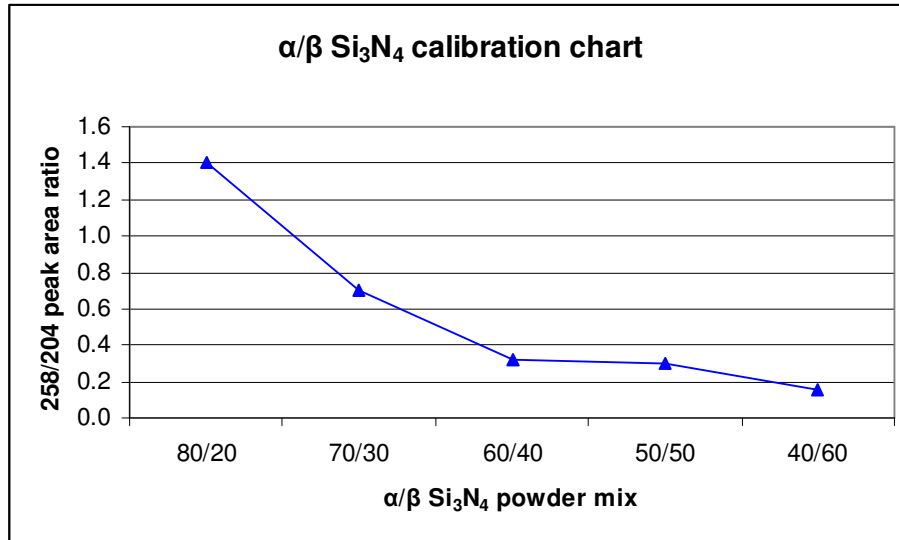


*Figure 4-18: Raman spectra correlation chart expressing the ration of 258/204 peak area as a function of $\alpha$ /$\beta$ $Si_3N_4$ powder mix ratio.*

.

## 4.5. X-ray photoelectron spectroscopy (XPS)

In this work, X-ray photoelectron spectroscopy (XPS) has been used to identify and quantify the different species in the SNBSC composite i.e. silicon, silicon carbide, silicon nitride, and silicon oxide. This analytical method has the ability not only to identify the elements in the sample, but also to provide information about their chemical state and bonding. However, it should be noted that this method is analysing only the surface (the top 2-5 nm) of the solid samples and not the bulk material, making it sensitive to any oxidation or coating layer that is formed on the sample surface. The sample can be presented as a powder but the same considerations apply.

The XPS technique involves bombardment of a material *in vacuo,* in this case with a monochromatic source of radiation, capable of penetrating many micrometers into the bulk. The X-ray photon is absorbed by an atom in a molecule or solid leading to ionization and emission of electrons (photoionisation) from the tightly-bound core or from the weakly-bound valence levels. The photoelectron emission energy is analysed to produce a spectrum of electron intensity as a function of energy (the number of emitted photoelectrons as a function of their kinetic energies). The photoelectron kinetic energy can be expressed as:

*Equation 4-2*          $E_K = h\nu - E_B - \Phi sp$

Where hν is the energy of the exciting X-ray photos, $E_B$ is the electron binding energy and it measured with respect to the Fermi-level of the solid. $\Phi sp$ is the work function of the specific spectrometer [70]. For each and every element, there is a characteristic binding energy associated with each core atomic orbital.

The most commonly employed X-ray sources are Mg Kα radiation (hν = 1253.6 eV) and Al Kα radiation (hν = 1486.6 eV). The spectrum will then be located within the range of the kinetic energy of the emitted electrons ≈ 0 to1250 eV for Mg Kα radiation or 0 to1480 eV for Al Kα radiation. Briggs and Grant [71] provide extensive detailed information about the XPS technique.

 **Sample Preparation**:
Samples from the exterior and the core of block H were cut using a diamond wheel to size of 15x 15 mm in thickness of around 5 mm. The samples were ground on a 40µm diamond grinding

wheel and later polished on a grinding wheel using 9µm diamond paste. The samples were further polished, by applying polishing cloth with 6µm, 3µm and 1µm diamond pastes. The samples were cleaned in iso-propanol in an ultrasonic bath prior to changing to the finer diamond pastes.

**XPS analysis**

XPS spectra were collected using a Kratos Axis ultra DLD instrument equipped with an UHV analytical chamber. The chamber base pressure was around 5 x $10^{-10}$ Torr. Spectra were excited using monochromatised AlKα radiation (hν = 1486.6 eV) and an electron energy analyser with delay-line detector was used. For analysis, the samples were mounted on a stainless steel stub using double-side adhesive tape.

Survey spectra were collected with analyser pass energy of 160 eV and narrow spectral regions with pass energy of 20 eV. XPS data were corrected for a sample charging during X-ray irradiation using adventitious hydrocarbon referencing (C 1s at 285.0 eV). The quantification of spectra was carried out using modified Scofield cross-sections from the Kratos element library.

A silicon wafer and pure powder samples of silicon carbide, silicon nitride, and silicon oxide were analysed separately to serve as standards for identifying the specific binding energies of the different compounds in a SNBSC sample. The resulting binding energy of each standard compound observed in the Si2p region, is listed in Table 4-8 and the corresponding Si2p region spectra are shown in Figure 4-19.

*Table 4-8: Binding energies in the Si2p region of Si, SiC, $Si_3N_4$, and $SiO_2$.*

| Compound | Binding energy of pure element (eV) | Binding energy according to the literature [72] (eV) |
|---|---|---|
| Si | ¾ - 99.1 | 99.1 |
| Si | ½ - 99.7 | 99.7 |
| SiC | ¾ -100.3 | 100.2 |
| SiC | ½ -101.1 | 101.5 [73] |
| $Si_3N_4$ | 102.2 | 101.7 |
| $SiO_2$ | 103.8 | 103.2 |

The silicon wafer Si2p spectra shown in Figure 4-19 represent a sputtered silicon wafer. The two peaks observed are the spin-orbit split Si 2p ³⁄₂ (at 99.1eV) and Si2p ½ (at 99.7eV).

The Si2p spectrum of the silicon carbide powder contain a single spin-orbit split doublet with a spin-orbit splitting of 0.7 eV the two peaks were observed at 101.0eV and at 100.3 eV had an area ratio of 2:1.

**Si 2p of standard materials**
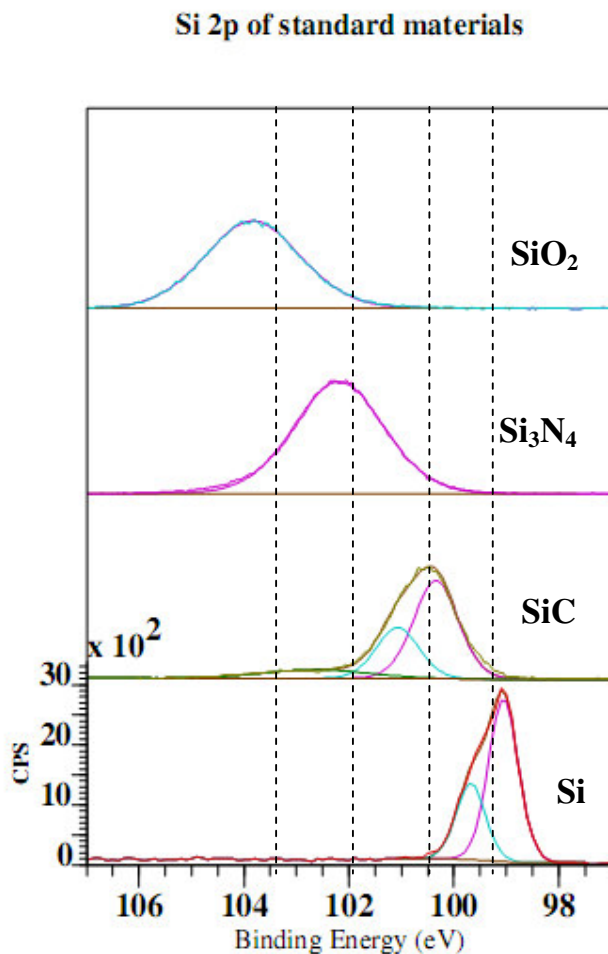


*Figure 4-19: Spectra of Si2p region of silicon wafer, silicon carbide, silicon nitride, and silicon oxide powders. The dotted vertical lines represent the literature values. The spin-orbit splitting of the Si2p line is resolved for the Si wafer and the SiC.*

The Si 2p spectrum of the commercial silicon powder used as starting material for the nitridation reaction in the production of SNBSC refractory materials was analysed and the spectrum was compared to a non sputtered silicon wafer (Figure 4-20). In both samples a peak was observed at 100.1eV that relate to metallic silicon, and a peak at 103.4 eV relate to the silicon oxide phase. For the silicon powder sample, an additional peak was observed at a lower binding energy (98.3 eV) indicating contamination likely by a metal silicide such as Ni or Fe (literature values 98.4-

98.5eV). Commercial silicon powders contain typically 0.9% Fe, of which two-thirds is metallic introduced in the grinding process by the use of steel ball-mills [74].
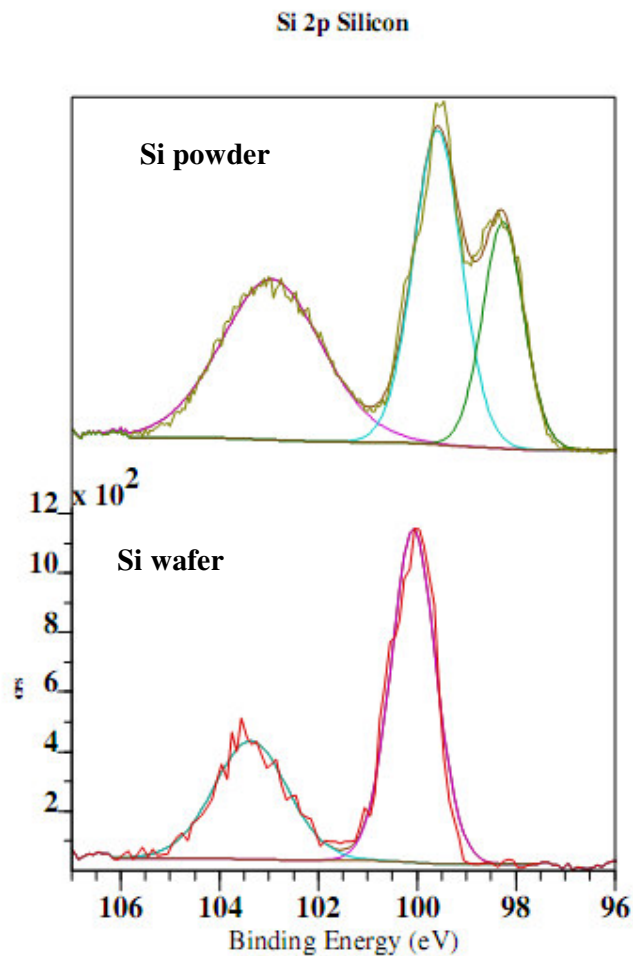
**Si 2p Silicon**



*Figure 4-20: Si 2p spectra of non spattered silicon wafer (bottom) and silicon powder that is used as a raw material in production of SNBSC material.*

In the carbon C 1s spectra of the pure silicon carbide powder, a peak was observed at 282.7 eV consistent with silicon carbide (282.4 eV according to the literature [75]) and an adventitious carbon peak was observed at 285.0 eV (Figure 4-21). The adventitious carbon peak was the only peak observed in the C1s spectra of all other standard materials (Figure 4-21).

**C 1s Standard materials**
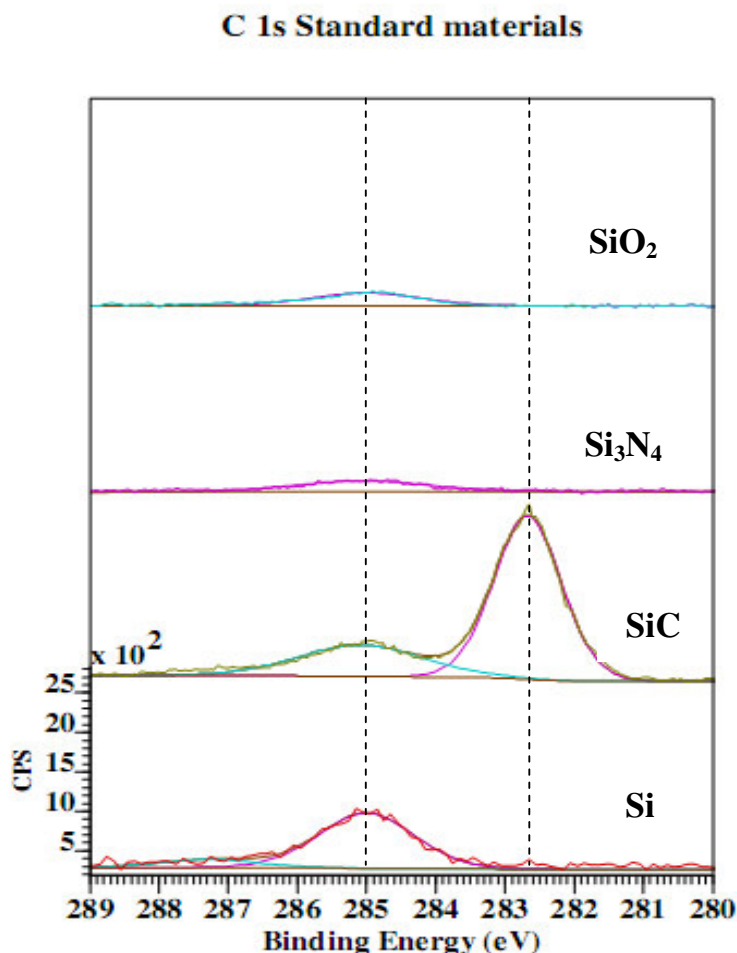


*Figure 4-21: C1s spectra of Si wafer, SiC, Si$_3$N$_4$ and SiO$_2$ powders. The dotted line at BE= 282.7eV represent the position of carbide peak and the line at BE=285.0 the position of adventitious carbon.*

Interior and exterior polished samples from SNBSC brick H were then analysed by XPS. The atomic percent of the various elements observed in these samples (based on the wide scan) are listed in Table 4-9. In the Si 2p spectra (shown in Figure 4-22), the presence of silicon carbide, silicon nitride, and silicon oxide were identified on the basis of the binding energies observed from the pure powder samples (Table 4-10). A metallic silicon peak was not observed in the spectra. Quantification of the different species in the samples, based on deconvolution of their Si 2p spectra, is shown in Table 4-11.

*Table 4-9: Atomic percent of elements in exterior and interior parts of block H.*

| Sample | O 1s (%) | N 1s (%) | C 1s (%) | Si 2p (%) |
|---|---|---|---|---|
| H exterior | 19.2 | 2.3 | 68.5 | 10.1 |
| H interior | 20.8 | 1.3 | 67.7 | 10.3 |
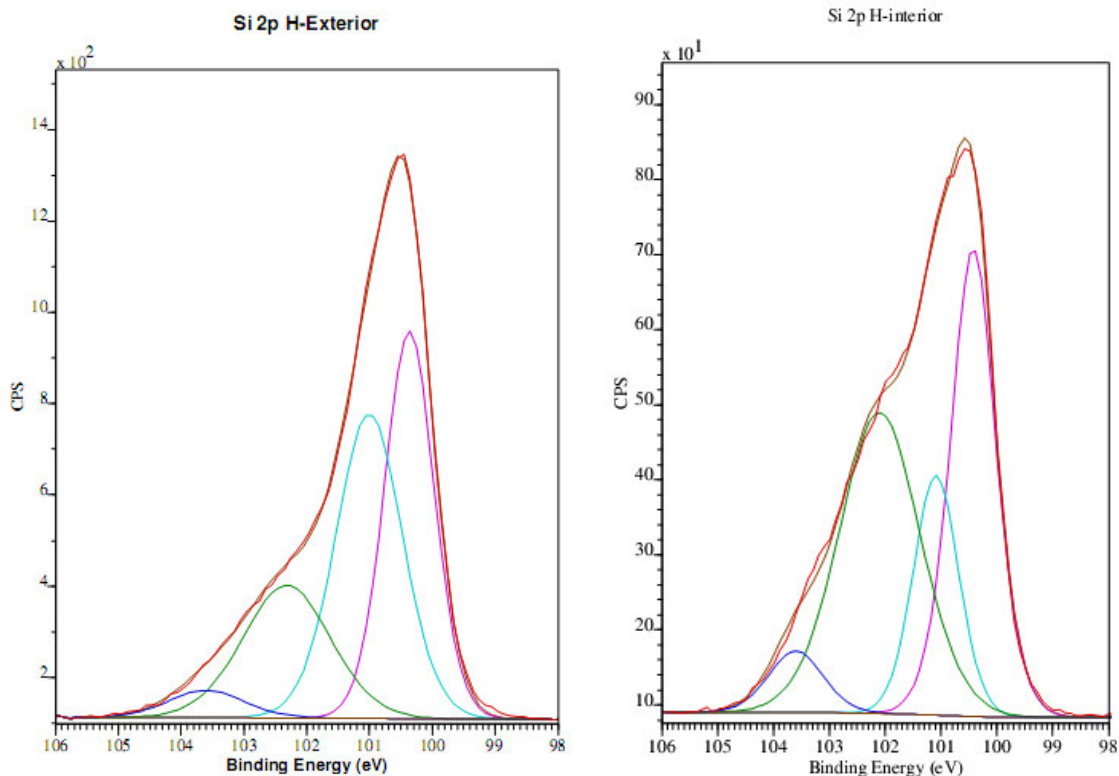
*Figure 4-22: Si 2p spectra of exterior (left) and interior (right) parts of SNBSC block H.*

*Table 4-10: Peaks in the Si 2p region (after charging correction) of samples from the interior and exterior of block H.*

| Peak | Interior Binding energy (eV) | Exterior Binding energy (eV) | Values from standard materials (eV) |
|---|---|---|---|
| Free Si | -- | -- | 99.1 |
| Carbide ³⁄₂ | 100.4 | 100.4 | 100.3 |
| Carbide ½ | 101.1 | 101.1 | 101.1 |
| Nitride | 102.1 | 102.1 | 102.2 |
| Oxide | 103.6 | 103.6 | 103.8 |

*Table 4-11: Quantification of the different silicon species, in samples taken from the exterior, and interior of SNBSC brick H.*

| | Free Si (%) | SiC (%) | $Si_3N_4$ (%) | $SiO_2$ (%) |
|---|---|---|---|---|
| H exterior | -- | 69 | 27 | 4 |
| H interior | -- | 54 | 40 | 6 |

The composition of the different species from Table 4-11 show that the exterior sample shows a typical composition of SNBSC material that is in line with composition results determine by XRD analysis. The composition of the interior sample show higher content of $Si_3N_4$, due to focus of the electron beam on the bonding phase.

The C1s region of the samples from the exterior and interior of brick H revealed a silicon carbide peak at 282.6 eV. The atomic ratio between the silicon carbide peak in the Si 2p spectra and the silicon carbide peak at the C 1s spectra was 1:1.3. The adventitious carbon peak was observed at 285 eV and another two carbon species were observed at higher binding energy (Figure 4-23). The peak at 286 eV could be associated with the C-O bond from interaction of the material with air moisture or an organic solvent residue (e.g. iso-propanol), creating a micron size layer on the surface of the sample.

The peak at 288 eV could be assigned to a C-N species. The presence of an additional peak in the N 1s spectra (Figure 4-24) at a higher binding energy (399.8 eV) than the nitride peak (397.4 eV) is supporting evidence for the presence of such a C-N species.
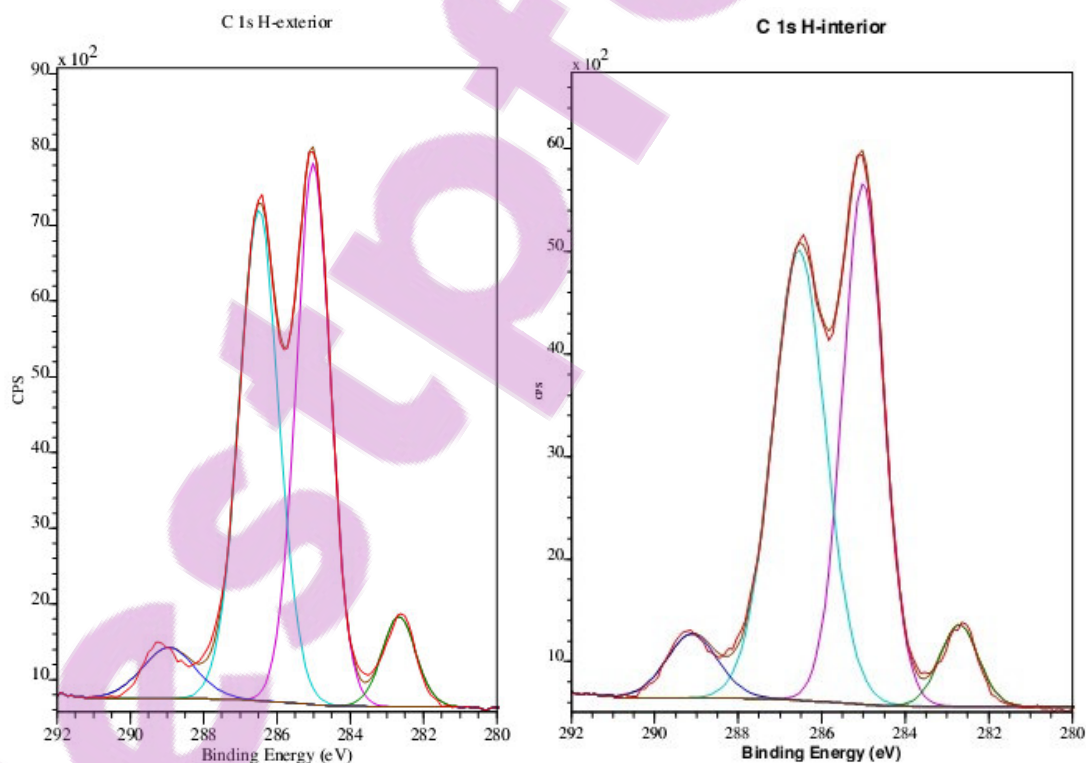


*Figure 4-23: Spectra of C 1s region of sample from the exterior part of brick H (left) and the interior part (right), the carbide peak at ~282 eV is clearly separated fro the adventitious carbon peak (at 285 eV).*

The XPS is analysing only the sample surface and can be very sensitive to any surface contamination that could introduced in the preparation of these hard and rough samples. A carbonitride was not detected by XRD analysis, suggesting that the small amount of this compound was associated with such surface contamination.
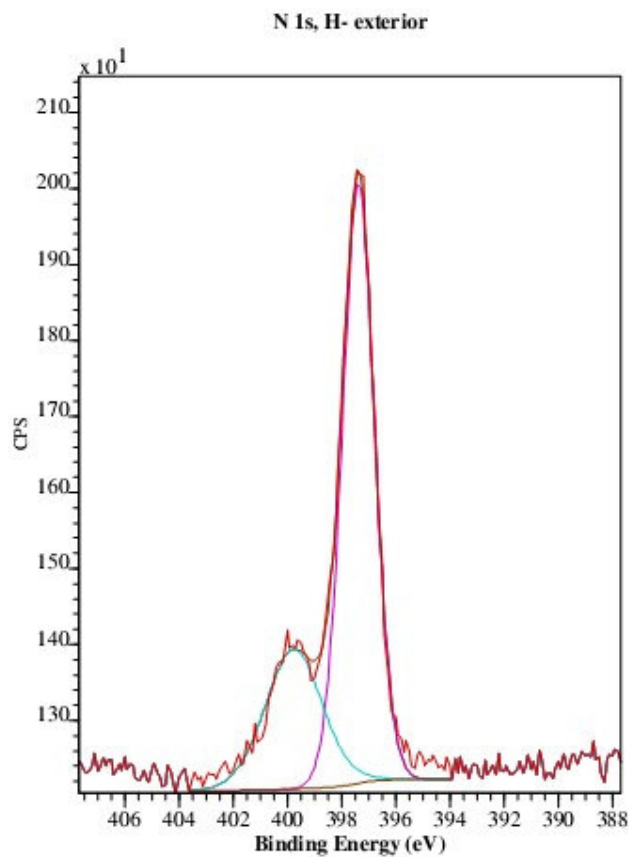


*Figure 4-24: Spectra of N 1s region showing the Si$_3$N$_4$ peak at 397.4 eV and another peak at 399.8 eV associated with a carbonaceous species.*

## 4.6. SNBSC material morphology

SNBSC refractory material is a composite material with a complex morphology. The material contains SiC grains in mm size encapsulated in a binder with micron size particles that consist mainly of two different phases of $Si_3N_4$, ($\alpha$ and $\beta$), minor phases of oxides ($SiO_2$ and $Si_2N_2O$) and unreacted silicon.

Morphology study of the different phases in the SNBSC can provide information about:
- The distribution of the different phases within the material, including contaminants.
- The difference in the particle shape of each phase.
- Distribution of pores within the different phases.

Changes in physical properties of the material such as an increase porosity and surface area after thermal treatment can be attributed to changes in the morphology of the different phases of the material. Variation in the morphology of the different phases can shade a light on the reasons for the differential corrosion rate observed in materials with different phase content.

Scanning electron microscope (SEM) was used to study the material morphology by using its ability to provide high magnification imaging (4000x to16,000x) enabling to observe the crystals shape and arrangement of the different phases. The energy dispersive x-ray (EDX) analysis provides the ability to identify and quantify the objects observed on the SEM image. The material could be studied in extreme condition of elevated temperatures and different gaseous environment by using environmental Scanning electron microscope (ESEM), its abilities were used to observe changes in morphology of the SNBSC phases as they happening.

### 4.6.1. SEM analysis

**Sample preparation**: Samples were cut from sections of refractory blocks using a diamond cutting wheel (Buehler Isomet 1000 precision diamond wafer saw). The cut samples were glued with a resin to a metal stub and ground using a 40 µm diamond grinding wheel with water as a lubricant. They were further polished using a grinding wheel with a 9 µm diamond paste and an oil based lubricant, then on silk paper with three diamond pastes, starting with 6µm and moving gradually to 3µm. The final polishing was done using a 1µm diamond paste. Between steps, the samples were ultrasonically cleaned in iso-propanol to ensure that no diamond paste was left on

the sample surface. After the final polish, the sample were ultrasonically cleaned in iso-propanol and taken off the metal stub. The remaining resin on the sample was cleaned in acetone and the sample dried in an oven. Prior to the SEM analysis, the samples were gold coated to avoid any possible electron charging of the sample surface. The samples were then attached to a stainless steel stub using double-sided adhesive tape.

An FEI Quanta 200F field-emission scanning electron microscope (SEM) at 20kV electron energy was used, with a spot setting of 4.0, as high magnification (4000x to16,000 x) imaging tool with either a secondary electron detector or a backscattered electron detector. The instrument is equipped with an energy dispersive x-ray analyser (EDX).  The EDX technique was used to identify the main species in the sample or any contamination /abnormal species, rather than as an analytical tool for high precision quantification.

Environmental scanning electron microscopy (ESEM) with a backscattered electron detector was used to observe oxidation in a $CO_2$ environment in a temperature range of 400°C to1000°C. The $CO_2$ pressure was kept at 1.54 Torr and the temperature ramp rate was 5°C / minute. The samples analysed were made to fit the ESEM crucible (5mm diameter).

The ESEM allows the study of samples under different environments and high temperatures (up to 1500°C).  Thus samples could be studied in real-time in a simulated corrosion environment. When the sample was studied under high temperature and a $CO_2$ atmosphere, changes were observed as the temperature increased (as seen in the marked circles in Figure 4-25). However, no sign of oxidation, such as the formation of a macroscopic oxide layer on the silicon nitride surface, could be observed on this scale.
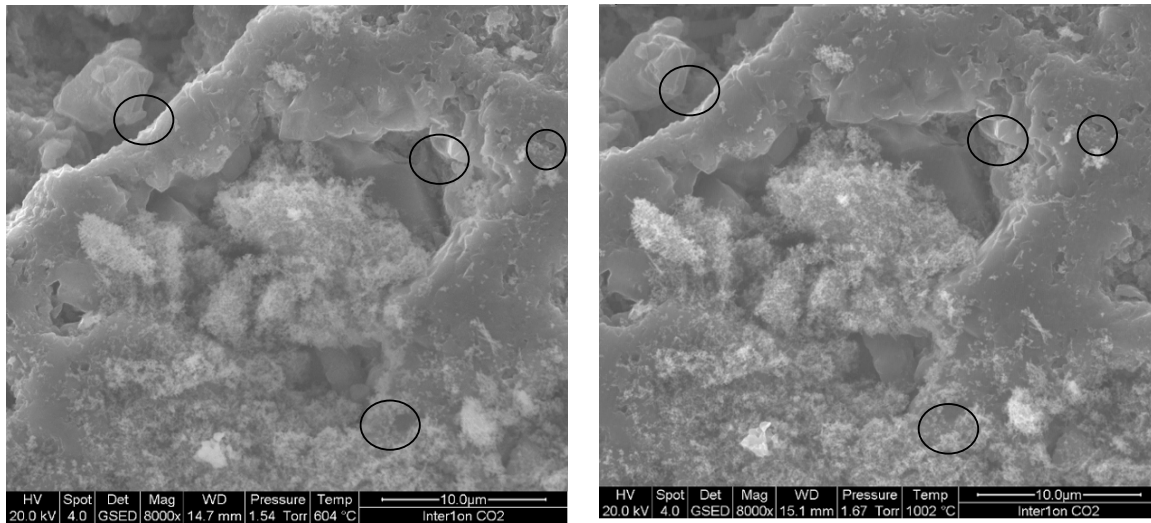
*Figure 4-25: ESEM image of SNBSC sample in $CO_2$ atmosphere at 600°C (left) and 1000°C (right) - changes are observed in the regions marked with a circle.*

Observation of SNBSC material by SEM showed large silicon carbide grains (these appear as darker areas of mm size) surrounded by smaller silicon nitride crystals (light grey colour and micron size). Large pores (of mm size) are observed in the silicon nitride bonding phase. Figure 4-26 shows a low magnification image of the SNBSC surface, with large SiC grains surrounded by the $Si_3N_4$ matrix.
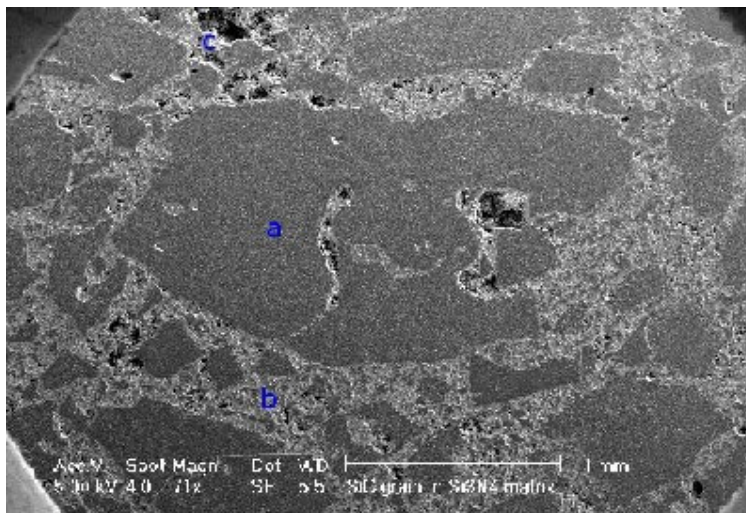


*Figure 4-26: SEM image of SNBSC sample (magnification x71). The dark grey areas are SiC grains (marked a), the light grey area surrounding them is the $Si_3N_4$ matrix (marked b) and the black areas are pores (marked c).*

A distinctly lighter area than the SiC grain and the bonding phase appeared inside the SiC grain in some samples when a backscattered electron detector was used (Figure 4-27 right). Analysis of this lighter colour material by EDX detected a high concentration of metallic silicon. This

silicon was usually accompanied by contamination such as iron, vanadium, and manganese, that could probably originated from the tools used in the silicon milling process during the production of silicon carbide.

A comparison between the images when a secondary electron detector was used (left) and when a backscattered electron detector was used (right) can be seen in Figure 4-27. The free silicon and the contamination are highlighted in the backscattered electron detector image. The areas of interest (marked numbers 1 to 4 on the right image of Figure 4-27) were analysed using EDX and the results are listed in Table 4-12.
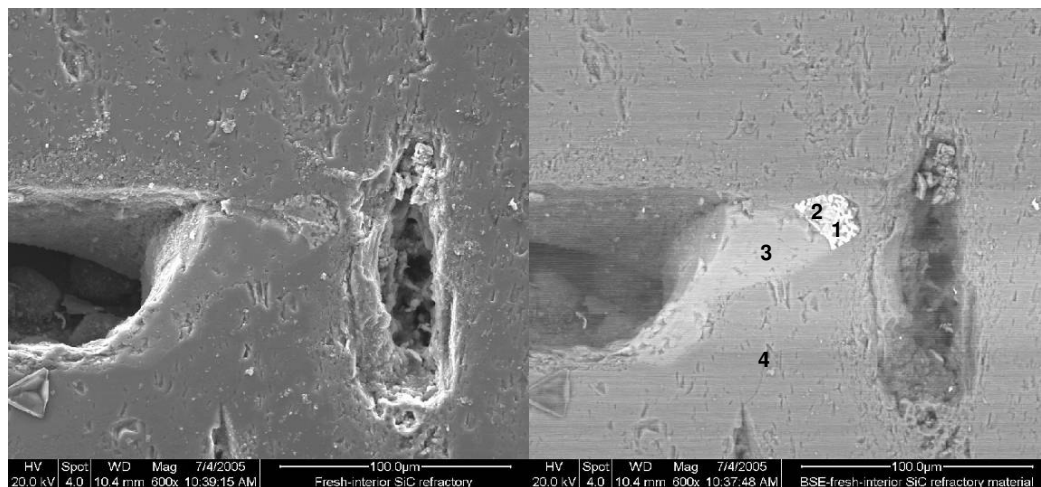


*Figure 4-27: SEM image of silicon particle inside silicon carbide grain (magnification x600). For the image on the left a secondary ion detector was used, and a back scattered electron detector was used for the image on the right. On the right image, points 1 and 2 are contaminants within the silicon, area 3- silicon particle, and area 4- silicon carbide grain.*

*Table 4-12: EDX analysis of points 1-4 in Figure 4-27observed within the silicon carbide grain in SNBSC material.*

| Element | C (At %) | O (At %) | Si (At %) | N (At %) | Mn (At %) | Fe (At %) | V (At %) | Ni (At %) |
|---|---|---|---|---|---|---|---|---|
| Point 1 | 13.00 | 3.41 | 55.83 | - | 10.51 | 15.07 | - | 1.40 |
| Point 2 | 11.9 | 13.76 | 44.32 | 10.69 | 3.43 | 1.25 | 14.06 | - |
| Point 3 | 8.67 | 2.33 | 88.97 | - | - | - | - | - |
| Point 4 | 44.38 | 2.24 | 53.38 | - | - | - | - | - |

The backscattered electron image (on the right of Figure 4-27) made it easy to observe these silicon spots. It is important to note that the elemental silicon was only observed within the silicon carbide grains and not in the bonding matrix.

SEM observations of the silicon nitride bonding phase at high magnification (400x and above), clearly revealed the variations in morphologies of the different silicon nitride phases. Three main crystal types were observed in the silicon nitride bonding phase: The first type, shown in Figure 4-28, has long fine needle-like crystals that were observed only within the pores. This type of crystals is usually seen in samples with a high $\alpha$ Si$_3$N$_4$ content.
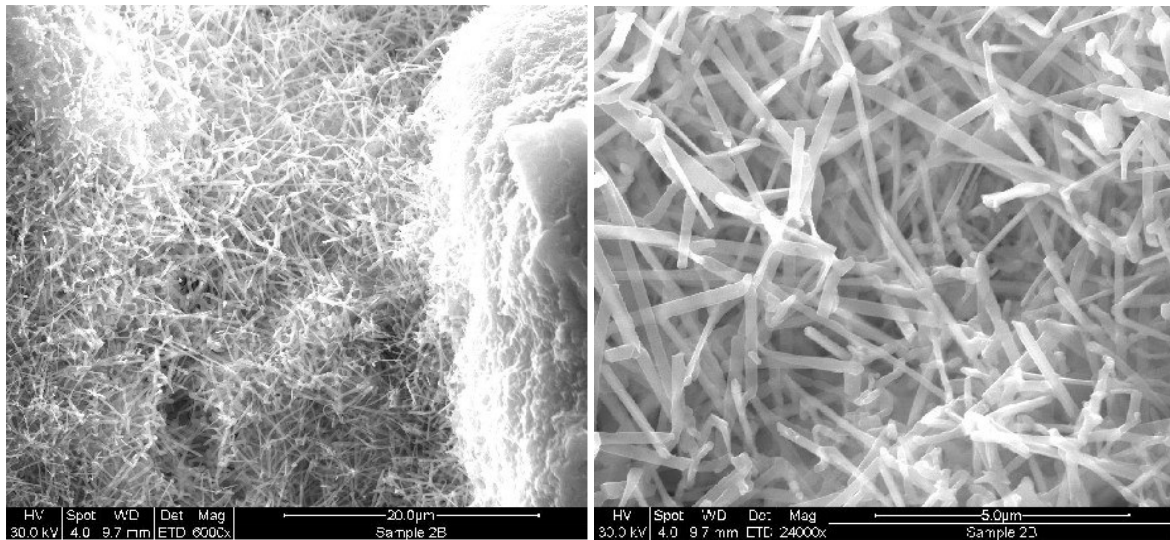


*Figure 4-28: SEM image of long, fine crystals growing into a pore in SNBSC sample (left), and close up view on the right.*

Confirmation that this crystal morphology is associated with $\alpha$ Si$_3$N$_4$ crystals was made by Jennings et al [76], that associated the fine needle-like crystals with an aspect ratio >25 with $\alpha$ Si$_3$N$_4$. He observed that these crystals form at temperatures between 1350°C and 1400°C from a less pure silicon powder and grow into the porosity of the original compact (Figure 4-29). These observation is supported by Riley [21] who claims that the whisker-like, fibrous, low-density phase consists almost entirely of $\alpha$ Si$_3$N$_4$.
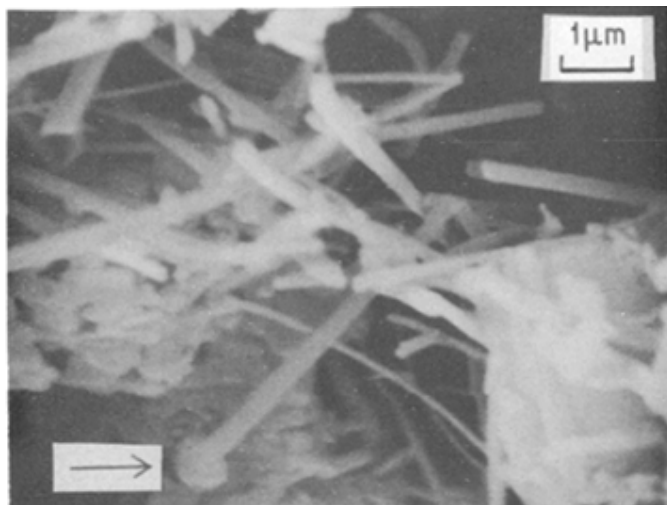
*Figure 4-29: Needles of α Si₃N₄, as observed by Jennings et al [76].*

The second type of crystal morphology that was observed is a flat, matte-like crystal (Figure 4-30). This crystal morphology is found in samples with a high $\alpha$ $Si_3N_4$ content (as measured by XRD).
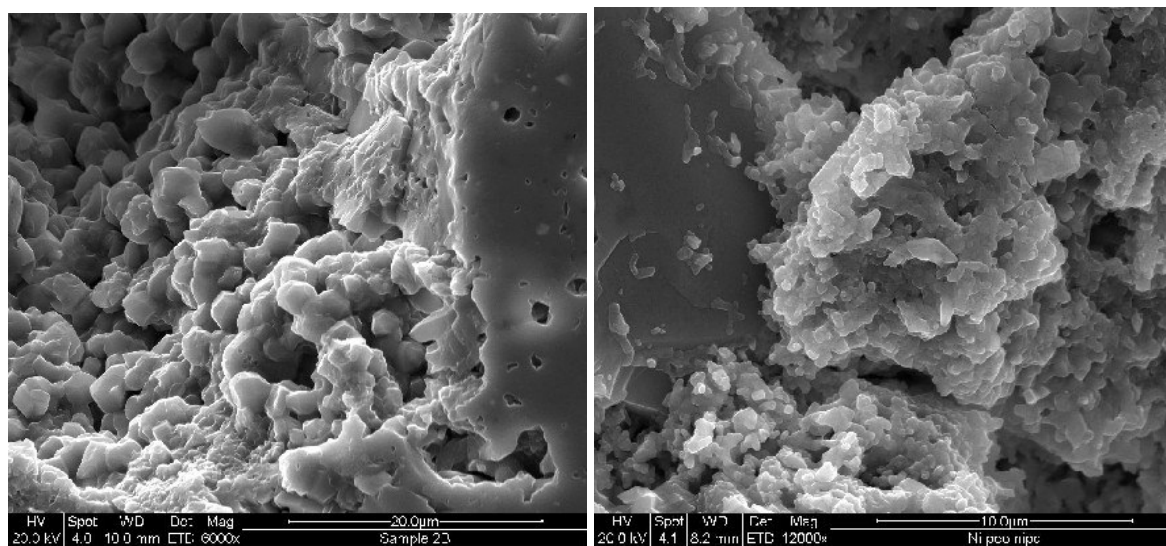


*Figure 4-30: SEM images of two different samples having silicon nitride bonding phase that consisted mainly of flat-shaped crystals. Left magnification 6000x, right magnification 12,000x.*

Jennings et al [76], who observed this kind of fine grained matte (<0.5 μm) structure, claim that the formation of this crystal morphology is predominantly $\alpha$ $Si_3N_4$. This matte phase is favoured when the smallest fine and pure silicon grains react at a heating rate of 300°C/ hour to temperature of less than 1400°C, with low gas flow over the material.

The third type of crystals that was observed has an elongated shape, with a hexagonal cross section (Figure 4-31). This type of crystals was usually seen in samples with high β Si$_3$N$_4$ content.
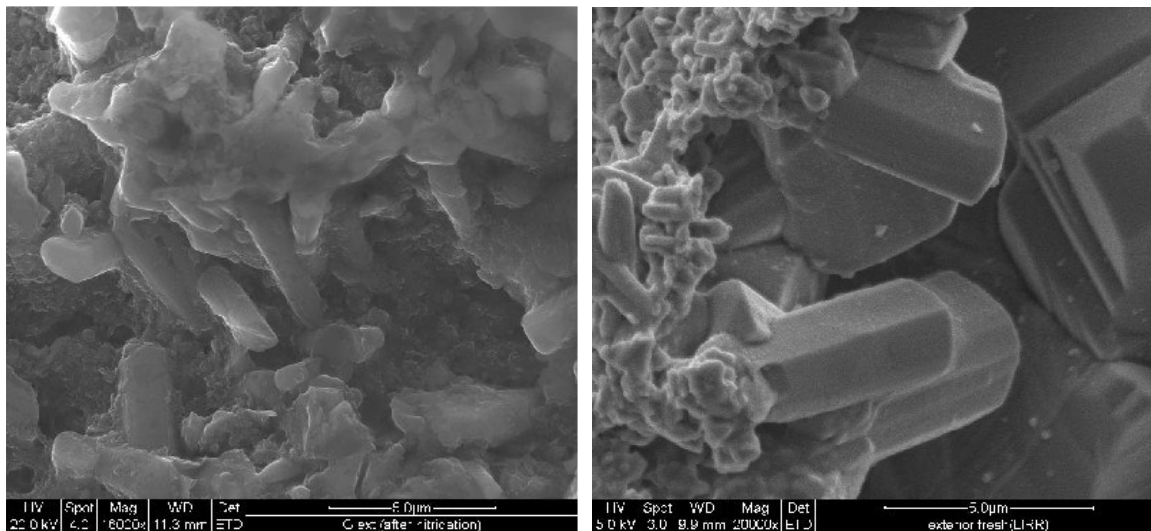


*Figure 4-31: SEM images of bonding phase with long hexagonal crystals. The magnification on the right 6000x, and the magnification on the left 20,000x, shows a close up image of the elongated crystals.*

Spike-like, elongated shaped crystal with hexagonal cross section morphology is associated with β Si$_3$N$_4$ crystals and well documented in the literature[76-80]. An example from the literature is given in Figure 4-32.
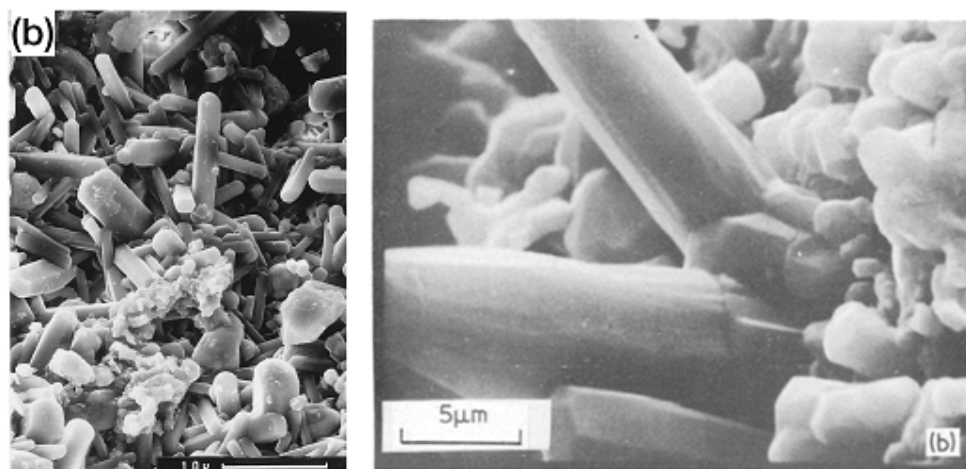


*Figure 4-32: On left: rod microstructures in β Si$_3$N$_4$ in over-etched surface as observed by Hoffmann [21]. On right: growth of β Si$_3$N$_4$ spikes as observed by Jennings et al [76].*

Mixture of the three different morphologies was often observed in the samples analysed by SEM as can be seen in Figure 4-33.
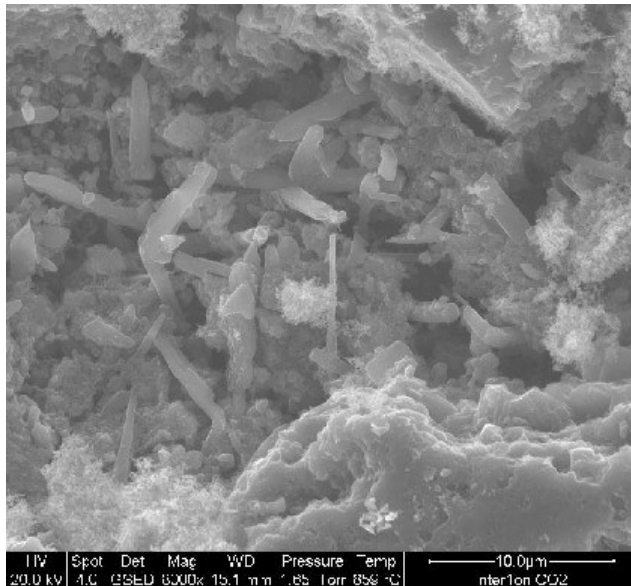
*Figure 4-33: SEM image of silicon nitride bonding phase with mixed type of crystals, on the lower right corner flat crystal and long hexagonal crystals in the middle of the image.*

In order to relate the silicon nitride bonding phase to the crystal morphology, a SNBSC sample was heat treated at temperature above 1600°C in a nitrogen atmosphere to produce a bonding phase with high β $Si_3N_4$ content (Chapter 6.3). The treated sample was then compared with the untreated material, which has a bonding phase rich in α $Si_3N_4$. In the untreated sample, large pores filled with thin, needle-like crystals were observed (Figure 4-34) and the bonding phase contained mainly short flat crystals (Figure 4-35).
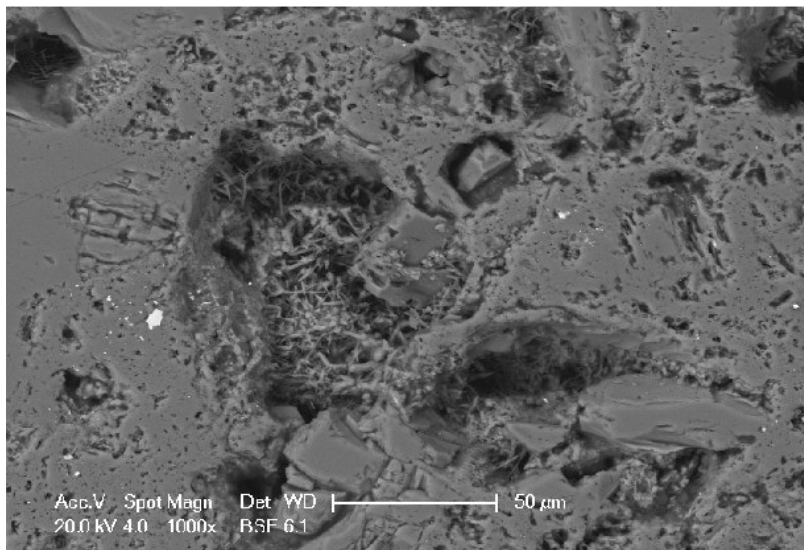


*Figure 4-34: SEM image of bonding phase of SNBSC sample before nitridation. Large pores filled with thin needle crystals and short, flat crystals dominate the bonding phase.*
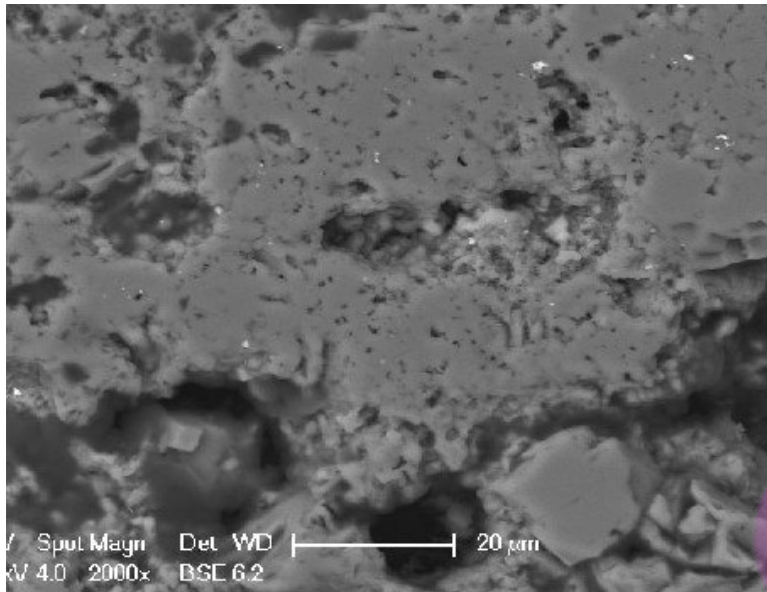
*Figure 4-35: The silicon nitride bonding phase consists of mainly small flat crystals of untreated SNBSC sample.*

In the heat treated sample, long spike-like, hexagonal crystals dominated the bonding phase (Figure 4-36 and 4-37), while the large pores with thin needle crystals (observed in the untreated sample) were absent.
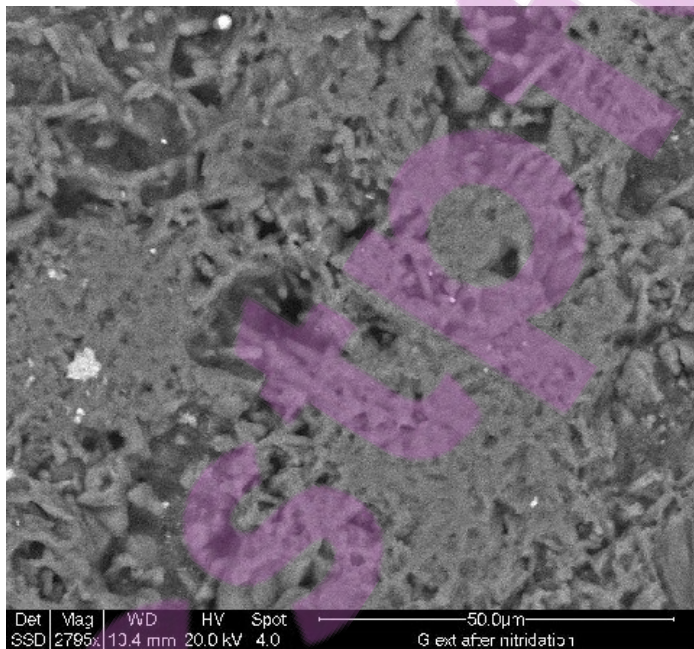


*Figure 4-36: SEM image of bonding phase of SNBSC sample after nitridation, showing long hexagonal crystals dominating the bonding phase.*

101
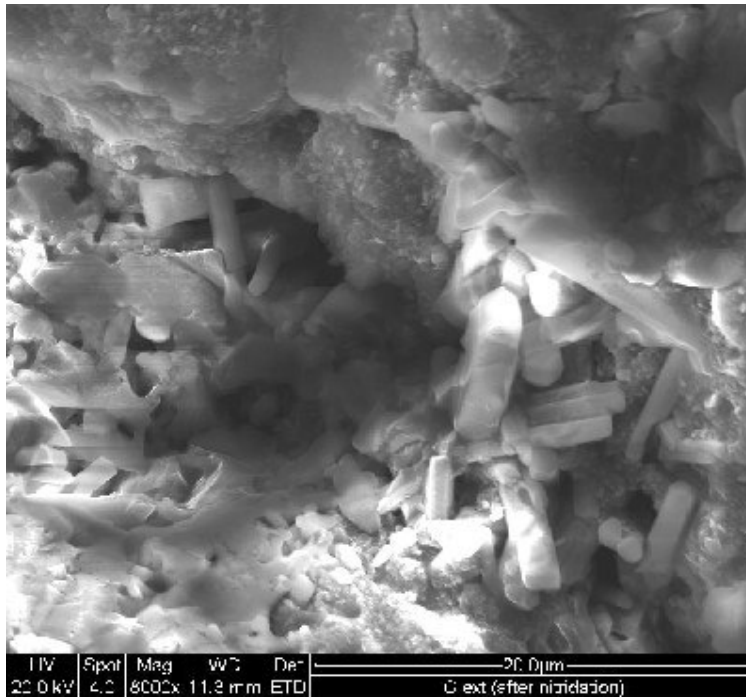
*Figure 4-37: A close up view (magnification 8000x) of the bonding phase of the heat-treated sample, elongated hexagonal β Si₃N₄ crystals can be seen in the middle of the image.*

The aspect ratio measured for the long, hexagonal $\beta$ $Si_3N_4$ crystals found in the treated sample was ~ 6 (Figure 4-38).
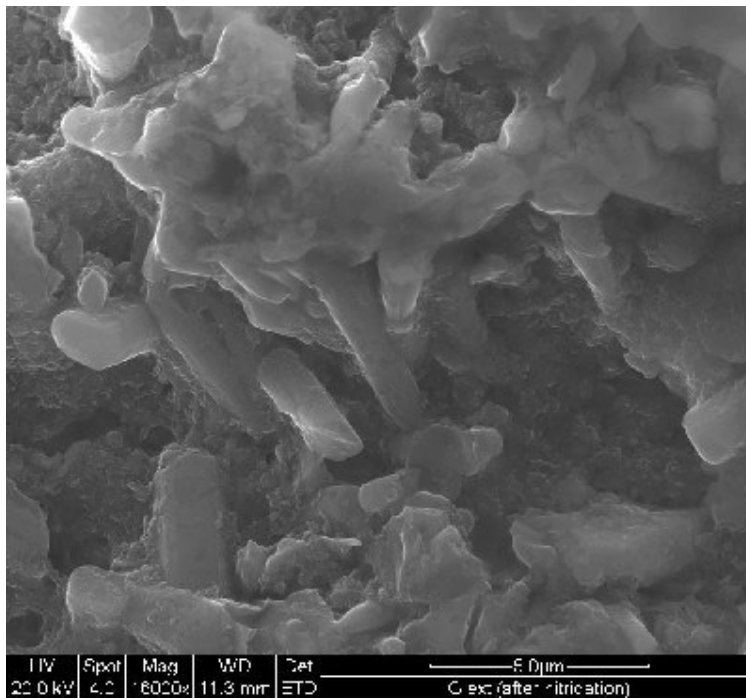


*Figure 4-38: Elongated β Si₃N₄ crystals observed in the bonding phase of a treated sample.*

## 4.7. Summary

Several analysis techniques were employed to study the microstructure of the SNBSC samples. The information gathered from the X-ray diffraction, solid state NMR, Raman spectroscopy, XPS, and SEM, provide a comprehensive understanding of the various phases of these materials and their morphology.

Quantification of the phase composition of SNBSC samples containing different silicon nitride and silicon carbide phases proved challenging by x-ray diffraction, due to preferred orientation effects for both silicon carbide and α silicon nitride. To overcome these obstacles, the silicon carbide preferred orientation was reduced substantially by pulverizing the sample to a fine powder where both silicon carbide grains and silicon nitride crystals were homogenised. In addition, rotation of the samples during analysis contributed to further minimisation of the preferred orientation effect, particularly of the silicon carbide phase. Separation and quantification of overlapping peaks in the different silicon nitride phases is challenging due to the preferred orientation of α silicon nitride. Quantification of the overlapping silicon nitride peaks was resolved by using the Gazzara and Messier quantification method of averaging peak heights, as discussed in section 4.2.

The x-ray diffraction quantification method was the most accurate and least cumbersome of the analytical methods tested for this phase analysis. The accuracy of the XRD quantification method in analysing SNBSC materials is due to the high crystalinity of the different phases in the analysed samples. This high crystalinity, and the absence of an amorphous phase, were confirmed by solid state NMR analysis (Section 4.3).

Analytical results from number of SNBSC samples clearly showed variations in α and β $Si_3N_4$ content between the bricks and within the same brick, where significantly higher β $Si_3N_4$ concentration was detected in the interior parts of some bricks. This effect could be attributed to elevated temperature, due to the exothermic reaction during the nitridation process, and the difficulty of heat dissipation from the core of the brick.

^{29}Si MAS NMR has been used to provide an independent microstructural analysis to XRD, in particular in checking the detection and identification of amorphous phases. This provides more comprehensive data on the SNBSC materials which could not be obtained from X-ray diffraction

techniques. Samples of pure α-SiC, α-$Si_3N_4$ and β-$Si_3N_4$, which represent the main structural phases in SNBSC materials, were analyzed and used as standards. The spectra from these samples were then used to identify and analyze phases in the commercially produced SNBSC refractories.

The interior section of commercially produced brick A indicates a dominance of α $Si_3N_4$ in the $Si_3N_4$ content. Samples taken from the peripheral and core sections of brick H revealed variations in the content of the α and β $Si_3N_4$ phases. The core sample consists mainly of β $Si_3N_4$ while the peripheral sample also shows the presence of α $Si_3N_4$.

A small amount of $Si_2ON_2$ was detected in sample taken from the interior area of brick H (Figure 4-14A the peak at -61.3 ppm). This phase was not identified in the exterior part of the sample, which confirms XRD analysis findings. In all the samples analyzed, no amorphous structural phase was detected.

The quantitative analysis of the α-$Si_3N_4$ and β-$Si_3N_4$ phases in SNBSC materials using NMR is difficult due to the low concentration of $Si_3N_4$ compared to SiC. Thus, the α/β ratio can only be tentatively estimated. The data obtained from the phase analysis can provide useful information about the degree of crystalinity of the phases. The high crystalinity of phases detected by ^{29}Si NMR provides confirmation that the results obtained by the x-ray diffraction, can be used as an accurate quantitative analysis technique.

There are a few complications in the application of Si NMR to SNBSC samples. It is important to ensure that pulse repetition times allow the system to fully relax, as silicon nitrides in particular have long relaxation times. In addition, the presence of paramagnetic species and structural defects can (completely or partly) broaden the signal considerably, making quantitative analysis more difficult.

The different phases found in SNBSC refractory have different Raman shifts with good separation between the peaks as it was examined by analysis of pure phases. The very different Raman shifts of the different SNBSC phases making the Raman spectroscopy a good tool for qualitative analysis of these materials. However, an attempt to produce a calibration chart for quantification of the different silicon nitride phases using mixtures of different α/β $Si_3N_4$ ratios,

showed no correlation between the peak area of characteristic Raman peaks and the α and β $Si_3N_4$ powder mixture ratios.

The bonding phase peak area of samples, from the interior and the exterior of SNBSC brick B and H was analysed. Although an accurate quantification was not viable, the spectra reveal that in the bonding phase of the interior sample, β $Si_3N_4$ was dominant over α $Si_3N_4$, and in the exterior sample a mixture of both phases was observed (Figure 4-17).

X-ray photoelectron spectroscopy (XPS) was also used to identify the different species in samples taken from a cross section of a SNBSC brick. Pure powder samples were used as standards to establish binding energies for the likely species found in the SNBSC samples.

In the XPS analysis of SNBSC brick cross section, SiC, $Si_3N_4$, and $SiO_2$ were successfully identified. The quantification observed in the XPS technique for samples from the exterior area of the SNBSC brick showed similar composition to the quantification obtained by XRD analysis and from the production recipe. The spectra of samples taken from the exterior area, suggests the preparation and analysis of the cross-sections over estimates the silicon nitride content and underestimates the silicon carbide content. The high content of silicon nitride observed in the XPS spectra compared to other analysis techniques could come from the high surface area of the porous nitride binder or from the scanned area that was mainly focus on the binder. However, it does identify elevated levels of the $SiO_2$ phase in the interior area that could indicate poor control of the nitridation process. Contamination was observed in the silicon powder used as raw material for the production of these SNBSC refractories. The additional peak in the Si2p spectra of the silicon powder, at lower binding energy of free silicon, indicates the presence of a metal silicide that may originated from the silicon milling process.

XPS is a surface sensitive technique with an average sampling depth considerable less than 100Å [71]. Species found on the surface of the samples that are not visible for other analytical techniques are detected and quantified; hence discrepancies in composition of sample could rise between the results of different analytical methods.

The morphology and microstructure of the SNBSC was samples studied using SEM analysis. The different particle size of the SiC grain and the $Si_3N_4$ crystals makes it easy to distinguish

between them. Of much interest is the silicon nitride bonding phase, where three different crystal morphologies were observed:

1. Thin, needle-like crystals that have grown into pores and cavities associated with samples with high $\alpha$ $Si_3N_4$ content.

2. Flat, matte crystals found in samples with high $\alpha$ $Si_3N_4$ content.

3. Elongated, rod-like crystals with hexagonal cross section observed in samples with high $\beta$ $Si_3N_4$ content.

In an experiment described later in this thesis, this morphology is manipulated. A fresh SNBSC sample containing high $\alpha$ $Si_3N_4$ in the bonding phase was heat treated in high temperature in nitrogen atmosphere to produce a high $\beta$ $Si_3N_4$ concentration. Changes in the morphology were observed after the heat treatment. The original bonding phase containing flat crystals with large pores filled with thin, needle-like crystals was replaced with increasing domination of elongated, hexagonal $\beta$ $Si_3N_4$ crystals.

# Chapter 5: Experimental methodology for corrosion testing

The central aim of this research work is to better understand the mechanism by which these complex, composite refractories degrade in the industrial reduction cell environment and to explore options for improved materials. Central to this is lab-scale testing of corrosion behaviour where conditions can be best controlled. The lab-scale corrosion test used in the current work was based on the experimental method developed by Skybakmoen and the SINTEF team [24]. However, it was up-scaled to a larger dimension crucible and samples, in order to reduce the error associated with bath level and chemistry fluctuations during the experiment. This test method exposes the SNBSC samples to various conditions such as $CO_2$ evolution, bath penetration and fluoride vapours that can affect corrosion. So far this method best simulates on lab-scale the conditions that the sidewall materials are exposed to in an industrial reduction cell.

Sample preparation: A cross section of the brick was cut using a diamond cutting wheel. The cross sectioned piece was further cut into four or five longitudinal 20x15x180 mm samples - two from the exterior, two from the interior and a core sample. The samples were marked by cutting grooves on the top and bottom of the sample in order to differentiate them after the corrosion test.

The sample volume, density and porosity were measured using the ISO 5017 standard method (see below) prior to the corrosion test. Two sets of experiments were carried out; in one set the samples were examined in the corrosion test without any prior treatment (i.e un-soaked samples). In the other set of experiments samples were soaked in a molten cryolite bath for 48 hours prior to the electrolysis experiment in order to simulate the conditions that the bricks are exposed to in an industrial reduction cell (i.e. pre-soaked samples). After the soaking stage, the impregnated samples were cleaned of the adhering bath by immersing them in an aluminium chloride solution in an ultrasonic bath to ease the adhering material which was later removed by using a knife. The samples were washed, dried in an oven (120°C) and when cooled the volume was measured again.

## 5.1. Quantifying volume loss using the ISO 5017 standard method

The ISO 5017 standard method was designed to measure bulk density, apparent and true porosity in dense shaped refractory products.

**Bulk density** ($\rho_b$) is the ratio of the mass of the material of porous body to its bulk volume, expressed in gram per cubic centimetres ($g/cm^3$) or in kilogram per cubic meter ($kg/m^3$)

The bulk density was measured using Equation 5-1:

*Equation 5-1*
$$\rho_b = \frac{m_1}{m_3 - m_2} \times \rho \, H_2O$$

Where $m_1$ is mass of the dry sample, $m_2$ is the mass of the sample suspended in water, and $m_3$ is the mass of the sample pre-soaked in water. The samples were dried in an oven and were allowed to cool down to room temperature prior to the measurement. A semi analytical balance with accuracy of 0.01g was used for the mass measurements.

The mass of the dry samples ($m_1$) was measured before the samples were placed in an air tight desiccator and a slight vacuum was applied for 20 minutes to evacuate the air from the open pores. Water was introduced via a dropping fennel into the desiccator while maintaining the vacuum, until the samples were fully immersed in the water. The immersed samples were kept for another 20 minutes under vacuum, before air was introduced, bringing the vessel back to atmospheric pressure.

To measure the mass of the immersed samples ($m_2$) - the balance was placed on a stand with a hole to allow the sample to be suspended on a thin steel wire from the load pan point of the balance while completely immersed in the water (Figure 5-1). The temperature of the water was measured to ± 1°C accuracy.

The mass of the soaked sample ($m_3$) was measured by removing the droplets from the sample surface with a wet cloth, and weighing the wet sample on the balance. The density of the water was calculated using the values in Table 5-1:

*Table 5-1: Water density in temperature range of 15-25°C.*

| Temp (°C) | 15 | 16 | 17 | 18 | 19 | 20 | 21 | 22 | 23 | 24 | 25 |
|---|---|---|---|---|---|---|---|---|---|---|---|
| Water density ($g/cm^3$) | 0.999 | 0.999 | 0.999 | 0.999 | 0.998 | 0.998 | 0.998 | 0.998 | 0.997 | 0.997 | 0.997 |
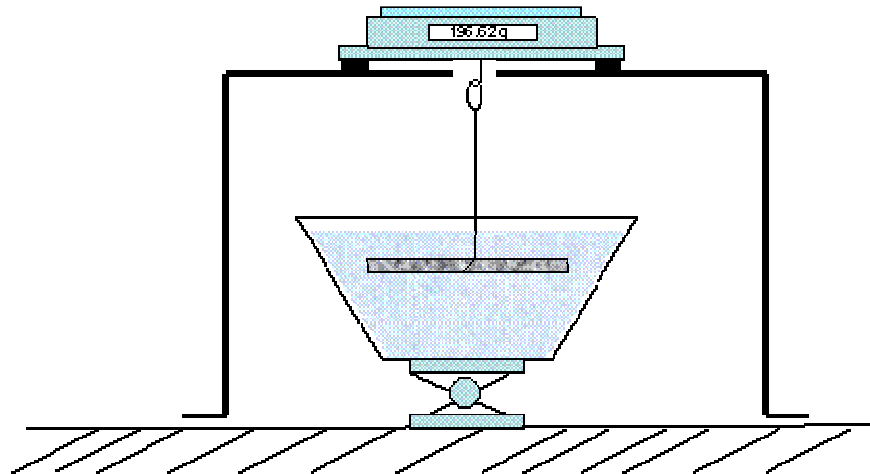
*Figure 5-1: Apparatus for volume measurement, density and porosity using the ISO 5017 standard method. The sample is suspended in the water from the loading pan at the bottom of the balance.*

**Apparent porosity** ($\pi_a$) is the ratio of the total volume of the open pores in a porous body to its bulk volume, expressed as a percentage of the bulk volume. The apparent porosity was measured using Equation 5-2:

*Equation 5-2*   $\pi_a = \dfrac{m_3 - m_1}{m_3 - m_2} x100$

The volume (Vs) of the samples expressed in cubic centimetres was calculated using Equation 5-3:

*Equation 5-3*    $Vs = \dfrac{m_1}{\rho_b}$

Where $m_1$ is the sample's dry weight and $\rho_b$ is the density of the sample. An example of calculations of porosity and volume of samples can be seen in Table 5-2.

*Table 5-2: A spreadsheet with the name, the marking of the samples, and the calculation of their density, volume, and porosity.*

| Sample | A core 1 | A core 2 | G ext 1 | G ext 2 |
|---|---|---|---|---|
| Marking | ⊞ | ⊞ | ⊟ | ⊞ |
| Weight - dry (g) | 35.35 | 37.07 | 48.50 | 53.30 |
| Weight – suspended (g) | 24.11 | 25.31 | 33.16 | 36.47 |
| Weight – wet (g) | 37.46 | 39.32 | 51.51 | 56.16 |
| Density (g/cm³) | 2.64 | 2.64 | 2.64 | 2.70 |
| Volume (cm³) | 13.37 | 14.03 | 18.37 | 19.71 |
| Porosity (%) | 15.81 | 16.06 | 16.40 | 14.53 |

## 5.2.  Lab scale corrosion testing with electrolysis

### 5.2.1. "Half immersed" configuration

The corrosion rig was assembled using a high temperature furnace (manufactured by Tetlow, Australia) consisting of 6 heating elements arranged around an Inconel® can. The furnace is capable of heating the content of the can up to 1200°C. The Inconel can is sealed using a lid equipped with ports to allow insertion of anode and cathode rods, an inlet for the shield gas (nitrogen) and gas exhaust ports (see Figure 5-2). The Inconel® can is closed with an air tight seal during the experiments with a continuous purge of nitrogen to avoid the oxidation of samples and burning of the graphite crucible.

In the second set of experiments the samples were soaked for 48 hours in a cryolitic bath with similar composition to that used in the corrosion test.  After soaking, the samples were immersed in aluminium chloride solution for a day and the adhering bath was removed using a knife. The sample volume was measured again prior to the corrosion test, using the ISO 5017 method.

In the corrosion test the samples were placed symmetrically in a graphite crucible (internal diameter 120 mm with 190mm depth) through holes in the graphite crucible lid.  A powdered bath mixture with a composition of 78% cryolite, 7% alumina, 10% $AlF_3$ and 5% $CaF_2$ was mixed and poured into the crucible through the anode hole in the crucible lid. The bath weight was calculated to produce a level of 8cm of molten bath (2.12g/ml bath density was assumed based on previous experiments).

A graphite anode (30mm in diameter and 80mm in length) was screwed into a threaded Inconel® rod.  The graphite crucible wall serves as the cathode and the connection to the power supply was made by a threaded Inconel® rod screwed into the crucible wall.  Once the crucible containing the samples and the bath were sealed inside the Inconel® can, the furnace was heated gradually to 1010°C (to ensure a final 1000°C bath temperature) over 12 hours and this temperature was held throughout the duration of the experiment.

When the temperature of the bath reached 1000°C and the bath was completely melted, the anode was lowered into the bath and set 4 cm above the crucible floor. This distance was set to ensure the current flow from the crucible wall to the anode circumference and not from the

crucible floor to the anode bottom. This current flow direction allows a larger anode surface contact and eliminates the need to adjust the anode – crucible floor distance, as the anode is consumed. A schematic of the corrosion test rig can be seen in Figure 5-2.
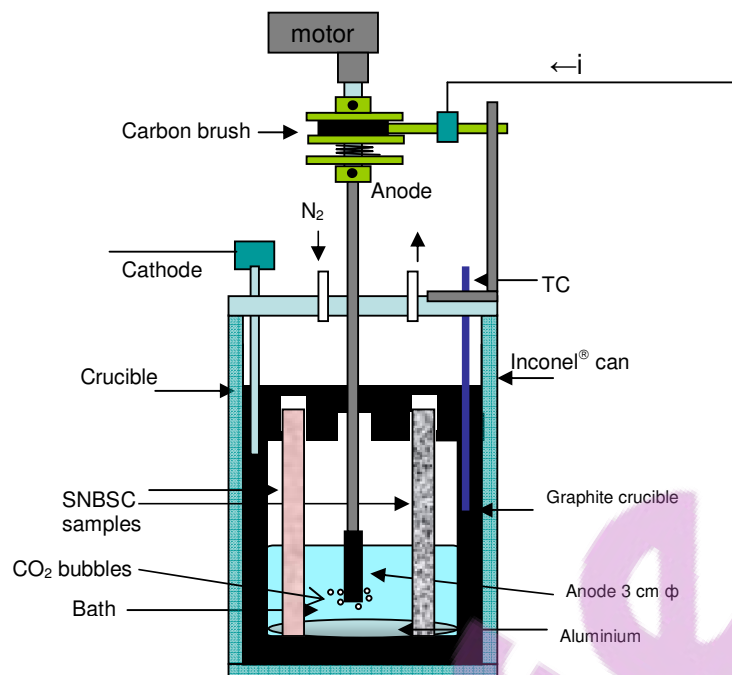


*Figure 5-2: The corrosion testing rig in the half immersed configuration.*

A constant current of 15A was supplied using an Agilent power supply. The voltage limit was restricted to 8V and the cell operating voltage was maintained in the range of 3.0-4.2 V during the experiment. Both the current and voltage were monitored using a data taker sampling every 20 seconds.

During the experiment a mixture of alumina and cryolite (60/80 g respectively) was fed into the bath through the anode hole in the crucible lid, by opening the can lid and removing the anode. The feeding rate was 10 hours, 24 hours and 35 hours from the initiation of electrolysis. The graphite anode was replaced after 24 hours. The experiment was terminated after 48 hours of electrolysis, and the anode and the crucible lid were removed. The samples were taken out of the crucible using metal tongs and the molten bath was poured out.

Post experiment treatment: after cooling, the samples were immersed in an aluminium chloride solution in an ultrasonic bath to soften the adhering bath, prior to using a knife to remove it. The

111

clean samples were washed and dried in an oven before their volume was measured (by the ISO 5017 standard method).

### 5.2.2. Electrolysis corrosion experiments using a rotating anode

An anode stirring mechanism was installed to allow the anode to rotate during the electrolysis experiments. The stirring was carried out for short periods of time (15 minutes) every few hours to break the carbon dust build up on the crust in order to avoid a short circuit between the anode and the crucible wall. The stirring allows better dispersion of the $CO_2$ bubbles in the bath and stabilising the voltage.

The anode connection rod was attached to the carbon brush assembly made of a stationary graphite disc sandwiched between two rotating brass discs (Figure 5-3). A good contact between the stationary carbon disk and the rotating brass disks was maintained using a spring that push the lower brass disk onto the graphite disk. The top part of carbon brush assembly was connected to the shaft of an electric motor and the bottom part was connected to the anode Inconel® rod. A brass rod was screwed into the graphite disc and mounted on a supporting stand. The current was passed from the brass rod to the graphite disc and to the brass discs and into the Inconel® anode connecting rod (Figure 5-3).
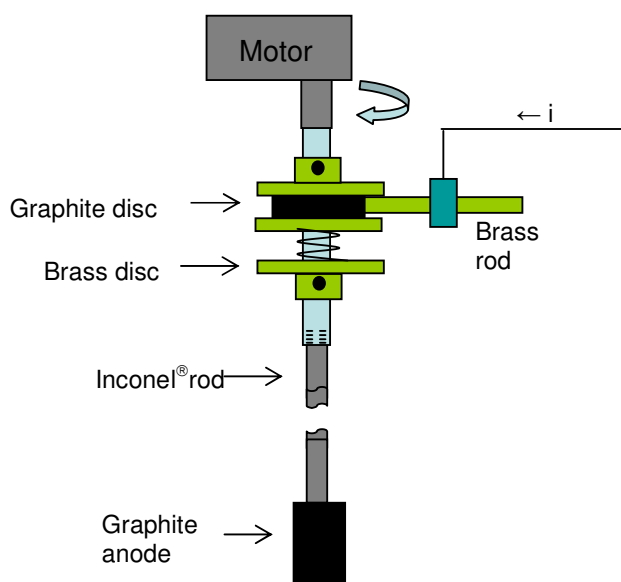


*Figure 5-3: Rotating anode device.*

### 5.2.3. Gas phase corrosion test configuration

A similar graphite crucible as in the half immersed configuration was used in the gas phase corrosion test configuration. The crucible lid was removed and the smaller samples (10 x15 x 50mm) were held in a graphite "basket" (Figure 5-4).
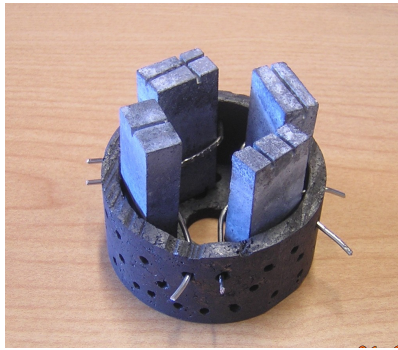


*Figure 5-4: Samples in the graphite basket prior to electrolysis test.*

A centre hole in the basket allows access for the anode rod. Holes were drilled in the basket floor and walls to allow good contact between the gases and the samples. A graphite spacer was placed between the graphite anode and the basket to avoid contact between the samples and the bath (Figure 5-5).
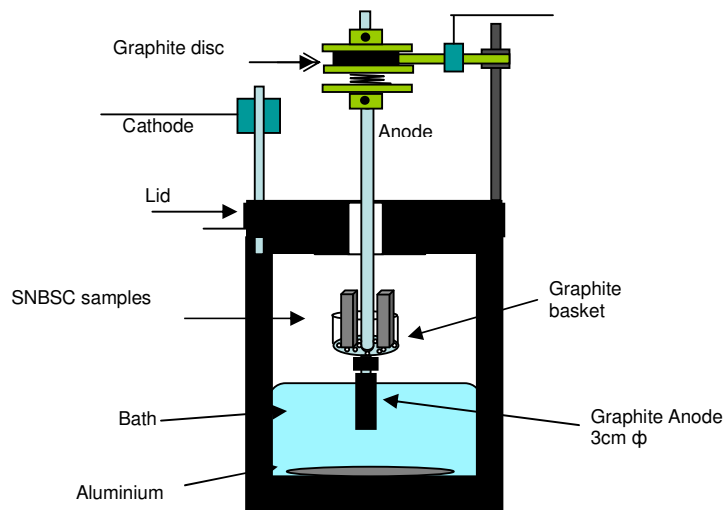


*Figure 5-5: Gas phase corrosion test rig with the samples held in the gas phase above bath level.*

During the experiment, the anode was not rotating in order to avoid displacing the samples from the basket. During replacement of the anode (after 24 hours) the complete anode assembly, including the graphite anode rod and spacer, was replaced.

The pre-electrolysis bath soaking procedure was carried out in a similar graphite basket. A small graphite spacer was mounted onto the Inconel® rod instead of the graphite anode so the basket with the samples could be fully immersed in the bath (Figure 5-6). The samples were soaked for 48 hours without applied current.
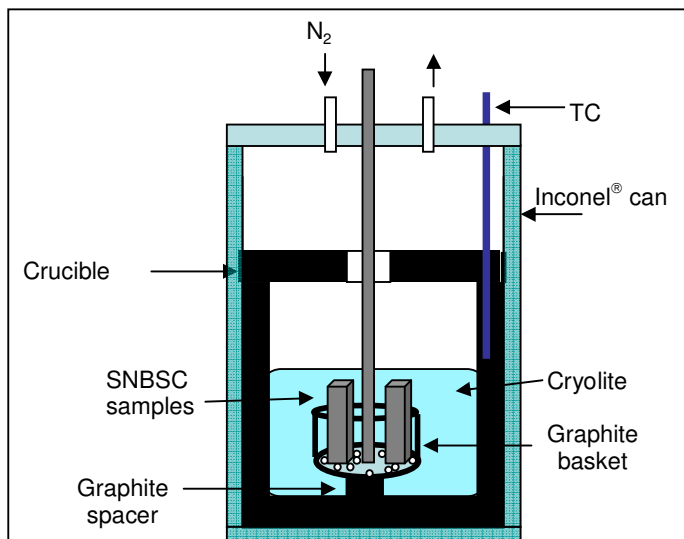


*Figure 5-6: Schematic of the soaking rig. Samples were immersed in the cryolitic bath for 48 hours in the pre electrolysis experiment.*

## 5.3. $CO_2$ sparging experiment

Both industrial cell autopsies and laboratory scale experiments revealed that the SNBSC refractory bricks were attacked most severely in the gas phase just above the bath level. The corrosive attack is tied to the gas evolution during the electrolysis reaction. $CO_2$/CO produced on the anode surface, are the main gases exist in the reduction cell environment. Production of HF occurs due to moisture from the alumina and air, and $NaAlF_4$ is formed due to direct volatilisation from the electrolyte.

A sparging experiment was carried out in order to isolate the effect of $CO_2$ gas on the corrosion of SNBSC material. In this experiment the configuration and the parameters of the electrolysis experiments (crucible size, samples size, bath amount and composition etc') were kept, but $CO_2$ gas was passed through the Inconel® connecting tube and graphite sparging head into the bath instead of the electrical current. As in the electrolysis test in the "half immersed configuration" (Figure 5-2, Chapter 5.2.1) the SNBSC samples were immersed with only half of their length in the molten bath at a temperature of 1000°C. Most of the graphite sparging head was immersed and the $CO_2$ gas was bubbled through the molten bath as demonstrated in Figure 5-7.
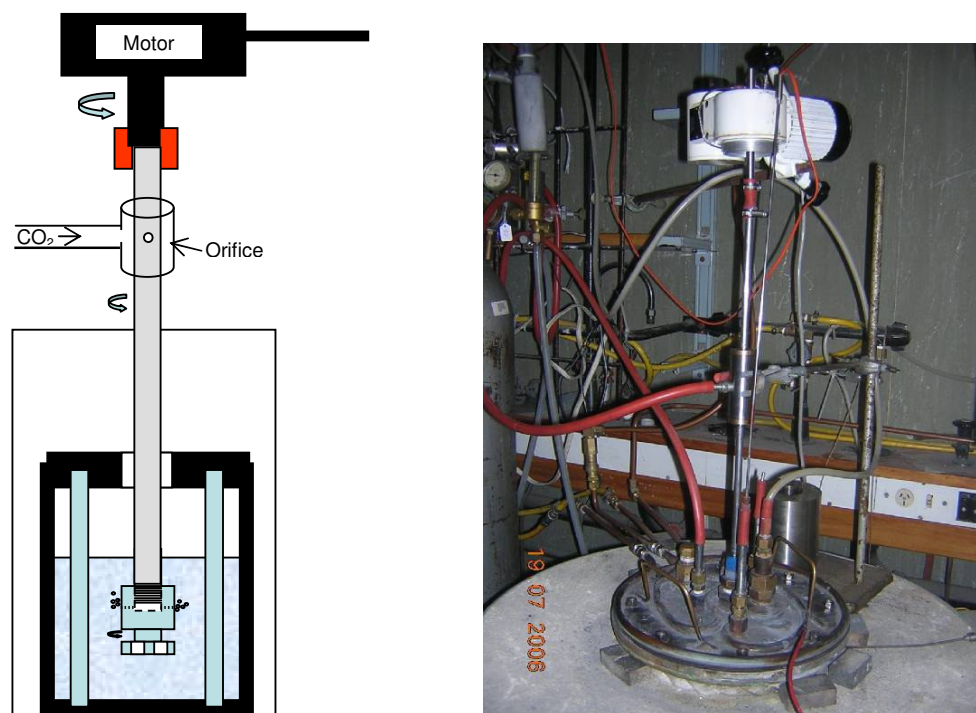


*Figure 5-7: Sparging experiment set up in half immersed configuration. On the left: a diagram of the system, and on the right: view of the part of the system outside of the furnace.*

The anode sparging device (Figure 5-8) was built of an Inconel® tube connected to graphite sparging head. An orifice in the bottom part of the Inconel® tube allows the gas to pass into the graphite head. The sparging device was rotated in order to get good dispersion of the gas in the bath. A sealed chamber with a gas inlet was designed to allow gas flow into the rotating tube. The chamber was fitted with O-rings and springs to keep it sealed while the Inconel® tube was rotating internally, and $CO_2$ was passed into the chamber through the orifice.
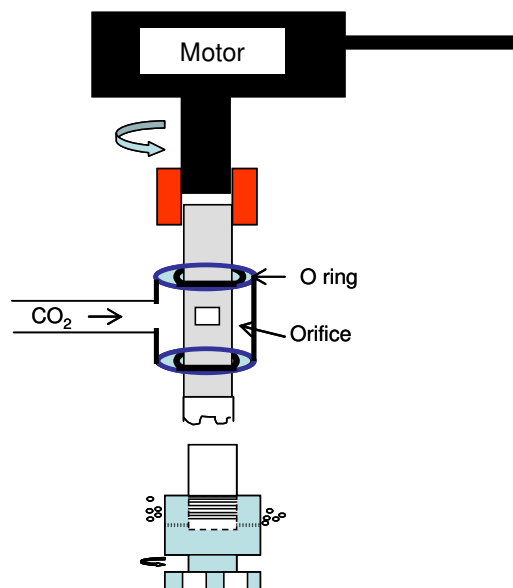


*Figure 5-8: Rotating sparging device made of Inconel® tube and stainless steel chamber to allow gas flow into the rotating tube.*

Holes were drilled in the bottom of the graphite sparging head to allow the gas to bubble out into the bath. Fins were shaped in the bottom of the sparging head to enhance stirring of the bath (Figure 5-9).
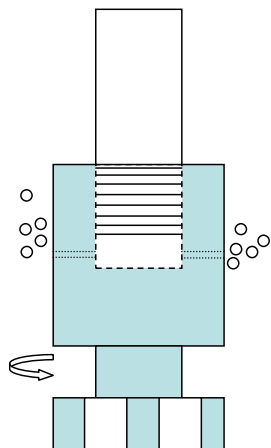
*Figure 5-9: Schematic view of the graphite sparging head fitted with Inconel$^{\circledR}$ tube.*

The four SNBSC samples (taken from brick C) were half immersed in molten bath and supported by holes in the crucible graphite lid while the sparging head was rotating in the centre of the crucible. The $CO_2$ flow rate was kept constant at 1l/min for the duration of the experiment. The experiment was terminated after 24 hours due to corrosion of the sparging head as can be seen in Figure 5-10.



*Figure 5-10: Corroded sparging head.*

## 5.4. Summary

Two configurations were used in the corrosion test:
1. Half immersed configuration, where half of the sample was immersed in the bath and the other half was exposed to the gas phase above the bath level. This configuration was

based on the SINTEF configuration, but was larger in size. Two sets of experiments were carried out using this configuration. The first set the samples were pre-soaked for 48 hours in the bath prior to the corrosion test, while the second set the samples had no treatment prior to the corrosion test. A carbon brush device was used to allow the anode to rotate during the experiment. A constant current of 15A was passed during the experiment while the voltage was kept at a 3-4V range for 48 hours.

2. Gas phase configuration - in this configuration the samples were held in a graphite basket above the bath level and exposed to the gasses emitted during the electrolysis reaction.

An additional sparging experiment was carried out isolating the impact of $CO_2$ exposure. The samples in this experiment were half immersed in the bath and were exposed to $CO_2$ gas bubbling into the bath at a flow of 1l/min.

# Chapter 6: Corrosion of SNBSC refractories in an aluminium reduction cell environment

## 6.1. Industrial scale trial

A comparison test in corrosion behaviour between samples from seven different SiC refractory manufacturers has been conducted by immersing samples in an operating, industrial aluminium reduction cell. All of the samples were commercial $Si_3N_4$ bonded SiC bricks as used for
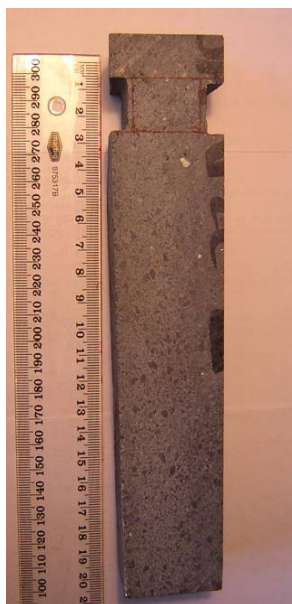


sidewall lining in aluminium reduction cells. The samples (labelled A-H, where F and H were bricks from the same manufacturer) were cut to a sample size 300x350x190mm with grooves to allow mounting on a sample holder (Figure 6-1).

The sample weight, dimension, volume, and density were recorded using the ISO 5017 standard method (Chapter 5.1) and the samples were mounted onto a metal frame (Figures 6-2 and 6-3).

*Figure 6-1: Samples cut with a groove for mounting in the frame, before experiment.*



*Figure 6-2: Samples mounted in the metal frame before insertion in the reduction cell. Sample B, second from the left, was fractured during shipping and thus shorter than the remaining samples in the trial.*
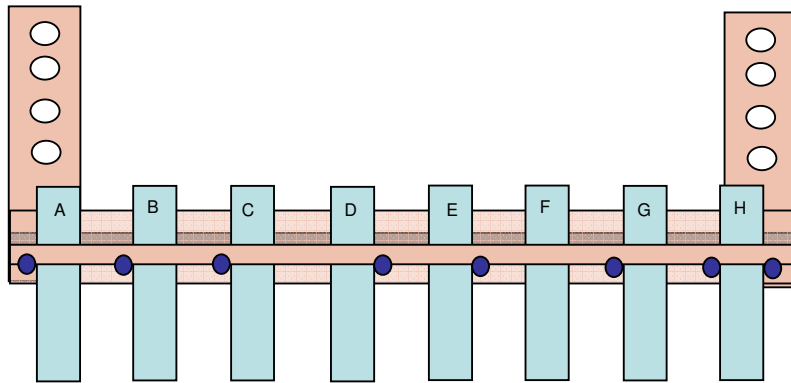
*Figure 6-3: Schematic view of the metal frame with the mounted samples. Two metal bars were mounted to the frame to allow adjusting the frame height. This frame was then hung in the reduction cell.*

**Pre-experiment test**

In order to examine the corrosion rate, and evaluate the optimum duration for the full experiment, a single sample (labelled D2) was mounted in a steel frame and was dipped into reduction cell, between the anode and the sidewall, for 30 hours. After 30 hours, corrosion was observed to some degree (Figures 6-4 and 6-5), but corrosive attack was not extensive, therefore a significantly longer duration was chosen for the full trial.



*Figure 6-4: Sample after 30 hours exposure to electrolysis condition.*

*Figure 6-5: Sample D2 removed after 30 hours partially immersion in the cell.*

**The full experiment**:

Following the single sample trial, the stainless steel rack holding the 8 samples was dipped into a cell between the anode block and the sidewall. The height of the rack was adjusted so the samples were immersed to approximately half of their height in the molten bath. The steel frame was insulated with a rock wool blanket in order to prevent excessive heat loss through the frame. The frame was set in the crust (Figure 6-6) and the experiment was carried out with the cell hoods in place.



*Figure 6-6: Sample frame set in the crust in the reduction cell between the anode and the sidewall.*

The cell that was chosen for the experiment had its anode beam in the 2/3 raised position, and the samples were immersed immediately after a metal tap, so that during the experiment no significant beam movement was required before the next metal tap. After 48 hours the sample frame position was re- adjusted to compensate for the change of bath level after a metal tap. The

full duration of the experiment was 77 hours. At the end of the experiment the samples were taken out (Figures 6-7 and 6-8) and left to cool.



*Figure 6-7: The samples are taken out of the cell after 48 hours for examination during the height adjustment, before being repositioned in the cell.*



*Figure 6-8: Samples with the crust at the end of the experiment (after 77 hours).*

**Post experiment analysis and results:**

The samples ware taken out of the metal frame and soaked in aluminium chloride solution to loosen the adherent frozen bath, which was then, removed using a knife. The clean samples were dried in an oven overnight. The volume and density of the cleaned samples was measured using the ISO 5017 standard method (chapter 5.1).

The in-cell test demonstrated significant differences in corrosion behaviour (Figure 6-9). Samples C and B showed relatively intense corrosion compared to the other samples (although Sample B was shorter than the rest of the samples to begin with – as seen in Figure 6-2). The "necking" behaviour observed suggests dominance of vapour phase attack. Samples D-H and A shows a measurable degree of corrosion and taper towards the bottom end of the sample (immersed in the bath) but are otherwise relatively intact.
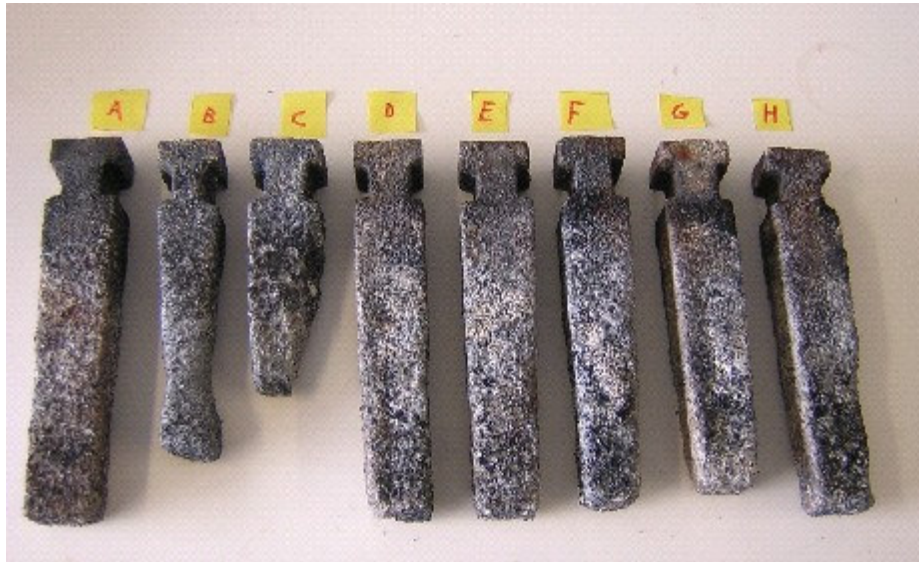


*Figure 6-9: Samples A- H after experiment and removal of adhering bath.*

*Table 6-1: Initial porosity and corrosion rate of samples after industrial-scale corrosion test.*

| Sample | Initial porosity (%) | Corrosion rate (%) |
|--------|---------------------|--------------------|
| A | $14.13 \pm 0.01$ | $17.6 \pm 0.01$ |
| B | $15.10 \pm 0.02$ | N/A* |
| C | $14.31 \pm 0.01$ | $56.1 \pm 0.1$ |
| D | $11.69 \pm 0.02$ | $15.8 \pm 0.1$ |
| E | $12.88 \pm 0.01$ | $17.2 \pm 0.1$ |
| F | $11.85 \pm 0.02$ | $16.2 \pm 0.1$ |
| G | $12.16 \pm 0.02$ | $6.4 \pm 0.1$ |
| H | $11.42 \pm 0.02$ | $14.4 \pm 0.1$ |

* Sample B was broken during shipping and was modified before the experiment.

The $\alpha$ and $\beta$ $Si_3N_4$ content of the exterior and interior areas of the bricks was measured using X-ray diffraction, based on calculation using the Gazzara and Messier method [61]. High $\beta$ $Si_3N_4$

levels were observed in samples B, C, and H, especially in the interior part of these bricks. The results are shown in Table 6-2 and Figures 6-10 and 6-11.

*Table 6-2: α and β $Si_3N_4$ content of samples A-H from exterior and interior parts of the bricks [61].*

| Brick | Exterior | | Interior | |
|-------|----------|----------|----------|----------|
| | % α $Si_3N_4$ | % β $Si_3N_4$ | % α $Si_3N_4$ | % β $Si_3N_4$ |
| A | 87.3 ± 1.4 | 12.7 ± 1.4 | 88.2 ± 1.4 | 11.8 ± 1.4 |
| B | 72.1 ± 1.4 | 27.9 ± 1.4 | 35.1 ± 1.4 | 64.9 ± 1.4 |
| C | 74.7 ± 1.4 | 25.3 ± 1.4 | 60.2 ± 1.4 | 39.8 ± 1.4 |
| D | 89.5 ± 1.4 | 10.4 ± 1.4 | 92.4 ± 1.4 | 7.5 ± 1.4 |
| E | 91.7 ± 1.4 | 8.3 ± 1.4 | 90.3 ± 1.4 | 9.7 ± 1.4 |
| F | 80.0 ± 1.4 | 20.0 ± 1.4 | 75.7 ± 1.4 | 24.3 ± 1.4 |
| G | 85.7 ± 1.4 | 14.3 ± 1.4 | 86.4 ± 1.4 | 13.6 ± 1.4 |
| H | 48.5 ± 1.4 | 51.5 ± 1.4 | 24.6 ± 1.4 | 75.4 ± 1.4 |



*Figure 6-10: α and β $Si_3N_4$ content of samples A-H from exterior part of the bricks.*
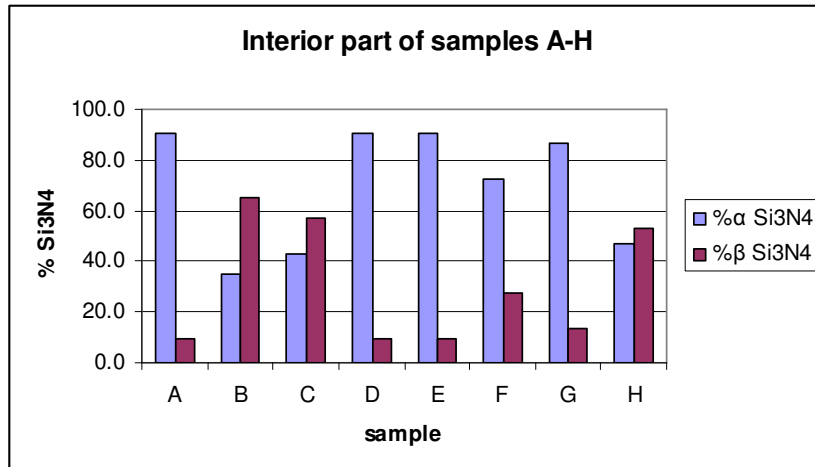
*Figure 6-11: α and β Si₃N₄ content of samples A-H from interior part of the brick.*

The sample profiles after the experiment (Figure 6-7) indicate considerable performance differentiation. Several samples show massive attack over this time interval. All the samples were exposed to the molten bath and vapours above the bath for the same length of time (77 hours) and in the same environment. However, it was evident that when the samples were taken out at the end of the experiment - but not after the first 48 hours (see Figures 6-7 and 6-8), samples D-H had more frozen bath attached to them and had a harder crust around the metal frame at this end of the rig compared to the samples A-C. This may have afforded more protection, progressively increasing for samples D-H over the last 30 hours of the test. However, the excellent performance of sample A suggests the overall effect of the extra crust is minor.

The tapering of samples as opposed to necking implies that the corrosion was heaviest on the part of the sample that was immersed in the molten bath and not in the region attacked by bath vapours above the bath/vapour interface. This is somewhat in contrast to the lab experiments, but may well be due to the frozen bath that covered the samples above the bath interface. This suggests possible improvements which could be made in the methodology of the experiment, for example improved insulation of the frame and wider sample spacing. However the comparative behaviour is still very useful. The corrosion mechanism appears to be similar across all samples. The attack is preferentially concentrated in the binder (nitride) phase, leading to exposure of a coarse, crumbly exterior. The surface of the sample used in the pre-trial demonstrates this quite well (Figure 6-12).
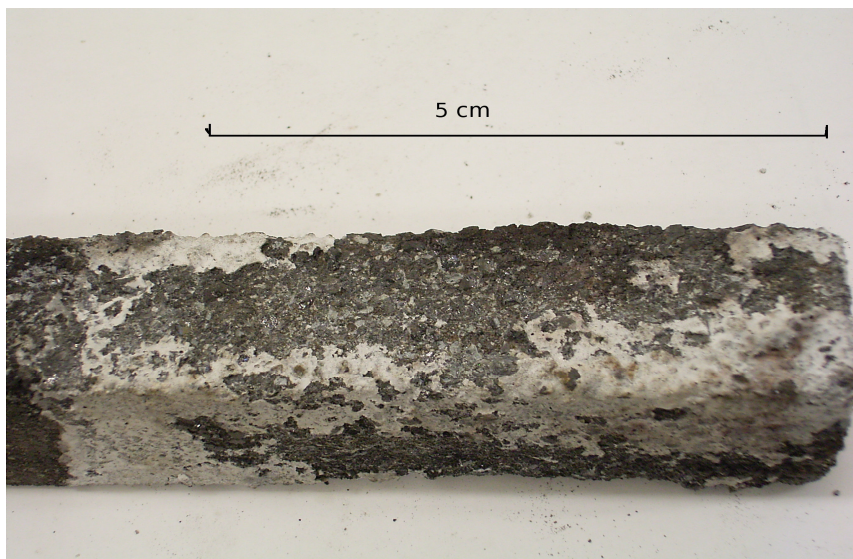
*Figure 6-12: Surface of the single sample recovered after 30 hours of immersion.*

Another initial observation is that the rate of attack appears to accelerate in the latter stages of the trial. The samples when observed during the 48 hour repositioning of the rig (see Figure 6-7) appear largely intact, in as much as this is able to be observed, with limited bulk loss of material. However the samples recovered at the completion of the trial (after 77 hours) showed more extensive attack, to the extent that in one case the immersed part of the sample is completely removed. The accelerated attack late in the trial is consistent with smelter operational observation of silicon carbide wall attack, which typically becomes more rapid later in the life of the refractory, as the cell walls are progressively exposed to periods of molten bath contact [24].

The X-ray diffraction results show high $\beta$ $Si_3N_4$ content especially in the interior part of the brick in samples H, B and C. The last two of these show higher corrosion rates compared to all other samples. Although sample H did not show a high corrosion rate in this trial, the fact that there is a significant difference in the corrosion rate between sample A which was exposed adjacent to samples B and C, but is rich in $\alpha$ $Si_3N_4$, raises the hypothesis that the $\alpha/\beta$ $Si_3N_4$ ratio makes a significant contribution to the corrosion mechanism of SNBSC materials in the reduction cell environment. This factor was later tested more carefully in controlled lab scale experiments to confirm the importance of $\alpha/\beta$ $Si_3N_4$ ratio on the corrosion rate and to shed some light on the corrosion mechanism (Chapter 6.2.3).

## 6.2. Laboratory scale corrosion experiments

To better analyse and understand the corrosion mechanism, cross sectioned samples of SNBSC bricks from various manufacturers were examined in a corrosion test using the "half immersed' configuration test method (Chapter 5.2). These samples were cut from SNBSC bricks manufactured in various widths as listed in Table 6-3.

*Table 6-3: Width of the different bricks tested in the corrosion test.*

| Brick Id | Width (mm) |
|----------|------------|
| A | $90 \pm 0.5$ |
| B | $100 \pm 0.5$ |
| C | $75 \pm 0.5$ |
| D | $75 \pm 0.5$ |
| F | $75 \pm 0.5$ |
| G | $75 \pm 0.5$ |
| H | $100 \pm 0.5$ |

- The samples tested were taken mainly from bricks H, B, C, due to their wide variation in porosity levels and composition of the bonding phase. The corrosion rate of the samples was defined as: CR= $-\frac{(Vf - Vi)*100}{Vi}$ where CR is the corrosion rate, $V_i$ is the initial volume of the sample prior to the exposure to electrolysis condition and $V_f$ is the sample volume after the electrolysis experiment. The volume loss was measured by the ISO 5017 standard method as describe in Chapter 5.1. The corrosion rate was analysed as a function of three main parameters:
- Porosity levels
- $\alpha/\beta$ $Si_3N_4$ ratio
- $SiC/Si_3N_4$ ratio

Two sets of experiments were conducted. In one set, samples were tested without any prior treatment. In the second set, samples were soaked in the molten bath (with the same composition as the bath in the corrosion test) for 48 hours without applying any current prior to the corrosion test. The soaking treatment was done to study the influence of the penetrated bath on the corrosion rate. This simulates the condition in commercial reduction cell where refractories in the lower part of the sidewall are exposed to the liquid bath, if not during cell start-up, then

certainly during temperature excursions when the frozen ledge is melted by high cell temperatures. Thus the corrosion of both fresh and bath impregnated samples is of interest.

Four samples, placed symmetrically around the anode, were tested in each corrosion experiment. The samples and the powdered bath mixture were placed in the crucible and heated to 1000 °C over 12 hours and kept at this temperature during the experiment. The graphite anode was inserted into the bath when the bath temperature reached 1000 °C and a current of 15A was applied for 48 hours. The voltage was kept at 3.0-4.0V by adjusting the anode-cathode distance.

The tested samples, both from the un-soaked and pre-soaked experiments, were made in different widths. Initially wider samples were tested in order to reduce the error in the volume and porosity measurements. Due to the variations in the porosity and α and β $Si_3N_4$ content observed along the bricks cross section (as describe in chapter 6.2.1 and 6.2.3), narrower samples were tested in order to reduce these variations.

The sample volume and porosity were measured according to the procedure described in Chapter 5.1 before and after the soaking treatment, and after the corrosion test (the adhering bath was removed prior to the measurement). The soaking treatment had minimal influence on the sample volume, but a reduction of open porosity was observed related to the bath penetration into the open pores. The sample area that was immersed during the soaking treatment was placed at the top of the sample in the corrosion test orientation, exposing it to the gas phase during the test. The conditions of the corrosion test were similar for the un-soaked and the pre-soaked samples.

## 6.2.1. Effect of porosity in SNBSC bricks

The apparent porosity of segments cut along a SNBSC brick cross-section was measured. Figure 6-13 shows the locations of the segment cut from a cross section.



*Figure 6-13: Segment location in a cross section of SNBSC brick.*

The graphs in Figures 6-14 to 6-17 represent typical porosity variations as measured in segments cut from the cross section of the same bricks. Although it is difficult to reach any conclusion from Figure 6-14, the porosity data does support variation in porosity levels of the segments across the cross section of the bricks.
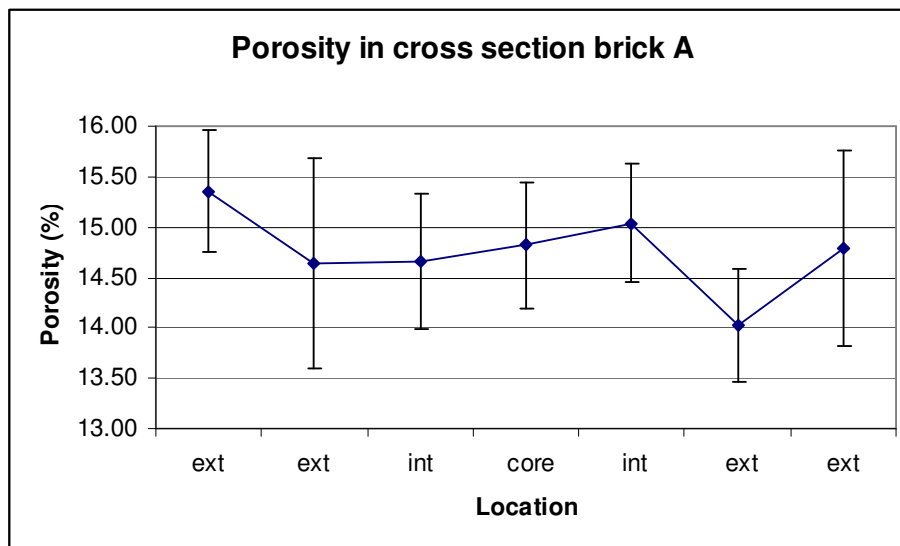


*Figure 6-14: Porosity of segments cut from a cross section of SNBSC brick A.*
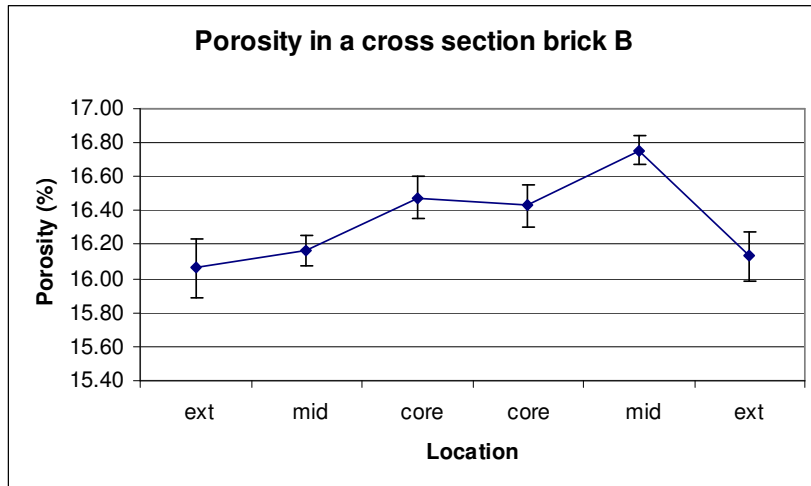
*Figure 6-15: Porosity of segments cut along a cross section of brick B.*
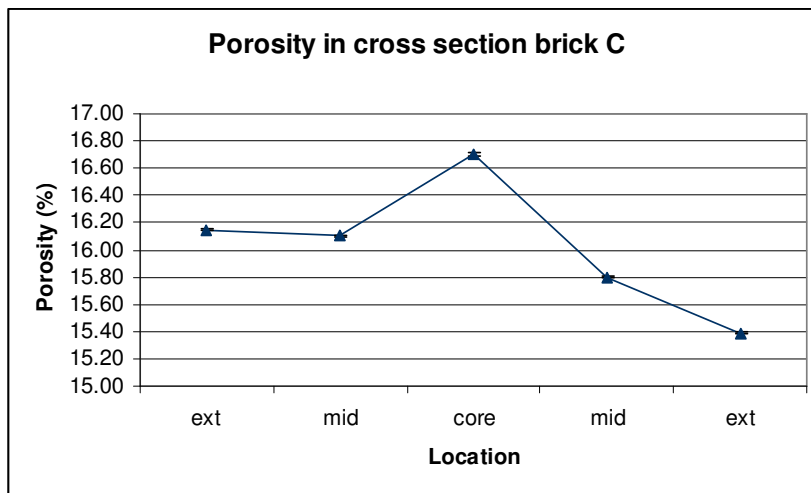


*Figure 6-16: Porosity of segments cut along a cross section of brick C.*
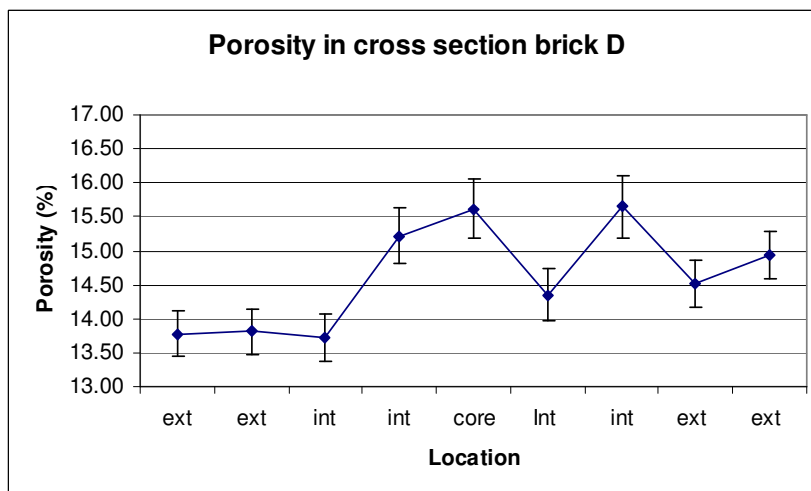


*Figure 6-17: Porosity of segments cut along a cross section of brick D.*

Bricks B, C, and D show higher porosity in the internal part of the brick compared to the exterior part. The exterior areas of samples C and D show a difference in the porosity level of the two exterior areas: one exterior face of the brick showed higher porosity levels than the other face. This phenomenon was observed in a few cross sections cut from brick C, as seen in Figure 6-18.
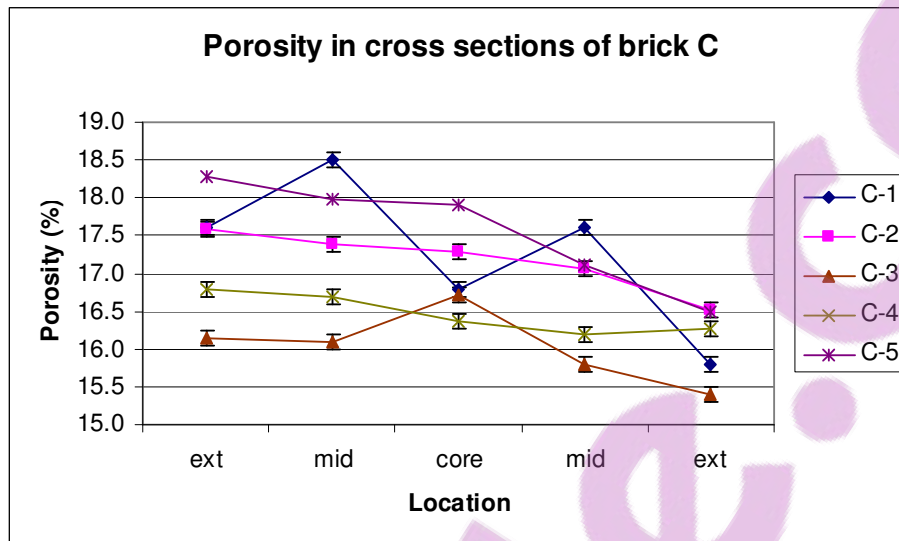


*Figure 6-18: Porosity of segments cut from a cross section of brick C. Curves C-1 to C-5 represent different cross sections cut from brick C.*

Variations in porosity levels (up to 2% difference in porosity in some cross sections) of the two exterior parts of the same brick could be related to the stacking arrangement of the bricks in the furnace during the nitridation process (Figure 6-19).



*Figure 6-19: A sketch of a trolley with "green" SNBSC bricks before loading into the nitridation furnace. Any random stacking creates differential exposure to the nitrogen flow. Exposure to the nitrogen flow lowers the porosity of the exposed area.*

The random stacking of the bricks on the rack during the nitridation procedure could vary the exposure of the exterior face of the bricks to the nitrogen gas flow. Bricks that stand apart from each other with enough space between them would have better exposure to the nitrogen flow leading to better penetration of the nitrogen gas into the green brick, causing an enhanced nitridation reaction, and forming a denser silicon nitride phase.

The porosity levels of samples taken from the interior and the exterior areas of the bricks examined in the corrosion test were measured. Figures 6-20 to 6-22 show the area and the porosity levels in the samples from bricks B, C, and H (ranked from the lowest to the highest porosity) and their locations. Samples from the exterior part of the brick are marked in red and samples from the interior are marked in blue.
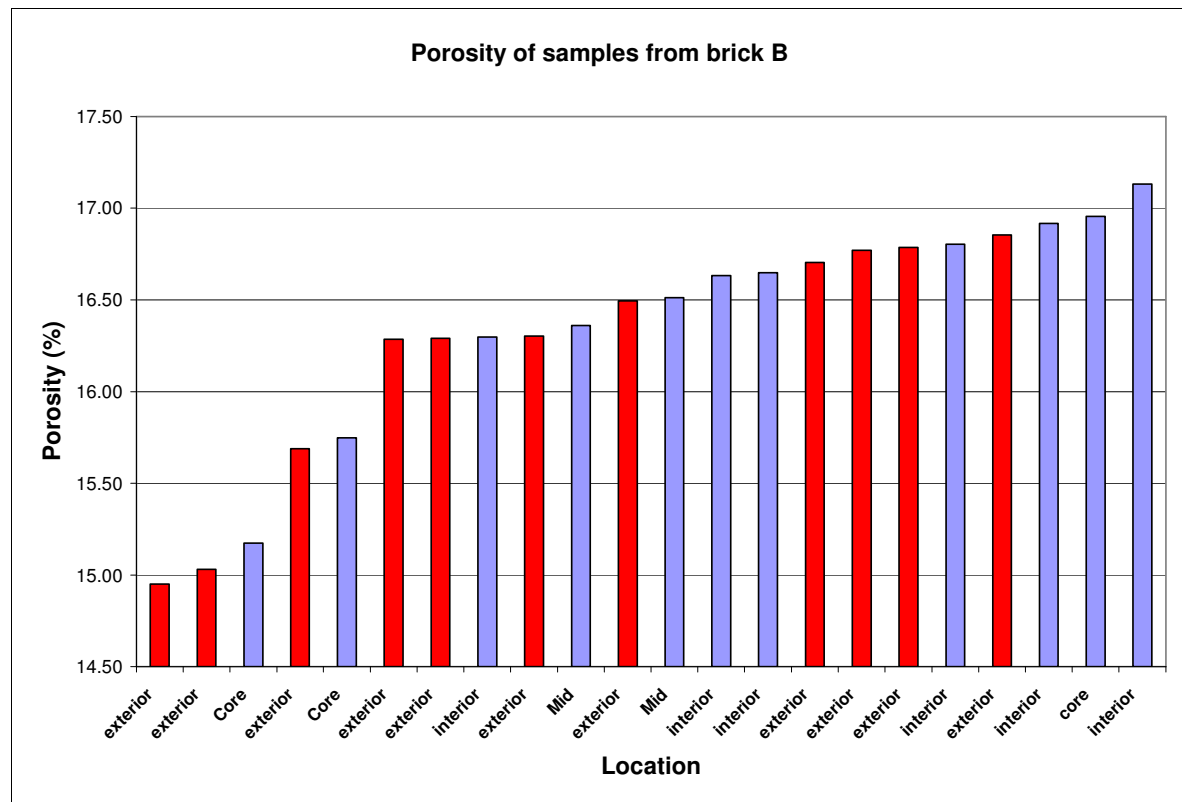


Figure 6-20: Porosity of samples cut from a cross section of brick B. Samples are ranked according to their porosity levels. The red bars represent the samples from the exterior area and the blue bars samples from the interior regions of the cross-section.

*Figure 6-21: Porosity levels of samples cut from a cross section of brick C. Samples are ranked according to their porosity levels. The red bars represent the samples from the exterior area and the blue bars samples from the interior area.*



*Figure 6-22: Porosity levels of samples cut from a cross section of brick H. Samples are ranked according to their porosity. The red bars represent the samples from the exterior area and the blue bars samples from the interior area.*

Although considerable brick to brick variation is observed, in general, higher porosity levels are associated with the interior part of the bricks, as seen in Figures 6-20 to 6-22. The reason for the lower variations in porosity levels between the samples taken from the interior area compared with samples that were taken from the exterior area is related to the sample size. It is difficult to obtain samples which are located solely in the exterior or the interior zones, hence homogenising the porosity of each sample to some degree.

## 6.2.1.1. The effect of porosity on corrosion

The apparent porosity of fresh SNBSC samples from different bricks was measured prior to the corrosion test. The corrosion rate of the samples (measured as: -1 * volume loss (%)) as a function of their porosity level is shown in Figures 6-23 and 6-24. Figure 6-23 shows the corrosion rate of samples that were soaked in a bath for 48 hours, prior to the polarized corrosion test (pre-soaked samples). A linear regression curve fitted to the corrosion results shows that there is a correlation between the porosity and the corrosion rate of the samples that were pre-soaked in the bath. The coefficient of determination ($R^2$) was 0.31, indicating that this regression model can explain 31% of the variation in corrosion of the samples as a function of variations in porosity. The calculated p-value of 0.001 indicates a 99% confidence level in this correlation.
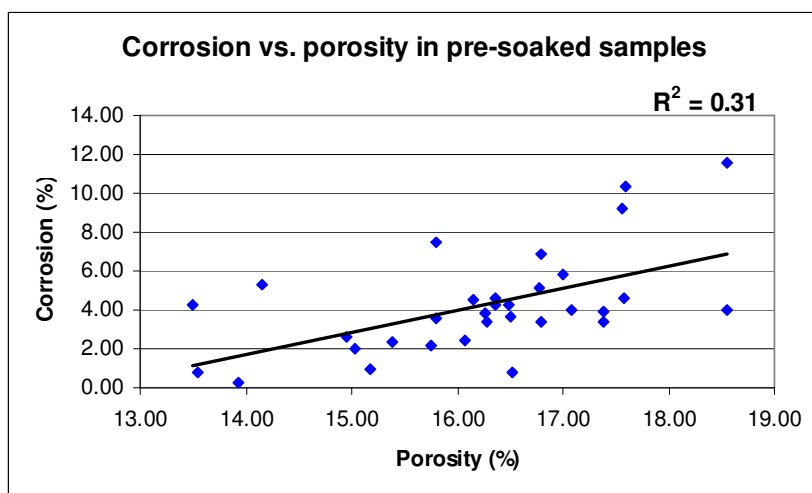


*Figure 6-23: Corrosion of samples taken from SNBSC brick as a function of their apparent porosity. These samples were soaked for 48 hours in cryolitic bath prior to the corrosion test.*

Figure 6-24 shows the corrosion rate of samples that were not pre-soaked in a cryolitic bath prior to the corrosion test (un-soaked samples). The results shown in Figure 6-24 indicate that no correlation was observed between the corrosion of the un-soaked samples and their porosity.
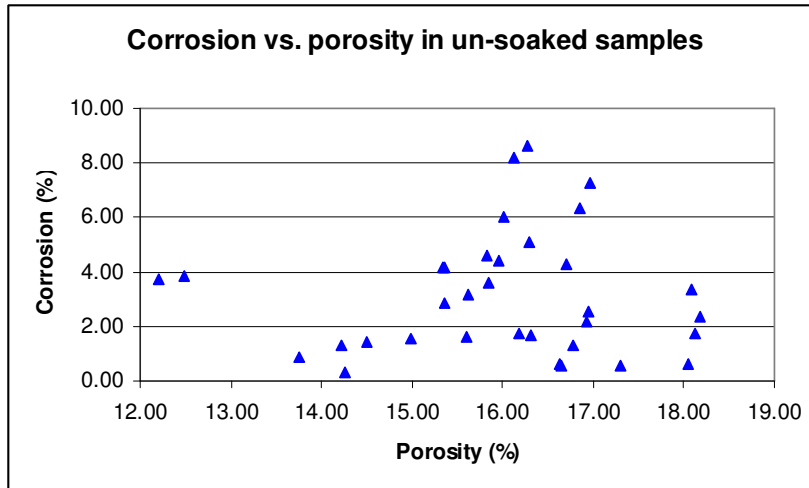
*Figure 6-24: Corrosion of samples taken from SNBSC bricks as a function of their apparent porosity. These samples were not soaked in a cryolitic bath prior to the corrosion test.*

The corrosion results of the un-soaked samples were sorted according to the sample width. The corrosion rate as a function of porosity level was plotted in two groups – the narrower samples having a width under 16mm (Figure 6-25) and the wider samples with a width above 16mm (Figure 6-26).
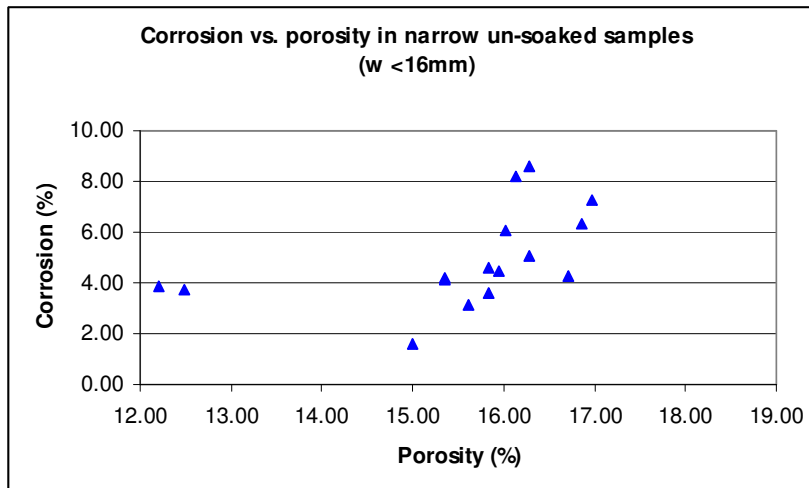


*Figure 6-25: Corrosion rate as a function of porosity in narrow un-soaked sample having a width <16mm.*
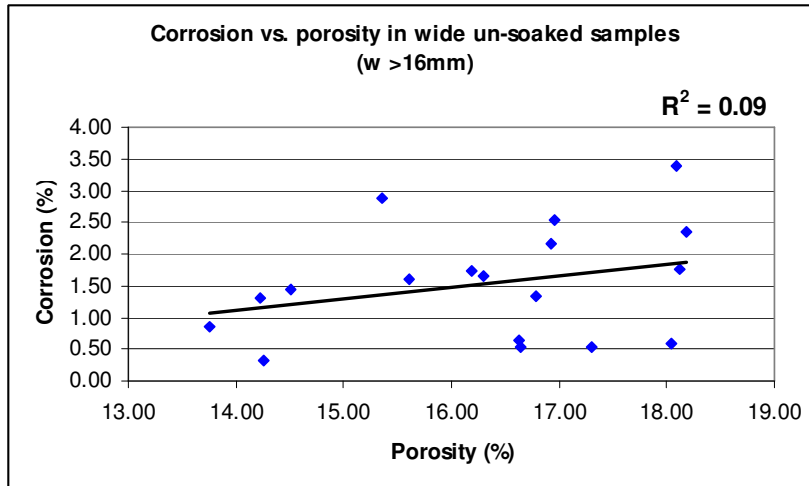
*Figure 6-26: Corrosion rate as a function of porosity in wide un-soaked sample having a width >16mm.*

The results, shown in Figure 6-25, indicate that samples, having a width smaller than 16mm, show some correlation between the corrosion rate and porosity level. Two samples from brick G show a significantly lower porosity level than the rest of the group and higher corrosion rate than expected for this porosity level. These samples although having low porosity had a relatively high amount of binder, and that is proposed to contribute to their high corrosion rate (the connection between corrosion rate amounts of binder phase is discussed in chapter 6.2.2)

The correlation between the corrosion rate and porosity of the un-soaked narrow samples, without the two samples from brick G, was plotted in Figure 6-27 and shows an improved correlation between corrosion rate and porosity level with $R^2 = 0.43$.
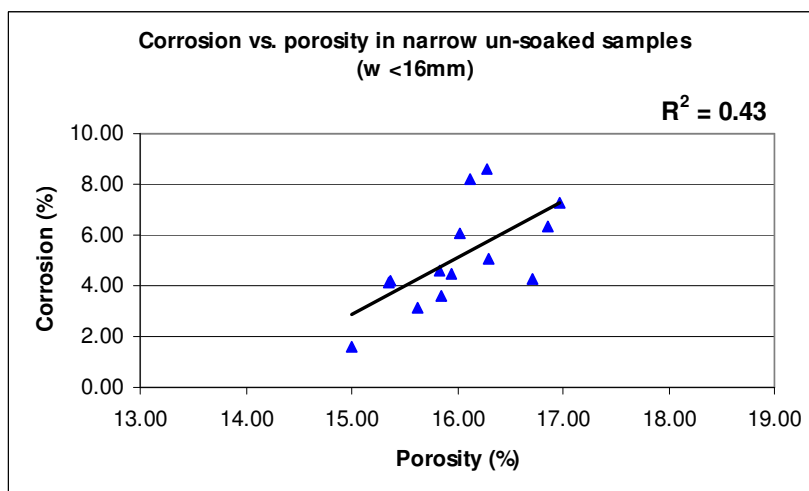


*Figure 6-27: Corrosion rate of narrow un-soaked samples (width<16mm) as a function of porosity level. The calculated $R^2$ of 0.43 for these results indicates high correlation between the corrosion rate and porosity level.*

The pre-soaked samples were also sorted according to their width, and the corrosion rate as a function of porosity level was plotted in two different graphs- one for the narrow samples with width under 16mm (Figure 6-28) and another for the wider samples having a width above 16mm (Figure 6-29).
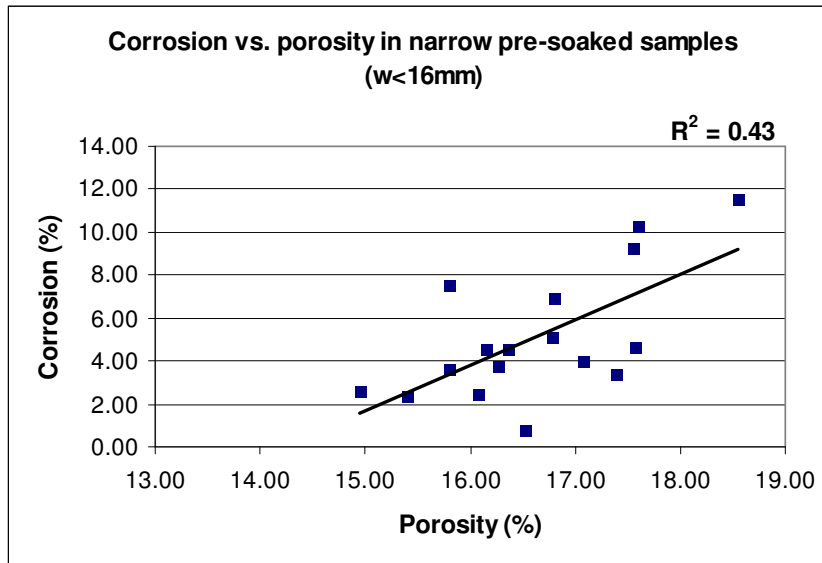


*Figure 6-28: Corrosion rate of narrow soaked samples (width<16mm) as a function of porosity level. The calculated $R^2$ of 0.43 for these results indicates high correlation between the corrosion rate and porosity level.*
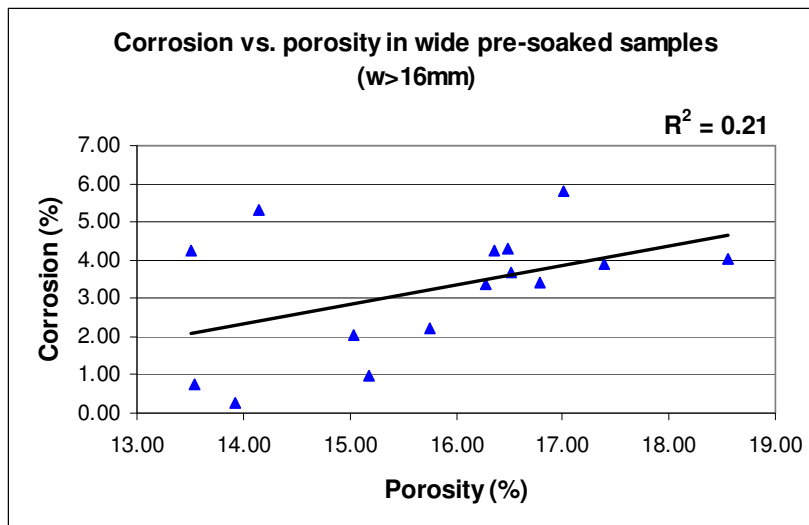


*Figure 6-29: Corrosion rate of wide soaked samples (width>16mm) as a function of porosity level. Lower correlation between the corrosion rate and porosity was found for the wider samples with calculated $R^2 = 0.21$.*

The corrosion results of the narrow pre-soaked samples having a coefficient of determination of 0.43 indicate higher correlation when compared to all the soaked samples results. The wider

samples, although having a low coefficient of determination of 0.21, still show a trend of higher corrosion rate for higher porosity level (two samples from brick H reducing the correlation coefficient from $R^2 = 0.70$ to 0.21).

The experimental data points from the narrow samples (having a width below 16mm), both in the pre-soaked samples and un-soaked samples, indicate that there is a correlation between corrosion rate and porosity level. The wider samples (especially in the un-soaked samples) show less correlation between the corrosion rate and the porosity due to incorporation of zones with different porosity levels into each sample. The corrosion rate is a function of the porosity of the surface exposed to the corrosive gases; thus in wider samples the measured porosity of the samples does not necessarily represent the surface area accessible to attack.

The soaked samples showed a higher correlation between the corrosion rate and porosity level compared to the un-soaked samples. This is evident especially for the corrosion results of the wider samples. The bath penetration during the 48 hours of the soaking stage is enhanced with higher porosity. The higher correlation between the corrosion rate and porosity level for the pre-soaked samples indicates that the bath penetration has an active role in the corrosion mechanism.

To examine the effect of brick dimensions four samples from brick H were cut in different width size and were tested under similar conditions. The widths of the two wider samples tested were 18.2mm and 19.7mm, while the two other samples had smaller widths of 10.9mm and 11.0mm (Figure 6-30). When the samples' corrosion was measured as a function of their porosity, the thicker samples showed no correlation between the corrosion and porosity level, while the two thinner samples showed such a correlation.

*Figure 6-30: Four samples cat from brick H that were tested in the same experiment. On the right thinner samples that showed higher correlation between corrosion rate and porosity level compared to the wider samples (on the left).*

Materials with a large difference in porosity were also tested in the same experiment in order to minimise the environmental variations that can occur in different experiments. Figure 6-31 shows the corrosion rate of samples taken from the same brick cross section where samples covered a range of porosity levels. Figure 6-32 shows samples from two different bricks: G (red bars) with lower porosity level and C (blue bars) with significantly higher porosity level.
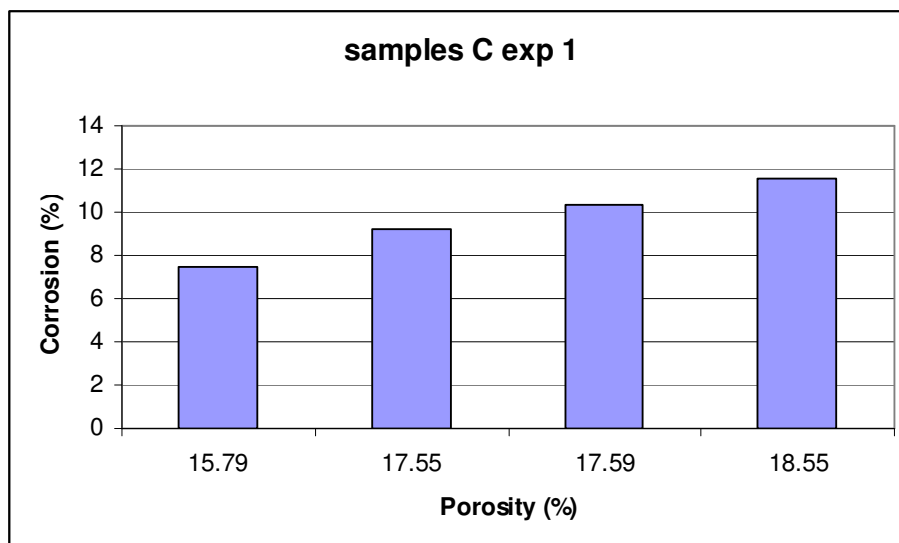


*Figure 6-31: Corrosion as a function of porosity level of samples taken from brick C that were tested in the same experiment, Significant higher corrosion rate observed in sample with the highest porosity level.*

**corrosion vs. porosity exp mixed 1**
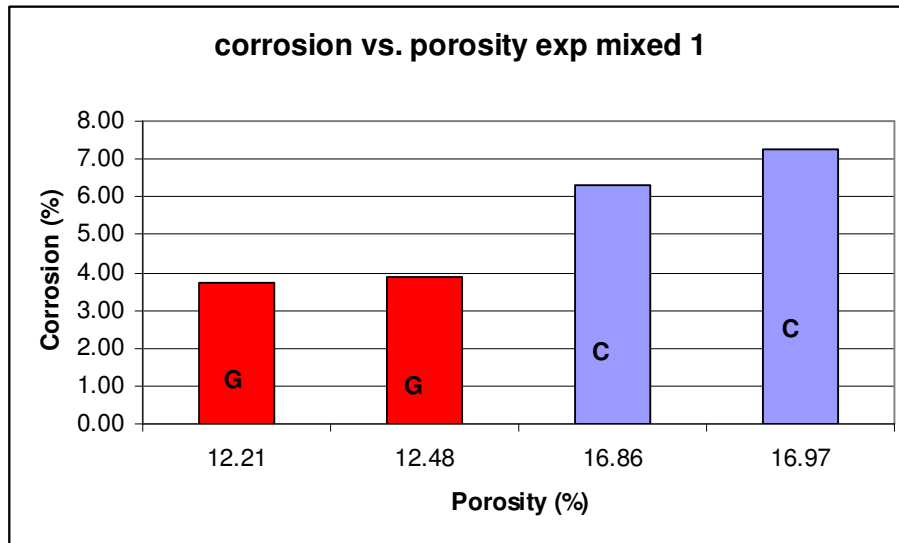
*Figure 6-32: Corrosion of samples with different porosity level tested in the same experiment. Samples with low porosity taken from brick G (marked in red) show a lower corrosion rate compared with samples with higher porosity level taken from brick C (marked in blue).*

The samples with relatively low porosity levels taken from brick G showed significantly lower corrosion rates compared to the samples taken from brick C with the higher porosity when tested under similar experimental conditions.

**6.2.2. Summary**

- Variation in porosity levels was observed in segments that were cut across the cross section of the SNBSC bricks.
- A difference in the porosity levels of two exterior faces from the same brick was observed; these variations in porosity levels could be related to the stacking arrangement of the bricks in the furnace during the nitridation process
- ]The corrosion results of the un-soaked and the pre-soaked samples were sorted according to the sample width, the narrower samples having a width under 16 mm and the wide samples having a width above 16 mm.
- The un-soaked narrow samples showed correlation between corrosion rate and porosity level with $R^2 = 0.43$, while the wide un-soaked samples showed very weak correlation.
- The pre-soaked samples showed correlation between the corrosion rate and porosity levels especially for the narrow samples having $R^2 = 0.43$. The wider samples, although having a low coefficient of determination of 0.21, still showed a trend of higher corrosion rate for higher porosity level.

- The reduced correlation between corrosion rate and porosity levels in the thicker samples was attributed to incorporation of zones with different porosity levels into each sample due to the variation in porosity levels along brick cross section.

**6.2.3. Effect of SiC/Si$_3$N$_4$ ratio on the corrosion rate of SNBSC bricks**

Thermodynamic calculations suggest that the binder phase of the SNBSC bricks is prone to attack by oxidising agents (CO, CO$_2$, and O$_2$) and corrosive gases (HF and NaAlF$_4$) present in the aluminium reduction cell atmosphere (see Chapter 7.1). The binder phase contains mainly $\alpha$ and $\beta$ Si$_3$N$_4$, low concentrations of oxides (Si$_2$N$_2$O and SiO$_2$) and some unreacted Si. The binder phase and SiC grains differ in their particles size. The SiC grains are in the mm range while both the Si$_3$N$_4$ phase and the oxide phases are in the micron and sub-micron range. The SiC content of samples tested in the lab-scale corrosion test was measured by XRD analysis (see Chapter 4.2). The corrosion rates of the samples (expressed as: $CR = -\frac{(Vf - Vi)*100}{Vi}$, see page 127) are presented as a function of their SiC content in order to study the effect of the binder phase concentration on the corrosion rate.   Figure 6-33 shows the corrosion rate of samples without prior exposure by soaking in electrolyte (un-soaked samples), as a function of SiC content.
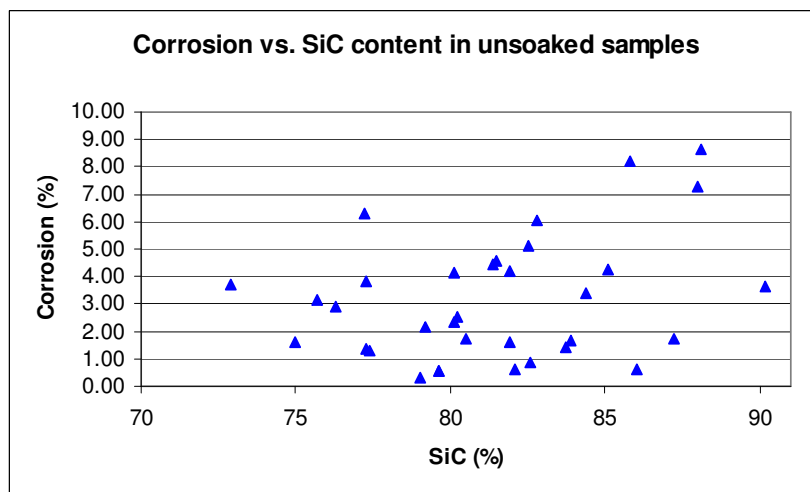


*Figure 6-33: The corrosion rate of un-soaked samples as a function of SiC content.*

The corrosion rate of samples pre-soaked in electrolyte is presented as a function of SiC content in Figure 6-34.
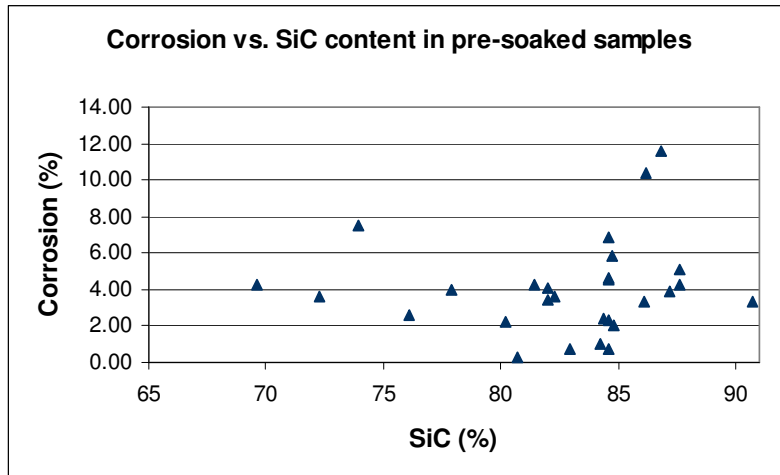
*Figure 6-34: The corrosion rate of pre-soaked samples as a function of SiC content.*

As anticipated, the pre-soaked samples show higher corrosion rates, however the data also suggest a local minimum is reached at a SiC content of around 80%. Despite the scatter, which is expected for these relatively complex composite materials, higher corrosion rates are observed in samples with low SiC content and particularly when the SiC content exceeds around 85%. Corrosion results of un-soaked samples with SiC content less than 80% are presented as a function of SiC content in Figure 6-35.
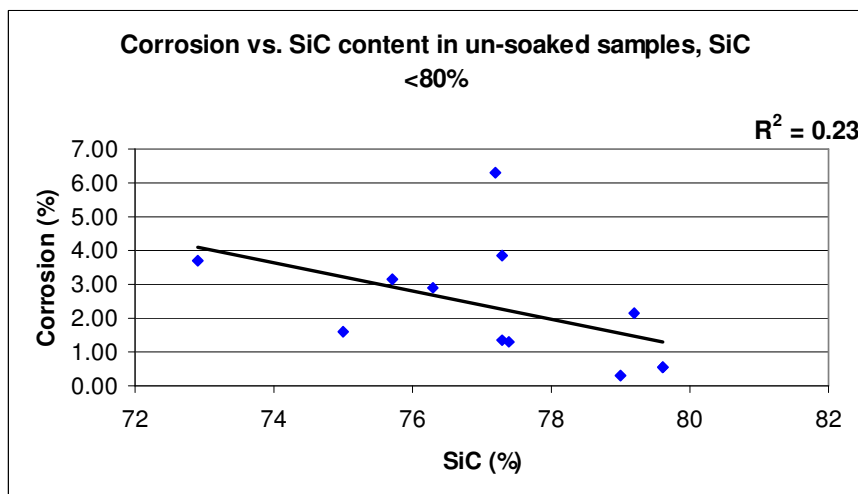


*Figure 6-35: Corrosion rate as a function of SiC content for un-soaked samples (SiC < 80%).*

Figure 6-35 show that the corrosion rate was reduced with the increase in SiC content. The calculated coefficient of determination ($R^2$) was 0.23 indicating the correlation is weak, but that some of the corrosion variation can be explained by the variation in SiC content.

The corrosion rate of samples with SiC content higher than 80% was plotted as a function of their SiC content (Figure 6-36). These results show that the corrosion rate is increased in as SiC content is increased and above 86%.
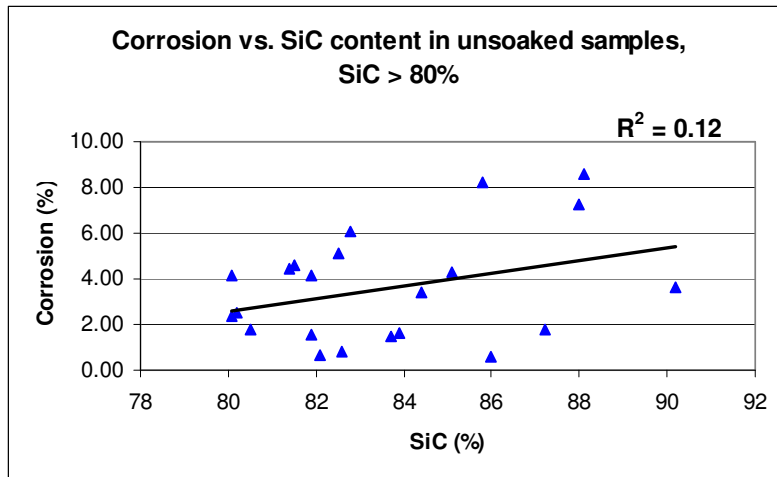


*Figure 6-36: Corrosion rate as a function of SiC content for un-soaked samples with SiC content > 80%.*

Pre-soaked samples showed the same trend of corrosion rate reduction with an increase in SiC content. The minimum corrosion rate point was observed at higher SiC percentage when compared with the un-soaked samples. Corrosion rates results of the pre-soaked samples with SiC content lower than 83% were plotted as a function of their SiC contents (Figure 6-37).
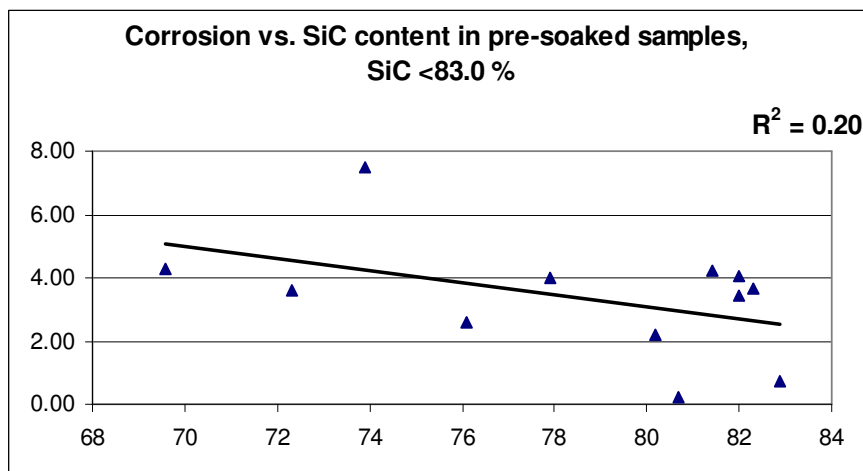


*Figure 6-37: Corrosion rate as a function of SiC content for pre-soaked samples (SiC < 83%).*

Figure 6-38 shows the correlation between the corrosion rate and SiC content for samples with SiC content >84%, these results indicates that a similar trend is observed as in Figure 6-36 with a similarly weak but positive correlation with SiC content.
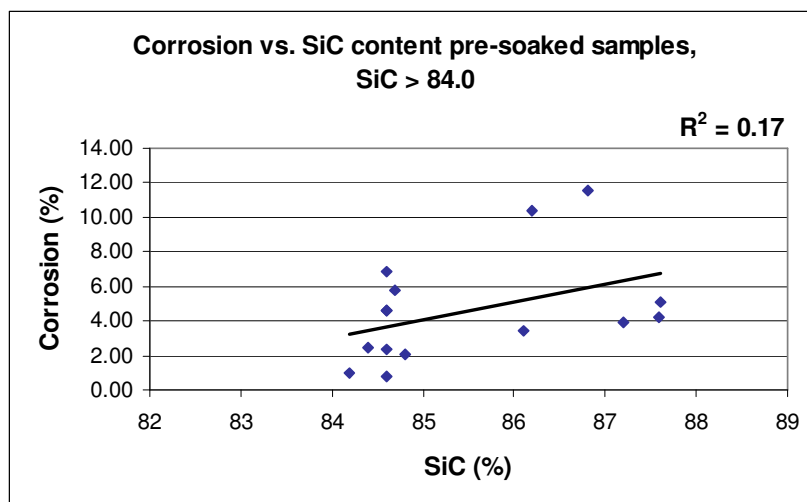


*Figure 6-38: Corrosion rate as a function of SiC content for pre-soaked samples (SiC > 83%).*

Figures 6-33 to 6-38 confirm a trend which is common in such composite materials where the binder phase is more reactive than the main matrix component. Thus lower binder content improves corrosion resistance, until the stage where there is insufficient to effectively pore fills and binds the composite together. Corrosion rate then increases as the loss of the remaining binder means large grains are readily plucked from the surface.

**Summary**

- The corrosion rates of the samples as a function of their SiC content was measured in order to study the effect of the binder phase concentration on the corrosion rate.
- Higher corrosion rate were observed in samples with low SiC content and also when SiC content exceed 80-85%.
- Corrosion test results showed maximum corrosion resistance at SiC concentration of 80% for the un-soaked samples and 85% for the pre-soaked samples.
- The results confirm a trend which is common in composite materials where the binder phase is more reactive than the main matrix component. Thus lower binder content improves corrosion resistance, until the stage where there is insufficient to effectively pore fills and binds the composite together.

**6.2.4. Effect of α/β Si$_3$N$_4$ ratio on the corrosion rate of SNBSC bricks**

As discussed in section 4.1 Si$_3$N$_4$ exists as two polymorphs, designated as α and β. The α and β Si$_3$N$_4$ content of the binder phase from eight different SNBSC bricks was quantified using XRD analysis by the Gazzara & Messier method [61]. Samples taken from the exterior and interior area of a cross section slice of each brick showed an uneven distribution of α and β Si$_3$N$_4$ along the cross section. Higher β Si$_3$N$_4$ content was usually observed in the interior part of the brick as seen in Table 6-4.

*Table 6-4: α and β Si$_3$N$_4$ content in samples from the exterior and interior parts of the SNBSC brick cross section.*

| Brick | Exterior | | Interior | |
|:---:|:---:|:---:|:---:|:---:|
| | % α Si$_3$N$_4$ | % β Si$_3$N$_4$ | % α Si$_3$N$_4$ | % β Si$_3$N$_4$ |
| A | 87.3 ± 1.4 | 12.7 ± 1.4 | 88.2 ± 1.4 | 11.8 ± 1.4 |
| B | 72.1 ± 1.4 | 27.9 ± 1.4 | 35.1 ± 1.4 | 64.9 ± 1.4 |
| C | 74.7 ± 1.4 | 25.3 ± 1.4 | 60.2 ± 1.4 | 39.8 ± 1.4 |
| D | 89.5 ± 1.4 | 10.4 ± 1.4 | 92.4 ± 1.4 | 7.5 ± 1.4 |
| E | 91.7 ± 1.4 | 8.3 ± 1.4 | 90.3 ± 1.4 | 9.7 ± 1.4 |
| F | 80.0 ± 1.4 | 20.0± 1.4 | 75.7 ± 1.4 | 24.3 ± 1.4 |
| G | 85.7 ± 1.4 | 14.3 ± 1.4 | 86.4 ± 1.4 | 13.6 ± 1.4 |
| H | 48.5 ± 1.4 | 51.5 ± 1.4 | 24.6 ± 1.4 | 75.4 ± 1.4 |

The figures shown in Table 6-4 are average values that vary in different samples taken from the same brick and the same location in the cross section. High uncertainty in this parameter was observed especially for bricks B, C, and H. Segments that were cut along the cross section of brick B showed a reduction in the β Si$_3$N$_4$ content from core to exterior. Figure 6-39 show the location of segments analysed along the cross section of brick B, and the variation in the β Si$_3$N$_4$ content in the binder of samples from two cross sections is shown in Figure 6-40.

*Figure 6-39: Cross section taken from brick B, and the location of the segments that were analysed.*
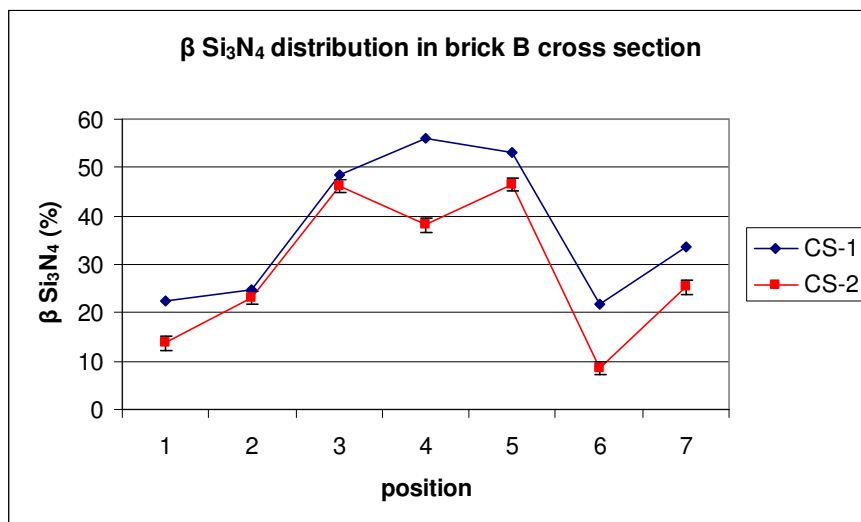


*Figure 6-40: β Si₃N₄ content in the binder measured on segments that were cut along two cross sections taken from brick B. The numbered locations are shown in Figure 6-39.*

The $\beta$ $Si_3N_4$ fraction in the binder along the brick cross section shown in Figure 6-40 indicate that variations in $\beta$ $Si_3N_4$ content can be found even in the same location in the brick cross section. Bricks H and C also showed an increase in $\beta$ $Si_3N_4$ content from the exterior to the core area of the cross section. The high $\beta$ $Si_3N_4$ content in the internal area of some bricks is likely attributed to high temperatures during the nitridation stage of the fabrication process. Excess heat is generated during the nitridation reaction due to the exothermic nature of this process, as discussed in Chapter 2. The excess heat will dissipate more easily from the exterior part of the brick rather than from the interior. The high temperature in the interior creates conditions which favour the production of $\beta$ $Si_3N_4$. A temperature above 1500°C and the presence of a molten

liquid silicon phase, enhance the conversion from $\alpha$ to $\beta$ $Si_3N_4$ resulting in higher $\beta$ $Si_3N_4$ content in the interior of the brick.

6.2.4.1. Corrosion rate as function of $\beta$ $Si_3N_4$ content

Given that the binder is more reactive than the SiC matrix (see section 6.2.2 and 7.1), it is then worth examining the influence of different phase compositions in the binder itself. The corrosion rate of the pre-soaked samples was thus measured as a function of their $\beta$ $Si_3N_4$ content. The $\beta$ $Si_3N_4$ content of the corrosion tested samples was measured by cutting 5mm cross section from each sample pulverised it and analysing using the XRD method as described in Chapter 4.2.

The corrosion rate of the pre-soaked samples was plotted as a function of their $\beta$ $Si_3N_4$ content (Figure 6-41) and a weak, but positive, correlation between the corrosion rate and $\beta$ $Si_3N_4$ content was observed. The calculated p-value of 0.003 indicates that the contribution $\beta$ $Si_3N_4$ content to the corrosion rate is significant (for further explanation about p-value see section 7.3).
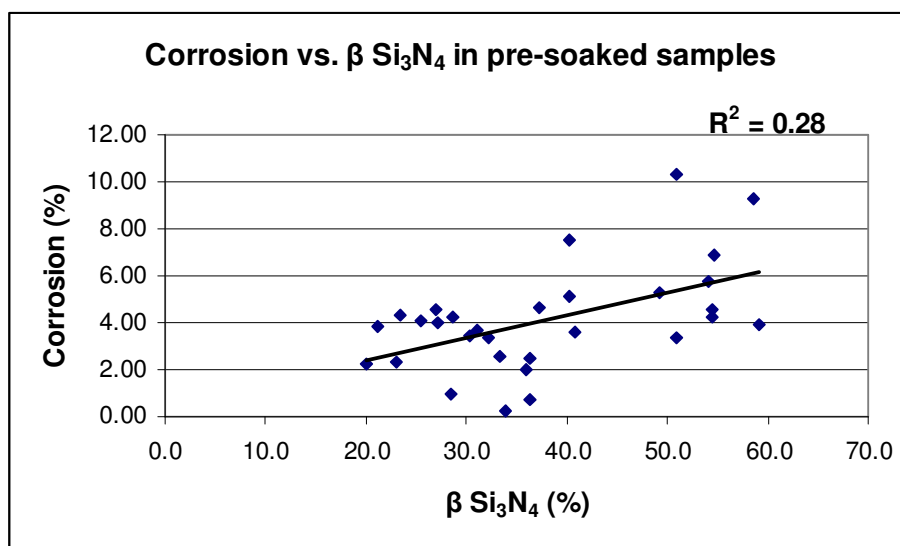


*Figure 6-41: Corrosion rate as a function of $\beta$ $Si_3N_4$ content of the bonding phase in samples that were pre-soaked in bath prior to corrosion test.*

The corrosion rate of samples that were not soaked in cryolitic bath (electrolyte) prior to the corrosion test is plotted as a function of their $\beta$ $Si_3N_4$ content (Figure 6-42). The results indicate little or no correlation between the corrosion rate of the un-soaked samples and their $\beta$ $Si_3N_4$ content.
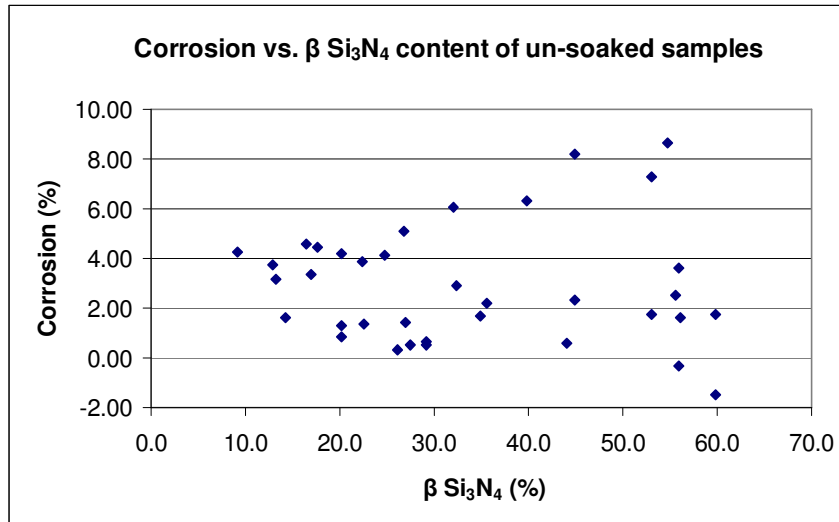
*Figure 6-42: Corrosion rate as a function of β Si₃N₄ content of the bonding phase in samples that were not soaked in bath prior to corrosion test.*

As is apparent in Figure 6-39, the size of the samples used in these trials does affect the ability to sample a unique (rather than a graded) composition. This is most apparent near the exterior of the brick. Thus several corrosion tests were undertaken on un-soaked samples, as a function of sample dimension (width of the cross-section) to test this effect. The thickness of the un-soaked samples was measured using a Vernier calliper and the data was sorted according to their ranking from the thinnest to the thickest. A discontinuity of correlation between β Si₃N₄ content and corrosion rate observed in samples with thickness above 16mm, hence samples were classified as above or below this level. The corrosion rate is plotted as a function of β Si₃N₄ content for the thin samples with width < 16 mm (Figure 6-43) and for the wider samples with a thickness above 16 mm (Figure 6-44).
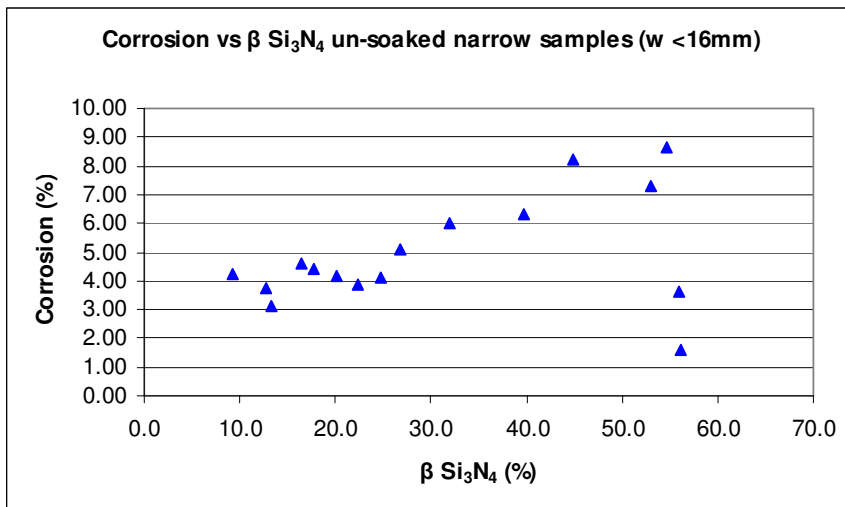
*Figure 6-43: Corrosion as a function of β Si$_3$N$_4$ content for the un-soaked sample with a thickness below 16mm.*
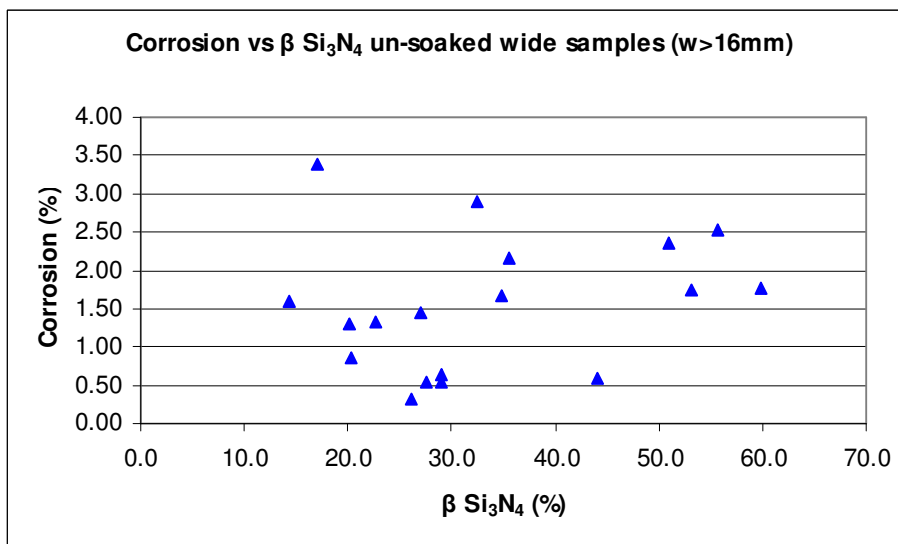


*Figure 6-44: Corrosion as a function of β Si$_3$N$_4$ content of un-soaked sample with a thickness above 16mm.*

The corrosion rate for samples with thickness below 16mm showed a higher correlation between corrosion rate and β Si$_3$N$_4$ content. Corrosion results for two of the thin samples deviate significantly from the rest of the data points in that group. These samples differ from the rest of the samples in the group by having a depth of 30mm compared with 15mm for the rest of the samples (Figure 6-45). Thus this deviation can also be attributed to sample dimension.
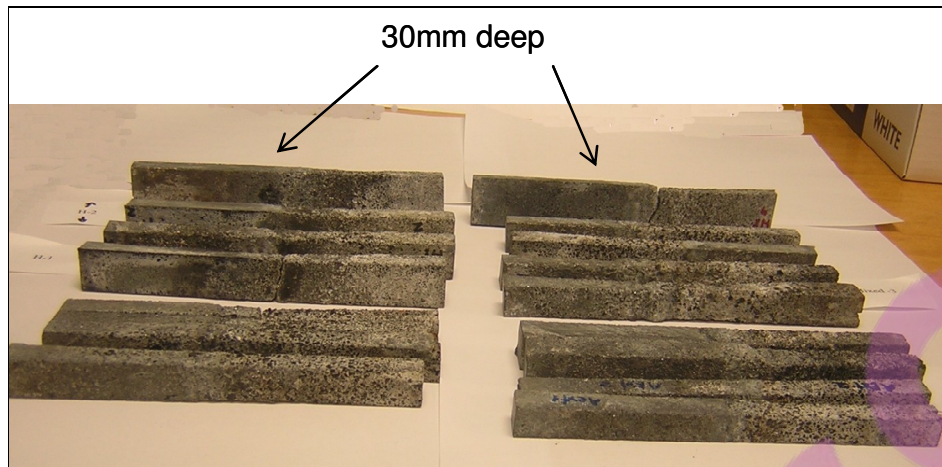
*Figure 6-45: Un-soaked narrow samples after corrosion test. In the back of the picture, the two samples, having a depth of 30mm compared to the other samples with a depth of 15mm.*

The correlation between the corrosion rate and the $\beta$ $Si_3N_4$ content of the narrow samples, without the two deeper samples, is substantially higher (Figure 6-46).
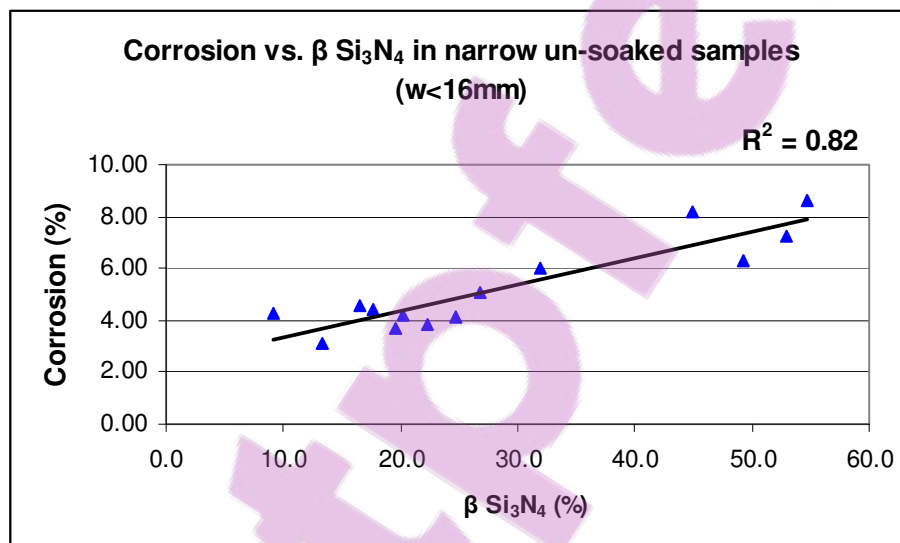


*Figure 6-46: Corrosion rate as a function of $\beta$ $Si_3N_4$ content of un-soaked samples. High correlation was found between the corrosion rate and $\beta$ $Si_3N_4$ content with calculated $R^2 = 0.82$.*

The correlation between the corrosion rate and the $\beta$ $Si_3N_4$ content of the thicker (>16mm) un-soaked samples remains low with calculated $R^2 = 0.04$. However this is also dominated by one outlier that shifts the coefficient of determination from 0.20 to 0.04.

The lower correlation between the corrosion rate and $\beta$ $Si_3N_4$ content of the thicker samples can be related to incorporation of zones with the different $\beta$ $Si_3N_4$ content into each sample. The variations in the $\beta$ $Si_3N_4$ content that were observed along the bricks cross sections (Figure 6-40)

means that the measured $\beta$ $Si_3N_4$ content of the sample taken from wider area of the brick cross section does not represents accurately the $\beta$ $Si_3N_4$ content of the surface exposed to corrosion attack.

**Summary**

- An uneven distribution of $\alpha$ and $\beta$ $Si_3N_4$ was observed along the cross section of several SNBSC bricks.  Higher $\beta$ $Si_3N_4$ content was usually observed in the interior part of the brick.
- The high $\beta$ $Si_3N_4$ content in the internal area of some bricks is attributed to presence of high temperatures during the nitridation stage. The exothermic nitridation reaction can lead to generation of excess heat creating the conditions, as presence of a molten liquid silicon phase, which favours the production of $\beta$ $Si_3N_4$.
- The corrosion rate of the pre-soaked samples showed positive correlation with $\beta$ $Si_3N_4$ content with $R^2 = 0.28$. The low p-value of 0.003 indicates that the contribution $\beta$ $Si_3N_4$ content to the corrosion rate is statistically significant.
- Positive correlation between corrosion rate and $\beta$ $Si_3N_4$ content was observed only in the narrow (width< 16 mm) un-soaked samples.

### 6.2.5. The effect of free silicon on the corrosion rate of SNBSC bricks

The high reactivity of silicon suggest the hypothesis that the corrosion rate of SNBSC materials in the aluminium reduction cell atmosphere could be related to the free silicon content and its distributed within the SNBSC bonding phase. The free Si arises from incomplete reaction of the binder phase precursor. Bulk analysis based on X-ray diffraction or ISO standard method (928/5:1997) [24] suggests that the concentration of the free silicon is minimal in most samples.

A published cross-sectional micrographs [33] show that the Si metal phase is inter grown into both the SiC and the $Si_3N_4$ phases (Figure 6-47). Assuming that the phase assignment in the photomicrographs is correct, it is significant because it indicates that this part of the Si phase must form or migrate during the fabrication of the block.

The indication from this intergrowth is that the Si forms a liquid during the fabrication of the block and thus temperatures in excess of $1400^oC$ are being reached in the interior of at least some of the commercial samples, during formation of the $Si_3N_4$ bond phase. Any Si freezing from the liquid phase will be difficult to convert to $Si_3N_4$ bond phase due to the low surface area and thus slow kinetics of this reaction.
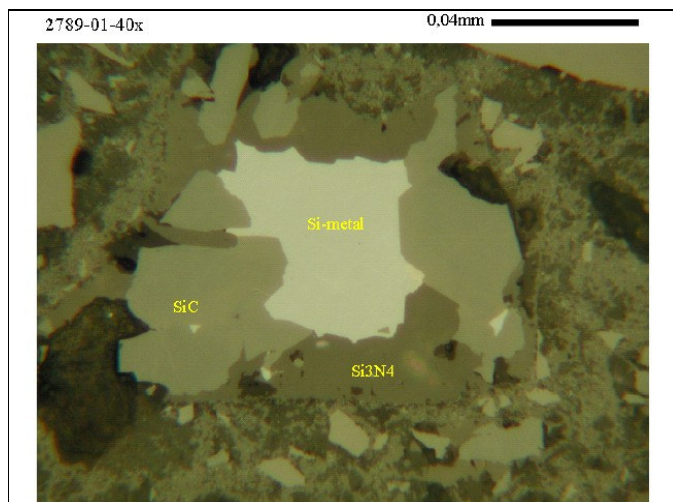


*Figure 6-47: Intergrowth of molten silicon between the phases. The Si metal is clearly in intimate contact with the SiC phase, indicative of inter growth of the Si around the SiC grains [33].*

Analytical results on SNBSC indicate that residual free Si is sometimes present, however the amount and location of Si again is debatable. The amount of silicon phase is difficult to quantify especially if some of the Si phase is amorphous (as it could be from freezing of a melt zone and formation of Si glass) and thus not seen in the X-ray diffraction pattern.

XPS analysis on a range of samples did not identify the same differences in free Si content. The free Si peak at BE = 99-100eV did not appear and peaks of silicon carbide (at BE = 100.4-101.1eV) dominated the spectrum (Figure 6-48).
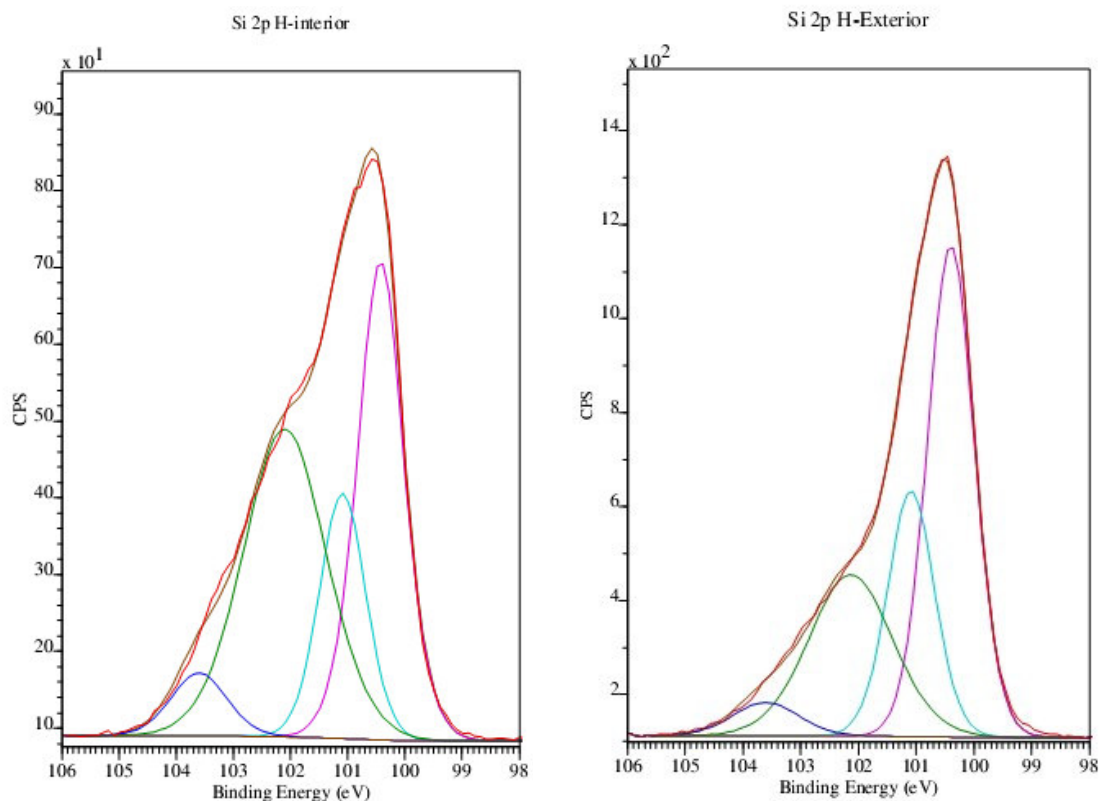


*Figure 6-48: XPS Si 2p analysis of sample H, internal zone (left) and external zone (right).The free Si peak at the BE = 99-100eV is absent. The dominant phase is SiC (BE =100.4 and 101.1), other phases are nitride (BE = 102eV) and Oxide (BE = 103eV).*

XRD analysis of samples taken from various parts of the blocks (from seven different manufacturers) indicates the presence of free silicon in some of the bricks (bricks B, C and H). The maximum content of free Si observed was ~ 7%. Higher Si concentration was observed in samples taken from the interior part of the bricks and usually accompanied with higher $\beta$ $Si_3N_4$ content (Figure 6-49).
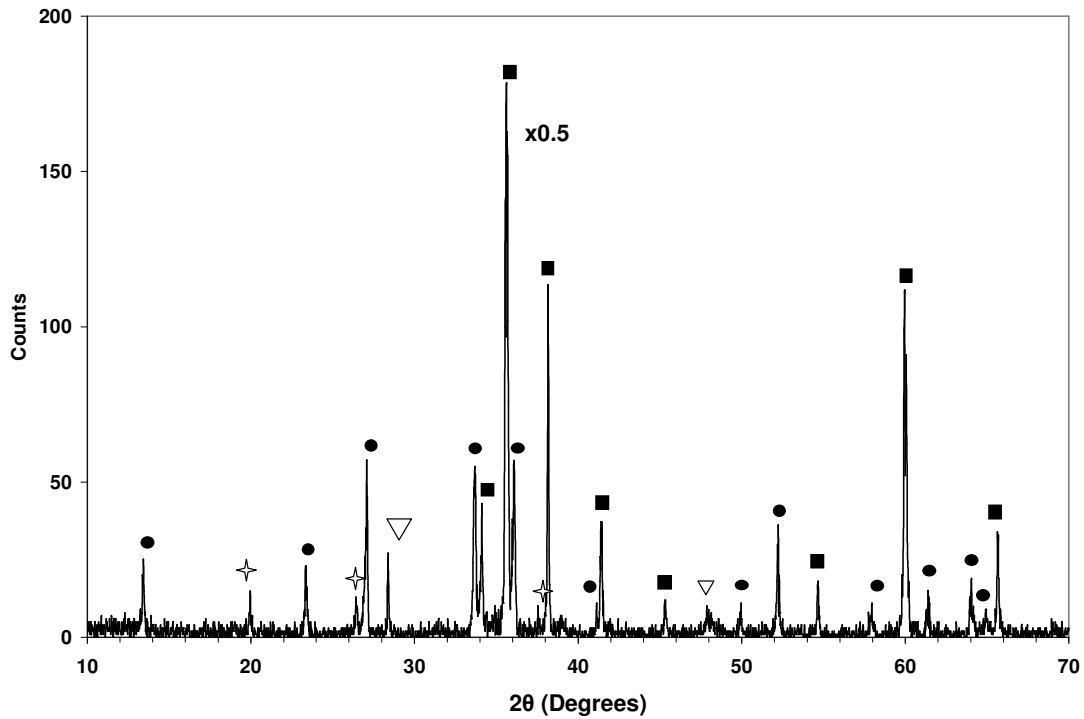
*Figure 6-49: XRD analysis of core part of brick H confirming the presence of free Si, and among the $Si_3N_4$ phases only the $\beta$ $Si_3N_4$ is present. ($\triangledown$) Si (7.0%), ($\star$) $Si_2N_2O$ (7.9%), ($\bullet$) $\beta$ $Si_3N_4$, ($\blacksquare$) SiC.*

SEM-EDS analysis indicates that the free Si was mainly observed in the core of a SiC grain and not in the bonding matrix (Figure 6-50). The free Si was easily observed when using a back-scattered electron detector, and appeared white compared to the grey SiC grain or $Si_3N_4$ phases.
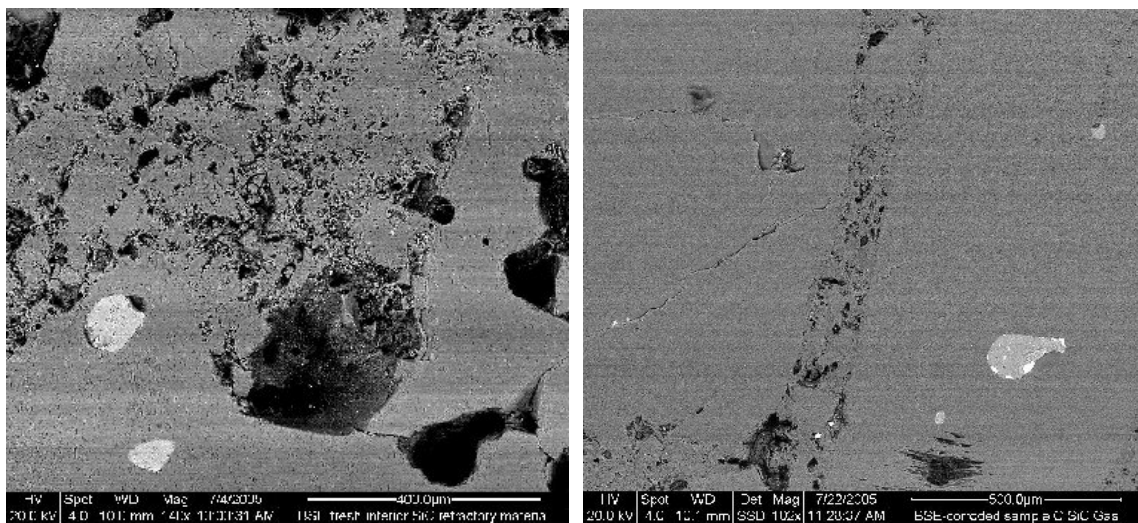


*Figure 6-50: Back scattered electron SEM image of un- exposed sample H (left) and corroded sample C (right) depict free Si in the core of the SiC grain (white spots) and not in the bonding matrix.*

SEM analysis of a large number of samples from various bricks did not reveal any silicon in the bonding phase, and the phenomenon of free silicon intergrowth into the SiC grains as shown by the micrograph published by Andersen (Figure 6-47) was not seen.

The presence of amorphous silicon is relatively hard to detect using X-ray diffraction, hence Solid State NMR analysis was used to identify and quantify the amorphous silicon. This technique can detect both crystalline and non-crystalline phases that can not be detected by XRD analysis. Analysis of SNBSC materials using solid state NMR showed that all the phases found in the samples were crystalline including the free silicon (Figure 6-51). Amorphous phases that might be hard to quantify by XRD were not observed.
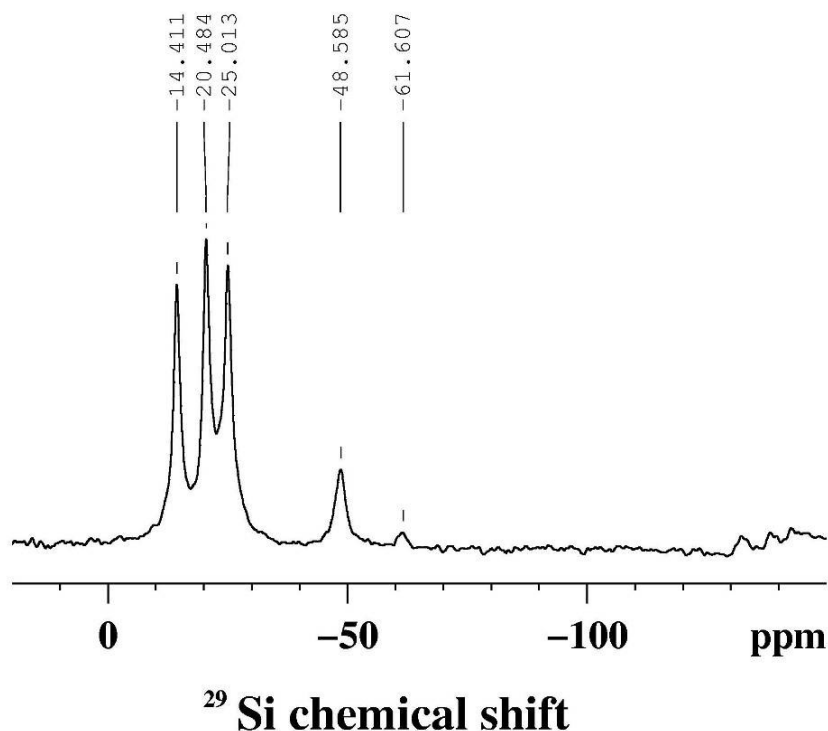


*Figure 6-51: Solid state NMR of fresh sample B showing the presence of SiC (peaks at -14.41, -20.48, -25.0 ppm) $Si_3N_4$ (peak at -48.58ppm) and $Si_2N_2O$ (peak at -61.60ppm) with absence of free Si (peaks around -100ppm).*

The free silicon content observed by Solid State NMR was very low and confirms the results obtained from the XRD analysis. The confirmation that the free silicon present in the SNBSC sample is in crystalline form means that the XRD analysis could be used as an accurate method to quantify its content. The free silicon that was detected by XRD analysis could be attributed to the silicon found within the core of the SiC grains (as observed in our SEM analysis). These

observations rule out the hypothesis of unreacted silicon during the nitridation process was fused to a glass phase and is a significant contributor to the corrosion rate of SNBSC material in the aluminium reduction cell atmosphere.

### 6.2.6. The effect of environment -bath phase vs. gas phase attack

SNBSC materials in the reduction cell sidewall are exposed to cryolitic bath, and to gases both emitted during the electrolytic reaction, and diffusing from the surrounding cell environment. These two chemical environments are both observed to contribute to the corrosion rate of the sidewall materials. Thermodynamically, the potential of the SNBSC materials to react with the cryolitic bath is low because of the positive Gibbs free energies ($\Delta G$) of the reactions between $Si_3N_4$ and SiC with cryolite (as calculated in Chapter 7.1). Corroded samples showed degradation mainly on the area exposed to the gas phase while the part immersed in the electrolyte bath stayed intact (Figure 6-52).



*Figure 6-52: SNBSC samples* (25x20x185mm) *after corrosion test. Degradation of the samples is observed mainly in the bath-gas interface and in gas phase.*

The reactivity of the SNBSC samples with the cryolitic bath was measured by soaking samples for 48 hours in bath using a similar bath composition and temperature as used in the corrosion test, but without applying electric current. After the soaking treatment (when the adhering bath was removed) the exterior surface was undamaged, except for a slight change in colour (Figure 6-53).

*Figure 6-53: SNBSC sample after soaking treatment for 48 hours. No damage observed on the samples except colour change.*

The corrosion rates of samples after soaking treatment was compared to the corrosion rates of the same samples after the polarized corrosion test (Figure 6-54).
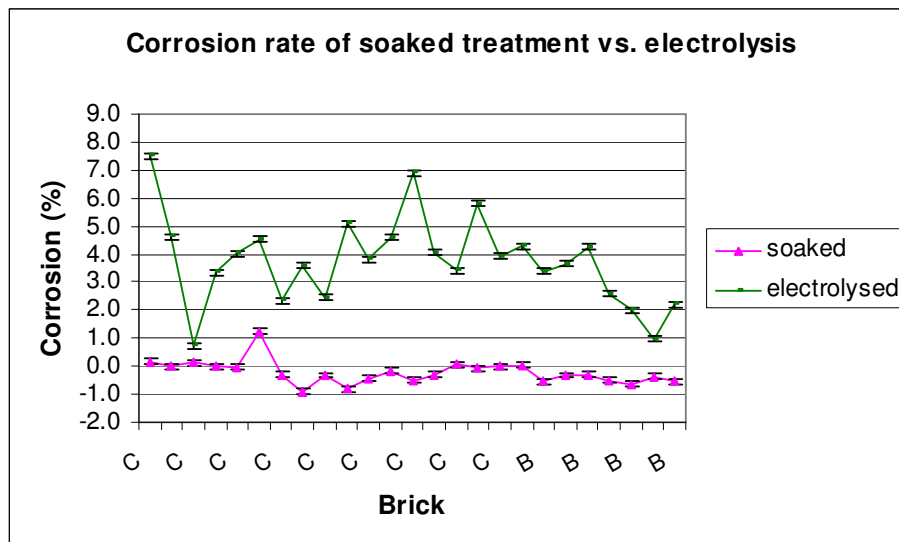


*Figure 6-54: Comparison between corrosion rates of samples exposed to bath and to electrolytic conditions.*

The corrosion rates in the soaking treatment were much lower compared to the corrosion rates in the polarized corrosion test. A slight volume increase occurred after the soaking treatment in some of the samples. The swelling can be related to bath penetration.

An experiment was designed in order to isolate the corrosion associated solely with the emitted cell gases, from the corrosion contributed by exposure by immersion in the cryolitic bath.

Samples were placed in a graphite "basket" attached to the anode connecting rod above the cryolitic bath level in the electrolysis set-up. The electrical current applied, bath composition, and temperature conditions, were similar to those of the half–immersed configuration (Chapter 5.2.1) used in the corrosion test. The corrosion rate was measured after 36 hours exposure to the cell gases and again after an additional 96 hours of exposure. These samples were then soaked in bath for 48 hours without applying electrical current, and again placed in the graphite basket to allow exposure to the gas phase for 48 hours during electrolysis. The corrosion rate of the samples in the various exposure regimes are listed in Table 6-5.

*Table 6-5: Corrosion rate of samples exposed to gas phase for 36 and 96 hours, and 48 hours after bath soaking for 48 hours.*

|  | Sample D1 | Sample D2 | Sample D3 | Sample D4 |
|---|---|---|---|---|
| Porosity | $13.6 \pm 0.4$ | $15.6 \pm 0.6$ | $14.9 \pm 0.4$ | $16.4 \pm 0.6$ |
| Corrosion after 36 hours exposure to gas phase (%) | -0.4 | -0.4 | -0.2 | -0.4 |
| Corrosion after 96 hours exposure to gas phase (%) | $1.0 \pm 0.7$ | $0.9 \pm 1.0$ | $1.2 \pm 0.5$ | $0.8 \pm 1.2$ |
| Corrosion after 48 hours exposure to gas phase post 48 hours bath soak (%) | $8.48 \pm 0.07$ | $11.61 \pm 0.07$ | $3.5 \pm 0.2$ | $4.3 \pm 0.2$ |

No corrosion occurred after 36 hours exposure in the gas phase during electrolysis, but a slight volume increase was measured. The corrosion rate after an additional 96 hours exposure was lower than the corrosion rate of samples exposed to electrolysis for 48 hours in the half immersed configuration. Significant corrosion occurred in two of the samples D1 and D2 (11.6% and 8.5% respectively) after exposure to the gas phase, following soaking treatment. The other two samples (D3 and D4) showed corrosion rates similar to the results from the half immersed configuration.

The corrosion rates in Table 6-5 highlight the combined effect of the exposure to cryolitic bath and to corrosive gases released from the reduction cell. The samples that were only exposed to the gas phase did not show any measurable corrosion over the period of the test. This is probably due to formation of a protective layer of $SiO_2$ that was formed as a result of oxidation of SiC and $Si_3N_4$ by $CO_2$. It can be concluded that the low reactivity of $SiO_2$ to corrosive gasses

such as HF and NaAlF$_4$ (as discussed in Chapter 7.1) inhibits the further corrosion of the SNBSC material on this time scale.

Exposure of the oxidized samples to the cryolitic bath caused dissolution and removal of the protective SiO$_2$ layer. Penetration of sodium into the samples enhanced the oxidation to form sodium silicates. The high reactivity of sodium silicate compared to original phases (SiC, Si$_3$N$_4$) and the exposure of the entire samples surface area to the corrosive environment caused extensive degradation.

.

## 6.3. Alteration of SNBSC samples in the gas phase, during electrolysis tests.

Commercial SNBSC bricks contain a $Si_3N_4$ binder with a mixture of both α and β $Si_3N_4$ phases in various ratios, both between different blocks, and within different regions of the same block. However, In order to examine the influence of β $Si_3N_4$ content in the binder phase on reactivity of the samples, samples with wider range of β $Si_3N_4$ content, and especially high content, should be tested.

Selective heat treatment in nitrogen atmosphere of a commercial SNBSC material was undertaken in order to produce samples with very high β $Si_3N_4$ content. Converting α $Si_3N_4$ to the high temperature β phase was carried out by exposing SNBSC material to temperatures above 1600°C in a nitrogen atmosphere, in a controlled atmosphere furnace for 4 to 8 hours.

Transformation of α $Si_3N_4$ to β $Si_3N_4$ and formation of material enriched in β $Si_3N_4$ content on an industrial scale is usually done by hot pressing $Si_3N_4$ to produce dense components. The densification is achieved by pressureless sintering, hot and hot–isostatic pressing by using sintering aids such as magnesia, yttria, or silica, to form a suitable liquid phase, at temperatures between 1600-1800°C [81]. This promotes the rearrangement and growth of the elongated β $Si_3N_4$ crystals. The final product show strong dense polycrystalline $Si_3N_4$ material with β phase crystalline structure and elongated fibre-like grains morphology. It was suggested that the elongated grain structure was responsible for the high strength of $Si_3N_4$ hot-pressed materials produced from α $Si_3N_4$ powder [80].

The α/β $Si_3N_4$ transformation temperature, during sintering with oxide additives, is closely related to the melting point of the additives and is rapidly completed at higher temperatures [21]. In the experiment shown below the transformation was performed without any oxide additives to assist in the formation of a glass phase, as the glass itself may compromise the corrosion resistance of the samples.

### 6.3.1. Thermal treatment of SNBSC samples

SNBSC samples from a commercial grade block were cut to a 50x20x5 mm size. The sample volume and porosity were measured using the ISO 5017 standard method (see Chapter 5.1). The amount of α and β phases of $Si_3N_4$ in the material was measured by XRD using the Gazzara and Messier method [61].

The samples were then placed in a graphite crucible within a controlled atmosphere furnace. The furnace chamber was evacuated, and nitrogen was introduced in a pressure of 1 atmosphere. The furnace temperature was raised to 1700-1800°C and kept under the nitrogen atmosphere for 4 to 8 hours (see Table 6-6).

The volume and porosity of the cooled samples was measured again, and a specimen from each sample was taken in order to measure $\alpha$ and $\beta$ $Si_3N_4$ content. The properties of these samples are shown in Table 6-6.

*Table 6-6: Parameters of nitridation experiments, and properties of the nitrided samples.*

| Experiment # | Sample | Initial $\beta$ $Si_3N_4$ content (%) | Final $\beta$ $Si_3N_4$ content (%) | Max temperature of nitridation (°C) | Holding time at max temperature (Hours) |
|---|---|---|---|---|---|
| 1 | D exterior | $10.7 \pm 1.4$ | $63.6 \pm 1.4$ | 1800 | 8 |
| | D interior | | $82.9 \pm 1.4$ | | |
| 2 | B mid 1 | $19.6 \pm 1.4$ | $68.7 \pm 1.4$ | 1750 | 4 |
| | B mid 2 | | $66.5 \pm 1.4$ | | |
| 3 | B core | $56.2 \pm 1.4$ | $98.6 \pm 1.4$ | 1800 | 8 |
| | G ext 1 | $13.7 \pm 1.4$ | $98.6 \pm 1.4$ | | |
| | G ext 2 | $19.6 \pm 1.4$ | $98.3 \pm 1.4$ | | |

After the heat treatment process, an increase in the porosity was observed for samples taken from bricks B and G while the porosity of sample from brick D was not changed (Table 6-7).

*Table 6-7: Porosity and $\beta$ $Si_3N_4$ fraction in the binder changes in SNBSC samples after the nitridation process.*

| Sample | Initial $\beta$ $Si_3N_4$ content (%) | Final $\beta$ $Si_3N_4$ content (%) | Initial porosity (%) | Final porosity (%) |
|---|---|---|---|---|
| D exterior | $10.7 \pm 1.4$ | $63.6 \pm 1.4$ | $13.8 \pm 0.4$ | $14.9 \pm 0.4$ |
| D interior | | $82.9 \pm 1.4$ | $15.6 \pm 0.4$ | $16.4 \pm 0.6$ |
| B mid 1 | $19.6 \pm 1.4$ | $68.7 \pm 1.4$ | $16.5 \pm 0.2$ | $14.3 \pm 0.2$ |
| B mid 2 | | $66.5 \pm 1.4$ | $16.4 \pm 0.2$ | $18.8 \pm 0.2$ |
| B core 1 | $56.2 \pm 1.4$ | $98.6 \pm 1.4$ | $16.3 \pm 0.2$ | $20.1 \pm 0.2$ |
| B core 2 | $56.2 \pm 1.4$ | $98.6 \pm 1.4$ | $16.7 \pm 0.2$ | $20.6 \pm 0.2$ |
| G ext 1 | $13.7 \pm 1.4$ | $98.6 \pm 1.4$ | $16.4 \pm 0.2$ | $21.0 \pm 0.2$ |
| G ext 2 | $19.6 \pm 1.4$ | $98.3 \pm 1.4$ | $14.5 \pm 0.2$ | $19.1 \pm 0.2$ |

The increased open porosity that was observed after the nitridation process can be related to the conversion from α Si₃N₄ to β Si₃N₄. This phenomenon can be explained by the changing morphology of the crystals, leading to rearrangement of the round α Si₃N₄ closely packed crystals into the elongated β Si₃N₄ crystals. This rearrangement causes interlinking of the micro-pores, hence increasing the open porosity.

### 6.3.2. Morphology changes

When examining the bonding phase of "fresh" samples (before thermal treatment) using SEM analysis, areas with small equiaxed crystals around the SiC grains (as can be seen in Figure 6-56) are observed. Large pores are also evident in the bonding phase with thin long needle-like crystals growing into the cavity of the pores (Figures 6-55, 6-56).
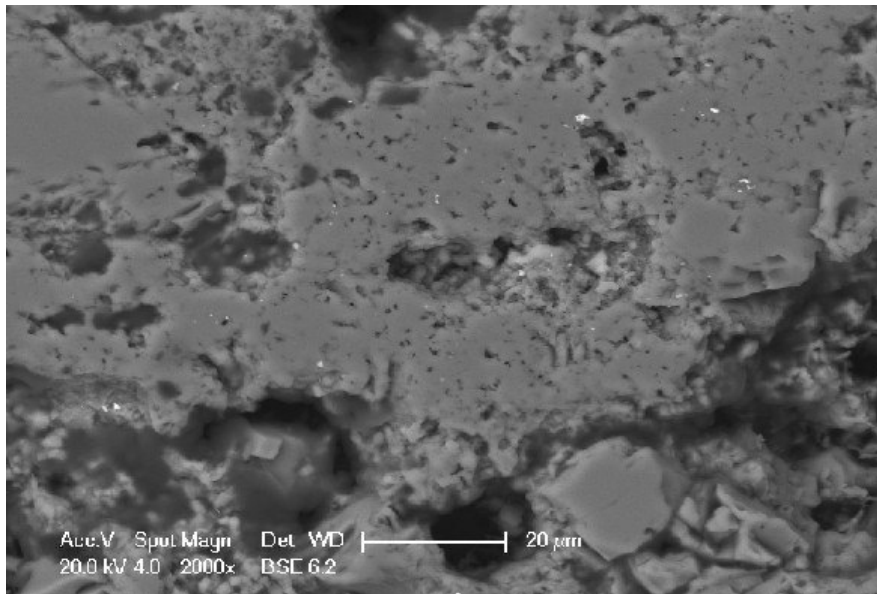


*Figure 6-55: SEM image of Si₃N₄ bonding phase of the fresh sample, characterized by short grain crystals.*
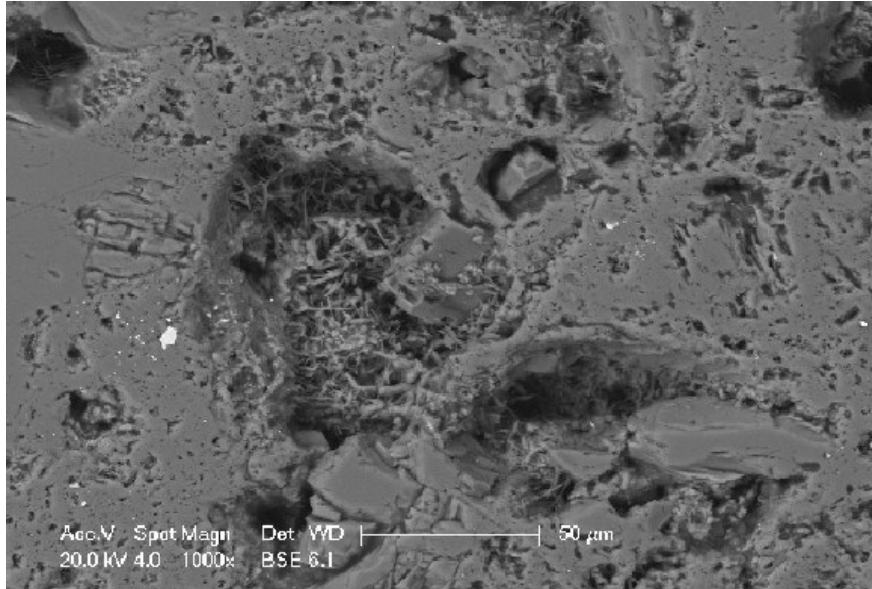
*Figure 6-56: SEM image of Si₃N₄ bonding phase of fresh sample with long needle-like crystals now prominent in the pores.*

Observation of the samples after thermal treatment (Figures 6-57 and 6-58) reveals a denser bonding phase with domination of long thick rod-like crystals. The large pores with the thin needle-like crystals, as seen in Figure 6-56, can not be seen.
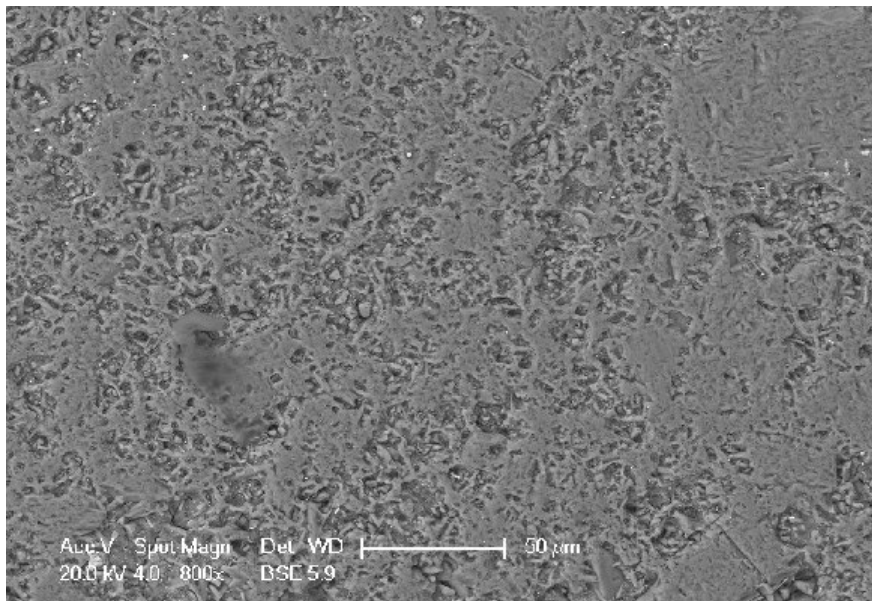


*Figure 6-57: SEM image of a cross section of a SNBSC sample after heat treatment. Long grained crystals of Si₃N₄ are prevailing the bonding phase.*
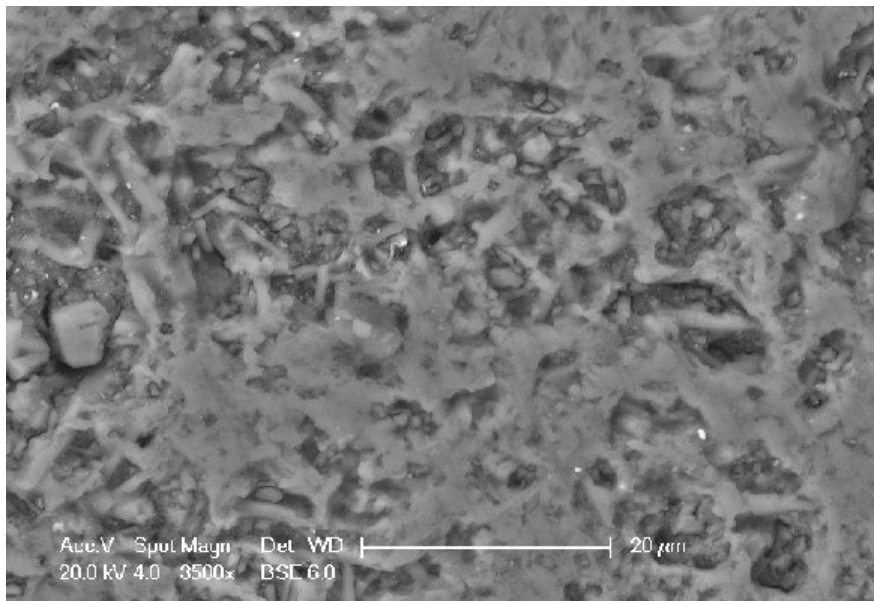
*Figure 6-58: A higher magnification(x3500) SEM image of the Si$_3$N$_4$ bonding phase of SNBSC sample after heat treatment.*

### 6.3.3. Electrolysis corrosion test

The corrosion resistance of the altered samples was examined in a corrosion test. Two altered samples (after heat treatment) and two untreated samples were inserted into a graphite basket, and soaked in molten electrolyte bath at 1000℃ for 48 hours. When cooled, the adhering bath was removed and the volume was measured. The dry pre-soaked samples were inserted again into a graphite basket (Figure 6-59) and tested by an electrolysis corrosion test in a gas phase configuration (see Chapter 5.2.3) for 48 hours.
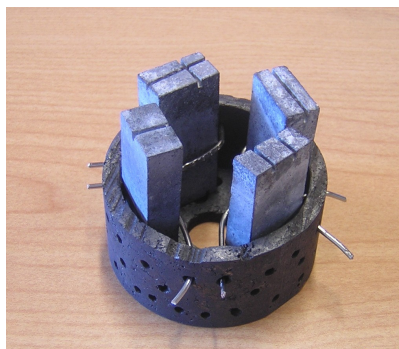


*Figure 6-59: Samples in graphite basket before electrolysis.*

On completion of the test, the samples were cooled and the adhering bath was removed by loosening in an aluminium chloride solution. The sample volume was measured (by the ISO 5017 standard method) and the volume loss was calculated.

The first set of samples (samples D) were tested in the gas-phase basket configuration for 36 hours, without being soaked in the electrolyte, showed very little corrosion. The experiment was repeated for another 96 hours but the cumulative corrosion rate remained small. The samples were then pre-soaked in the electrolyte for 48 hours and then electrolysed for 48 hours in the gas phase and only then showed significant degradation. The cumulative corrosion rate expressed in Figure 6-60 is calculated according to:   Corrosion rate $= -\frac{(Vf - Vi)*100}{Vi}$ (as mentioned in page 127).
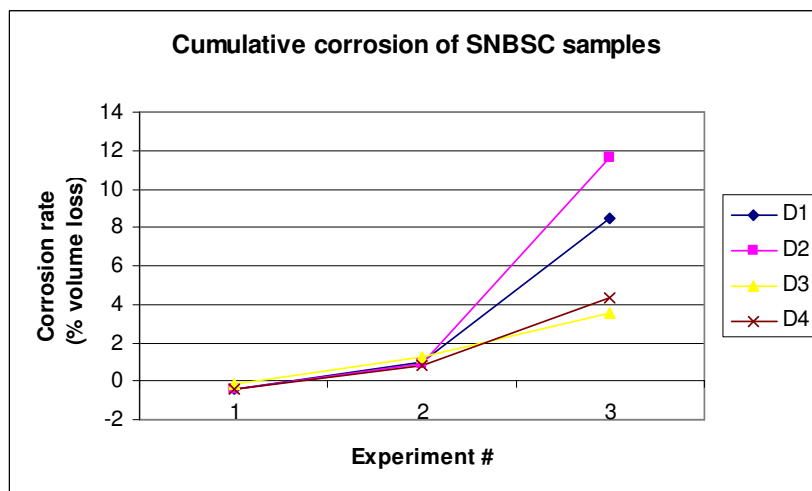


*Figure 6-60: Cumulative corrosion rate of samples D in three repetitive experiments. Samples D1 and D2 are fresh samples and D3 and D4 were altered by nitridation.*

Samples taken from interior area of cross section of brick B were thermally treated at 1800°C (B mid 1 and B mid 3) and were examined in a corrosion test with un-treated samples taken from similar location of brick B (B mid 2 and B mid 4). These samples were pre-soaked in cryolitic bath for 48 hours prior to exposure to the gas phase for 48 hours during electrolysis. The heat treated samples with the higher $\beta$ $Si_3N_4$ fraction in the binder (69% and 66% $\beta$ $Si_3N_4$ compared to 20% of the untreated samples) showed significantly higher corrosion rates compared to the un-treated samples with the lower $\beta$ $Si_3N_4$ content in the binder (Table 6-8 experiment 4).

Another set of samples taken from the interior area of brick B (B core and B mid 5, 6) that were tested under the same conditions showed a low corrosion rate after the first electrolysis test. The corrosion experiment was repeated and the heat treated samples showed higher corrosion rate compared to the un-treated samples.  Un-treated samples from brick A and G were tested with heat treated sample (G ext) in the same corrosion experiment. The altered sample with binder with 100% $\beta$ $Si_3N_4$ did not show a higher corrosion rate compared to un-treated sample taken from similar location in that brick. (Table 6-8 experiment 7). The cumulative corrosion rate in

the electrolysis experiments with the samples porosity and β $Si_3N_4$ content is listed in Table 6-8 and shown in Figure 6-61.
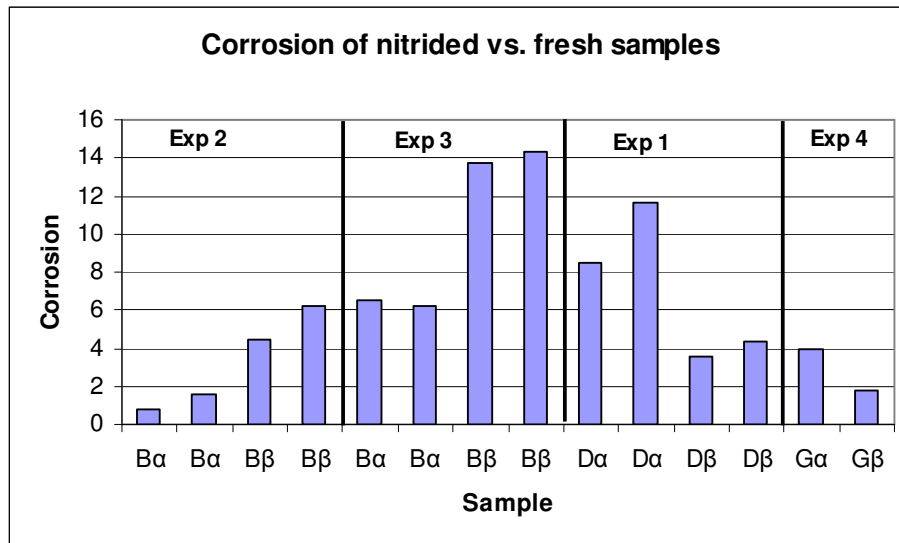


*Figure 6-61: Cumulative corrosion rate of nitrided and normal SNBSC samples: α- samples with high α-$Si_3N_4$ content, β-samples with high β-$Si_3N_4$ content. See Table 6-8 for experiments results.*

*Table 6-8: Cumulative corrosion rate of nitrided and normal SNBSC samples. Samples D corrosion test was repeated three times and samples B mid 5-6 and B core was repeated twice.*

| Experiment # | Samples | Porosity (%) | β Si$_3$N$_4$ content (%) | Cumulative corrosion rate (%) |
|---|---|---|---|---|
| 1-3 | D1 | 13.6 ± 0.4 | 10 | 8.5 |
|  | D2 | 15.6 ± 0.6 | 10 | 11.6 |
|  | D3 | 14.9 ± 0.4 | 63 | 3.5 |
|  | D4 | 16.4 ± 0.6 | 83 | 4.3 |
| 4 | B mid 1 | 14.3 ± 0.2 | 69 | 4.4 |
|  | B mid 2 | 12.4 ± 0.2 | 20 | 0.8 |
|  | B mid 3 | 18.8 ± 0.2 | 66 | 6.3 |
|  | B mid 4 | 11.0 ± 0.3 | 20 | 1.6 |
| 5-6 | B core 1 | 20.1 ±0.2 | 100 | 13.7 |
|  | B core 2 | 20.6 ± 0.2 | 100 | 14.3 |
|  | B mid 5 | 16.8 ± 0.3 | 22 | 6.6 |
|  | B mid 6 | 16.2 ± 0.2 | 22 | 6.3 |
| 7 | A core 1 | 15.8 ± 0.3 | 28 | 0.7 |
|  | A core 2 | 16.1 ± 0.2 | 28 | 0.1 |
|  | G ext1 | 21.0 ± 0.2 | 100 | 1.8 |
|  | G ext 2 | 14.8 ± 0.2 | 14 | 3.9 |

The contribution of high β Si$_3$N$_4$ content, in the bonding phase of the nitrided samples, to the corrosion rate was observed only in samples B, where the high β Si$_3$N$_4$ content was correlated with higher corrosion rate. This trend was observed both for the samples that were taken from the same location in the block (samples B mid 1-4) and the samples taken from a different location in the same block (samples B core and B mid 5-6). The altered samples (post heat treatment) have both higher porosity and higher β Si$_3$N$_4$ content comparing to the untreated samples. These two factors can both contribute to the higher corrosion rate. The lower corrosion rate and higher porosity of sample B mid 2 comparing to B mid 4, indicates that the contribution of the higher porosity to the corrosion rate was less significant than the contribution of the higher β Si$_3$N$_4$ content.

Sample D and G showed the opposite trend to sample B, the untreated samples with low β Si$_3$N$_4$ content, showed a higher corrosion rate. The high porosity and high β Si$_3$N$_4$ content of sample G ext1 did not give a higher corrosion rate when compared to the untreated sample from the same

material (sample G ext 2). Samples A had both higher $\beta$ $Si_3N_4$ content and porosity levels compared to the untreated sample G, but had lower corrosion rate.

In this set of experiments, the hypothesis that high open porosity levels or high $\beta$ $Si_3N_4$ content will contribute to high corrosion rate was only supported in samples taken from material B. High corrosion rate was observed in samples from material B which had higher $\beta$ $Si_3N_4$ content. The other materials tested did not show high corrosion rates associated with either high $\beta$ $Si_3N_4$ content, or even high porosity as seen in sample from material G which had very low $\beta$ $Si_3N_4$ content and showed higher corrosion rate compared to sample from the same material but with 100% $\beta$ $Si_3N_4$ content.

## 6.4. Summary

SNBSC samples from eight different commercial bricks were tested in an industrial aluminium cell environment. The samples were placed between the sidewall and the anode, with the bottom half of the sample immersed in the bath, and the other half exposed to the gas phase above the bath level. The samples showed little corrosion after 48 hours exposure, however after 77 hours exposure extensive attack and differentiation between samples was observed. XRD analysis of the samples, taken from internal and external areas of the bricks, identified high $\beta$ $Si_3N_4$ content in the internal part of the bricks that were most significantly corroded.

In the lab-scale trials the effects of five main factors on the corrosion rate were examined: porosity levels, amount of binder, $\alpha/\beta$ $Si_3N_4$ ratio, free Si content in the binder, and different corrosion environment.

The effect of porosity:
Porosity measurements conducted on segments taken along a SNBSC brick cross section show variation with position. However the nature of this variation is different for particular bricks. Brick A did not show large variations in porosity levels between the exterior and the interior parts of the brick. Bricks B, C, and D showed higher porosity in the interior areas.

Bricks C and D also showed porosity variation in the outer faces. The porosity levels of segments taken from the exterior area of one face of each brick were higher than those taken from segments of the exterior part of the opposite face. The difference in the porosity between the two exterior parts may be due to differential exposure to nitrogen gas flow because of the stacking arrangement of the bricks in the nitridation furnace.

The porosity of the samples used in the corrosion test was measured. Samples taken from the interior area of the brick showed similar porosity to samples taken from the exterior area, although a cross section of these bricks showed higher porosity in the interior area. The samples size taken both from the interior and the exterior area were large enough to include zones with varying porosity levels hence homogenising porosity levels to some degree.

The corrosion rates of the SNBSC samples were measured as a function of their porosity. Samples that were soaked for 48 hours in a cryolitic bath prior to the corrosion test showed some correlation between the corrosion rate and their porosity levels. The calculated coefficient of

171

determination ($R^2$) indicates that only 31% of the variability of the corrosion rate results can be explained by the variations in porosity levels. When these corrosion results were divided into two groups according to the sample dimension particularly thickness, those with the lower thickness (width<16mm) showed higher correlation between the corrosion rate and porosity level with $R^2$ of 0.43 compared to $R^2 = 0.21$ calculated for samples having a width above 16mm. The corrosion results of most of the wider soaked samples show a trend of higher corrosion rate with higher porosity level. The coefficient of determination $R^2$ is shifted from 0.70 to 0.21 with two extreme samples.

The effect of the sample width on the correlation between corrosion rate and porosity is more profound in the corrosion results of the samples that were not pre-soaked in cryolitic bath before the corrosion test. The corrosion rate of the narrow un-soaked samples showed good correlation between the corrosion rate and porosity levels with a calculated $R^2$ of 0.43. The thicker un-soaked sample with sample width above 16mm show no correlation between the corrosion rate and porosity with calculated $R^2 = 0.09$.

The higher correlation between the corrosion rate and porosity levels of the soaked samples compared to the un-soaked samples, observed especially in the thicker samples, indicates that bath penetration, which is enhanced with higher porosity levels, contributes to the corrosion rate.

Samples with a significant difference in porosity levels, both from the same brick and from two different bricks that were tested in the same experiment showed significantly higher corrosion rates for the higher porosity samples.

The effect of binder content
The corrosion rate of SNBSC samples was measured as a function of their SiC content. Despite the scatter in the data, the corrosion results of both the samples pre-soaked in electrolyte and the un-soaked samples showed an optimal SiC content in terms of corrosion resistance. The minimum corrosion rate was observed in samples having 80% to 85% SiC.

When examining the corrosion in terms of samples SiC content the observed trends are attributed to the preferred reactivity and the different particle size of the binder phase compared with the SiC phase. The binder phase is thermodynamically more reactive with both oxidising species and corrosive gases present in the reduction cell environment.  Samples with lower SiC content and

more binder phase will thus be more readily attacked by the corrosive gases. Reducing the binder by increasing SiC content will increase the corrosion resistance of the material until the lack of binder to fill interstices increases corrosion rate, due to the easy detachment of the large SiC particles.

Although the trends are reasonably clear, it is worth considering the scatter observed in these plots which integrate the data from difficult experiments on a range of refractories. It must be remembered that the binder phase is itself complex with both variations in the form of the $Si_3N_4$ (a factor that was also examined in this chapter), and varying amounts of the minor oxy-nitride phases.

The effect of $\alpha/\beta$ $Si_3N_4$ ratio

The influence of $\alpha$ and $\beta$ $Si_3N_4$ phases found in the binder on the corrosion rate was examined in this chapter. These two phases are not evenly distributed in the SNBSC brick, as segments cut along the central cross section of bricks B, C, and H showed variations in $\beta$ $Si_3N_4$ content with an increase of the $\beta$ $Si_3N_4$ content from the exterior part of the brick to the core.

Samples pre-soaked in cryolitic electrolyte (bath), showed a weak correlation between corrosion rate and the $\beta$ $Si_3N_4$ content in the binder phase, with $R^2 = 0.28$. However, the regression low p-value (0.003) indicates that correlation between $\beta$ $Si_3N_4$ content and the corrosion rate is statistically significant.

Un-soaked samples showed low correlation between the corrosion rate and $\beta$ $Si_3N_4$ content. The thinner un-soaked samples (width < 16mm) showed high correlation between corrosion rate and $\beta$ $Si_3N_4$ content with $R^2 = 0.81$ compared to the thicker un-soaked samples that show no correlation with $R^2 = 0.04$. Samples with low thickness but higher depth showed reduction in the corrosion rate compared with the other thinner samples and little correlation between the corrosion rate and $\beta$ $Si_3N_4$ content.

The low correlation between the corrosion rate and $\beta$ $Si_3N_4$ content of the wider samples is related to zones with different $\beta$ $Si_3N_4$ content that were incorporated into each sample. The $\beta$ $Si_3N_4$ content measurement of the wide samples represents an average value of these zones and not the $\beta$ $Si_3N_4$ content of the active surface exposed to the corrosive gases.

The corrosion rate results presented in this chapter show a statistically significant connection between materials with higher $\beta$ $Si_3N_4$ content and higher corrosion rate as indicated by the p-value of the regression. The $\beta$ $Si_3N_4$ content is one factor out of several (also examined in this work) that contribute to high corrosion rates, hence a lower correlation between corrosion rate $\beta$ $Si_3N_4$ content in isolation should be expected.

To further explore the connection between high $\beta$ $Si_3N_4$ content in SNBSC material and corrosion rate, commercial SNBSC samples were heat treated in high temperatures leading to conversion of $\alpha$ $Si_3N_4$ to $\beta$ $Si_3N_4$ in the bonding phase, without the use of additional oxide additives to catalyse the reaction. The conversion rate was governed by the temperature and duration of the heat treatment.

An increased open porosity was observed after the heat treatment process. This phenomenon can be explained by rearrangement of the round $\alpha$ $Si_3N_4$ closely packed crystals into the elongated $\beta$ $Si_3N_4$ crystals which causes interlinking of the micro-pores, hence increasing the open porosity. Although the fresh unaltered sample exhibits bigger pores than the altered samples (comparing Figures 6-57 with Figure 6-58) these pores are not connected, explaining the low open porosity comparing to the altered samples.

Higher corrosion rate was observed in heat treated samples from brick B with high $\beta$ $Si_3N_4$ content in the binder compared with non-treated samples from similar location in that brick. The heat treated samples have both higher porosity and higher $\beta$ $Si_3N_4$ content comparing to the untreated samples, which contributed to the higher corrosion rate. Sample D and G showed the opposite trend to sample B, the untreated samples with low $\beta$ $Si_3N_4$ content in the binder, and low porosity levels showed a higher corrosion rate.

In these set of experiments, the hypothesis that high open porosity levels or high $\beta$ $Si_3N_4$ content will contribute to high corrosion rate was only supported in samples taken from material B. The other materials tested did not show high corrosion rates associated with either high $\beta$ $Si_3N_4$ content, or even high porosity.

The effect of free Si content
Silicon that is not reacted with nitrogen during the fabrication process of SNBSC materials, due to elevated temperature inside the green brick, can melt and form a glass phase that will become

a weak phase in the final SNBSC material. Thermodynamically this phase has a high reactivity and could lead to rapid degradation in the presence of molten bath or corrosive gasses. However the free silicon detected in the examined material was in crystalline form with maximum concentration of 7%, and observed mainly within the core of the SiC grains, rather than in the bonding matrix. The absence of free silicon in the bonding phase rules out the hypothesis that free silicon is the main contributor to the corrosion rate of the SNBSC materials.

Effect of environment

Samples used in the corrosion tests showed accelerated degradation in the area exposed to the gas phase (above the bath level) while the areas immersed in the electrolyte show much lower corrosion. However exposure only to cell gases, even for 96 hours showed little corrosion compared to 48 hours exposure to both bath and gas phase in electrolysis conditions.

On the other hand, high corrosion rates were measured when samples were soaked in bath and then exposed only to the gas phase. Therefore it can be concluded that the combination of bath penetration, and subsequent exposure to the corrosive gases emitted during electrolysis, significantly enhances the corrosion rate.

# Chapter 7: Mechanisms of degradation of SNBSC refractories

## 7.1. Reactivity of sidewall materials to reduction cell atmosphere

The experimental tests discussed in Chapter 6 examine the effects of various parameters on the corrosion rate of SNBSC materials. The corrosion test results identified several parameters as contributors to the corrosion of these materials. Thermodynamic analyses that assess the reactivity of SiC and $Si_3N_4$ towards various components in the environment of the aluminium reduction cell can explain the preferred reactivity observed in the corrosion results and provide further understanding of the corrosion mechanism. The thermodynamic calculations, shown in this chapter, were conducted using the HSC Chemistry 6 software package [82]. Such calculations give a guide to the reactions which are possible in this environment and are helpful in identifying the components which have higher reactivity to the cell environment.

The operating temperature of the reduction cell lining varies with location, and with bath temperature, which is usually kept between 940-960°C. However this can rise to above 1000°C particularly during cases of anode effect. The average temperature gradient between the bath and the top of the alumina cover is 400-500°C [4] as can be seen in an isothermal contour of the reduction cell components (Figure 7-1) [83] . The temperature of the hot face of the sidewall can vary from 1000°C in the part that is exposed to the bath, to ~320°C in the upper part of the sidewall near the alumina cover.
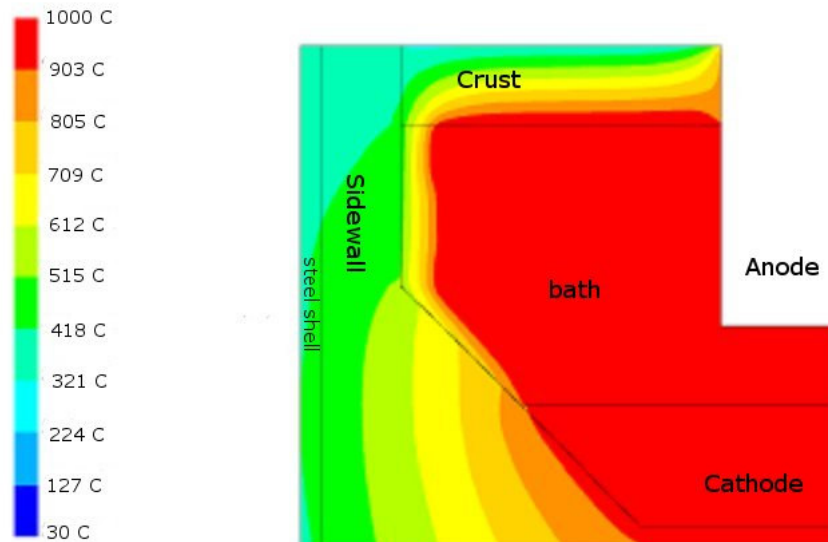


*Figure 7-1: Isothermal contours in conventional reduction cell with passive cooling [83].*

The Gibbs free energy ($\Delta$G) was used as a measure of reactivity of the different components since it is a measure of the thermodynamic stability of compounds in a given reaction; higher negative values for the Gibbs free energy indicating a higher thermodynamic tendency for a reaction to take place spontaneously. The $\Delta$G of the reaction was plotted as a function of temperature in order to assess the reactivity of $Si_3N_4$ and SiC towards the different gases and compounds that could potentially react with them in this environment.

**In the gas phase -** Above the bath level in the reduction cell, the SNBSC bricks are exposed to attack both by corrosive gases such as HF and $NaAlF_4$, and oxidising agents such as $O_2$, $CO_2$, and CO (see Figure 3-12 and 3-15 in section 3.3). The reactivity of SiC and $Si_3N_4$ was thus compared in different gaseous environments, over the temperature range of 350°C to 1000°C.

The gas phase is predominantly saturated with $CO_2$, CO and air. The $CO_2$ and CO are produced at the carbon anode surface during the reduction of alumina to aluminium in the electrolytic process (see Equation 1-1). These gases can react with $Si_3N_4$ and SiC in the SNBSC refractory sidewall according to reactions 7-1 to 7-4:

| | |
|---|---|
| *Equation 7-1* | $Si_3N_4 + 3CO_2\,(g) = 3SiO_2 + 2N_2\,(g) + 3C$ |
| *Equation 7-2* | $SiC + CO_2\,(g) = SiO_2 + 2C$ |
| *Equation 7-3* | $Si_3N_4 + 6CO\,(g) = 3SiO_2 + 2N_2\,(g) + 6C$ |
| *Equation 7-4* | $SiC + 2CO\,(g) = SiO_2 + 3C$ |

The reactivity of SiC and $Si_3N_4$ (expressed as the $\Delta$G of the reaction) with $CO_2$ in the temperature range 350-1000°C was plotted according to Equations 7-1 and 7-2 (Figure 7-2). The corresponding data for reactions 7-3 and 7-4 is plotted in Figure 7-3.

**CO$_2$ environment**

**$\Delta$G (kJ)** vs **Temperature ($^\circ$C)**

Legend: Si3N4, SiC
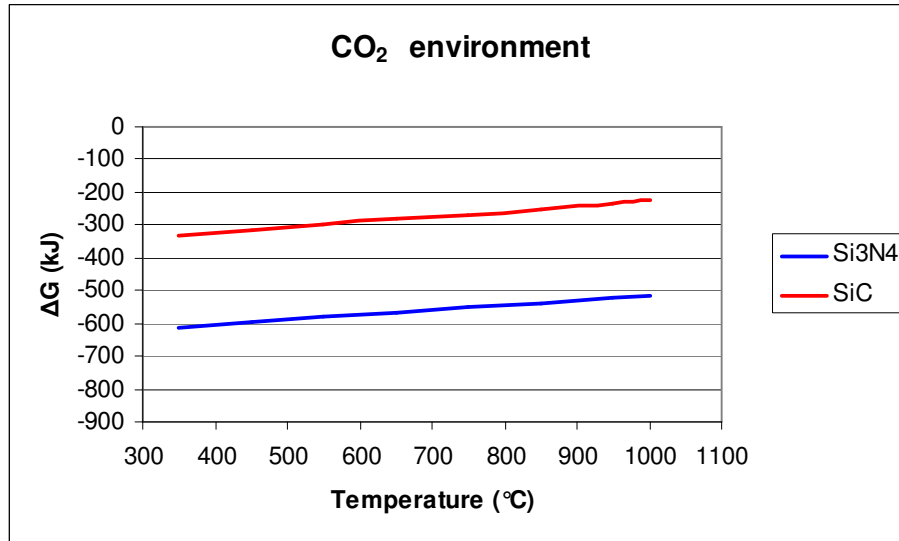
*Figure 7-2: The reactivity of Si$_3$N$_4$ and SiC with CO$_2$ in the temperature range of 350-1000°C.*

**CO environment**

**$\Delta$G (kJ)** vs **Temperature ($^\circ$C)**

Legend: Si3N4, SiC
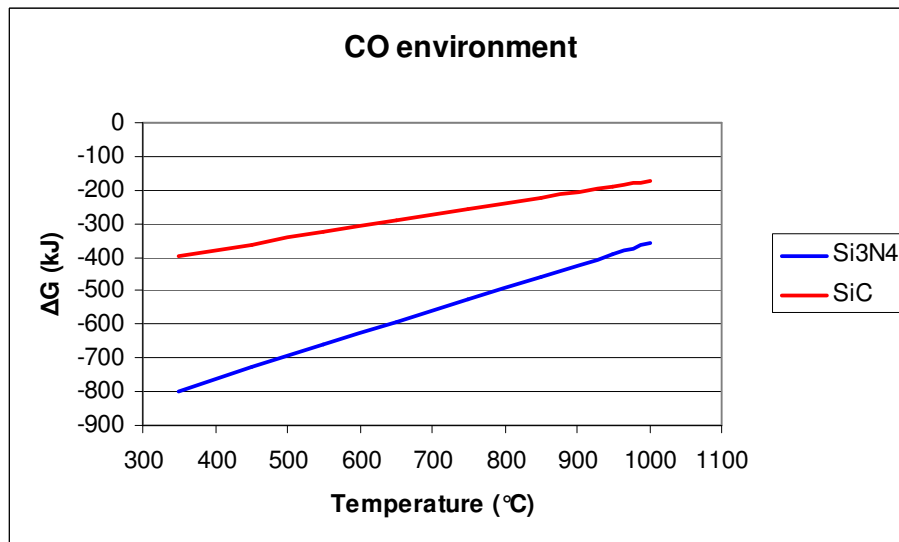
*Figure 7-3: The reactivity of Si$_3$N$_4$ and SiC with CO in the temperature range of 350-1000°C.*

From Figure 7-2 and 7-3 it is clear that the reactivity of Si$_3$N$_4$ is higher than that of SiC with CO$_2$ and CO; and the reactivity difference increases in the cooler parts of the sidewall.

Although under the hard crust cover of the operating cell oxygen is less abundant in the atmosphere than CO$_2$, it is a strong oxidant that can penetrate into the gas phase above the bath line when the crust is broken or removed. O$_2$ will react with Si$_3$N$_4$ and SiC according to reactions 7-5 and 7-6 to produce SiO$_2$. The data for these reactions is plotted in Figure 7-4.

*Equation 7-5*        $Si_3N_4 + 3O_2(g) = 3SiO_2 + 2N_2(g)$

*Equation 7-6*        $SiC + 2O_2(g) = SiO_2 + CO_2(g)$

178
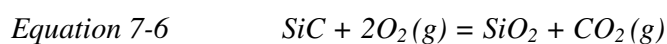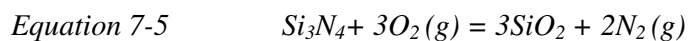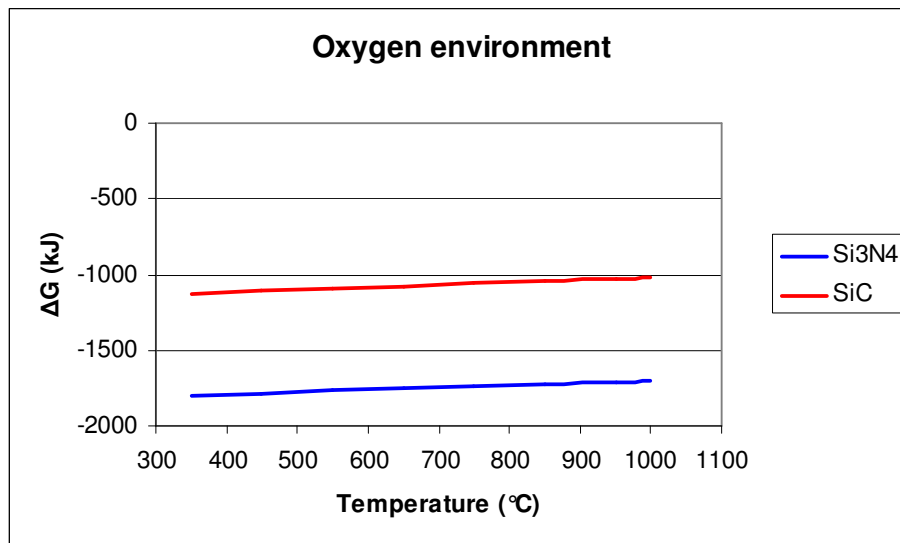
*Figure 7-4: The reactivity of $Si_3N_4$ and SiC with oxygen according to reactions 7-5 and 7-6.*

Both reactions are strongly thermodynamically favoured; however $Si_3N_4$ is more reactive to oxygen than SiC.

In the operating cell, the moisture in the alumina feed reacts with the bath compounds to produce gaseous HF [43]. This corrosive gas attacks the sidewall and reacts with $Si_3N_4$ and SiC according to reactions 7-7 and 7-8. The $\Delta G$ of these reactions is plotted in Figure 7-5.

*Equation 7-7*  $Si_3N_4 + 12HF\,(g) = 3SiF_4\,(g) + 4NH_3\,(g)$

*Equation 7-8*  $SiC + 4HF\,(g) = CH_4\,(g) + SiF_4\,(g)$
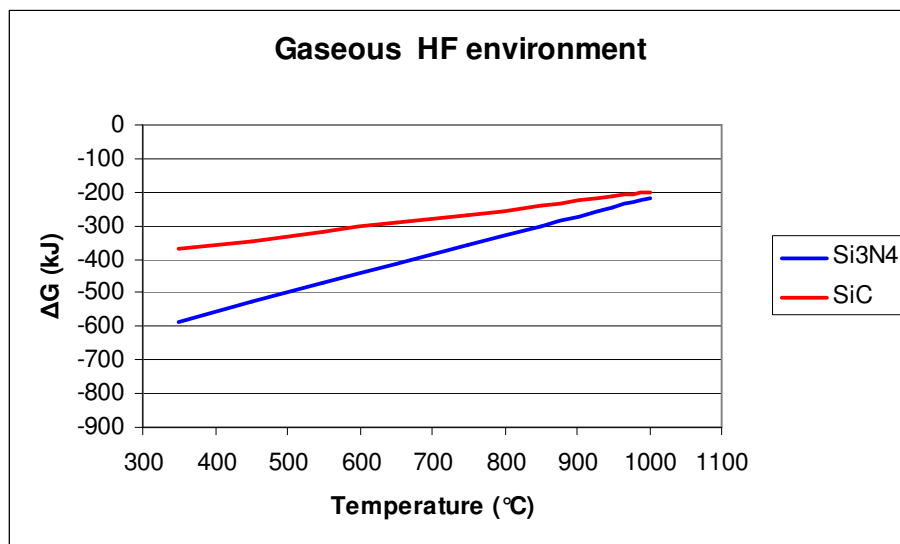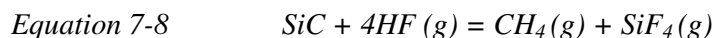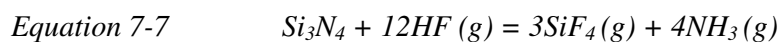


*Figure 7-5: The reactivity of $Si_3N_4$ and SiC with HF in the temperature range of 350-1000°C.*

The reactivity difference between $Si_3N_4$ and SiC with HF is relatively small in the high temperature zone near the bath level but in the upper part of the sidewall in the gas phase where temperatures are in the range of 350-500°C, the $Si_3N_4$ bonding phase is more reactive and can be attacked by HF more severely than the SiC particles. The calculation shown here is for dry HF gas, the corrosive effect of HF could be more severe in the presence of water vapour. In dry gaseous HF the hydrogen and fluoride atom are strongly bonded in a covalent bond however in the presence of water vapour and especially under the dew point, HF will react as a strong acid.

$NaAlF_4$ is another corrosive gas emitted from the bath during electrolysis [12, 24, 41]. The combination of $NaAlF_4$ and $CO_2$ gases emitted from the anode was emphasised by Skybakmoen in earlier work [24] as the main agents in the corrosion mechanism in the gas phase for these materials. This combination of gases will react with $Si_3N_4$ and SiC according to reactions 7-9 and 7-10.

*Equation 7-9*     $Si_3N_4 + 1.5NaAlF_4 (g) + 3CO_2 (g) = 1.5SiF_4 (g) + 1.5NaAlSiO_4 + 3C + 2N_2 (g)$

*Equation 7-10*       $2SiC + NaAlF_4 (g) + 2CO_2 (g) = SiF_4 (g) + NaAlSiO_4 + 4C$
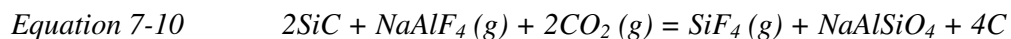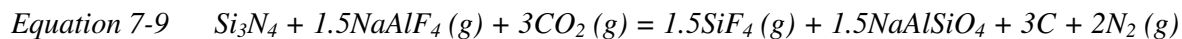
The reactivity of these gases as shown in Figure 7-6 indicating that SiC has slightly higher reactivity than $Si_3N_4$ in the lower temperature range, but at higher temperatures $Si_3N_4$ has a higher tendency to react with this gas combination.
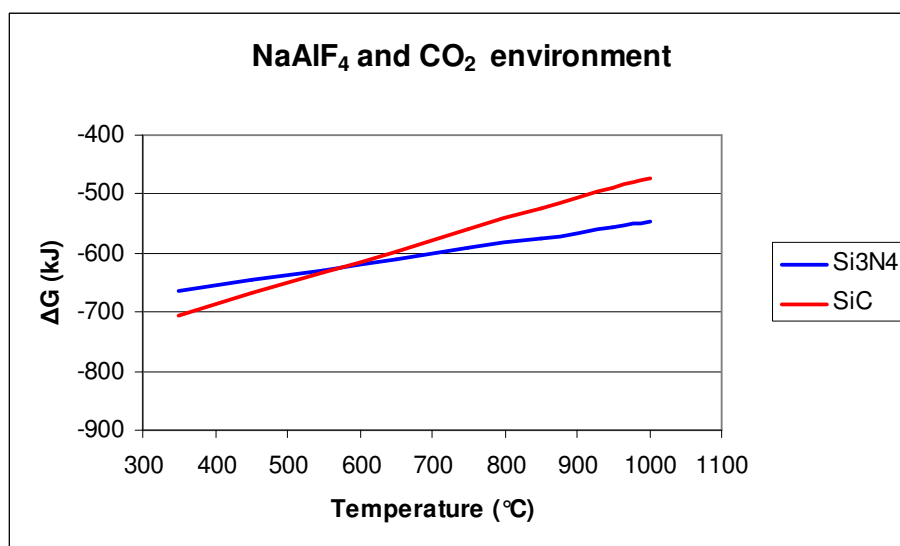


*Figure 7-6: The reactivity of $Si_3N_4$ and SiC with $NaAlF_4$ and $CO_2$ in the temperature range of 350-1000°C.*

The reactivity of $Si_3N_4$ towards the various gases found in the reduction cell environment was plotted over the temperature range of 350 to1000°C (Figure 7-7). The reactivity of $Si_3N_4$ with $O_2$ was not included in Figure 7-7 due to the higher magnitude of the ΔG (1800-1700 kJ) of this reaction. Figure 7-7 shows that the reactivity of $Si_3N_4$ with these gasses is declining with temperature and this is especially evident with CO. The thermodynamic drive for reaction of CO with $Si_3N_4$ increases (by more than 400 kJ/mol) as the temperature drops from 1000°C to 350°C.

According to Figure 7-7 and Figure 7-3, the reactivity of $Si_3N_4$ towards the different gases found in the aluminium reduction cell environment, in terms of the thermodynamic feasibility, could be ranked in two orders according to the temperature range. In the upper part of the sidewall near the crust in a temperature range of 350-500°C the reactivity ranks as follows: $O_2$>> CO >$NaAlF_4$ +$CO_2$> $CO_2$ > HF. Near the bath level where the temperature could reach 1000°C the ranking is: $O_2$>> $NaAlF_4$ +$CO_2$> $CO_2$ >CO > HF.
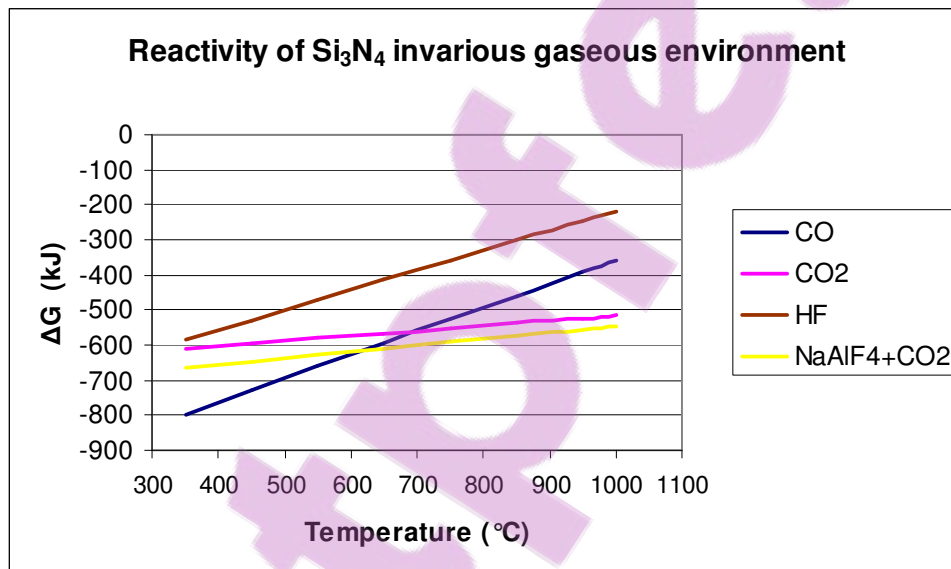


*Figure 7-7: Reactivity of $Si_3N_4$ towards different gases present in the reduction cell atmosphere at the temperature range of 350-1000°C.*

The high reactivity of $O_2$ with $Si_3N_4$ and SiC and the constant exposure of the sidewall materials to $CO_2$ and CO above the bath level will readily form a $SiO_2$ layer that will inhibit further oxidation due to the low oxygen diffusion rate. This oxide layer formation is indicated by a fast drop of thermal conductivity of the SNBSC material as observed by Jorge et al [39]. Corrosion of the sidewall due to exposure to gaseous HF and $NaAlF_4$ will be reduced in the presence of the oxide layer. The ΔG value of the reactions of $SiO_2$ with HF and $NaAlF_4$ (reactions 7-11 and 7-

12) is positive in the higher temperature range (above 850°C) and therefore reactions 7-11 and 7-12 will not occur spontaneously. However, dry HF shows negative ΔG value at temperatures below 850°C (as shown in Figure 7-8) hence it will tend to react with $SiO_2$ in the colder parts of the sidewall.

*Equation 7-11*        $SiO_2 + 4HF\,(g) = SiF_4\,(g) + 2H_2O\,(g)$

*Equation 7-12*        $SiO_2 + NaAlF_4\,(g) = SiF_4\,(g) + NaAlO_2$
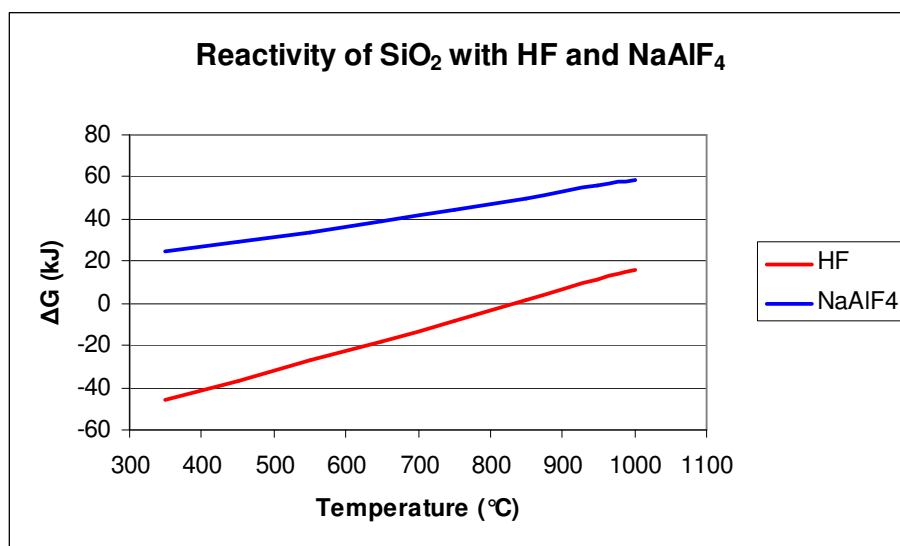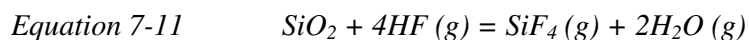


*Figure 7-8: Reactivity of $SiO_2$ with HF (red curve) and $NaAlF_4$ (blue curve) according to reactions 7-11 and 7-12. Spontaneous reaction could occur with HF in temperature below 850°C.*

The presence of water vapour will enhance the corrosive attack of HF on the oxide protecting layer. The water vapour will bond to the polar surface of the oxide layer creating an interfacial aqueous environment that will capture the gaseous HF, forming a strongly acidic environment that will attack the silicon oxide layer. Figure 7-9 shows the enhanced reactivity of HF in the aqueous environment.  Silicon oxide will react with HF in this environment, but it is still less reactive than silicon nitride.
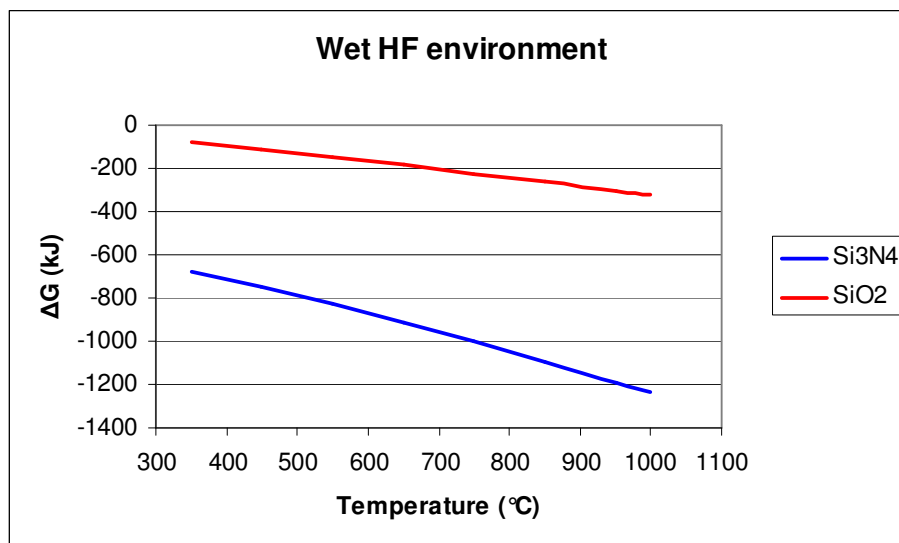
*Figure 7-9: Reactivity of $Si_3N_4$ and $SiO_2$ in aqueous HF environment.*

**In the bath zone,** the temperature range for reactions could reach up to 1000°C in the case of anode effect. The reaction of $Si_3N_4$ and SiC with cryolite has a positive $\Delta G$ (~ +500kJ) in the temperature range of the cryolitic bath and therefore these reactions will not occur spontaneously. However in the presence of $CO_2$ bubbles, produced at the anode bottom surface, the reaction with the sidewall can take place according to reactions 7-13 and 7-14:

*Equation 7-13*    $Si_3N_4 + 1.5Na_3AlF_6 + 3CO_2\,(g) = 3NaF + 1.5SiF_4\,(g) + 1.5NaAlSiO_4 + 2N_2\,(g) + 3C$

*Equation 7-14*    $2SiC + Na_3AlF_6 + 2CO_2\,(g) = 2NaF + SiF_4\,(g) + NaAlSiO_4 + 4C$
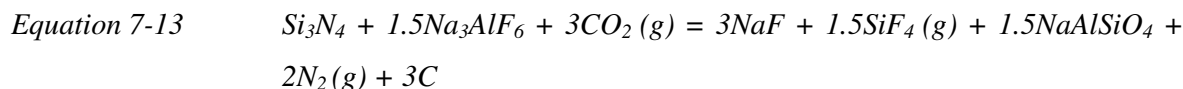
In such an environment, the $\Delta G$ of the reaction 7-13 becomes more negative with rising temperature making this reaction more feasible. The reaction with SiC however, shows the opposite trend- the $\Delta G$ value of reaction 7-14 is becoming less negative as seen in Figure 7-10. The difference in the $\Delta G$ value between SiC and $Si_3N_4$ for these reactions is relatively small.
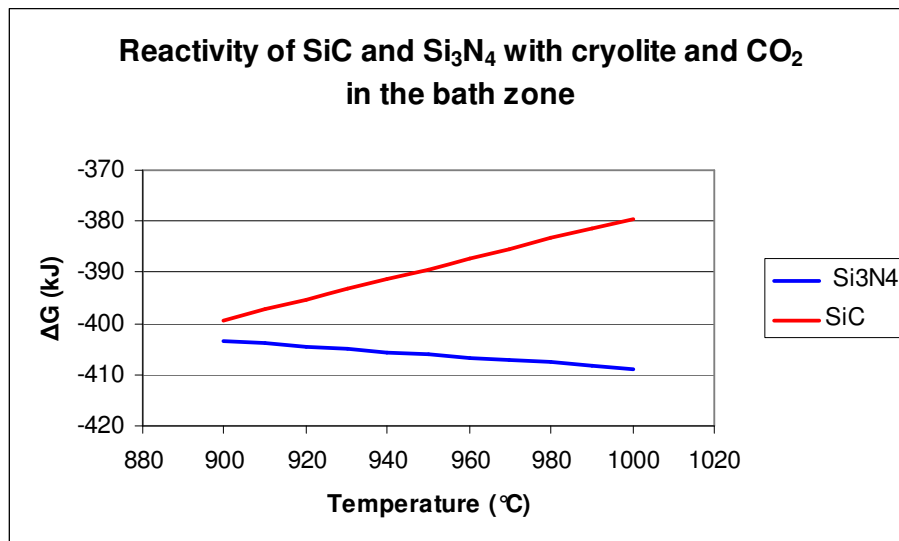
*Figure 7-10: The reactivity of $Si_3N_4$ and SiC with cryolite and $CO_2$ in the bath zone. The reactivity of $Si_3N_4$ is increasing with increasing temperature while the opposite trend occurs in the SiC phase.*

Exposure of the sidewall to the cryolitic bath leads to penetration of bath and particularly sodium ions into the SNBSC refractory. Penetrated sodium salts can be found above the bath level due to capillary transport in the refractory pore system. Sodium enhances the oxidation of $Si_3N_4$ by oxygen to form sodium silicate according to reaction 7-15:

*Equation 7-15*      *$1.25Si_3N_4 + 7NaF + 10O_2(g) = Na_2O*2SiO_2 + 5NaNO_3(g) + 1.75SiF_4(g)$*
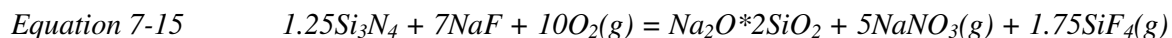
When the vitreous $SiO_2$ is replaced with a sodium silicate layer the oxygen diffusion becomes relatively fast especially in the upper temperature range where the silicate glass layer will be molten (melting point of sodium silicate is 874°C compared to 1723°C of silicon oxide). Further oxidation of the $Si_3N_4$ bonding phase in the presence of silicate liquid could occur up to $10^6$ times faster than oxidation in presence of $SiO_2$ layer [84]. The effect of sodium ion penetration on the chemical stability of the sidewall was demonstrated by Skybakmoen et al [35] where corrosion increases with cryolite ratio (increased sodium content in the bath-see section1.1) The $SiO_2$ oxidation product form on the silicate/ $Si_3N_4$ interface will dissolve in the sodium silicate liquid according to reaction 7-16:

*Equation 7-16*      *$SiO_2 +Na_2O*xSiO_2 = Na_2O*(x+1)SiO_2$*

The sluggish oxidation process of $Si_3N_4$ in pure oxygen or air is due of the presence of $SiO_2$ and $Si_2N_2O$ which serve as diffusion barriers for oxygen (see section 1.2.2.2). In the presence of

sodium ions and absence of an oxide layer between the sodium silicate and $Si_3N_4$ bonding phase the oxidation will occur at a faster rate [84] (Figure 7-11).
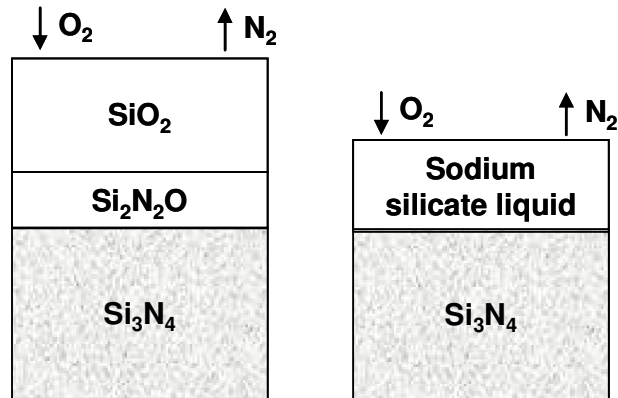


*Figure 7-11: Schematic oxidation of $Si_3N_4$ in oxygen or air (left) the $SiO_2$ and $Si_2N_2O$ serving as diffusion barrier for oxygen. On the right, formation of sodium silicate layer with enhanced oxygen diffusion [84].*

An oxidation study of $Si_3N_4$ in the presence of an alkali containing atmosphere (from $NaNO_3$) by Sun et al [84] showed that the oxidation rate of $Si_3N_4$ in alkali-containing atmosphere was approximately $10^2$ to $10^4$ times faster that oxidation of $Si_3N_4$ in pure oxygen (depending on the type of $Si_3N_4$ material) and the parabolic reaction characteristics commonly associated with pure oxidation of $Si_3N_4$ were not observed (Figure 7-12).
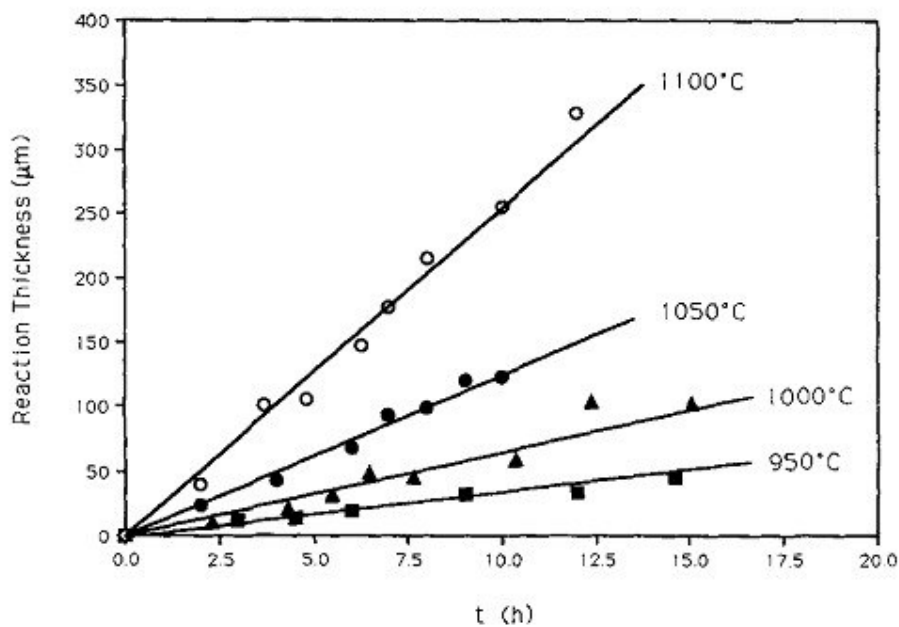


*Figure 7-12: Oxidation of $Si_3N_4$ in dry air containing 0.98vol% naNO3 vapours. The oxidation rate was measured by thickness of the $Si_3N_4$ samples [84].*

An oxidation study by Mayer and Riley [85] compared the oxidation rate of normal $Si_3N_4$ material with sodium silicate coated $Si_3N_4$ in wet air (the samples were coated with sodium carbonate that reacted with the samples to form sodium silicate). They observed accelerated oxidation in the presence of sodium silicate where the silicate glass composition was changing due to formation and dissolution of silica at the nitride-silicate interface. The reaction rate constant was sensitive to the absolute amount of alkali present. Termination of the fast stage of oxidation occurred when a certain value of $SiO_2$: $Na_2O$ is reached, and the value of this ratio was varying with temperature. The value of the parabolic rate constant depends on the amount of sodium oxide added as shown in Figures 7-13 and 7-14.
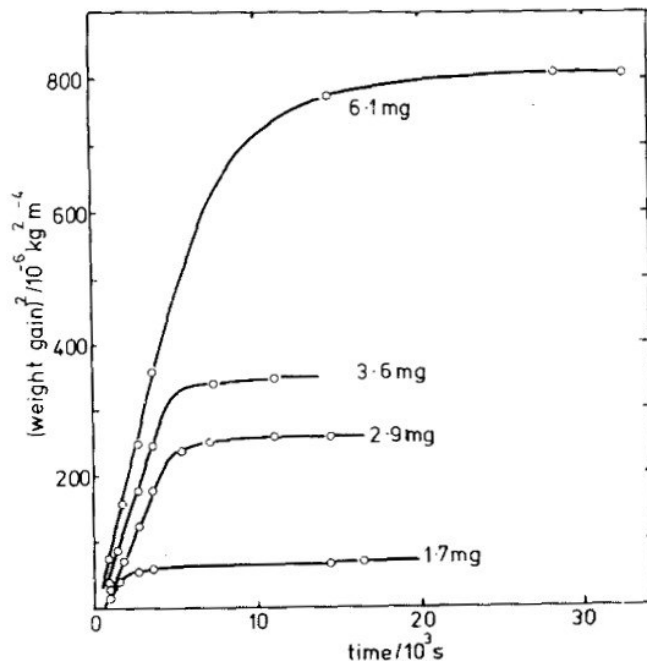


*Figure 7-13: Weight gain due to oxidation of sodium carbonate coated $Si_3N_4$ in wet air at 1300°C. Equivalent sodium oxide weights are shown as mg per bar [85].*
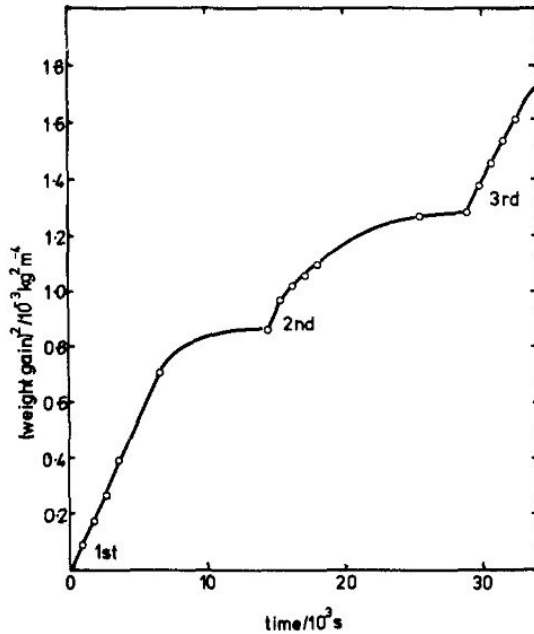
*Figure 7-14: Weight gain due to oxidation of $Si_3N_4$ in wet air. The $Si_3N_4$ sample was coated repeatedly with 5.9mg of sodium oxide [85].*

The oxidation products of the sidewall material (silicon oxide and sodium silicate) enhance the wettability of the sidewall to the bath [39] and are less resistant to cryolite and readily dissolve in cryolite. Hence, the accelerated oxidation of the sidewall due to presence of sodium salts will result in increased degradation of the sidewall in the bath zone, especially in absence of protective frozen ledge during anode effect.

The increased oxidation will also affect the degradation of the sidewall above bath level. Increased levels of oxidation products in the sidewall reduces the thermal conductivity of the sidewall and leads to high hot face temperatures and a less stable frozen ledge [39]. Thus the sidewall material is more often directly exposed to molten and gaseous bath components. Substitution of the silicon dioxide with sodium silicate will increase the reactivity of the sidewall to corrosive gases attack. Equation 7-17 and 7-18 show that both sodium silicate and silicon oxide can react with gaseous HF on the wet surface of the oxide to produce volatile products (Figure 7-15).

*Equation 7-17*      $Na_2O*2SiO_2 + 8HF\ (aq) = 2SiF_4(g) + 2NaOH + 3H_2O\ (g)$

*Equation 7-18*      $SiO_2 + 4HF\ (aq) = SiF_4\ (g) + 2H_2O\ (g)$
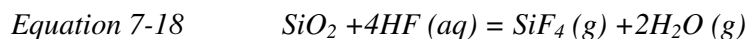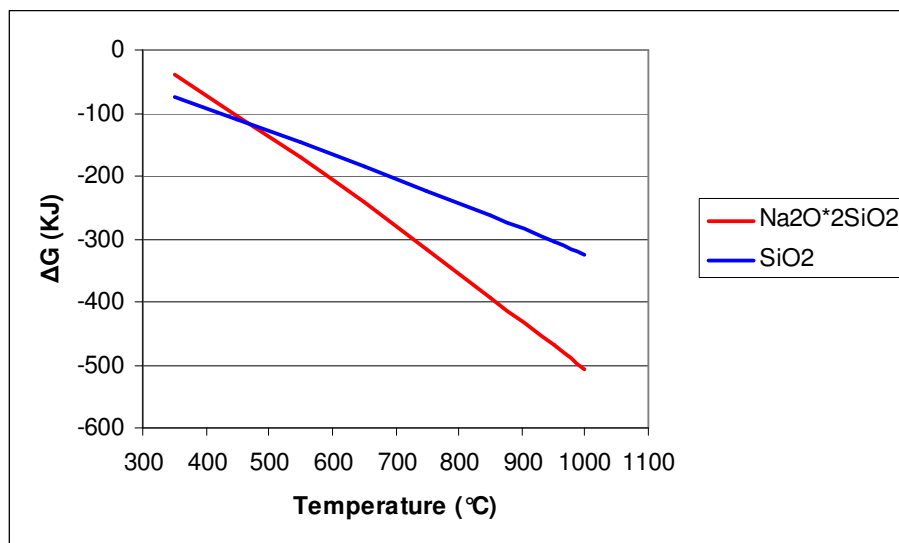
*Figure 7-15: Reactivity of silicon oxide and sodium silicate in wet gaseous HF atmosphere. In the upper temperature range the sodium silicate oxidation layer is more reactive than $SiO_2$.*

Reduction cell autopsies, reported by Andersen et al [33], identify the presence of mainly the original sidewall materials (SiC and $Si_3N_4$) and a weak presence of silicate ($SiO_2$) and fluoride bearing phases, in samples taken from bricks above bath level. The crumbly appearance of the brick in this location indicates formation of a volatile $SiF_4$ product, due to attack of HF and moisture. The absence of Al in the phases of the bricks located above bath level contradicts the assumption that the volatile $NaAlF_4$ plays a role in the degradation of the sidewall above bath level [24].

## 7.2. Hypothesis – α vs. β Si₃N₄ and the influence of morphology on corrosion rate

A correlation between high corrosion rate and high $\beta$ $Si_3N_4$ content was observed in pre-soaked and in narrow, un-soaked SNBSC samples. It is known that the morphology of $\beta$-$Si_3N_4$ differs in having crystals with higher aspect ratio between length to volume compared to $\alpha$ $Si_3N_4$ crystals, [76, 86] and thus it is possible that this morphology difference could contribute to the high corrosion rate.

The dominant morphologies observed in the bonding phase of the SNBSC materials are flat matte crystals associated with $\alpha$ $Si_3N_4$ (Figure 4-30, Chapter 4.6.1) and elongated rod-like $\beta$ $Si_3N_4$ crystals with hexagonal cross section (Figure 4-31, Chapter 4.6.1). Another minor phase, observed only in pores and cavities, is $\alpha$ $Si_3N_4$ phase with needle –like crystals morphology (Figure 4-30 Chapter 4.6.1).

To test the $\beta$ $Si_3N_4$ hypothesis, SNBSC samples were thus heat treated in a nitrogen atmosphere at temperatures above 1700°C to increase their $\beta$ $Si_3N_4$ content (as described in Section 6.3), and subsequently subjected to corrosion testing. XRD analysis confirmed an increase from 10% to 100% $\beta$ $Si_3N_4$ content in the heat treated samples.

SEM analysis of the bonding phase before heat treatment showed short flat crystals as the main bonding phase morphology. An additional minor crystal morphology composed of thin needle-like crystals is found only in large pores (Figure 7-16).
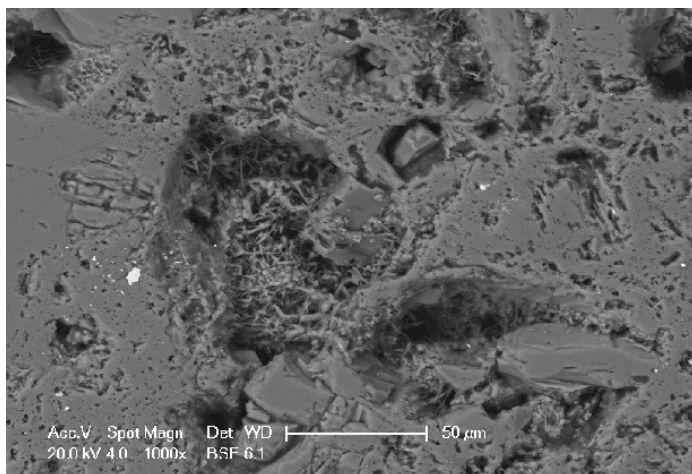


*Figure 7-16: SEM image of bonding phase of SNBSC sample before heat treatment. Large pores filled with needle-like α Si₃N₄ crystals and short flat crystals were observed in the bonding phase.*

The domination of the elongated rod-like crystal morphology was observed in the bonding phase of samples after heat treatment. The large pores with the thin needle-like crystals were absent, and the flat matte crystals could not be seen (Figure 7-17).
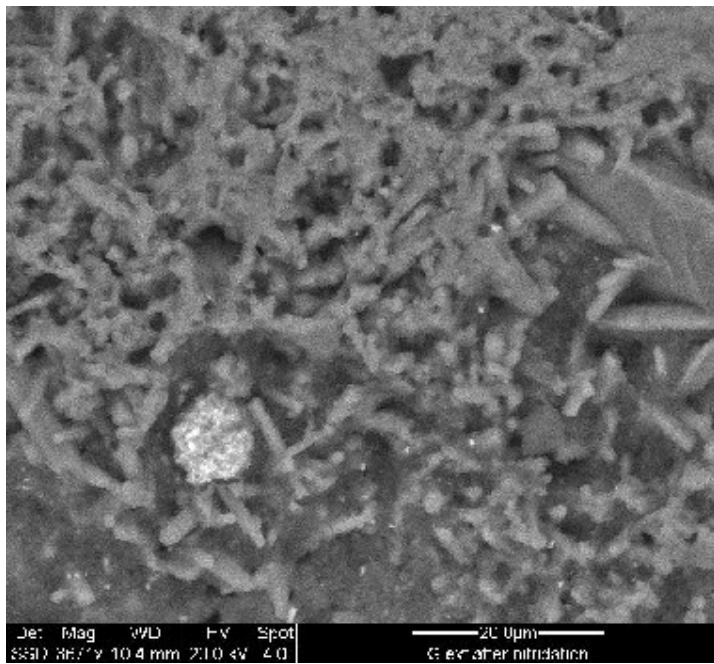


*Figure 7-17: SEM image of bonding phase of SNBSC sample after heat treatment with domination of elongated spike-shape β Si₃N₄ crystals.*

The BET surface area of the SNBSC sample was compared before and after heat treatment. The surface area of the fresh sample (containing 10% $\beta$ $Si_3N_4$) was 0.24m$^2$/g. The heat treated sample (containing 100% $\beta$ $Si_3N_4$) showed an increase to 0.43m$^2$/g. The conversion to 100% $\beta$ $Si_3N_4$ content thus results in a very significant increase in the internal surface area of the SNBSC material.

The open porosity of the sample increased from 14.5% for the fresh sample, to 19.1% for the heat treated sample. However SEM observation indicates the large pores in the bonding phase of the un-treated material were absent in the treated material. This suggests the interlinking of the micro-pores, hence increasing the open porosity. Nitrogen adsorption analysis confirms reduction in the average pore radius from 8.3nm for the fresh sample, to 4.7nm for the heat treated sample. These results are supported by porosity measurements along the cross sections of SNBSC bricks, showing higher porosity and $\beta$ $Si_3N_4$ content in the interior area compared to the exterior area (see Chapters 6.2.1 and 6.2.3).

The reduced pore radius and the increased surface area measured in samples that were thermally treated and thus contained high $\beta$ $Si_3N_4$ levels, indicates that the shape and arrangement of the $\beta$ $Si_3N_4$ crystals provide improved access for gas penetration through the small pores. Furthermore the elongated spike-shape crystals mean that a higher surface area of the crystals in the binder phase is exposed to gas attack. This is correlated with the a higher corrosion rate in corrosion of these materials (Chapter 6.2.3), although whether it is the increased internal surface area alone which causes this, or other effects induced by the phase transformation, is not clear.

## 7.3. Discussion of the laboratory scale results

The corrosion rate of SNBSC material sourced from various commercial refractory manufacturers was examined. The contribution to corrosion rate of porosity levels, $\beta$ $Si_3N_4$ content, and the amount of binder phase have been examined in laboratory trials which attempted to isolate the impact of each of these parameters. Porosity levels and $\beta$ $Si_3N_4$ content showed variation along the cross section of the bricks. In general, high porosity and high $\beta$ $Si_3N_4$ content were observed in the interior areas of the brick.

There are significant practical difficulties in preparing these samples, as the matrix is very hard and brittle. This makes it challenging for example to prepare samples uniquely associated with the exterior and core regions of the brick cross-section. In this respect, the strength of correlation between corrosion rate and porosity was influenced by sample dimension. Thinner samples showed a higher correlation between corrosion rate and porosity. The reduced correlation observed in thicker samples was attributed to incorporation of zones with differing porosity within the samples examined. The measured values of porosity in these larger samples was an average of the porosity zones within in each sample, and thus do not accurately represent the porosity of the surface exposed to the corrosive environment. The correlation between corrosion rate and $\beta$ $Si_3N_4$ content suffered from a similar problem.

Although the corrosion rate shows a similar and increasing trend with regard to porosity and $\beta$ $Si_3N_4$ content, no correlation was observed between porosity levels and $\beta$ $Si_3N_4$ content in the pre-soaked samples (Figure 7-18) and only a weak correlation was observed for the un-soaked samples (Figure 7-19).
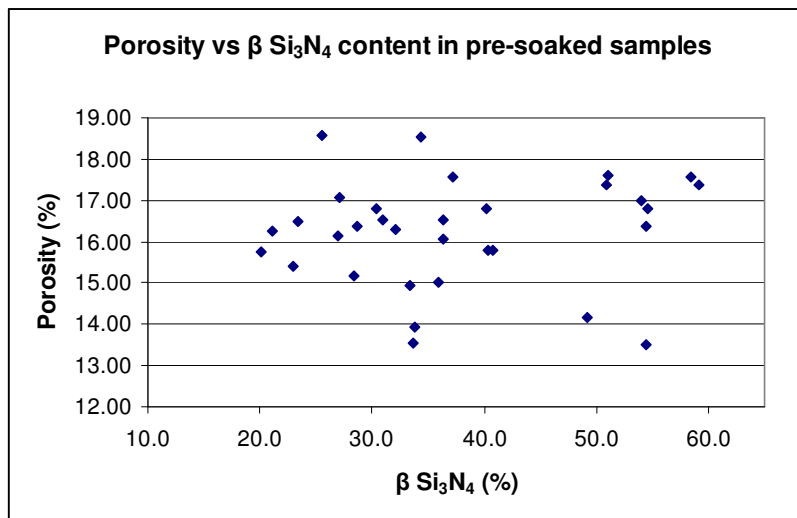
*Figure 7-18: Porosity levels as a function of β Si$_3$N$_4$ content in pre-soaked samples. No statistically significant correlation is observed.*
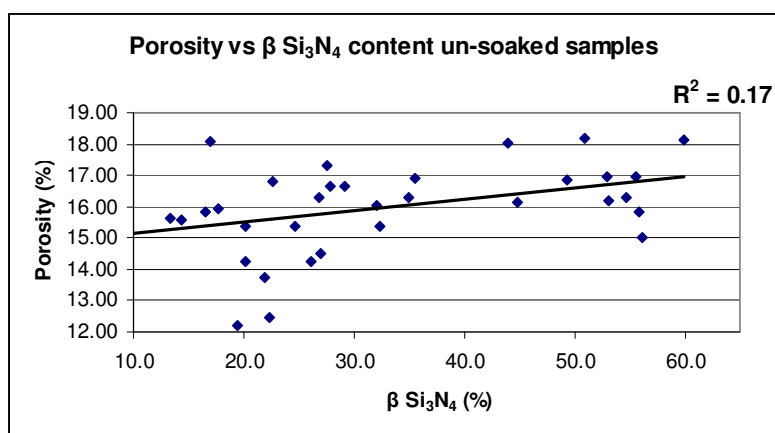


*Figure 7-19: Porosity as a function of β Si$_3$N$_4$ content in un-soaked samples. A very weak correlation was observed with $R^2$ =0.17.*

Although limited correlation was found between the corrosion rate and the amount of binder, an optimal SiC content in terms of corrosion resistance was observed between 80-85% SiC. Corrosion rate increased when the amount of binder was higher, due to the higher reactivity of Si$_3$N$_4$ compared to SiC (as discussed in Chapter 7.1). When the amount of binder is reduced beyond a critical point, a lack of material to fill interstices means corrosion rate increases due to the easier detachment of the large SiC particles.

A multivariate regression statistical model based on the results obtained from the pre-soaked samples was designed. Linear correlation, interaction, and quadratic effects between the three different parameters (porosity levels, β Si$_3$N$_4$ content, and SiC content) contributing to the corrosion rate were studied. This model can identify factors that have a statistically significant

contribution to the corrosion rate, although some of these factors would be hard to explain in meaningful physical terms.

To test whether there is statistically significant correlation between the parameters and the corrosion rate a null hypothesis test was applied. The null hypothesis ($H_0$) declares there is no correlation between the parameter and the corrosion rate. The level of confidence ($\alpha$) that was chosen was 0.05 meaning the null hypothesis can be rejected with 95% confidence. The p-value is the smallest significance level at which the null hypothesis may be rejected. To reject the null hypothesis with 95% certainty, the computed p-value should be $\leq 0.05$. Four parameters with a significant contribution to corrosion rate were identified: porosity levels, $\beta$ $Si_3N_4$ content, ($\beta$ $Si_3N_4$ content)$^2$ and the interaction between $\beta$ $Si_3N_4$ content and SiC content ($\beta$ $Si_3N_4$*SiC). This latter correlation is not surprising as it incorporates two factors known to influence corrosion, the $\beta$ $Si_3N_4$ content and the SiC: binder ratio. The squared component ($\beta$ $Si_3N_4$ content)$^2$, indicates that the corrosion rate is highly sensitive to $\beta$ $Si_3N_4$ content beyond a linear dependence. The calculated p-value for SiC content alone was 0.06, indicating a lesser contribution to the corrosion rate than the other factors. However, this factor can not be excluded from the model because of the significance of the interaction between $\beta$ $Si_3N_4$ content and SiC content on the corrosion rate.

The contribution of each factor was optimised by giving it a coefficient (estimated regression coefficients) that quantifies its relative contribution to the overall corrosion rate. Table 7-1 lists the factors that contribute to this rate, together with their p-value and estimated regression coefficients.

*Table 7-1: The factors that contributed to the corrosion rates according to the statistical model, and their estimated regression coefficients with p-values for each factor.*

| Term | Coefficient | P-value |
|---|---|---|
| Constant | -38.8566 | 0.021 |
| Porosity levels (%) | 0.9960 | 0.001 |
| $\beta$ $Si_3N_4$ content (%) | 0.9729 | 0.020 |
| SiC content (%) | 0.3531 | 0.060 |
| $\beta$ $Si_3N_4$ (%) * $\beta$ $Si_3N_4$ (%) | 0.0042 | 0.040 |
| $\beta$ $Si_3N_4$ (%)* SiC (%) | -0.0147 | 0.006 |

A regression equation incorporating all the significant factors established by the statistical model that can estimate the corrosion rate is shown in Equation 7-19:

*Equation 7-19:* **Corrosion rate** *= -38.86 + porosity level (%) + 0.973 β Si$_3$N$_4$ content (%)*
*+0.35 SiC content (%) + 0.0042 (β Si$_3$N$_4$ content)$^2$ - 0.015 (β Si$_3$N$_4$ content \*SiC content)*

The coefficient of determination ($R^2$) calculated for the regression equation based on all the data from the pre-soaked samples was 0.70 indicating reasonable predictive capacity in the model, given the inhomogeneous nature of these materials.

The corrosion results from pre-soaked samples showed a normal distribution with no evidence of skewness, outliers, or unidentified variables, as can be seen from the plot of the residual value against expected values (Figure 7-20).
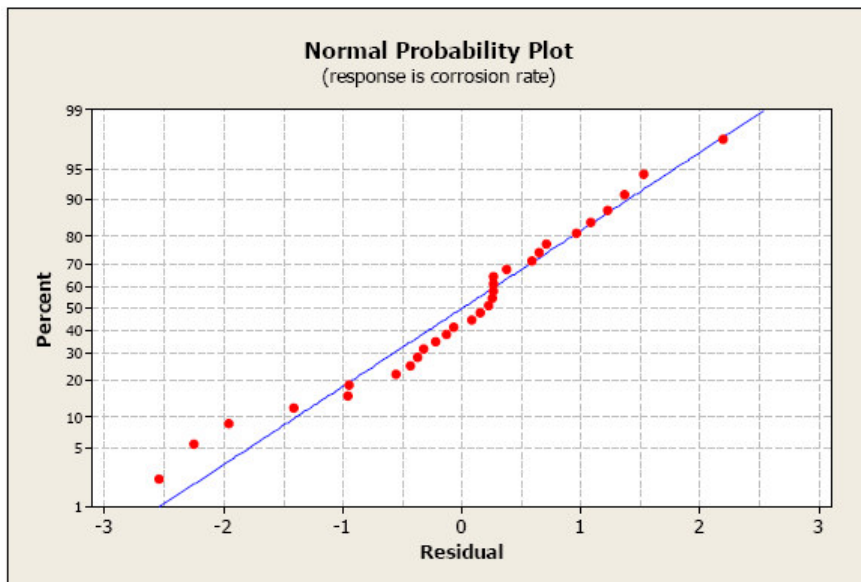


*Figure 7-20: Normal plot of the residuals.*

Based on the regression equation (Equation 7-19), three-dimensional surface plots were drawn, to visualise the interaction and contribution of two different factors to the corrosion rate. The effect of porosity levels and β Si$_3$N$_4$ content (with constant 80% SiC) on the corrosion rate can be seen in Figure 7-21.
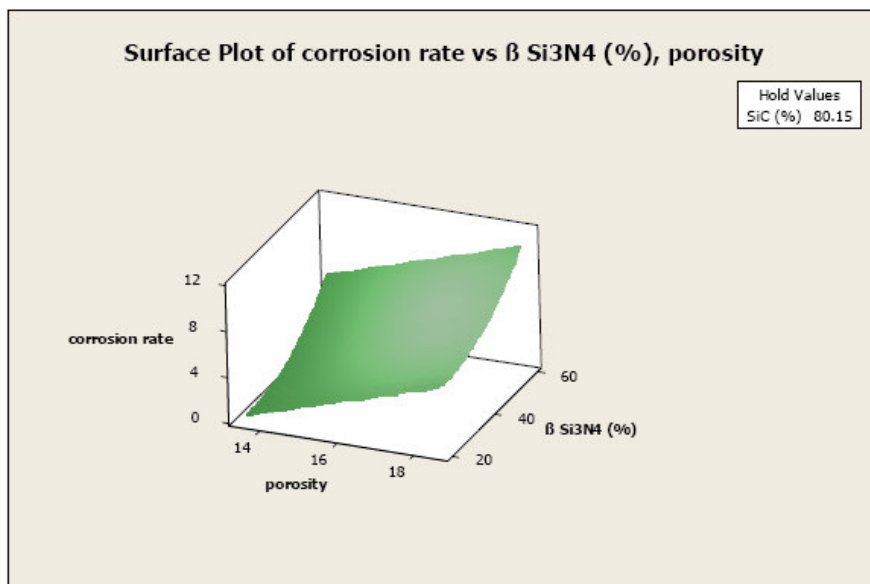
*Figure 7-21: Surface plot of corrosion rate as a function of porosity and β Si₃N₄ content at 80.15% SiC content.*

Figure 7-21 shows that a low corrosion rate is predicted for materials with low porosity levels and low β Si₃N₄ content. Maximum corrosion rate is expected when porosity and β Si₃N₄ content are at maximum levels.

The interaction between porosity and SiC content, and their relative impact on the corrosion rate (when the β Si₃N₄ fraction in the binder is constant at 39.6% of the total binder content) is depicted in Figure 7-22. Minimum corrosion rate is expected at low porosity levels and high SiC content. Within the compositional range considered, maximum corrosion rate is predicted for SNBSC material with 70% SiC content and porosity of 18%. The surface plot does not predict an increase in the corrosion rate when SiC content is higher than 80% (as observed in Chapter 6.2.3). However the surface plot in Figure 7-23 (representing corrosion rate as a function of SiC content and % of β Si₃N₄ in the binder) shows an increase in the corrosion rate between 80% and 90% SiC. A high corrosion rate is predicted for a material with 70% SiC content and 60% of the binder as β Si₃N₄, as seen in the surface plot in Figure 7-23.
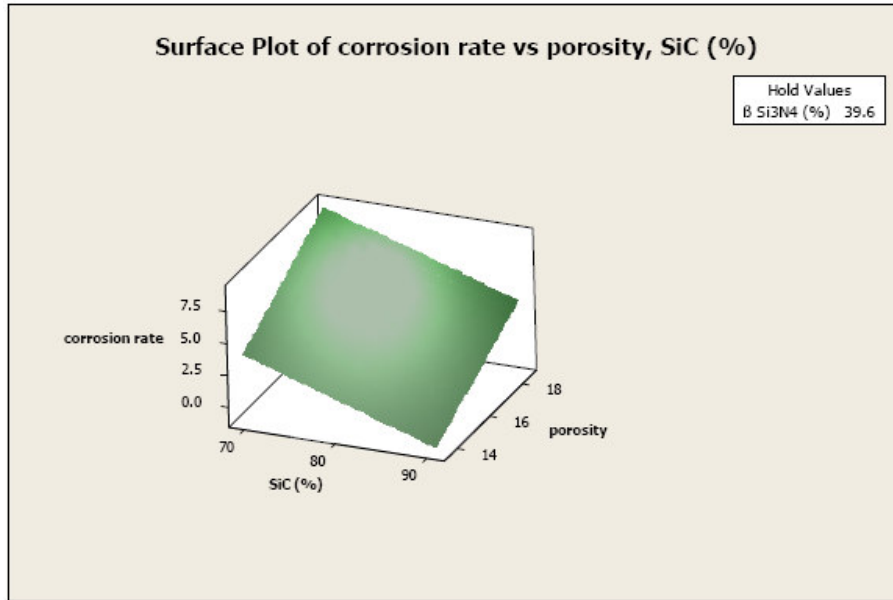
*Figure 7-22: Surface plot of corrosion rate as a function of porosity and SiC content.*
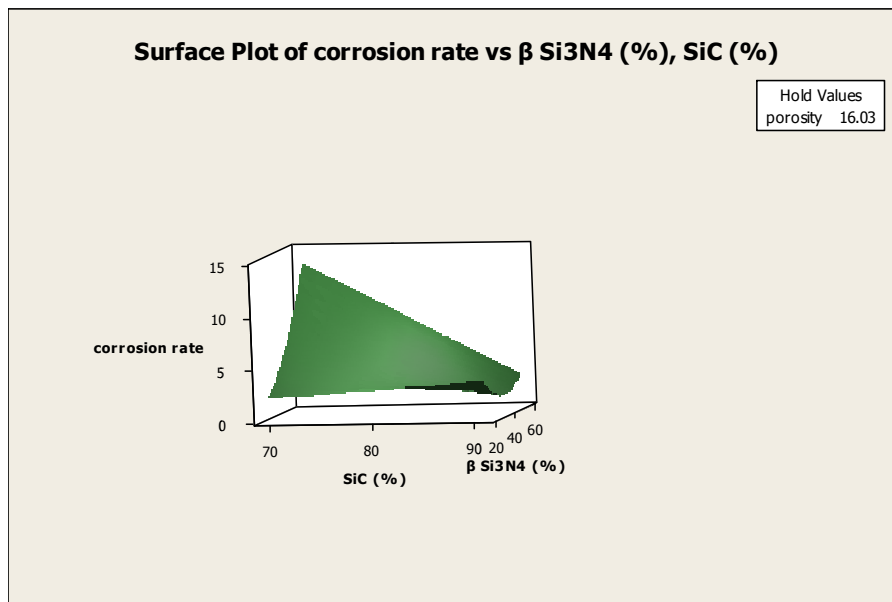


*Figure 7-23: Surface plot of corrosion rate as a function of SiC content and Si₃N₄ content.*

An optimization plot, based on the regression Equation 7-19, shows how the factors considered affect the predicted corrosion rate. The example shown in Figure 7-24 indicates that for 16.5% porosity, 41.1% of the binder as β $Si_3N_4$, and 81.0% SiC content, the predicted corrosion rate is 4.5 % in the lab-scale experiment conditions (48 hours electrolysis at 1000°C).
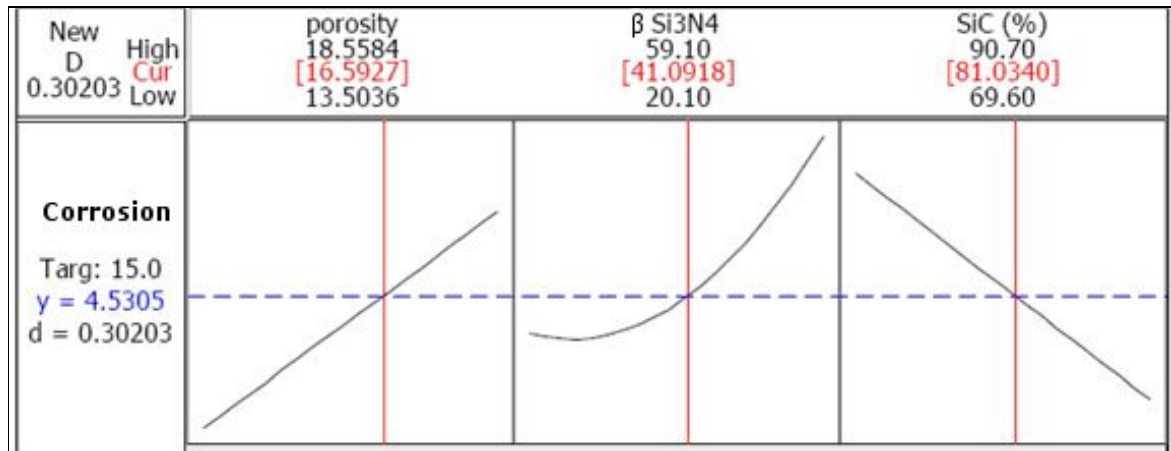
*Figure 7-24:* Optimization plot of the predicted corrosion rate as a function of increasing value of parameter in three different factors.

### 7.3.1. Proposed mechanism of degradation

With regard to the mechanism, corrosion was observed mainly in the gas phase and especially at the bath-gas phase interface, however corrosion appears to be driven by the combined effect of bath penetration into the porous SNBSC material, and exposure to the corrosive gasses. Based on the observations discussed in Chapter 6.2.5 and the thermodynamic calculations shown in section 7.1, the corrosion mechanism is proposed to be as follows:

- In the gas phase (above bath level), oxidation of the binder by $CO_2$ and air forms an $SiO_2$ layer that serves as a diffusion barrier to oxygen and protects the sidewall from further oxidation.
- In the bath zone, penetration of bath into the sidewall, and capillary transport of Na ions through the pore system of the binder phase extend into the area above the bath level.
- Temperature excursions due, for example to anode effects, and dissolution of the frozen ledge, will enrich the sidewall with Na ions.
- The interaction of water vapour with the polar $SiO_2$ layer forms an interfacial water layer that captures gaseous HF to form a strong acidic environment that corrodes the protective silica layer.
- In the absence of the protective oxide layer, exposure of the Na ion rich binder phase to $CO_2$ and oxygen will result in oxidation of the binder phase to form sodium silicate ($Na_2O*2SiO_2$).
- Further extensive oxidation of the binder phase is expected at temperatures above the melting point of the sodium silicate. The $SiO_2$ produced will dissolve into the silicate liquid as long as there is a constant supply of Na ions (in an absence of frozen ledge).

- Attack by corrosive gases such as HF and $NaAlF_4$ on the silicate glass / liquid to produce volatile $SiF_4$.

- Further oxidation of the binder phase by $CO_2$, and another cycle of attack by the corrosive gases.

- Fluctuations in bath level will increase degradation in the bath /gas interface due to dissolution of oxide or silicate into the cryolitic bath.

## 7.4.  Summary of the mechanism of degradation of SNBSC

The reactivity of $Si_3N_4$ and SiC, and their oxides in regards to the various environments, and at various temperature ranges presented in the aluminium reduction cell operation, was calculated using HSC Chemistry software. The Gibbs free energy ($\Delta G$) of the reactions served as a measure of the reactivity of these compounds. Higher reactivity is indicated by higher negative value of the Gibbs free energy.

In the gas phase, $Si_3N_4$ shows a higher reactivity than SiC towards both the corrosive gases HF and the $NaAlF_4+CO_2$ combination, and the oxidative gases CO, $CO_2$, and $O_2$. The reaction of the sidewall materials with the corrosive gases present, leads to the formation of a volatile $SiF_4$ phase causing degradation of the sidewall materials, while reaction with the oxidising agents yielding a protective layer of $SiO_2$ that is less reactive towards HF and $NaAlF_4$ than are $Si_3N_4$ and SiC.

 The reactivity of the sidewall materials with the gases is enhanced in the lower part of the temperature range (350-500°C) exists in the upper part of the sidewall near the crust. In this temperature range the reactivity of $Si_3N_4$ towards these gases could be ranked, in terms of thermodynamic feasibility as follow: $O_2$>> CO >$NaAlF_4$ +$CO_2$> $CO_2$ > HF. while in the upper limit of temperature range (1000°C near the bath level) the reactivity of CO with $Si_3N_4$ decreased by 400kJ leading to the following rank: $O_2$>> $NaAlF_4$ +$CO_2$> $CO_2$ >CO > HF.

The high negative $\Delta G$ value of the reaction of $Si_3N_4$ with oxygen suggests that the exposed surface of the sidewall will be covered with oxide layer ($SiO_2$) protecting it from further oxidation and corrosive attack by HF. However, this oxide layer although less reactive than $Si_3N_4$ is still subjected to corrosive gas attack in the presence of water vapour by formation of acidic aqueous interface that will corrode the oxide layer.

In the bath zone, both SiC and $Si_3N_4$ have a positive $\Delta G$ value for reaction with cryolite and thus will not spontaneously react with the bath. However the presence of $CO_2$ emitted from the anode surface, enhances the reactivity of the sidewall towards cryolite. Sodium ions (as salts) can penetrate into the sidewall from the bath and can migrate above bath level by capillary transport through the pore system of the bonding phase of the sidewall. An increase in porosity will increase the sodium ion absorption. The presence of sodium ions enhances the oxidation of $Si_3N_4$

by oxygen to form sodium silicate ($Na_2O*2SiO_2$), which is more reactive toward oxygen than silicon oxide. In the upper temperature range the silicate can form liquid phase, leading to extensive oxidation of the bonding phase due to increased oxygen diffusion. Unlike $Si_3N_4$ and SiC the oxide products $SiO_2$ and $Na_2O*2SiO_2$ can be easily dissolve in the cryolitic bath leading to degradation of the sidewall in the absence of frozen ledge (during anode effect).

A correlation between high corrosion rate and high $\beta$ $Si_3N_4$ content was observed in SNBSC samples in corrosion tests. This is potentially related to the crystal morphology of the beta phase. The long spike –like $\beta$ $Si_3N_4$ crystals have a higher surface area exposed to corrosive gas attack compared with the flat matte-like $\alpha$ $Si_3N_4$ crystals.

Test samples that were thermally treated in a nitrogen atmosphere at temperatures higher than 1700°C showed an increase of $\beta$ $Si_3N_4$ content from 10% to 100%. Observation of these samples using SEM analysis showed a change of crystal morphology after the thermal treatment. Elongated rod-like crystals replaced the flat matte-shape crystals in the binder phase and needle like crystals filled the large pores and cavities observed in bonding phase of the un-treated sample.

BET surface area measurement of SNBSC samples show that these materials have a relatively low surface area. After heat treatment of the particular sample tested, surface area increased from $0.24 m^2/g$ to $0.43$ $m^2/g$. The open porosity also increased from 14.5% to 19.1% and a reduction in the average pore radius from 8.3nm to 4.7nm was measured by BJH nitrogen adsorption.

The increase in $\beta$ $Si_3N_4$ content was followed by an increase in the samples internal surface area and reduction in average pore radius. This indicates that the elongated rod-like shape and arrangement of the $\beta$ $Si_3N_4$ crystals provides better accessibility for gas penetration and increased contact with the binder phase which can explain the higher corrosion rate observed for samples having high $\beta$ $Si_3N_4$ content.

A statistical analysis has been carried out, based on the results of more than 30 individual corrosion trials on a variety of SNBSC materials. Porosity levels, $\beta$ $Si_3N_4$ content, and SiC content are the parameters that show a measurable correlation with the corrosion rate. Porosity levels and $\beta$ $Si_3N_4$ content (i.e % $\beta$ phase in the $Si_3N_4$ binder) show a limited cross correlation, although higher corrosion rates are observed with increases of both parameters.

A multivariate regression statistical model, based on the corrosion results of the pre-soak samples, identified porosity levels, $\beta$ $Si_3N_4$ content, ($\beta$ $Si_3N_4$ content)$^2$, and SiC content* $\beta$ $Si_3N_4$ content as factors that show a statistically significant correlation with corrosion rate. The relative contribution of each factor is expressed by the regression coefficients. A regression equation, with coefficient of determination of 0.7, was made based on the contributing factors and their coefficients, that estimates corrosion rate for a given porosity level, $\beta$ $Si_3N_4$ content, and SiC content. The largest single factor affecting corrosion appears to be porosity levels. However, $\beta$ $Si_3N_4$ content in the binder and the binder**: SiC ratio also contribute.

This conclusion with regards to the contribution of porosity levels to the corrosion of SNBSC materials, is at variance with the results reported by Skybakmoen et al [35] in trials using smaller samples and without pre-soaking. The contribution of $\alpha$/ $\beta$ $Si_3N_4$ ratio to the corrosion is a factor that was mentioned by Skybakmoen et al [35] and Anderson et al [33] (see chapter 3.4) but has not been systematically examined before this work. The contribution of the amount of binder on the corrosion rate was known to be of high importance due to the higher thermodynamic reactivity of $Si_3N_4$ comparing to SiC (section 7.1). Zaho [23] indicate that a balance should be maintained in the binder content in order to minimise corrosion without compromising strength. However, prior to this work no systematic study has reported the influence of this parameter on the corrosion rate.

The proposed corrosion mechanism for SNBSC materials in the aluminium reduction cell atmosphere is based on combination of oxidation of the binder followed by attack of corrosive gases to produce volatile $SiF_4$. The corrosion starts with degradation of the protective $SiO_2$ layer by wet HF. This is followed by enhanced oxidation of the binder phase by $CO_2$ due to presence of Na ions that originate from bath penetration. The penetrated sodium ions can migrate above bath level by capillary transport through the binder pore system. Attack by corrosive gases, on the reactive silicates, produces volatile products. Further oxidation by $CO_2$ and dissolution of the oxide product into the silicate layer, is followed by another cycle of corrosive gas attack.

# Chapter 8: Summary and conclusions

## 8.1. Conclusions from this study

The lifetime of aluminium reduction cell is important factor in the operating economics of the aluminium smelter. This lifetime is increasingly determined by two components of the cell linings: the carbon cathode and the sidewall refractories. In this study the mechanisms of the corrosion of silicon nitride bonded silicon carbide refractories in an aluminium reduction cell environment were examined.

The microstructure of SNBSC refractories was studied in order to understand the impact on the corrosion mechanism. The contribution of four parameters to the corrosion rate was examined: porosity levels (section 6.2.1), amount of binder (section 6.2.2), $\alpha/\beta$ $Si_3N_4$ ratio (section 6.2.3) and unreacted silicon in the binder phase (section 6.2.4).

The sidewall materials are exposed to the reduction cell environment for years, hence to simulate the condition that lead to degradation of these materials in a shorter time frame in lab scale experiments, accelerated testing is required. Although the samples that were tested in lab-scale configuration are small, they do inform the corrosion mechanisms for these materials. The lab-scale electrolysis rig was based on the method developed by Skybakmoen et al [24] that exposes the sidewall materials to the various environments existing in a reduction cell: molten bath, $CO/CO_2$ and corrosive gasses such as HF and $NaAlF_4$. However this rig was scaled up and modified to reduce the error that occurs in the corrosion rate due to bath level fluctuations in a small crucible with small samples. Rotating the anode improved voltage stability and reduced the possibility of short circuit due to carbon build up on the crust. A new test method was developed in order to isolate the effect of gas phase environment on the corrosion rate. This test method enabled the examination of the corrosion of smaller altered samples and the comparison of the corrosion of samples that were not in contact with bath, to corrosion of pre-soaked samples.

Results from industrial and lab-scale corrosion tests showed that porosity levels and $\beta$ $Si_3N_4$ content have a statistically significant contribution to the corrosion rate. Higher corrosion rates were related to high porosity levels and /or high $\beta$ $Si_3N_4$ content. Although both parameters showed increased levels in the inner part of the brick compared to the exterior area, low cross correlation between the parameters was observed in the corrosion test samples.

Porosity levels showed a strong contribution to the corrosion rate of SNBSC samples, especially those that were pre-soaked in bath (section 6.2.1). The correlation between porosity levels and corrosion rate was affected by the sample dimension; samples with lower thickness showed higher correlation. The reduced correlation between corrosion rate and porosity levels in the thicker samples was attributed to incorporation of zones with different porosity levels into each sample due to the variation in porosity levels along brick cross section. The significant contribution of porosity to corrosion is in contradiction to a study by Skybakmoen et al [35] which finds no correlation between the two, however the effect of porosity on corrosion rate in this study was more profound in pre-soaked samples, a factor that was not tested by Skybakmoen.

The α/β $Si_3N_4$ ratio was mentioned in previous studies as a parameter that can influence the chemical resistance of SNBSC materials [33, 35]. However the effect of this parameter on corrosion was not systematically studied. In this study the effect of this parameter on the corrosion rate was tested by two different methods: examining the correlation between β $Si_3N_4$ content and the corrosion rate of commercial-grade SNBSC material (section 6.2.3) and by altering the commercial- grade materials to higher β $Si_3N_4$ content by thermal treatment. The corrosion rate of the samples before and after the heat treatment was then compared (section 6.3). A statistically significant correlation was found between high corrosion rates and high β $Si_3N_4$ content in the corrosion test of commercial-grade materials. Narrow samples showed a higher correlation for similar reasons as the study of porosity levels. The samples that were altered by heat treatment, to increase their β $Si_3N_4$ content, showed increased porosity levels with reduced pore radius. The increase in β $Si_3N_4$ content was accompanied with increase of the surface area. Some of the altered samples showed significantly higher corrosion rate compared to the un-treated samples having lower β $Si_3N_4$ content, while altered samples from different material did not show the same trend. The crystal morphology of β $Si_3N_4$ was suggested as the reason for the high reactivity of these materials. This morphology characterised by elongated rod-like shape crystals with hexagonal cross section, presents a higher surface area compared to α $Si_3N_4$ crystals.

The reduced pore radius and the increased surface area measured in thermally treated samples with high β $Si_3N_4$ levels, indicate that the shape and arrangement of the β $Si_3N_4$ crystals provide improved access for gas penetration through the small pores, although, whether it is the

increased internal surface area alone which causes this, or other effects induced by the phase transformation, is not clear.

In the commercial refractories, the formation of high levels of $\beta$ $Si_3N_4$ in the binder could be avoided by improved control of the nitridation reaction temperature. A computer model presented in this work shows that even at the temperatures used in industrial manufacturing of SNBSC materials, the core of the bricks could have significantly higher temperatures. The excess heat generated by the exothermic nitridation reaction, with poor heat dissipation due to the close stacking in the furnace, prevent efficient heat loss from the brick exterior surface. This leads to temperatures, above the melting point of silicon in the interior area of the bricks. As a result, a liquid phase is formed that promotes the growth of $\beta$ $Si_3N_4$ and reduces the silicon reactivity due to reduction in surface area.

The binder phase was identified by thermodynamic calculation as the more reactive component in the SNBSC materials (section 7.1). Corrosion test results showed maximum corrosion resistance at SiC concentrations of 80% to 85%. As expected, higher corrosion rates were observed in materials with higher levels of binder phase. Materials with too low binder levels (SiC > 86%) also showed higher corrosion rate because of insufficient binder to effectively bind the composite together leading to detachment of large SiC particles and enhanced degradation. This condition is a result of preferential reactivity of the binder phase, the formation of volatile product, and the different particle size of SiC which is in the mm scale compared to $Si_3N_4$ crystals of micron scale.

A multivariate regression statistical model, based on pre-soaked lab-scale corrosion test results, was design to quantify the relationship as well as the relative contribution to the corrosion rate of porosity levels, $\beta$ $Si_3N_4$ fraction in the binder (i.e. $\beta$ $Si_3N_4$ content), and binder content. The model identified: porosity levels, $\beta$ $Si_3N_4$ content, ($\beta$ $Si_3N_4$ content)$^2$, and SiC content* $\beta$ $Si_3N_4$ content as factors that show a statistically significant contribution to the corrosion rate. Porosity levels appeared to be the largest single factor affecting corrosion. The relative contribution of each factor was expressed by regression coefficients and the accumulate impact of these factors was expressed by regression equation with coefficient of determination of 0.7. The model can estimate corrosion rates of SNBSC materials in reduction cell atmosphere based on given porosity levels, $\beta$ $Si_3N_4$ content, and amount of binder.

The hypothesis that the corrosion rate of SNBSC materials in the aluminium reduction cell atmosphere is related to the presence of unreacted metallic silicon was examined.

Silicon as metallic unreacted material can melt and form an amorphous phase due to elevated temperature inside the green brick during the fabrication process. This amorphous phase will become a weak phase in the final SNBSC material due to its high thermodynamic reactivity. The free silicon detected in the materials examined was in crystalline form, as measured by solid state NMR (section 4.3) and XRD analysis (section 4.2), and was observed mainly within the core of the SiC grains rather than in the bonding matrix as seen by SEM analysis (section 4.6). The low concentration and absence of free silicon in the bonding phase indicate minimal contribution of this factor to the corrosion rate, hence this hypothesis was ruled out.

Based on thermodynamic calculations (section 7.1) and cell autopsies analysis the suggested corrosion mechanism in the gas zone is a combined effect of oxidation of the binder phase by penetrated bath and degradation of the formed oxide layer by attack of corrosive gasses. The sidewall above the bath level is protected by $SiO_2$ layer formed by oxidation of the binder phase by oxygen and $CO_2$. Sodium, as ion that penetrated from the bath, migrates above the bath level by capillary transport in the porous binder. Degradation of the protective $SiO_2$ layer by gaseous HF and moisture will expose the reactive sodium ion rich $Si_3N_4$ to oxidant as $CO_2$ emitted from the anode and oxygen leading to enhanced oxidation of the binder to produce sodium silicate. Extensive oxidation of the sidewall reduces the thermal conductivity of the material and leads to less stable frozen ledge thus exposing the sidewall more often to high temperatures, molten and gaseous bath components. The higher reactivity of the silicate layer to HF and moisture compared to $SiO_2$ will enhance the degradation of the binder phase due to production of volatile $SiF_4$. Further degradation occurs by oxidation of the exposed silicate material by $CO_2$ followed by another attack by corrosive gases. When critical amount of binder is lost, detachment of SiC grains and collapse of the material will occur.

## 8.2. Suggestions for future work.

This study has mainly focussed on the impact of three parameters (e.g. porosity levels, $\beta$ $Si_3N_4$ content, and binder content) on the corrosion rate of SNBSC materials, when exposed to a variety of environments relevant to their use in aluminium reduction cells.

This work was focused on examining the factors that contribute to the corrosion rate of commercial products that are used in aluminium smelters by simulating as closely as possible the degradation mechanism occur in industrial cell. However the use commercial materials presents challenges due to the limit range of values available for each of the contributing parameters and add complexity to the analysis due to the interplay of these parameters across the microstructure of individual samples. Further study could test custom fabricated samples with a broader range of values for these parameters and a greater level of homogeneity.

This study also provides some insight into the challenges in the commercial production process of refractory bricks, and ways to improve the corrosion resistance of the final product. The formation of material with high $\beta$ $Si_3N_4$ content could be avoided by eliminating the conditions, such as high temperature in the core of the brick and presence of liquid phase, that contribute to this formation.

Improved thermal control of the production process with temperatures below the melting point of silicon in the core of the brick could be achieved in two ways:
- Reduction of heat generation rate by the exothermic nitridation reaction
- Improving the heat dissipation from the brick

Elimination of metallic impurities that serve as catalysts will slow the reaction rate, hence reducing the heat generation rate. Iron in the silicon, originating from the milling process, and fluorides were identified as the main catalysts for the nitridation reaction, iron especially catalysing the formation of $\beta$ $Si_3N_4$ (see section 2.2). Another way to slow the reaction rate is by reducing nitrogen concentration by dilution with argon (especially in the faster stage of the reaction); this will maintain enough gas volume to effectively dissipate the heat while reducing the reaction rate.

Dissipation of the heat from the exterior surface of the brick could be improved by increasing the rate of convective heat transfer. If the bricks are closely stacked in the furnace, the lack of space between the bricks minimises dissipation of heat by convection and radiation. Maintaining a gap big enough between the bricks will allow the nitrogen to carry the heat away from the brick surface by convection and will increase the radiative heat loss from the surfaces between bricks. Forced convection by increasing the nitrogen speed in the furnace will further improve cooling the brick surface. The cooling effect of various brick spacing could be studied by inserting thermocouples inside the green bricks and monitoring temperatures during the nitridation process. Incorporating such thermocouples into the furnace control system will enable the synchronisation of the furnace ambient temperature according to the requirements of different reaction stages.

The heat radiation from the core to the exterior surface of the brick is governed by the thermal conductivity of SNBSC materials (typically 20 W/(m·K) at 900°C). Introducing an additional phase with higher thermal conductivity like graphitised carbon (116 W/m·K) into the bonding phase will improve the thermal conductivity of the brick without reducing its chemical resistance.

Inhibition of the growth of $\beta$ $Si_3N_4$ by avoiding the formation of liquid phase during the nitridation process could be achieved by using metallic contaminant free raw materials (particularly free of iron or aluminium). These contaminants form silicon alloys with lower melting points and lead to creation of voids and microstructural defects that increase the porosity of the final product (see section 2.2).

Another way to inhibit the formation of liquid phase is by addition of materials that react with the liquid silicon to form a solid material (similar approach as the formation of chemical barrier mention in section 1.1). A contaminant- free carbon has the thermodynamic potential to react with silicon to produce silicon carbide as a bonding phase in the temperature range of the nitridation process without reduction of corrosion resistance.

# References

1. Welch B.J., Hyland M.M., and James B.J., "Future materials requirements for the high-energy-intensity production of aluminium". *JOM*, 2001. **53**(2): p. 13-18.
2. Tabereaux  A.T, "Reviewing advances in cathode refractory materials". *JOM*, 1992. **44**(11): p. 20-21, 25,26.
3. Sorlie M. and Oye, H. A., *Cathodes in Aluminium electrolysis*. 1989: Aluminium-Verlag.
4. Grjotheim K. and Welch B.J., *Aluminium smelter technology*. 2nd ed. 1988: Aluminium verlag.
5. Grjotheim K. and Kvande H., *Introduction to aluminium electrolysis*. 2nd ed. 1993: Aluminium-Verlag.
6. Ascher R. C., *J. Inorg. Nucl. Chem.*, 1959. **10**: p. 238.
7. Pflugmacher I. and Boehm H. P. *3rd Conf. Ind. Carbons Graphite*. 1970 p 62.
8. Fickel A.F. , Rolofs B., and Temme P.W. On the oxidation behaviour of some pot lining refractories and the consequences of their practical application. *Light Metals (TMS)*. 1991 p 405-412.
9. Ødegård R., Sterten Å., and Thonstad J. On the solubility of aluminium carbide in cryolite melts-influence on cell performance. *Light metals (TMS)*. 1987. Denver Colorado p 295-302.
10. Gudbrandsen H., Sterten A, and Odgard R. Cathodic Dissolution of Carbon in Cryolitic Melts. *Light Metals (TMS)*. 1992 p 521-528.
11. Taylor M.P., Welch B. J., and Keniry J.T. Influence of Changing Process Conditions on the Heat Balance Transfer during the Early life of an Operating Cell. *Light Metals (TMS)*. 1983 p 437- 441.
12. Pawlek  R. P. SiC in electrolysis pots: update. *Light Metals (TMS)*. 2006 p 655-658.
13. Pawlek R.P. SiC in Aluminium Electrolysis Cells. *Light Metals (TMS)*. 1995 p 527.
14. Schoennahl J., Jorge E., Marguin O., Kubiak S. M., and Temme P. Optimization of $Si_3N_4$ bonded SiC refractories for aluminium reduction cells. *Light metals (TMS )*. 2001 p 251-255.
15. Fickel A.F., Kramass J.S., and Temme P.W. Silicon Carbide refractories in aluminium reduction cell linings. *Light Metals (TMS)*. 1987 p 183-188.
16. Kramss J. Silicon Carbide Side Wall Lining in Aluminium Reduction Cells. *2nd Australasian Aluminium Smelter Technology Course*. 1987. Sydney, Australia p 1p.
17. John D. The use of SiAlON bonded silicon carbide sidewall blocks in the aluminium electrolysis cell. *Aluminium: Strategies for the Nineties and Beyond*. 1991. Bangalore, India: Aluminum Association of India p 127-129.
18. Fickel A.F., Kramass J.S., and Temme P. Silicon Carbide Refractories for Aluminum Reduction Cell Linings. *Light Metals (TMS)*. 1987. Warrendale, PA, United States p 183-188.
19. Tabereaux  A.T and .Fickel A. Evaluation of silicon carbide bricks. *Light Metals (TMS)*. 1994 p 483-491.
20. Washburn M.E., "Hochfeuuefeste Erzeugnisse aus oxydnitridgebundenem Siliziumkarbid". *Keramische Zeitschrift*, 1963. **15**(4): p. 203-205.
21. Riley, F.L., "Silicon nitride and related materials". *J. Amer. Ceram. Soc* 2000. **83**(2): p. 245-65.
22. John D. and Maurage R., "Sialon bonded Silicon Carbide sidewall pieces for the Aluminium reduction cell". *Aluminium Today*, 1992: p. AT-138.
23. Zhao J. and Cheng Z. Comparison of Cryolite resistance of Silicon carbide materials. *7th Australasian Aluminium Smelting technology conf. and workshop*. 2001. Melbourne, Australia p 43-49.

References.

24. Skybakmoen E. , Gudbrandsen H. , and Stoen L.I. . Chemical resistance of sideline materials based on SiC and carbon in cryolitic melts -A laboratory study. *Light Metals (TMS)*. 1999 p 215-222.

25. Moulson, A.J., "Review Reaction- bonded silicon nitride: its formation and properties". *J. Mater. Sci.*, 1979. **14**: p. 1017-1051.

26. E.T.Turkdogan, P.M. Bills, P. M.;, and V.A. Tippett, "Silicon nitrides: Some physicochemical properties". *Journal of Applied Chemistry* 1958. **8**: p. 296-302.

27. Mangels, J.A., " Effect of Rate-Controlled Nitriding and Nitriding Atmospheres on the Formation of Reaction-Bonded Si$_3$N$_4$". *Am. Ceram. Soc. Bull.*, 1981. **60**(6): p. 613-17.

28. Kijima K. and Shirasaki S., "Nitrogen self-Diffusion in Silicon Nitride". *J. Chem. Phys*, 1976. **65**(7): p. 2668-2671.

29. Kunz  K. P., Sarin V. K., Davis R. F., and Bryan S. R., "Self Diffusion of Silicon -30 and nitrogen -15 in a Phase Silicon Nitride". *Mater.Sci. Eng*, 1988. **A105/106**: p. 47-54.

30. Carborundum Corp., "Silicon Nitride Bonded Article". *U.S. Patent No 2 618 565*, 1952.

31. Boyer S.M. and Moulson A.J., "A mechanism for the nitridation of Fe-contaminated silicon". *J. Mater. Sci.*, 1978. **13**: p. 1637-46.

32. Longland P. and Moulson A.J., "The growth of α- and β-Si$_3$N$_4$ accompanying the nitriding of silicon powder compacts". *J. Mater. Sci*, 1978. **13**: p. 2279-80.

33. Andersen F.B., Dörsam G., Stam M., and Spreij M. Wear of Silicon Nitride Bonded SiC Bricks in Aluminium Electrolysis Cells. *Light Metals (TMS)*. 2004 p 413-418.

34. Bearne G. and Jenkin A. The impact of cell geometry on cell performance  *Light Metals (TMS)*. 1995 p 378.

35. Skybakmoen E, Stoen H., Kvello J.H., and Darell O. Quality evaluation of nitride bonded silicon carbide sidelining materials. *Light Metals (TMS)*. 2005 p 773-778.

36. Thorley M. and Banks R., "Kinetic and mechanism of oxidation of Silicon Nitride bonded Silicon Carbide ceramic". *J. Therm. Anal*, 1994. **42**: p. 811-822.

37. Zhao J., Zhang Z, Wang W., Liu  G., and Zhu C. The properties of Si$_3$N$_4$ bonded SiC material for aluminium electrolysis cell. *Light Metals (TMS)*. 2000 Warrendale, Pennsylvania p 443-447.

38. Swain M. V. and Segnit E.R., "Reaction between Cryolite and Silicon Carbide refractories". *J.Austr.Ceram.Soc*, 1984. **20**: p. 9-12.

39. Jorge E., Marguin O., and Temme P. "Si$_3$N$_4$ Bonded SiC refractories for higher Aluminium reduction cell performance". *"Aluminium in Siberia"*. 2003. Krasnoyarsk p 166-177.

40. Hagen E., Einarsrud M, and Grande T. Chemical stability of ceramic sidelining in Hall-Heroult cells. *Light Metals (TMS)*. 2001 p 257-263.

41. Kvam K.R.  and Oye H.A. Homogeneity and degradation of SiC sidelining *9th Int. symp. On  Light Metals Production*. 1997. Trondheim -Norway p 313-320

42. Swift M. V. and Segnit E.R., *Cryolite reaction with Silicon Carbide bricks*, in *AML -82-84*, CSIRO , Division of Mineral Chemistry, Australia. p. 16.

43. Patterson E, Hyland M., Moxnes B., and Welch B. Reducing Hydrogen Fluoride emissions from Aluminum electrolysis cell. *7th Australasian Aluminium Smelting Technology Conference and Workshop*. 2001. Melbourne Australia.

44. Edwards D. P., Muddle B. C., Cheng Y. B., and Hannink R. H. J., "The development of microstructure in Silicon Nitride -Bonded Silicon Carbide". *J. Eur. Ceram. Soc.*, 1995. **15**: p. 415-424.

45. Messier D.R., Riley F.L., and Brook R.J., "The α/β silicon nitride phase transformation. " *J. Mater. Sci*, 1978. **13**: p. 1199-1205.

46. Kramer M. , Hoffmann M. J. , and Petzow G., "Grain Growth Studies of Silicon Nitride Dispersed in an Oxynitride Glass". *J. Am. Ceram. Soc.*, 1993. **76**(11): p. 2778-84.

# References.

47. Wang C.M., Pan X., Ruhle M., Riley F. L., and Mitomo M., "Review Silicon nitride crystal structure and observations of lattice defects". *J. Mater. Sci.*, 1996. **31**: p. 5281-5298.
48. Wild S., Grieveson P., and Jack K. H., *The crystal structure of alpha and beta silicon and germanium nitrides*. Special ceramics, ed. Popper P. Vol. 5. 1972: British Ceramic Society, Stoke-on-Ternt. 385-395.
49. Bando Y., "Weak Asymmetry in β-Si₃N₄ as Revealed by Convergent-Beam Electron Diffraction". *Acta Cryst.*, 1983. **B39**: p. 185-189.
50. Goodman P. and O'Keeffe M., "The Space Group of β-Si₃N₄". *Acta. Cryst.*, 1980. **B36**: p. 2891-2893.
51. Grün R., "The crystal structure of β-Si₃N₄: structural and stability considerations between α- and β-Si₃N₄". *Acta. Crystallogr.*, 1979. **B35**: p. 800.
52. Hampshire S., Park H. K., Thompson D.P., and Jack K. H., "α sialon ceramic". *Nature*, 1978. **274**: p. 880-882.
53. Wild S., Grieveson P., and Jack K. H., *ibid*, 1972. **5**: p. 385.
54. Colquohoun S., Wilde S., Grieveson P., and Jack K. H., *Proc. B. Ceram. Soc.*, 1972. **22**: p. 207.
55. Jack K. H., *Progress in nitrogen ceramics*, ed. Riley F. L. 1983, The Hague: Martinus Nijhoff.
56. Thompson D.S. and Pratt P.L., *Sci. Ceram.*, 1967. **3**: p. 33.
57. Blegen K., *Special Ceramics*, ed. Popper P. 1975, Manchester: George Faulkner Press.
58. Van Dijen F. K. and Metselaar R., "The chemistry of the carbothermal synthesis of β-silicon carbide: reaction mechanism, reaction rate and grain growth. " *J. Eur. Ceram. Soc*, 1991. **7**: p. 177-184.
59. Bauer J., Fiala J., and Hrichova R., "Natural α-silicon carbide". *American Mineralogist*, 1963. **48**: p. 620-634.
60. Dressler W. and Riedel R., "Progress in silicon-based non-oxide structural ceramics". *int. J. of Refractory Metals & Hard Materials*, 1997. **15**: p. 13-47.
61. Gazzara C. P. and Messier D. R., "Determination of Phase Content of Si₃N₄ by X-Ray Diffraction Analysis". *Bull. Amer. Ceram. Soc.*, 1977. **56**(9): p. 777-780.
62. Carduner R. K., Carter I. R. O., Milberg E. M., and Crosbie G. M., "Determination of phase composition of silicon nitride powders by silicon-29 magic angle spinning nuclear magnetic resonance spectroscopy". *Anal. Chem*, 1987. **59**: p. 2794-2797.
63. Chollon G., Hany R., Vogt U., and Berroth K., " A silicon- ²⁹MAS-NMR study of alpha-silicon nitride and amorphous silicon oxynitride fibres". *J. Euro. Ceram. Soc*, 1997. **18**: p. 535.
64. Dupree R., Lewis M. H., Leng-ward G., and Williams D.S., "Co-ordination of Si atoms in silicon-oxynitrides determined by magic-angle-spinning NMR ". *Journal of material science letters*, 1985. **4**: p. 393-395.
65. Dybowski C., E.J. Gaffney, A. Sayir, and Rabinowitz M., "Solid-state ¹³C and ²⁹Si MAS NMR spectroscopy of silicon carbide". *J. Colloids and Surfaces A*, 1996. **118**: p. 171.
66. Finlay, G.R., J.S. Hartman, M.F. Richardson, and B.L. Williams, "²⁹Si and 1% Magic Angle Spinning N.M.R. Spectra of Silicon Carbide Polymorphs". *J. Chem. Soc. Chem. Commun.*, 1985. **1112**: p. 115.
67. MacKenzie K.J.D. and Meinhold R.H., "Role of Additives in the Sintering of Silicon Nitride: A ²⁹Si, ²⁷AI, ²⁵M and *'Y MAS NMR and X-Ray Diffraction Study ". *J. Mater. Chem*, 1994. **4**(10): p. 1595-1602.
68. Guth J. R. and Petuskey. W. T., "Silicon-29 magic angle sample spinning nuclear magnetic resonance characterization of SiC polytypes". *J. Phys. Chem*, 1987. **91**: p. 201.
69. Leone, E.A., S. Curran, M.E. Kotun, G. Carrasquillo, R. Van Werren, and S.C. Danforth, "Solid-State ²⁹Si NMR Analysis of Amorphous Silicon Nitride Powder". *J. Am. Ceram. Soc.* , 1996. **79**: p. 513.

References.

70.	Metson J.B., "Charge compansation and binding energy referencing in XPS analysis". *Surf. Interface Anal.*, 1999. **27**: p. 1069-1072.

71.	Briggs D. and Grant T., *Surface analysis by Auger and X-ray photoelectron spectroscopy*. 2003: Surface spectra and IM publications.

72.	Briggs D. and Seah M.P., *Practicle surface analysis*. 2$_{nd}$ ed. Vol. 1. 1993: John Willey & Sons.

73.	Porte L. and Sartre A., "Evidence for a silicon oxycarbide phase in the Nicalon silicon carbide fibre." *J. Mater. Sci.*, 1989. **24**: p. 271-275.

74.	Arundale P. and Moulson A.J., "Microstructural changes during the argon sintering of silicon powder compacts". *J. Mater. Sci*, 1977. **12**: p. 2138-2140.

75.	De Angelis B.A., Rizzo C., Contarini S., and Howlett S. P., "XPS study on the dispersion of carbon additives in silicon carbide powders." *Applied Surface Science*, 1991. **51**: p. 177-183.

76.	Jennings H. M. and Richman M. H., "Structure, formation mechanisms and kinetics of reaction-bonded silicon nitride". *J. Mater. Sci.*, 1976. **11**: p. 2087-2098.

77.	Bjo¨rklund H, Wase´n J., and Falk L.K.L., "Quantitative microscopy of β Si$_3$N$_4$ ceramics". *J. Am. Ceram. Soc.*, 1997. **80**(12): p. 3061-3069.

78.	Björklund H. and Falk L. K. L., "β-Si$_3$N$_4$ grain growth, part II: Intergranular glass chemistry". *J. Eur. Ceram. Soc.* , 1997. **17**(11): p. 1301.

79.	Björklunda H., Falk L. K. L., Rundgrenb K., and Wasénc J., "β-Si$_3$N$_4$ grain growth, part I: Effect of metal oxide sintering additives ". *J. Eur. Ceram. Soc.*, 1997 **17** (11): p. 1285.

80.	Lange F.F., "Strong, high-temperature ceramics". *Annu. Rev. Mater. Sci.*, 1974. **4**: p. 365-390.

81.	Tsuge A. and Nishida K., "High- strength hot-pressed Si$_3$N$_4$ with concurrent Y$_2$O$_3$ and Al$_2$O$_3$ additions". *Am. Ceram. Soc. Bull*, 1978. **57**(4): p. 424-431.

82.	*HSC Chemistry software*, 6, Editor, OUTO KUMPO Technology.

83.	Haywood R., Sarvinis J., Monaghan A., and Baker P. W., "Intensive sidewall cooling in Hall Heroult cells". *COM Light Metals*, 2003: p. 77-90.

84.	Sun T., Pickrell G.R., and Browen J.J., "Corrosion kinetics of silicon nitride in dry air containing sodium nitrate vapors". *J. Am. Ceram. Soc*, 1994. **77**(12): p. 3209-3214.

85.	Mayer, M.I. and F.L. Riley, "Sodium-assisted oxidation of reaction-bonded Silicon Nitride". *Journal of material science*, 1978. **13**: p. 1319-1328.

86.	Hirao K., Nagaoka T., Brito M. E., and Kanzaki S., "Microstructure control of silicon nitride by seeding with rodlike β-silicon nitride particles". *J. Am. Ceram. Soc*, 1994. **77**(7): p. 1857-1862.